

**Annual Activity Report
on
Japan-ASEAN Science, Technology and
Innovation Platform (JASTIP),
Work Package 2 (WP2) –
Energy and Environment**

2020 Progress

Development of Carbons from Biomass for Energy Storage Applications

Research team:

Dr. Sumittra Charojrochkul, MTEC, NSTDA (Project leader, Thai side)

Prof. Dr. Takeshi Abe, Kyoto University (Project leader, Japan side)

Dr. Pimpa Limthongkul, MTEC, NSTDA

Dr. Yatika Somrang, MTEC, NSTDA

Asst.Prof. Dr. Yuto Miyahara, Kyoto University

Dr. Vituruch Goodwin, MTEC, NSTDA

Dr. Pannipa Tepamat, Thammasat University

Mr. Thanathon Sesuk, MTEC, NSTDA

2.1 Introduction

Thailand is an agricultural-based country which produces large amount of biomass but the majority of this abundant resources, especially agricultural leftover, has not yet been exploited extensively. Currently, the use of biomass in fuel application has been widely studied and practiced in order to reduce the reliance on petroleum-derived fuels. Not only its benefit as a substitute to conventional fuels, but bio-based economy can also be developed based on biomass. Biomass which mainly contains cellulose, hemicellulose and lignin can be converted into chemicals or valuable products. In fact, biomass is a major carbon source which can potentially be used in energy storage devices. Recently, there have been many previous works investigating the potential of using biomass as a source to produce carbons via carbonisation/hydrothermal carbonisation and/or chemical activation for energy storage applications. Pyrolysis or carbonisation is a conventional process; hence, it is not a complicate technology. Only some modification/configuration to the traditional method, i.e. introduction of porogen for pore activation, can significantly improve the properties of the carbon. Hence, due to its simplicity but high impact to the properties of carbon products, this technology is chosen in this work. However, the production of high-quality activated carbon from 'challenging' biomass, i.e. ash-containing biomass, particularly palm empty fruit bunch (PEFB), has not yet well established. In addition, the knowledge of how each biomass constituent affects the properties of activated carbon materials in aspect of physical and electrochemical characteristic is crucial to enhance the production of high-quality carbon materials for energy storage applications. This project, hence, aims to understand the role of precursor

constituents in various biomass on the electrochemical properties of the activated carbon and to develop method/conditions to produce the activated carbon from various type of biomass.

In this project, investigation of various ‘challenging’ biomass, i.e. palm empty fruit bunch (PEFB), durian peel and etc to produce activated carbon materials. This work is jointly collaborated between MTEC/NSTDA, responsible for producing activated carbon from biomass and performing physical characterisation of the obtained carbon, and Kyoto University, in charge of conducting electrochemical characterisation of the carbons for supercapacitor applications.

2.2 Scope of study

The schematic of an overall research scope and plan is shown in Figure 1.

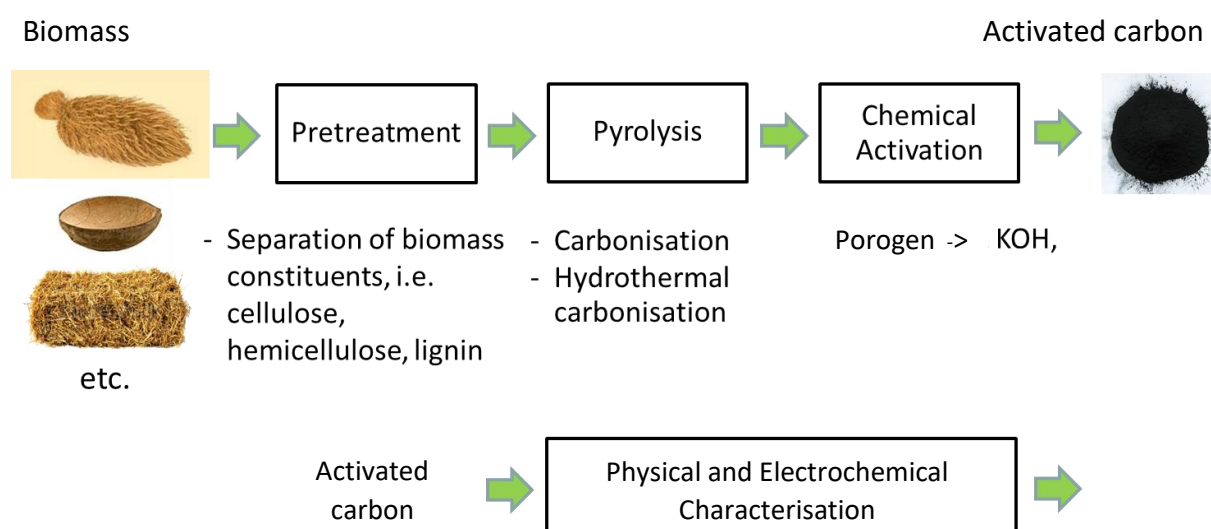


Figure 1 Schematic of an overall research plan.

Table 1 Yearly research plan

Year	Plan
2017-2018	- Carbonisation of various biomass from Thai agricultural residues
	- Characterisation of various biomass
	- Chemical activation of chars from carbonisation
	- Characterisation and Electrochemical properties evaluation of carbons
2019-2020	- Hydrothermal carbonisation of biomass
	- Characterisation of hydrochars
	- Chemical activation of hydrochars from hydrothermal carbonisation
	- Characterisation and Electrochemical properties evaluation of carbons

2.3 Research summary

2.3.1 Effect of activation temperature and KOH:Char ratio on carbonised biomass

Activated carbons from biomass were produced at different activation temperature and KOH:Char ratio. At KOH:Char = 1, specific surface area of activated carbon produced at 700-900 °C are insignificantly different. However, as per pore size distribution, the pore width of micropore decreases with increasing temperature as shown in Figure 2a. This causes shorter duration time of charge cycle (Figure 2b) and less capacitance (Figure 2c) in the carbon activated at 700 °C than those activated at higher temperatures. Figure 2c also shows that increasing activation temperature improves rate capability.

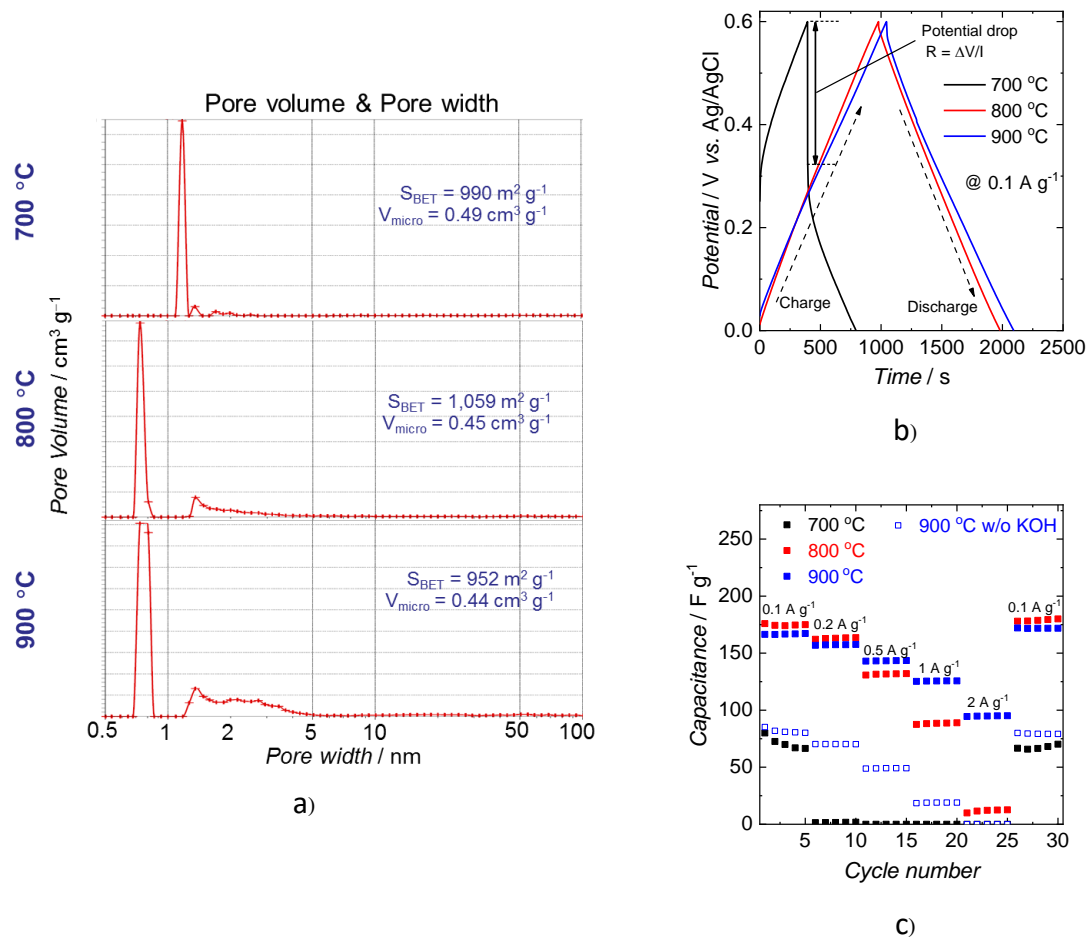


Figure 2 Physical and electrochemical properties of carbon produced at KOH:Char = 1. a) Surface area and pore size distribution; b) Potential profile vs. time; c) Capacitance at different current density

At KOH:Char = 3, increasing temperature improves both surface area and occurrence of mesopore as shown in Figure 3a. The charge cycle time of carbon produced at 700-900 °C (Figure 3b) are comparable while the rate capability improves with increase temperature as also observed at KOH:Char = 1. However, severe temperature (1,100 °C) results in crystalline structure (Figure 3d) and the EDLC performance of carbon appears to deteriorate.

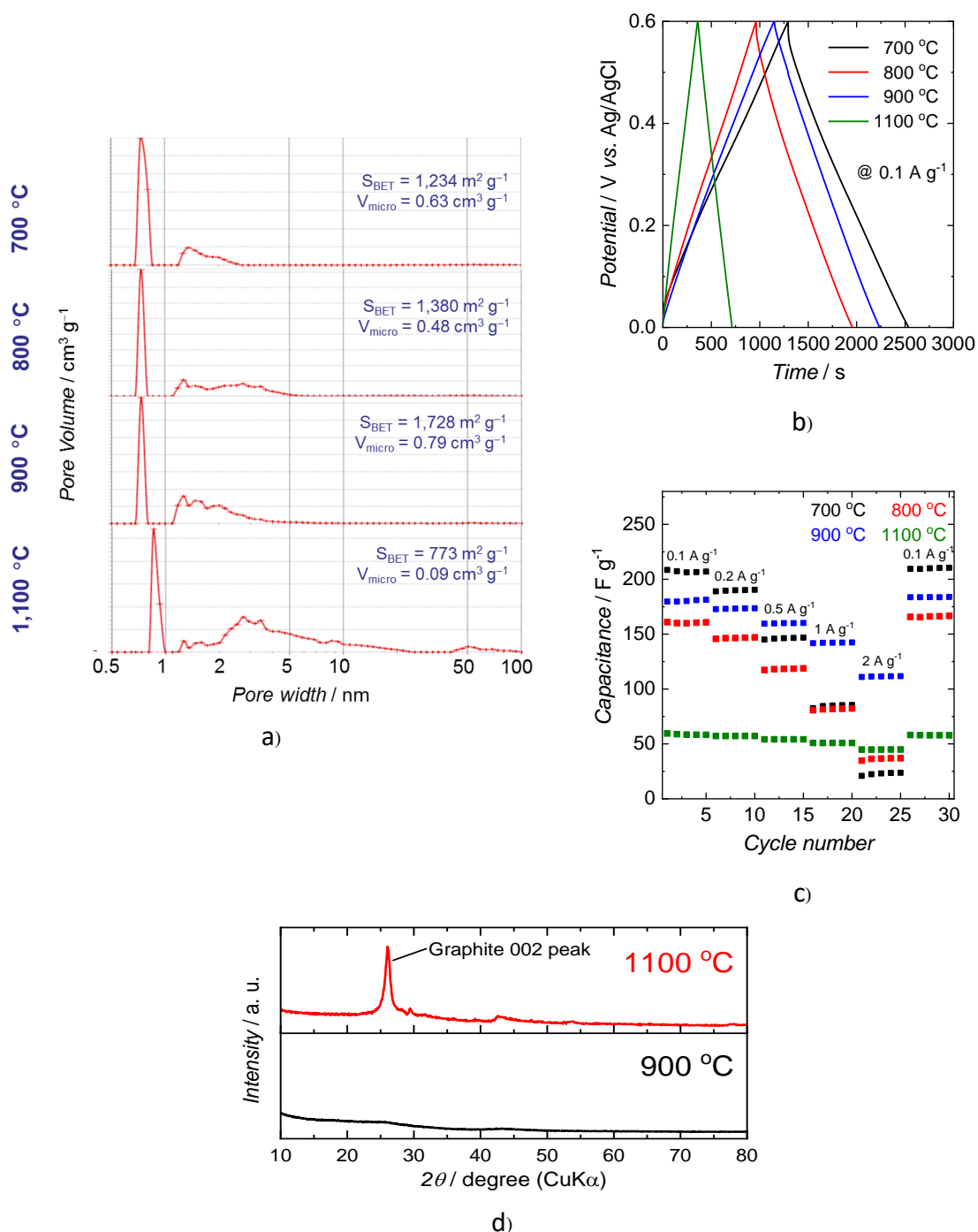


Figure 3 Physical and electrochemical properties of carbon produced at KOH/C = 3.

a) Surface area and pore size distribution; b) Potential profile vs. time; c) Capacitance at different current density; d) XRD spectra

At KOH:Char = 2, an increase in temperature improves both surface area and occurrence of mesopores as shown in Figure 2a. The charge cycle time of carbon produced at 700-900 °C (Figure 3b) are comparable while the rate capability improves with increasing temperature as also observed at KOH:Char = 1. However, severe temperature (1,100 °C) results in crystalline structure (Figure 3d) and the EDLC performance of carbon appears to deteriorate.

2.3.2 Effect of KOH-mixing sequence

Activated carbons from biomass were produced at different KOH-mixing sequence, i.e. KOH-Carbonisation-Activation (KCA) and Carbonisation-KOH-Activation (CKA). It can be observed that KCA yields better surface area and pore size distribution (high mesopore and smaller pore width of micropore) as shown in Figure 4a. This results in longer charge cycle time (Figure 4b). Moreover, as for KCA process, carbonisation at 500 °C appears to yield activated carbon with better pore morphology and, thus, electrochemical properties than that carbonisation at 300 °C.

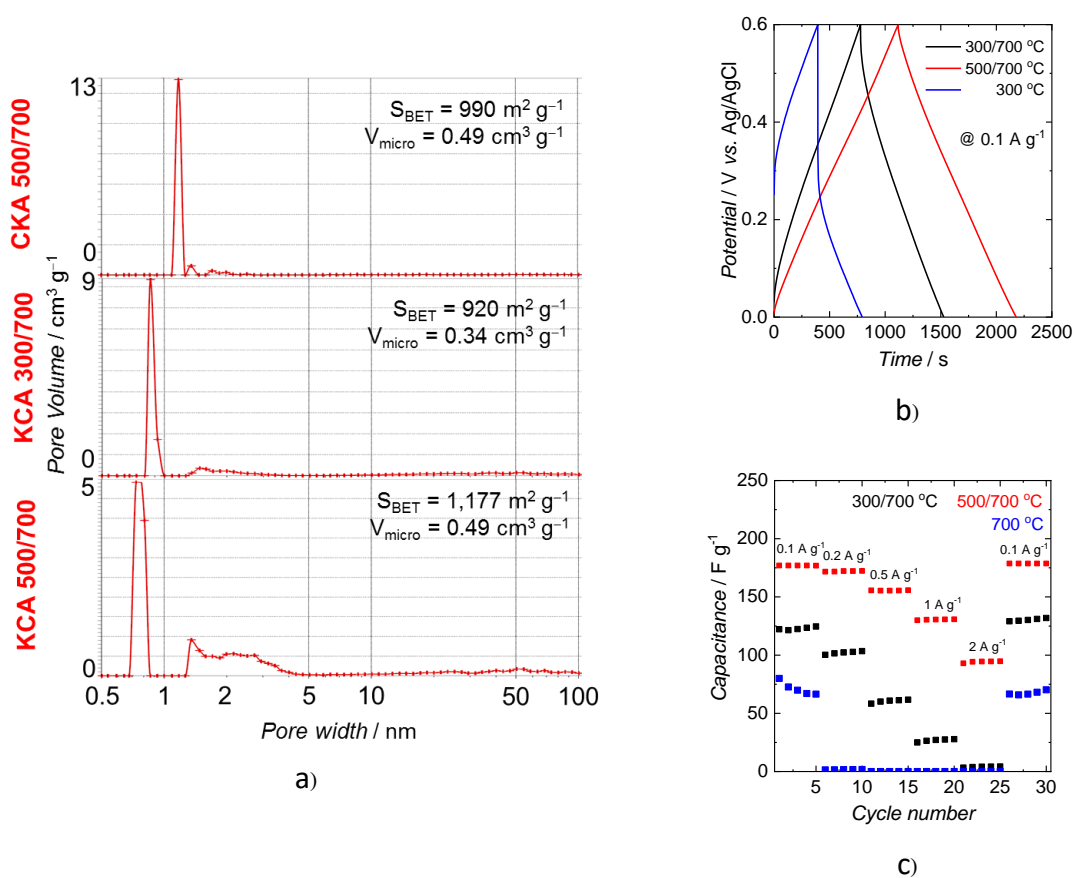


Figure 4 Physical and electrochemical properties of carbon with different mixing sequence. a) Surface area and pore size distribution; b) Potential profile vs. time; c) Capacitance at different current density

2.3.3 Characterisation results of biomass

Properties of biomass samples employed in this work were determined and tabulated in Table 2.

Table 2 Properties of biomass samples

Biomass	Proximate analysis (%db)			Ultimate analysis (%db)			
	Volatiles	Fixed Carbon	Ash	C	H	N	O
Palm empty fruit bunch (EFB)	77.3	17.0	5.7	46.2	5.7	1.4	40.9
Sugarcane bagasse (SB)	75.0	16.2	8.8	47.6	5.8	0.6	37.4
Palm shell (PS)	77.0	21.2	1.8	54.0	5.2	0.6	38.4
Eucalyptus wood chip (WC)	82.7	16.8	0.5	47.7	6.8	0.1	44.9
Durian peel (DUR)	77.5	18.2	4.3	44.3	5.9	1.2	44.3
EFB-C	80.3	15.3	4.4	41.8	6.1	0.7	47.0
EFB-S	82.7	15.4	1.9	46.5	6.2	0.9	44.5

Carbonisation of biomass samples were performed on various biomass from Thai agricultural residues, including palm empty fruit bunch (EFB), palm shell (PS), eucalyptus woodchip (WC), durian peel (DUR) and sugarcane bagasse (SB). All biomass was ground, milled and sieved to 75-150 μm and thermally carbonised at 500 $^{\circ}\text{C}$ to obtain char. The yield by weight of biomass chars and activated carbon are presented in Table 3.

Table 3 Yield of biomass char obtained by carbonisation at 500 $^{\circ}\text{C}$ and yield of activated carbon activated at 700 $^{\circ}\text{C}$.

Biomass	Char Yield (wt%)	Activated carbon Yield (wt%)
Palm empty fruit bunch (EFB)	27.28	13.06
Sugarcane bagasse (SB)	26.49	12.03
Palm shell (PS)	32.13	17.67
Eucalyptus wood chip (WC)	28.62	15.50
Durian peel (DUR)	31.54	12.83
Palm empty fruit bunch-Stem (EFB-S)	31.22	10.02
Palm empty fruit bunch-Core (EFB-C)	25.74	12.24

The proximate and ultimate analysis results of biomass revealed that palm shell contained the highest fixed carbon content at 21.2%. Other biomass samples have fixed carbon range from 15.3-21.2%. Palm shell gave the highest char and activated carbon yield as a result of its high fixed carbon content.

2.3.4 Characterisation of activated carbon from carbonisation of biomass

Biomass char samples were followed by chemical activation with KOH at 1:1 and 2:1 KOH:Char weight ratio (Effect of KOH:Char ratio on physical properties) under CO₂ atmosphere at 700-900 °C (Effect of activation temperature on physical properties). The activated carbon samples were characterised for their microstructure by SEM and TEM techniques. Specific surface area (BET) and porosity were analysed using N₂ adsorption. XRD patterns were obtained for crystalline and amorphous phase identification. X-ray diffraction patterns of all activated carbon samples from biomass shown two broad peaks at $2\theta = 24^\circ$ and 44° indicating amorphous carbon structure. No impurity phases were observed.

The specific surface area and pore volume of the activated carbons are summarized in Table 4. All activated carbon samples from carbonisation of biomass show micropores dominated pore structure, as indicated by the large surface area as well as high percentage of micropore volume (V_{micro}). The specific surface area is affected from activation temperature and KOH:Char ratio as previously discussed. Activated carbon from biomass prepared at activation temperatures of 700-900 °C showed the mesopore volume less than 50%. This may indicate both a widening of pores at high temperature and generation of new micropores by activating agent. The average pore diameter were nearly the same for all samples, approximately 4-6 Å. The size of the solvated HSO₄⁻ ion size is approximately 3-4 Å, therefore the pore size of activated carbon from biomass is large enough to accommodate H₂SO₄ electrolyte ions.

The effect of preparation conditions (KOH:Char ratio and activation temperature) of carbonised activated carbon samples including higher specific surface area as KOH:Char ratio increase from 1:1 to 2:1 and higher specific surface area as activation temperature increase from 700 °C to 900 °C.

Table 4 Specific Surface area (S_{BET}), total pore volume (V_{tot}), micro- (V_{micro}) and mesopore (V_{meso}) volume and percentage of micro- and mesopore volume in biomass activated carbon at 700-900 °C

Sample	S_{BET} (m^2/g)	V_{tot} (cm^3/g)	V_{micro} (t-plot)		V_{meso}		Pore width (Å)
			cm^3/g	%	cm^3/g	%	
11700-EFB	1103.35	0.43	0.40	93.02	0.03	6.98	6.01
21700-EFB	1203.80	0.47	0.46	97.87	0.01	2.13	4.17
11900-EFB	1545.13	0.65	0.58	89.23	0.07	10.76	4.35
21900-EFB	1571.03	0.83	0.53	63.86	0.30	36.14	5.22
11700-WC	1076.28	0.41	0.40	97.56	0.01	2.43	4.33
21700-WC	1432.08	0.57	0.53	92.98	0.04	7.54	4.21
11900-WC	1691.02	0.74	0.62	83.78	0.10	16.12	5.94
21900-WC	1702.06	0.77	0.62	80.15	0.15	19.48	4.22
11700-PS	1005.36	0.40	0.38	95.00	0.02	5.00	4.94
21700-PS	1540.34	0.61	0.59	96.72	0.02	3.27	4.26
11900-PS	1158.63	0.45	0.43	95.55	0.02	4.44	5.94
21900-PS	1470.07	0.59	0.55	93.22	0.04	6.77	4.26
11700-SB	1217.73	0.47	0.47	100	-	-	4.46
21700-SB	1850.69	0.81	0.68	78.16	0.13	16.04	5.73
11900-SB	1243.83	0.55	0.46	83.63	0.09	16.36	4.06
21900-SB	1542.29	0.74	0.54	72.97	0.20	27.02	5.35

Figures 5-8 are plots of pore volume vs. pore width showed that activated carbon (AC) produced with KOH:Char ratio equal to 1 contained mainly microspore and slightly developed mesopore. At 900 °C activation temperature microspore volume decreased compared to activation at 700 °C. While at KOH:Char ratio equal to 2, a development of mesopore is increased thus slightly decreased in microspore volume for activation temperature at 900 °C.

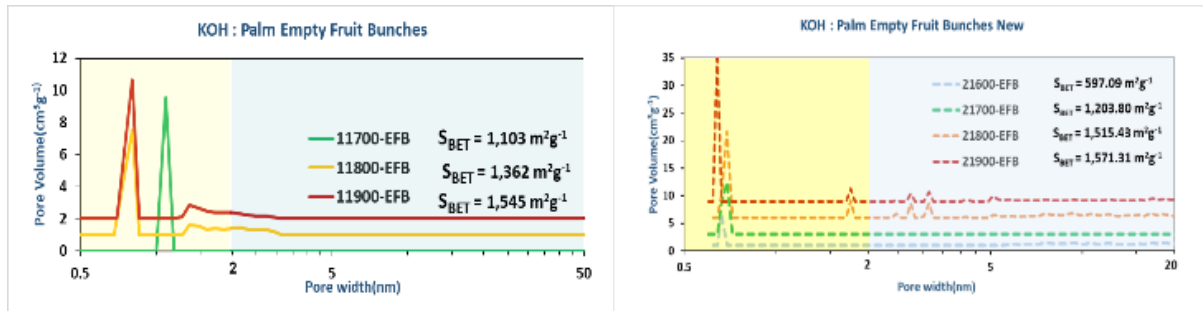


Figure 5 Pore volume vs. pore width of EFB AC with KOH:Char 1:1(left) and 2:1(right)

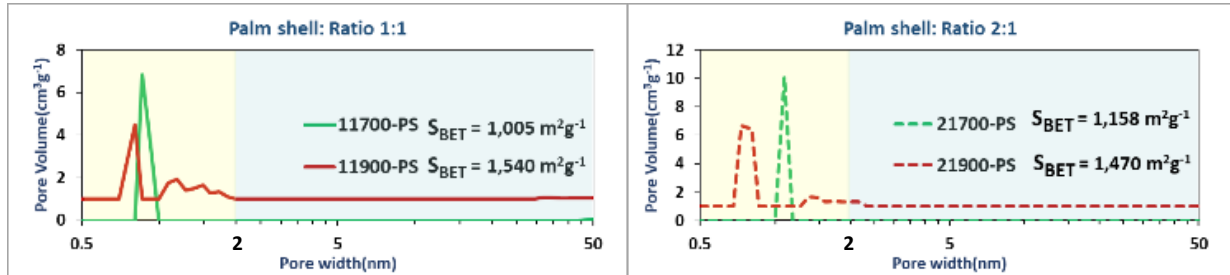


Figure 6 Pore volume vs. pore width of PS AC with KOH:Char 1:1(left) and 2:1(right)

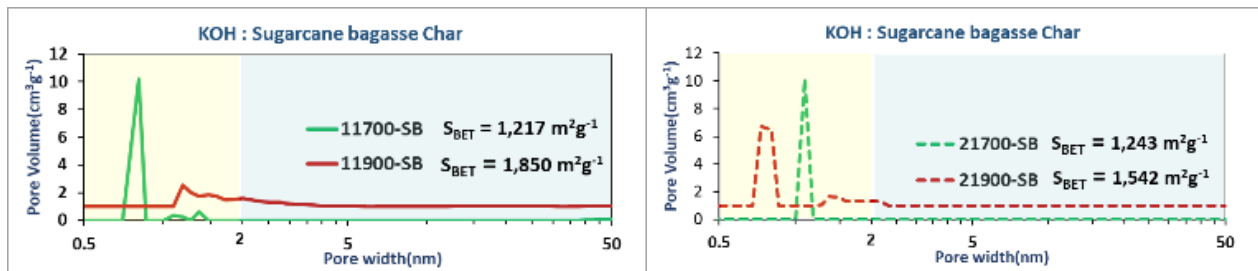


Figure 7 Pore volume vs. pore width of SB AC with KOH:Char 1:1(left) and 2:1(right)

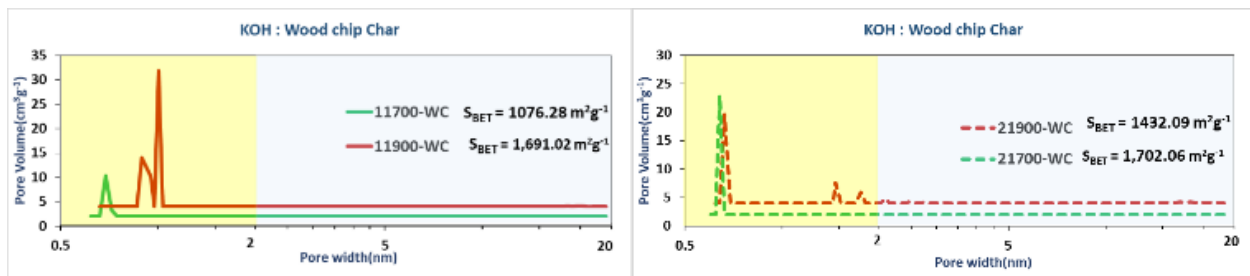


Figure 8 Pore volume vs. pore width of WC AC with KOH:Char 1:1(left) and 2:1(right)

In Figure 9 (a), X-ray diffraction results from activated carbon samples from EFB (21900-EFB) had a small peak at 26°. The peak corresponding to a short range order (graphite-like) structure which may be formed as indicated by the peaks at 20 □ 26.5° and 44.5° (JCPDS no. 75-1621) assigned to the (002) and (100) planes, respectively. The formation of graphite-like structure may have been facilitated by the combination of high temperature and high KOH content.

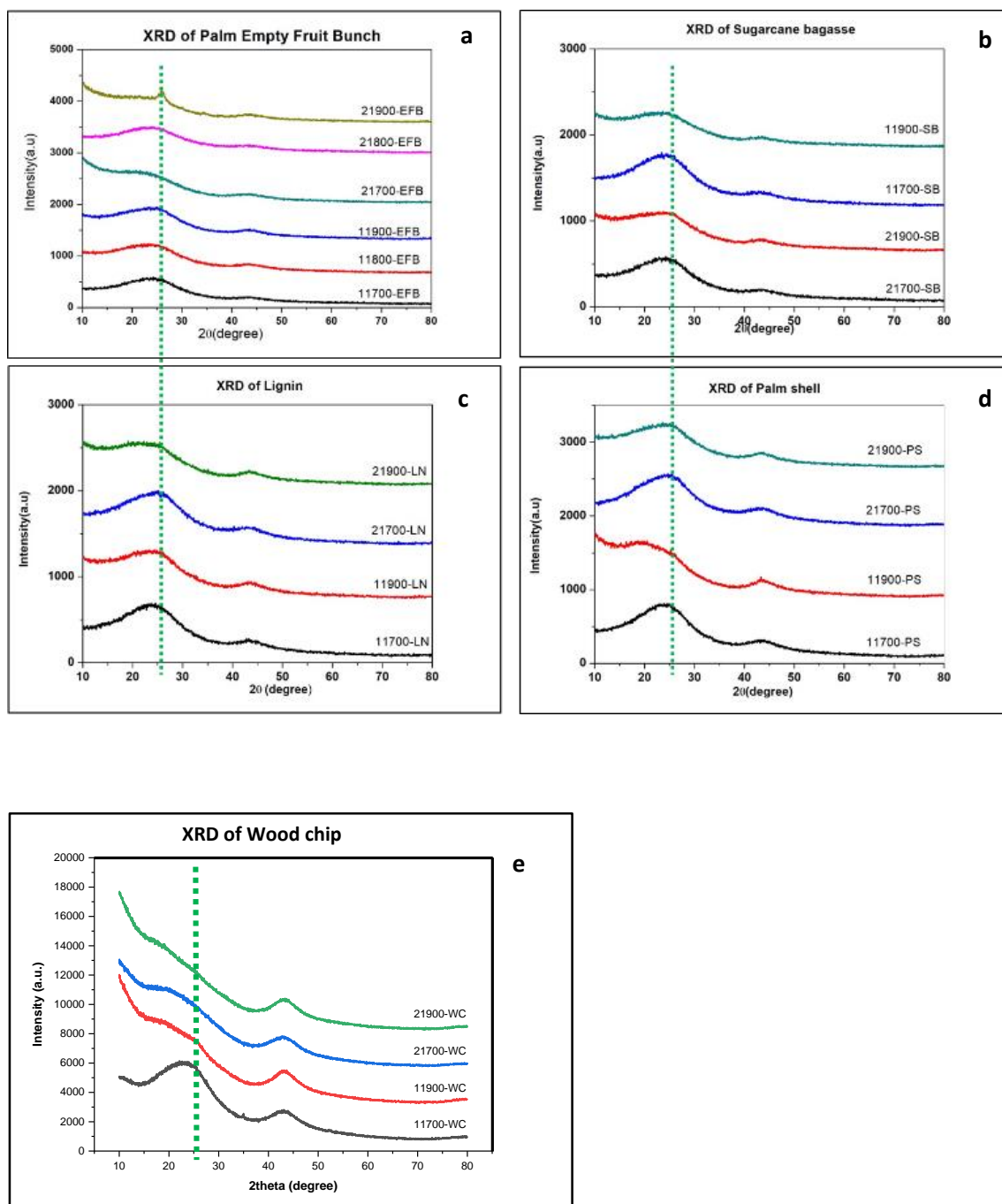
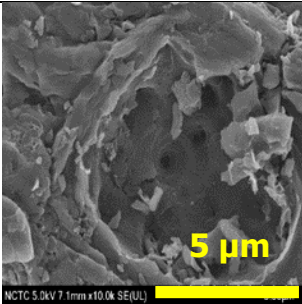
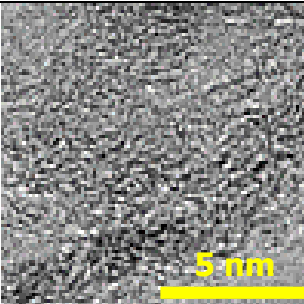
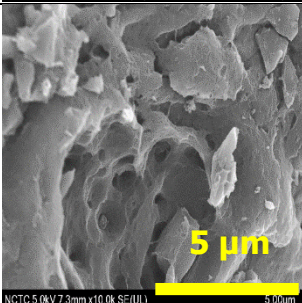
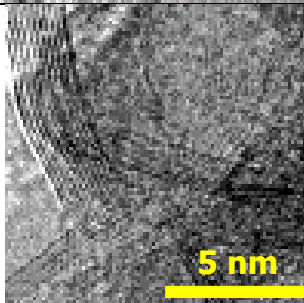
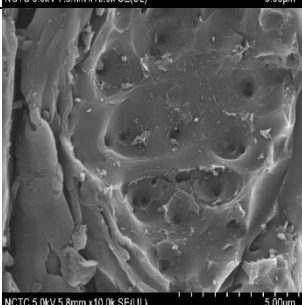
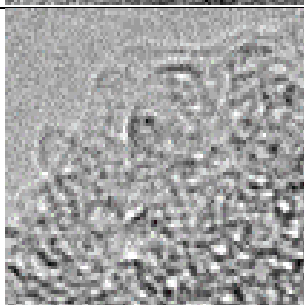
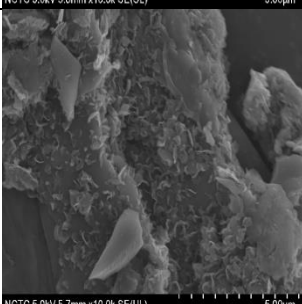
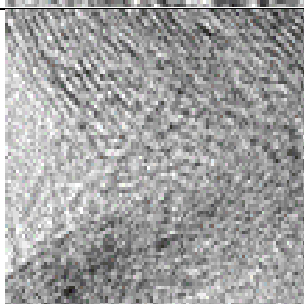
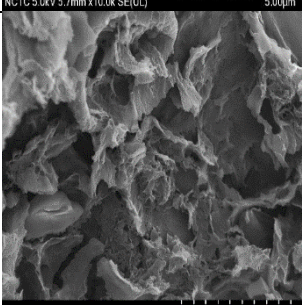
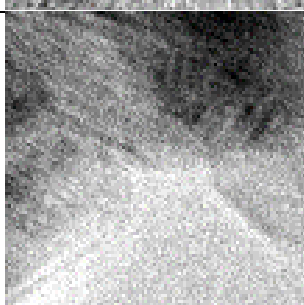


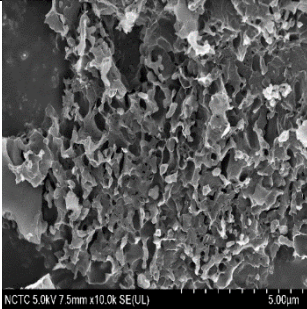
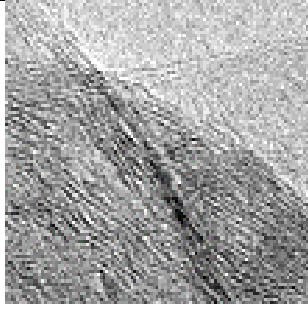
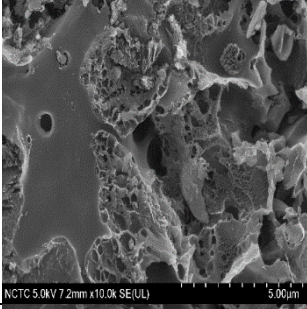

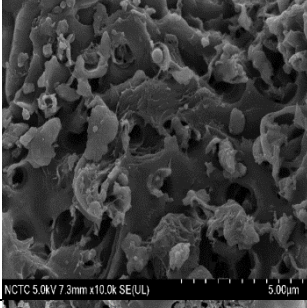

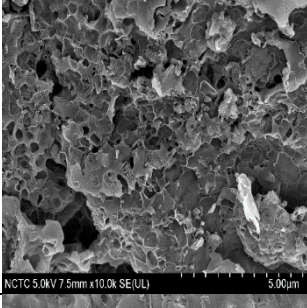
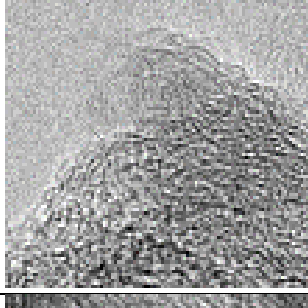
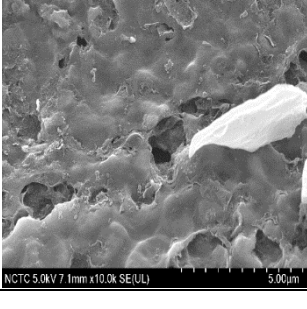

Figure 9 X-ray diffraction patterns of biomass activated carbon.

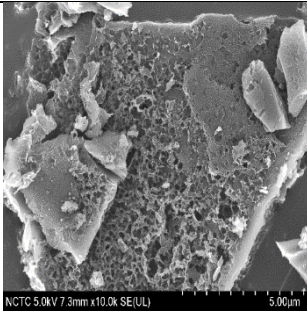
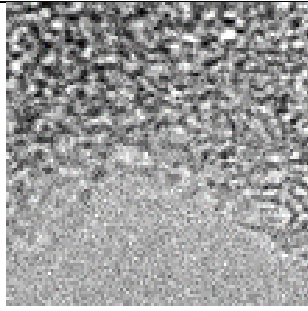
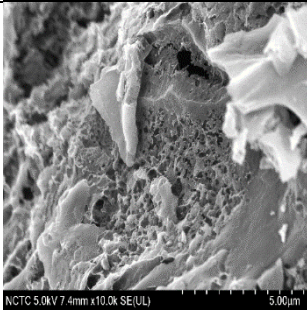
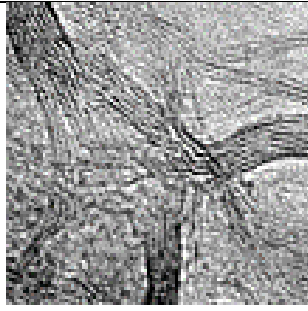
(a) EFB, (b) SB, (c) Lignin LN, (d) PS and (e) WC

Table 5 compiles Scanning electron images (SEM) and Transmission electron images (TEM) of activated carbons synthesised under various conditions.

Table 5 SEM and TEM images of biomass activated carbon

Biomass	KOH : Char (by weight)	Activation Temp. (°C)	SEM	TEM
Palm Empty Fruit Bunch (EFB)	1:1	700		
		900		
Palm Empty Fruit Bunch (EFB)	2:1	700		
		900		
Palm shell (PS)	1:1	700		

Biomass	KOH : Char (by weight)	Activation Temp. (°C)	SEM	TEM
		900		
Palm shell (PS)	2:1	700		
Palm shell (PS)	2:1	900		
Sugarcane bagasse (SB)	1:1	700		
		900		

Biomass	KOH : Char (by weight)	Activation Temp. (°C)	SEM	TEM
Sugarcane bagasse (SB)	2:1	700		
		900		

Scanning electron micrographs (SEM) for activated carbon from biomass samples activated at 700 °C using KOH:Char ratio equal to 1 have relatively smooth surface. When increasing the amount of KOH used to KOH:Char equal to 2:1, the activated carbon macrospores are clearly visible on the surface. Transmission electron micrographs (TEM) of all activated carbon samples contained amorphous carbon, except the activated carbon which was activated at 900 °C showed a small graphite-like structure which was a short range ordered structure imbedded in the amorphous matrix.

2.3.5 Electrochemical performance of activated carbon from carbonisation

To prepare working electrodes, activated material (Activated carbon) derived from various biomass was mixed with acetylene black (DENKA black Li-100) and binder PTFE (DuPont 6-J) in a mass ratio of 80:10:10, using ethanol as a dispersant. The obtained mixture was then made into a sheet and cut to 5mm x 5mm, then dried in vacuum oven at 80 °C for 12 hours. The electrochemical performance of the prepared electrodes was studied in a three-electrode system (Figure 10) using a HZ-Pro S12 Multi Electrochemical Measurement System (at Kyoto University, Japan). An Ag/AgCl electrode, and a Pt mesh were used as a reference electrode and a counter electrode, respectively. Aqueous 1M H₂SO₄ is a base electrolyte.

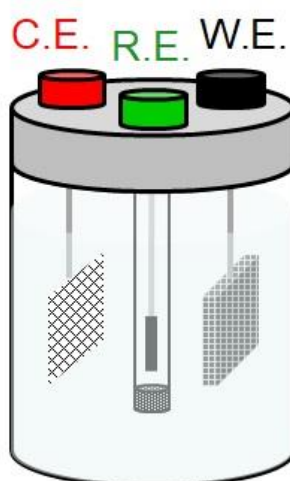


Figure 10 The three-electrode cells system for electrochemical performance testing.

Cyclic Voltammetry

The three-electrode cells with activated carbon electrode were subjected to cyclic voltammetry measurements, in order to determine the mechanism(s) for charge storage. A reaction peak in CV results would indicate that a charge storage takes place via reactions, which would yield pseudocapacitance. If no reaction peaks are observed, a charge storage is assumed to be mainly by electrostatic forces. Figure 11 shows the cyclic voltammetry results for the best-performing cells, where the carbon electrode is made from various biomass activated at 700 °C using KOH:Char = 2:1 by weight. The trend with voltage scan rate was typical for supercapacitor cells, in that a wider voltammogram, *i.e.*, higher current, was observed when a higher scan rate was used. The generated current is proportional to the scan rate. However, at slower scan rate, this process allows slower reaction to take place. Activation conditions affect the capacity, when increasing the KOH:Char ratio, the results tend towards high capacity and increasing of activation temperature tend towards the square shape and larger CV area at 20 mVs⁻¹. Activated carbon sample from EFB at KOH:Char ratio equal to 2 has the largest CV area and thus has the best electrochemical performance.

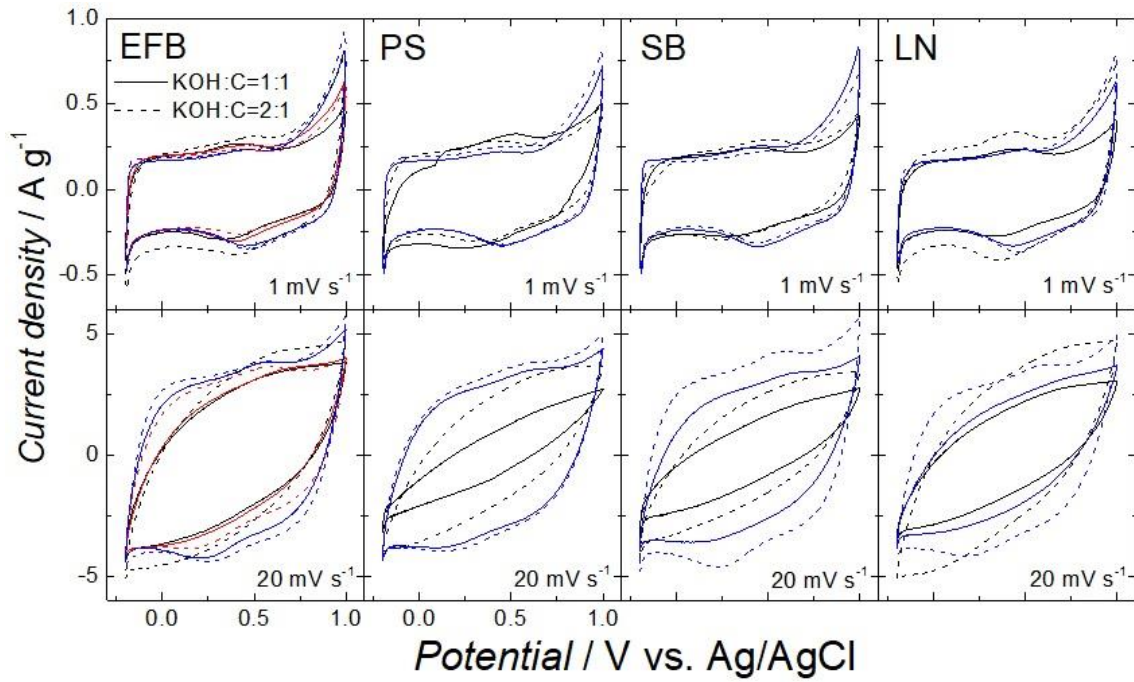


Figure 11 Typical cyclic voltammetry results of three-electrode supercapacitor cell with biomass activated carbon electrode.

Empty palm fruit bunch (EFB), Palm shell (PS), Sugarcane bagasse (SB) and Lignin (LN)

Galvanostatic Charge-Discharge

The three-electrode cells made from various biomass-derived activated carbons were tested by charging and discharging between 0 – 0.6 V using constant current levels of 0.1, 0.2, 0.5, 1 and 2 A/g of activated carbon. The specific capacitance, C_{sp} , which is calculated per weight of activated carbon was calculated from the discharge curves using the following equation:

$$C_{sp} \left(\frac{F}{g} \right) = \left(\frac{I \Delta t}{\Delta V} \right) \quad (1)$$

where I is the discharge current (A), Δt is the amount of time to discharge (s), ΔV is the difference in voltage from charged to discharged state (V), not including the IR drop due to equivalent series resistance (ESR) and M is the mass of the activated carbon in the electrodes (g). Typical charge-discharge diagram is shown in Figure 12.

A summary of the specific capacitance values obtained by galvanostatic charge-discharge test for the activated carbon samples synthesised under various conditions are shown in Figures 13-14. All activated carbons activated at 700 °C had slightly higher capacitance than those activated at 900 °C. For these samples, when comparing those treated using the same amount of KOH, the BET surface area and total pore volume values were not drastically different. However, the relative amount of micropore to mesopore was higher in those treated at 700 °C, which may have contributed to the higher capacitance. However, with increasing KOH:Char ratio at both activation temperatures, from 1:1 to 2:1 yielded higher

specific capacitance value that may be contributed by high BET surface area as well as high pore volume.

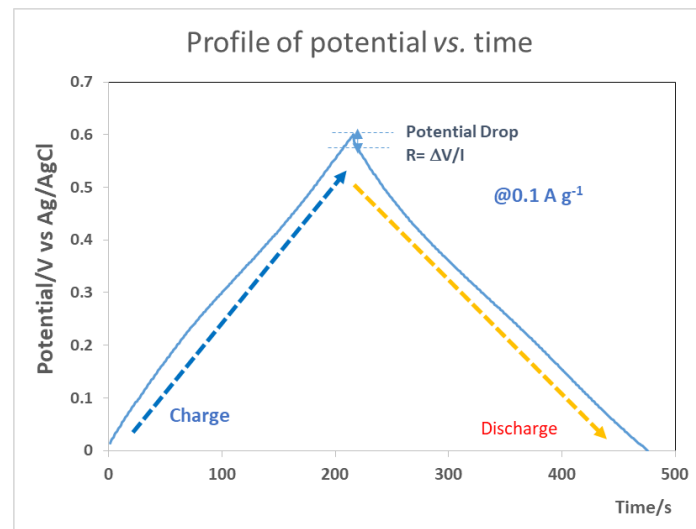


Figure 12 Typical Galvanostatic Charge-Discharge diagram.

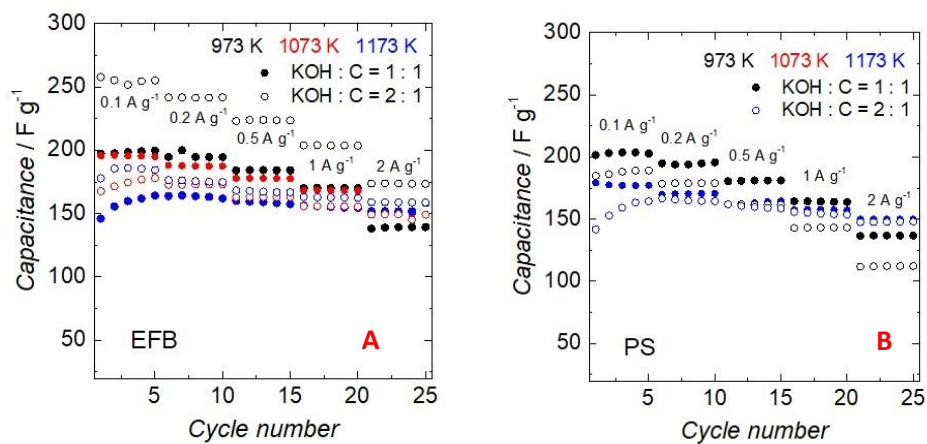


Figure 13 Capacitance VS cycle number at each current density
(A) EFB-Activated carbon and (B) PS-Activated carbon

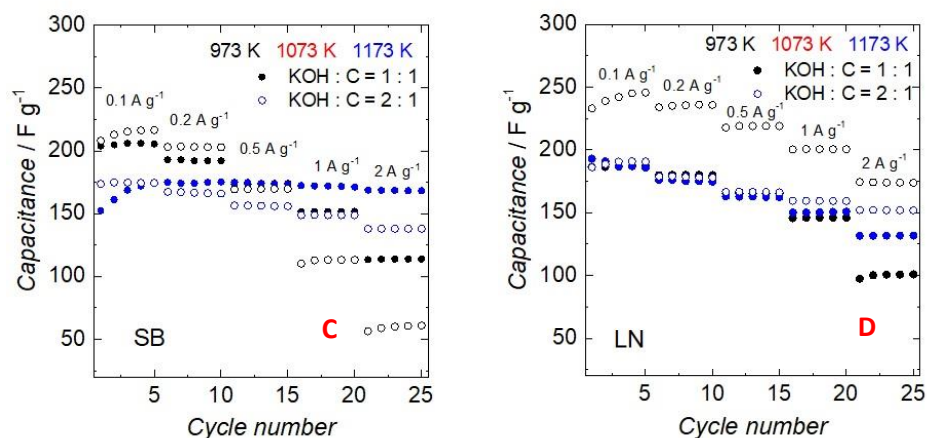


Figure 14 Capacitance VS cycle number at each current density
(C) SB-Activated carbon and (D) Lignin-Activated carbon

Table 6 Summary of capacitance of activated carbon electrodes from each condition

Materials	KOH:C	Activation Temp.	Capacitance at each current density, F g ⁻¹				
	by weight	°C	0.1 A g ⁻¹	0.2 A g ⁻¹	0.5 A g ⁻¹	1 A g ⁻¹	2 A g ⁻¹
Lignin (LN)	1:1	700	186.73	180.04	165.35	145.94	99.99
		900	176.55	170.39	160.41	149.38	123.28
	2:1	700	254.46	252.64	242.29	231.54	214.78
		900	189.35	178.36	166.47	159.40	151.99
Palm Empty Fruits Bunches (EFB)	1:1	700	198.58	195.80	184.25	170.30	139.07
		800	195.58	187.74	177.84	168.27	149.56
		900	157.61	163.53	158.94	155.39	153.20
	2:1	700	277.02	251.03	228.26	212.36	188.97
		800	175.28	172.93	163.08	155.87	148.55
		900	183.89	175.79	167.51	162.83	159.00
Sugarcane Bagasse (SB)	1:1	700	192.40	194.17	184.49	169.15	131.84
		900	165.78	174.73	174.21	171.87	168.51
	2:1	700	213.85	203.17	169.68	112.55	59.39
		900	178.14	166.72	156.29	148.84	138.06
Palm Shell (PS)	1:1	700	289.47	223.75	193.48	157.23	n/a
		900	182.06	170.43	163.30	157.59	149.97
	2:1	700	223.52	212.30	171.56	187.70	154.30
		900	156.31	165.37	159.99	154.61	147.82

A summary of the specific capacitance values obtained from galvanostatic charge-discharge testing for the activated carbons synthesised under various conditions is shown in Table 6. Activated carbon samples from EFB, SB, and Lignin prepared at activation temperature of 700 °C and KOH:Char ratio equal to 2 exhibit the highest capacity at 0.1 A/g charge/discharge rate, except PS (11700=PS) sample from KOH:Char = 1:1 has the highest capacity at 0.1 A/g charge-discharge rate. The rate capability should be evaluated together with

the specific capacity value. From current results, activated carbon prepared at activation temperature 900 °C and KOH:Char = 2:1 has shown better rate capability. Thus, optimization of activation conditions of biomass based activated carbon is crucial to improve both specific capacitance value and rate capability for the supercapacitor applications.

2.3.6 Hydrothermal carbonisation and characterisation of activated carbon

Activated carbon samples via hydrothermal carbonisation (HTC) were prepared from various biomass, similar to carbonisation samples described earlier. All biomass raw materials were ground, milled and sieved to 75-150 μm and hydrothermal carbonisation at 200 °C and 220 °C. Followed by chemical activation with 2:1 KOH:Char weight ratio. The HTC activated carbon samples were characterised for their microstructure by SEM and TEM techniques. The specific surface area (BET) and porosity of HTC activated carbon was analysed by N_2 adsorption at -196 °C. Table 7 displays surface area and pore properties of HTC activated carbon from biomass.

Table 7 Surface area, micro- (V_{micro}) and mesopore (V_{meso}) volume of hydrothermal activated carbon samples

Sample	S_{BET} (m^2/g)	V_{micro} (t-plot)		V_{meso}	
		cm^3/g	%Vol.	cm^3/g	%Vol.
HTC-A-200C	1560	0.64	91.64	0.06	8.36
HTC-B-200C	1552	0.61	91.80	0.06	8.92
HTC-C-200C	1272	0.45	87.92	0.06	12.08
HTC-A-220C	1239	0.43	94.60	0.02	5.40
HTC-B-220C	1341	0.52	92.95	0.04	7.05
HTC-C-220C	1373	0.47	86.33	0.08	13.67

Activated carbon from biomass hydrothermal carbonized at 200 °C results in high specific surface area from 1272-1560 m^2/g . These activated carbon had suitable surface and pore properties to be used in supercapacitor applications.

The three-electrode cells testing was performed using biomass-derived activated carbons from hydrothermal carbonisation. The charge and discharge voltage was set between 0 – 0.6 V using constant current levels of 0.1, 0.2, 0.5, 1 and 2 A/g of activated carbon. Typical charge-discharge diagram is shown in Figure 15.

For these biomass derived activated carbon samples, the relative amount of micropore to mesopore were high which may have contributed to the high capacitance. The report specific capacitance of biomass derived activated carbon samples in this project are ranged between 150-200 F/g

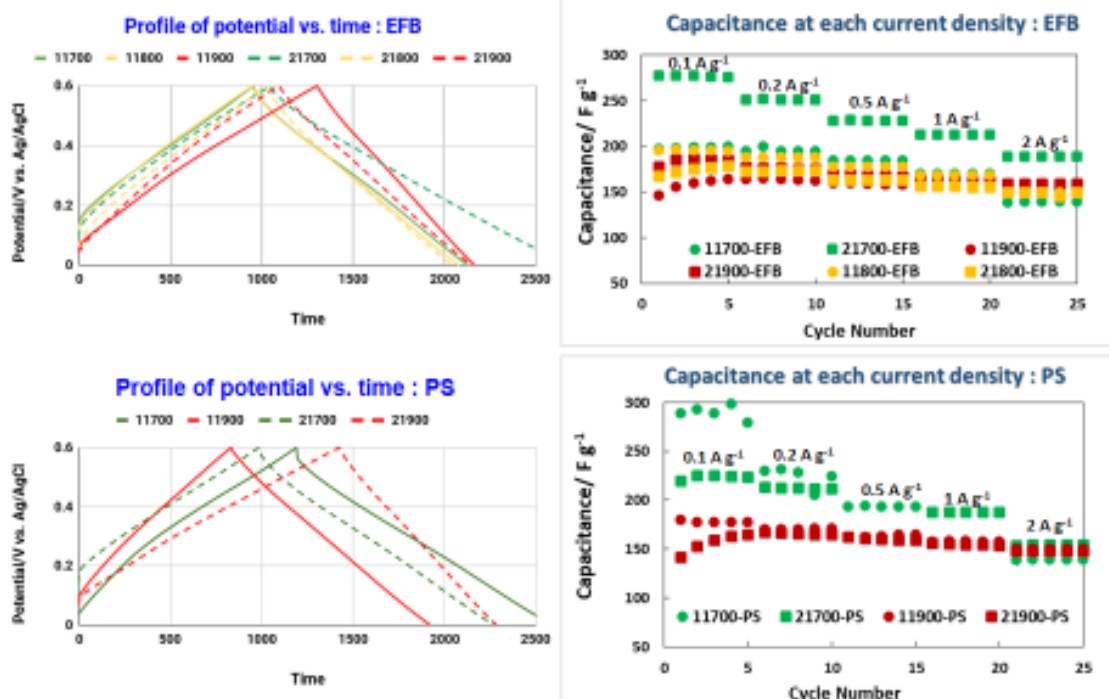


Figure 15 Typical Galvanostatic charge-discharge results of three-electrode supercapacitor cell with biomass activated carbon electrode tested at 0.1, 0.2, 0.5, 1 and 2 A/g

In summary, the specific capacitance values from galvanostatic charge-discharge testing for the activated carbons synthesised from biomass under various conditions were obtained. Both activated carbon samples from carbonisation and hydrothermal carbonisation of biomass activated with KOH:Char ratio equal to 2 exhibit the highest capacity at 0.1 A/g charge-discharge rate, in a range of 150 to 200 F/g. The rate capability should be evaluated from long term cycle stability test of supercapacitors. The coin cell configuration was chosen and during the two weeks visit at Kyoto University in 2019, MTEC researchers had an opportunity to learn the craft of electrode coating including slurry mixing, optimization of coating condition to achieve the electrode which is suitable for coin cell application. The supercapacitor coin cell can be prepared with the high standard similar to the commercial scale as shown in Figure 17. Selected supercapacitor coin cell long term cycling test of activated carbon from biomass results are shown in Figure 16.

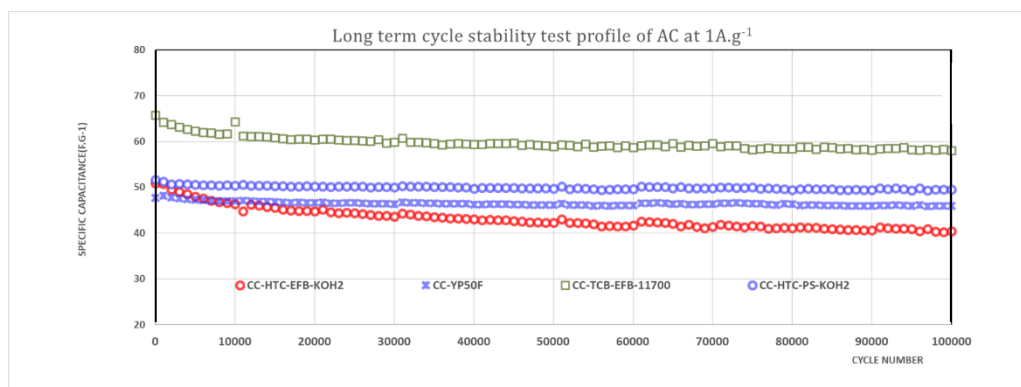


Figure 16 Long term cycling test results of selected coin cell supercapacitors








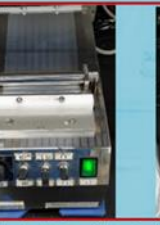
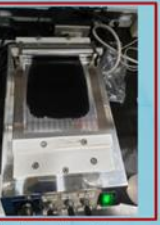



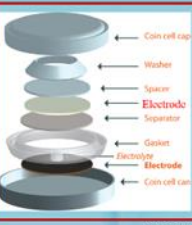



<h3>Casting Electrode</h3>  <p>1. Weigh & Grind AC with Conductive carbon in mortar (80:10 by wt.)</p>  <p>2. Transfer to mixing cup and weigh of liquid PVDF (10% by wt.) then, add NMP (solvent) until well mix</p>  <p>3. Mixing by Conditioning mixer for 10min at 1000rpm</p>	<h3>Casting Electrode</h3>  <p>1. Weigh & Grind AC with Conductive carbon in mortar (80:10 by wt.)</p>  <p>2. Transfer to mixing cup and weigh of liquid PVDF (10% by wt.) then, add NMP (solvent) until well mix</p>  <p>3. Mixing by Conditioning mixer for 10min at 1000rpm</p>
<h3>Casting Electrode (con.)</h3>  <p>4. Adjust applicator, lay aluminum foil on Coating Machine and pour ink on Aluminum foil, then switch on motor for moving the blade forward to cast</p>  <p>5. Dry in Vacuum oven overnight</p>  <p>6. Cut the electrode sheet in to a circle of coin cell size using high precision electrode cutting tool, weigh and measure thickness, then dry overnight</p>	<h3>Casting Electrode (con.)</h3>  <p>4. Adjust applicator, lay aluminum foil on Coating Machine and pour ink on Aluminum foil, then switch on motor for moving the blade forward to cast</p>  <p>5. Dry in Vacuum oven overnight</p>  <p>6. Cut the electrode sheet in to a circle of coin cell size using high precision electrode cutting tool, weigh and measure thickness, then dry overnight</p>
<h3>Coin cell assembly</h3>  <p>7. Assemble coin cell in glove box, using organic electrolyte TEABF₄/PC</p>   <p>Automatic Coin Cell Crimper</p>	 <p>Separator and Coin cells</p>

Figure 17 Carbon electrode casting and coin cell assembly for supercapacitor applications

Conclusions

From all the results, the performance of activated carbon used as a supercapacitor electrode depends very much on the processing conditions more than the raw materials and amount of lignin/cellulose/hemi cellulose. Activated carbon from Palm Empty Fruit Bunch (EFB) under hydrothermal preparation has shown a high potential to be used for this application from a long term cycle stability test. The specific capacitance was still nearly 60 F/g even after 100,000 cycles at 1 A/g which was better than a commercial reference. This part is under an IP filing process and would be the topic of our next phase research.

2.4 Project Output

2.4.1 Students and Researchers Exchange

- Four students from Thammasat University visited Kyoto University under the W&W Internship program in January and December 2018.
- Three researchers from MTEC visited Kyoto University in December 2019.

Year	Period	Name	
2019	17.11 - 03.12	Mr.Thanathon Sesuk	Asst. Researcher
		Dr.Vituruch Goodwin	Researcher
2018	27.11 - 27.12	Mr.Thanathon Sesuk	Asst. Researcher
		Mr.Tan Vongvarotai	BSc Student
		Ms.Sicha Arayatham	BSc Student
2018	04.01 – 26.01	Dr.Yatika Somrang	Researcher
		Ms.Nattida Konginyai	BSc Student
		Ms.Pakawan Prasatsoong	BSc Student

2.4.2 Conferences and Publications

- Somrang, Y., Sesuk, T., Miyahara, Y., Charojrochkul, S., Abe, T., Tepamatr, P. “Activated Carbon for EDLC Electrodes from Palm Empty Fruit Bunch”, 10th International Conference on Materials Science and Technology, 6-7 September 2018, Bangkok, Thailand.
- Goodwin, V., Sesuk, T., Miyahara, Y., Charojrochkul, S., Abe, T., Tepamatr, P. “Physical and Electrochemical Characterization of Activated Carbon for from Sugarcane Bagasse as Electrode for Supercapacitors”, Pure and Applied Chemistry International Conference 2020 (PACCON 2020), 13-14 February 2020, Bangkok, Thailand.
- Manuscript in preparation “Activated carbons from challenging biomass; role of precursor constituents on the electrochemical properties in supercapacitor applications”

2.4.3 Others

- drafted patent “Method of producing activated carbon from oil palm biomass for supercapacitor applications”



**Annual Activity Report
on
Japan-ASEAN Science, Technology and
Innovation Platform (JASTIP),
Work Package 2 (WP2) –
Energy and Environment**

2020 Progress

TABLE OF CONTENTS

<u>1. Innovations for Conversion of Biomass to High Value Chemicals by Photocatalytic Process</u>	4
<u>1.1Introduction and Rational</u>	4
<u>1.2Project Scopes</u>	6
<u>1.3Project Progress</u>	7
<u>1.4Conclusions</u>	63
<u>1.5Project Outputs</u>	64
<u>1.6References</u>	69

Innovations for Conversion of Biomass to High Value Chemicals by Photocatalytic Process

1. Innovations for Conversion of Biomass to High Value Chemicals by Photocatalytic Process

Surawut Chuangchote¹, Navadol Laosiripojana², Verawat Champreda³, Takashi Sagawa⁴

¹ Department of Tool and Materials Engineering, Faculty of Engineering, King Mongkut's University of Technology Thonburi (KMUTT), 126 Prachauthit Rd., Bangmod, Thungkru, Bangkok 10140, Thailand.

² The Joint Graduate School of Energy and Environment, Centre of Excellence on Energy Technology and Environment, King Mongkut's University of Technology Thonburi (KMUTT), 126 Prachauthit Rd., Bangmod, Thungkru, Bangkok 10140, Thailand.

³ National Center for Genetic Engineering and Biotechnology, 113 Phahonyothin Rd., Klong Luang, Pathumthani 12120, Thailand.

⁴ Graduate School of Energy Science, Kyoto University, Kyoto 606-8501, Japan.

Abstract

Application of photocatalytic processes for conversion of sugars which can be derived from lignocelluloses to energy and chemicals is considered a new promising environmentally friendly alternative which will play an important role in biorefinery and bioindustry related to valorization of sugars and agricultural wastes. This project aims to advance our technology on photocatalyst design under the JASTIP Renewable Energy program between NSTDA and Kyoto University (2015-2019). The project themes will cover (1) continual research on fabrication and modification of photocatalysts for conversion of sugars to high-value chemicals (*e.g.* functional sugar derivatives) by improving the catalyst's specificity by fabrication techniques or surface modification and (2) design and assembly of a prototype photocatalytic reactor. This concept on "photo-conversion on renewable biomaterials" will lead to the development of "photo-bio flow reactor" and will provide strong platform for conversion of sugars to value-added chemicals in integrative biorefinery.

Keyword Biomass, Photocatalysis, Sugar conversion, Lignin utilization, High-value chemicals, Sugar derivatives

1.1 Introduction and Rationale

Thailand is an agricultural-based country where lignocellulosic biomass can be considered as an important renewable energy resource for production of electricity, heat, liquid fuel, and commodity chemicals. This "biorefinery" concept can alleviate global warming due to the carbon neutral nature of the biomass and decrease the country's dependence of the depleting fossil resource. Biomass is the renewable resources (sustainable), which has its compositions similar to fossil fuel (contains C and H), and the products obtained from biomass are similar to those of petroleum. In details, lignocellulosic biomass is a multi-structure material. It consists mainly of three polymers *i.e.* cellulose, hemicelluloses, and lignin, which

are associated with each other in addition to small amounts of acids, salts, and minerals. Currently several technologies, including catalytic, thermochemical, and biotechnological routes have been investigated for conversion of biopolymers-derived intermediates from various agricultural wastes to a spectrum of value-added products. However, these technologies are thermochemically and/or biochemically conversion processes which are limited by some restrictions in practice, such as high cost of reagents and equipment, high energy consumption, and harsh reaction conditions. Some processes have to use high chemical contents and more production steps for efficient biomass conversion into fuels and chemicals. These cause high capital investment in term of energy input and chemical usage. The exploration of new routes for the production of platform chemicals or fuels from biomass thus becomes increasingly important.

Photocatalysis is one of promising processes for energy and chemical productions, because it can be performed under solar irradiation at room temperature and mild condition. It offers the possibility of extending the spectrum of applications to a variety of processes, including oxidations and oxidative cleavages, reductions, isomerizations, substitutions, condensations, and polymerizations. In addition, it is considered as clean, effective, energy-saving, technology simple, ecologically benign, and low cost strategy. Photocatalysis is a well-established technique for many applications, e.g. wastewater or air treatment, pollutant degradation, and hydrogen (clean fuel) production by water splitting. Titanium dioxide (TiO_2) is the most important photocatalyst for many applications, such as degradation of organic pollutants (Hwang *et al.*, 2012), production of hydrogen (Gomathisankar *et al.*, 2013), self-cleaning surfaces (Murugan *et al.*, 2013), and dye sensitized solar cells (Cheng *et al.*, 2013). TiO_2 is a white solid inorganic substance that occurs naturally in several kinds of rock and mineral sands. It is a semiconducting material, which can be chemically activated by light with band-gap energy (E_g) of 3.2 eV. TiO_2 exists in 3 different crystalline modifications, i.e. anatase, brookite, and rutile, where anatase exhibits the highest overall photocatalytic activity (Park *et al.*, 2013). It is a popular catalyst to use in photocatalytic reactions, because TiO_2 has a highly oxidative, chemically stable, inexpensive, and nontoxic nature. TiO_2 nanoparticles have been prepared by different methods such as, chemical precipitation (Mashid *et al.*, 2006), chemical vapor deposition (CVD) (Shi, J., & Wang, X., 2011), sputtering (Song *et al.*, 2009), sol-gel technique (Bahadur *et al.*, 2011), hydrolysis, micro-emulsion method (Shen *et al.*, 2011), aerosol-assisted chemical vapor deposition (Tahir *et al.*, 2012), spray deposition (Bujnova *et al.*, 2010), thermal plasma (Tanaka *et al.*, 2011), hydrothermal method (Oh *et al.*, 2009), microwave-assisted hydrothermal synthesis (Melis *et al.*, 2012), solvothermal method (Zhang *et al.*, 2009), and the flame combustion method (Zhao *et al.*, 2007). Among these methods, sol-gel method is one of the most popular techniques for preparation of nanosized metal oxide materials with high photocatalytic activities (Su *et al.*, 2004; Tseng *et al.*, 2010).

In this proposed project, the application of photocatalytic approach for chemical production will be investigated based on the close collaboration between JGSEE, BIOTEC, and The University of Kyoto under the JASTIP Renewable Energy collaboration. The work will include the development of novel photocatalysts for highly efficient conversion of sugars and lignin to value-added chemicals. Together with the design and assembly of photocatalytic reactor with the concept on development of bio-energy devices in combination with efficient

utilization of solar energy by Kyoto U., this collaboration will provide strong platform alternative technology for utilization of biomass in bio-industry which will contribute to the government's strategy on new S-curve industry.

1.2 Project Scopes

This project aims to develop high performance photocatalysts and photocatalytic reactor for production of target chemicals from glucose which can be obtained from 1st generation or 2nd generation raw materials in biorefinery. The project will focus on synthesis and fabrication of nano-scaled photocatalysts with improved performance and characterization of physicochemical properties of self-synthesized photocatalysts compared to commercial catalysts. The work will include the study of photocatalytic reactions on synthesis of high-value products (functional sugar derivatives) from glucose and application of the developed photocatalysts for production of target chemicals in photocatalytic reactor. The specific technical objectives are as follows:

- (a) To study the effects of fabrication conditions, doping and surface modification on morphotological appearances, physico-chemical properties, photocatalytic activity and selectivity of the photocatalysts
- (b) To study the effects of chemical structures of sugars on mechanisms of photocatalytic reactions
- (c) To study the reaction pathways for photocatalytic conversion of sugars (e.g. glucose) to its derivatives or unconventional sugars
- (d) To design and assemble a prototype laboratory-scale photocatalytic reactor (photo bio-flow reactor)
- (f) To study the reaction kinetics on sugar conversion to target chemicals in photo-bio flow reactor

1.3 Project Progress

As a major imported of solar source, photocatalysis process is one of the promising technologies which can be applied under solar irradiation at room temperature and mild condition. Heterogeneous photocatalysis employs as an alternative semiconductor material. Among them titanium dioxide (TiO_2) has been widely used to be the most attractive photocatalyst in term of chemical stability, non-toxicity, and expressed high photocatalytic activity [Pelaez, et al., 2012]. However, its main drawback is performed under UV light irradiation ($\lambda < 380 \text{ nm}$) corresponding to its large band gap energy. Therefore, modification of TiO_2 with additional of dopant is an aiming for the absorption of photocatalyst shift to visible light [Liu, et al., 2011; Gong, et al., 2015]. Moreover, modified new material is a point of view to improve yield and selectivity of valuable products [Ong, et al., 2016; Xu, et al., 2016, Kameyama, et al., 2015].

1.3.1 Materials and method

1.3.1.1 Materials

Titanium(IV) butoxide ($\text{Ti}(\text{OC}_2\text{H}_5)_4$; Sigma-Aldrich, USA), acetylacetone (ACA; Sigma-Aldrich, USA), and isopropyl alcohol (Sigma-Aldrich, USA) were used to prepare titanium dioxide (TiO_2) sol. All chemical for non-metal source include glucose ($\text{C}_6\text{H}_{12}\text{O}_6$); boric acid (H_3BO_3); ammonia (NH_3), and metals source: copper nitrate trihydrate ($\text{Cu}(\text{NO}_3)_2$); silver nitrate (AgNO_3); chromium(II) acetate ($\text{Cr}_2(\text{CH}_3\text{CO}_2)_4(\text{H}_2\text{O})_2$); indium(III) nitrate hydrate ($\text{In}(\text{NO}_3)_3 \cdot 3\text{H}_2\text{O}$); nickel(II) nitrate hexahydrate ($\text{Ni}(\text{NO}_3)_2 \cdot 6\text{H}_2\text{O}$); Strontium nitrate ($\text{Sr}(\text{NO}_3)_2$) were manufactured from (Wako, Japan) for modification of TiO_2 . Acetonitrile (ACN; RCI Labscan Co., Ltd., Thailand). Glucose monohydrate was obtained from Carlo Erba Reagents Co. (France) for photocatalytic reaction.

1.3.1.2 Synthesis of TiO_2 photocatalyst nanoparticle

A series of pure, non-metal and metal doped on TiO_2 were prepared using a sol-gel method. In details, a titanium precursor solution was prepared by mixing 4.36 ml of titanium butoxide with 1.26 ml of acetyl acetone under continuous stirring at room temperature which referred as solution A. Then, solution B was prepared by mixing 20 ml of 2-propanol, 15 ml of DI water and appropriate amount of non-metal and metal dopant. After that, solution B was added dropwise to solution A under continuous stirring. The resultant mixture was stirred for 3 hours at room temperature, followed by aging in oil bath at 80°C for 12 h. The obtained gel was dried by hot-pate at 100°C for 8 h. Finally, dry particles were grounded and calcined in a muffle furnace at 400°C for 3 h to obtain TiO_2 powders.

1.3.1.3 Synthesis of TiO_2 photocatalyst nanofiber

TiO_2 nanofibers were synthesized based on the electrospinning method in an in-house design. The solution was performed in methanol (10 mL) with 0.8 g of poly(vinylpyrrolidone) (PVP; Mw) 1 300 000, Aldrich), 4 g of titanium(IV) butoxide (TiBu; Aldrich), and 1.175 g of

acetylacetone (ACA; Aldrich). The obtained solution was stirred overnight (12 h) to obtain a homogenous solution. Then, the appropriate amount dopant was added into the solution and stirred overnight. The obtained spinning solution was loaded into a plastic syringe with the nozzle-end which adjustable of 22-gauge stainless steel needle. The emitting electrode of positive polarity from a Gamma High Voltage Research power supply was connected to the nozzle, while the grounding electrode was attached to a sheet of aluminum, used as the stationary collector plate. The distance between nozzle-end and collector was applied of 15 cm. with an electrical potential of 15 kV. The flow rate of syringe pump was 1.0 ml h^{-1} . The obtained fibers were collected approximately 5 hours under atmospheric condition to allow the complete hydrolysis. The electrospun fibers was then calcinated at 500°C for 2 hours.

In order to synthesized TiO_2 hollow nanofibers the in-house designed coaxial nozzle electrospinning was performed. The solution was prepared according to the previous procedure. Then, the solution was added two through syringe pumps. The flow rate of inner and outer were controlled at 1.0 ml h^{-1} and 2.0 ml h^{-1} , respectively. Further processes were conducted based on the previous procedure.

1.3.1.4 Synthesis of graphitic carbon nitride ($g\text{-C}_3\text{N}_4$)

The $g\text{-C}_3\text{N}_4$ (**Fig. 1**) was synthesized by thermal polymerization, 3 g of urea was put into a crucible which was then heated in a furnace at a rate of 4°C min^{-1} and kept for 2 h at 500°C . After cooled down to room temperature, it was ground to powder for further experiment.

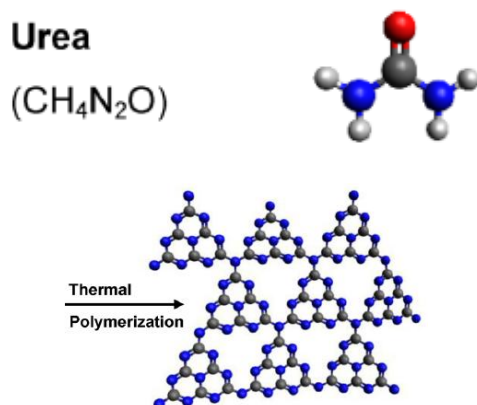


Fig. 1. Schematic structure of graphitic carbon nitride ($g\text{-C}_3\text{N}_4$) [Ong, W.J., et al., 2016]

1.3.1.5 Synthesis of nanoparticles $\text{ZnS}_{2(1-x)}\text{-AgInS}_x$ ($\text{ZAIS}(x)$)

The synthesis of quantum composite was studied according to previous method [Torimoto, et al., 2007]. Briefly, solid solution nanoparticles of ZnS-AgInS_2 were prepared by thermal decomposition of a metal ion-diethyldithiocarbamate complex of $(\text{AgIn})_x\text{Zn}_{2(1-x)}(\text{S}_2\text{CN}(\text{C}_2\text{H}_5)_2)_4$. The precursor powder was prepared by mixing 50 cm^3 of a sodium diethyldithiocarbamate aqueous solution ($0.050 \text{ mol dm}^{-3}$) with 50 cm^3 of an aqueous solution containing AgNO_3 , $\text{In}(\text{NO}_3)_3$ and $\text{Zn}(\text{NO}_3)_2$ with a mole ratio of $x:x:2(1-x)$ (total concentration of metal ions: $0.025 \text{ mol dm}^{-3}$) followed by washing with water and methanol several times and drying. A 100 mg of precursor powder was put into a test tube and heat-treated at 180°C for 3 min in an N_2 atmosphere. Then oleylamine (6.0 cm^3) was added the thus-obtained brown powder, followed by further heat treatment at 180°C for 3 min in an N_2 atmosphere. The

obtained mixture was centrifuged at 3,000 rpm for 5 min and the supernatant was collected by removing the larger particle. Suitable amount of methanol was added to the supernatant containing nanoparticles of ZAIS followed by centrifugation at 5,000 rpm for 5 min. The obtained ZAIS precipitate was dispersed in toluene for further study.

1.3.1.6 Characterization of photocatalysts

The synthesized photocatalytic samples were characterized according to the following techniques: The morphologies appearances of photocatalyst was conducted by an emission scanning electron microscope (FESEM; HITACHI SU-6600) with the use of energy-dispersive X-ray (EDX). The specific surface area, pore size and pore volume of the samples were carried out according to Brunauer-Emmett-Teller (BET) method (BEL Japan, BELSORP 18) by N₂ desorption at 77 K. The optical properties were analyzed using diffuse reflectance UV-vis absorption spectrophotometry (JASCO V-550). The UV-visible absorption spectra were acquired as the dry-pressed vessel of the samples with applying BaSO₄ as the reference sample (UV-vis DRS; Jasco V-550). The absorption spectra were recorded in air at room temperature with an integrating sphere in the range of 200-800 nm. The band gap values were calculated based on Tauc plot equation.

$$\alpha h\nu = A(h\nu - E_g)^n$$

where A is a constant, α is photo absorption coefficient, $h\nu$ is photon energy, E_g is average energy gap, and n is 2 for allowed indirect transition. The photoluminescence spectra (PL) were measured at room temperature using a Spectro-fluorophotometer (PL; JASCO FP-8600) with excitation wavelength of 270 nm with the scanning range of 300-900 nm. The crystalline and phase analysis were determined by X-ray diffraction (XRD; Rigaku, Smartlab) using Cu-K α radiation with the angles scanning of 20-80° (2 θ) at 40 kV and 30mA. The approximate crystalline size of sample was calculated using the Scherrer equation:

$$D = \frac{K\lambda}{\beta \cos \theta}$$

Where D is the crystalline size, the coefficient (K=0.94), β is the full-width at half-maximum (FWHM) of the diffraction peak of anatase phase [101], θ is diffraction angle, and λ is the wavelength of X-ray corresponding to the Cu K α irradiation ($\lambda = 1.5406 \text{ \AA}$)

1.3.1.7 Photocatalytic reaction of glucose under UV-light

The reaction was prepared in a mixture of distilled water and acetonitrile (10:90 v/v) (Colmenares et al., 2011). The prepared solution (400 ml) was transferred into a Pyrex cylindrical double-walled reactor. The concentration of glucose solution (1 g/l) and photocatalyst loading (1 g/l) were mixed together under dark condition and continuous stirring for 30 min to reach an absorption-desorption equilibrium. A mercury lamp 450 W (250-365 nm, UM-452, USHIO, Japan) located inside the reactor as a light source to irradiate the samples. The reaction temperature was maintained by a cooling water system at 25°C. The samples were taken from the photoreactor at specified times for analysis.

1.3.1.8 Photocatalytic reaction of glucose under visible-light

The glucose solution was prepared in a mixture of distilled water and acetonitrile (10:90 v/v) (Colmenares et al., 2011). The prepared solution was performed in quartz vessel with working volume of 3 ml. The various types of photocatalyst were presented in the photocatalytic reaction. The concentration of glucose solution (1 g/l) and photocatalyst loading (1 g/l) were mixed together under dark condition and continuous stirring for 30 min to reach an absorption-desorption equilibrium. The samples were irradiated under 450 W Xenon lamp equipped with controller (Wacom, Japan) and sharp cut-off filter (code number L38 $\lambda > 380$ nm and L42 $\lambda > 420$ nm; Hoya, Japan). The position between light source and reactor was fixed with 10 cm. The reaction temperature was maintained at room temperature ($\sim 25^\circ\text{C}$). The samples were taken from the photoreactor at specified times for analysis by HPLC.

1.3.1.9 Products analysis

The samples were taken from the photoreactor at specified times. The liquid product was filtered by a 0.22- μm nylon filter before analysis. The chemical products were monitored by a high performance liquid chromatography (HPLC, Shimadzu, LC-10AD pump, Japan) equipped with a refractive index detector (Shimadzu RID-10A, Japan). Separation was performed on an Aminex HPX-87H column (300 x 7.8 mm) (Bio-Rad, USA). The mobile phase was 5 mM sulfuric acid at a flow rate of 0.5 mL/min and injection volume was 20 μL . HPLC was used for analysis of the content of organic products and glucose conversion.

1.3.1.10 Preparation of TiO_2 coated on supporter

I. Dip coating technique

A titanium precursor solution was prepared by mixing 4.36 ml of titanium butoxide with 1.26 ml of acetyl acetone under continuous stirring at room temperature which referred as solution A. Then, solution B was prepared by mixing 20 ml of 2-propanol, 15 ml of DI water and appropriate amount of non-metal (NH_3) and metal dopant (AgNO_3). After that, solution B was added dropwise to solution A under continuous stirring. The resultant mixture was stirred for 30 min at room temperature. Supporter (ceramic, and alumina ball) was dipped into Ag-N/ TiO_2 sol and were remain for 2 min for complete adsorption of the catalyst. Then the catalyst was dried at 80°C for 30 min. After repeat 3 times, obtained catalysts were dried at 80°C for 24 h. Finally, it was calcined in a muffle furnace at 400°C for 3 h to obtained Ag-N/ TiO_2 coated on supporter.

II. Aging technique

The synthesis of Ag-N/ TiO_2 nanoparticles was carried out with the same procedure as mention before. For aging, ceramic balls were added into solution before aging in the oven. The obtained samples were dried by hot-pate at 100°C for 8 h. Finally, Ag-N/ TiO_2 coated on ceramic ball was calcined in a muffle furnace at 400°C for 3 h.

III. Evaporation technique

The process was performed in the same with dip coating step. Firstly, ceramic balls were mixed with the solution the vessel. Then, the suspension was heated by using a

rotary evaporator (90 °C, 50 mbar) to evaporate the solvent. After complete drying, it was calcined in a muffle furnace at 400°C for 3 h to obtained Ag-N/TiO₂ coated on supporter.

IV. Impregnation

Ag-N/TiO₂ powder was dispersed in ethanol and then ceramic balls were dipped into the suspension. The suspension was blended to achieve well dispersion for Ag-N/TiO₂ nanoparticles on surface of ceramic balls. After that, ceramic balls were calcined at 400 °C for 3 h to obtained Ag-N/TiO₂ coated on supporter.

V. Dip coating with binder (Polyvinyl alcohol, PVA)

The process was performed in the same with dip coating technique. In this step, polyvinyl alcohol (PVA) was added into DI water before mixing with 2-propanol. After that, solution was added dropwise to TiO₂ precursor under continuous stirring for 30 min at room temperature. Ceramic balls were dipped into Ag-N/TiO₂ sol and were remain for 2 min for complete adsorption of the catalyst. Then the catalyst was dried at 80°C for 30 min. After repeat 3 times, obtained catalysts were dried at 80°C for 24 h. Finally, it was calcined in a muffle furnace at 400°C for 3 h to obtained Ag-N/TiO₂ coated on supporter.

1.3.1.11 Photocatalytic reaction of dry degradation under UVC-light

The photocatalytic performance was evaluated by the degradation of methylene blue (MB) under UV irradiation. A UVC lamp (64 W, Philips brand) was used as lignin source. The initial aqueous solution of 100 mL MB (5 ppm) was prepared and mixed with 50 g of Ag-N/TiO₂ coated on supporter. The suspension was stirred under dark condition for 30 min to reach the adsorption equilibrium. To measure the MB concentration, an appropriate amount of sample was collected and filtered by a 0.22 µm nylon to remove the photocatalyst. The obtained solutions were analyzed the absorption spectra at 664 nm by using a UV-vis spectrophotometer (Spectrostarnano, BMG Labtech) to determine the degradation and concentration of MB. The recyclability of the synthesized photocatalyst was also done using the same procedure as mention above.

1.3.1.12 Photocatalytic reaction of glucose under UVC-light

The reaction was prepared in a mixture of distilled water and acetonitrile (10:90 v/v) (Colmenares et al., 2011). The prepared solution (400 ml) was transferred into a Pyrex cylindrical double-walled reactor. The concentration of glucose solution (1 g/l) and photocatalyst loading (1 g/l) were mixed together under dark condition and continuous stirring for 30 min to reach an absorption-desorption equilibrium. A mercury lamp 450 W (250-365 nm, UM-452, USHIO, Japan) located inside the reactor as a light source to irradiate the samples. The reaction temperature was maintained by a cooling water system at 25°C. The samples were taken from the photoreactor at specified times for analysis.

1.3.2 Photocatalytic conversion of glucose to high value fuels and chemicals

TiO₂ photocatalyst was synthesized by combination of sol gel and microwave with different concentrations of a surfactant, called CTAB. The surface morphology of the

photocatalyst was observed using a scanning electron microscope. It was found that the agglomeration of TiO_2 photocatalyst decreased with increasing concentration of CTAB (**Fig. 2**). Therefore, the particle size of TiO_2 decreased with increasing concentration of CTAB. This is due to CTAB could reduce the surface tension and made high dispersion of TiO_2 precursor in the solution during the preparation process. In addition, CTAB could increase surface area of obtained catalysts, leading to high photocatalytic activity.

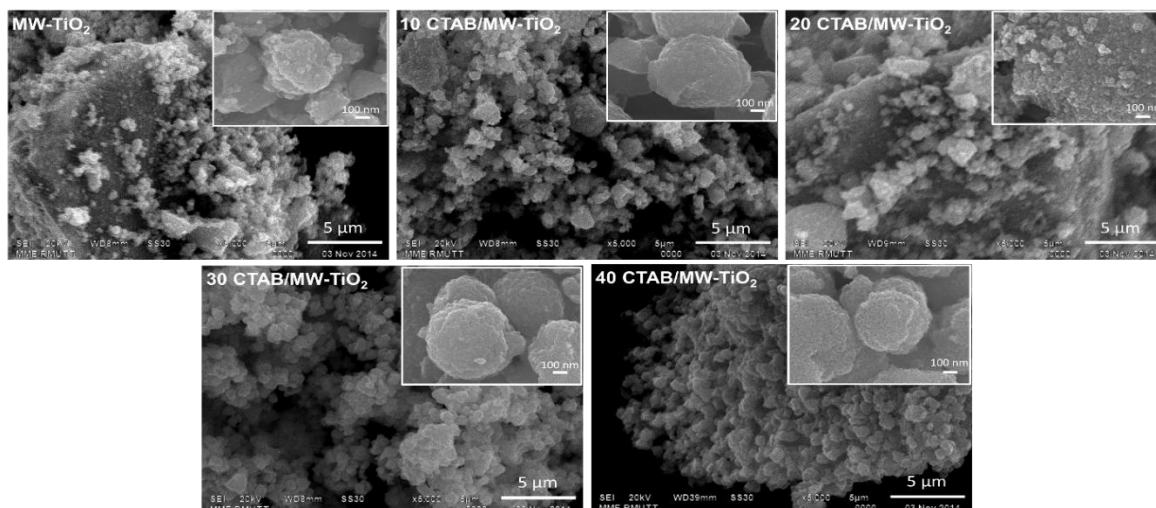


Fig. 2. SEM images of TiO_2 photocatalysts synthesized with different concentrations of CTAB.

The glucose conversions of various catalysts were carried out for 120 min under UV irradiation (wavelength = 365 nm). The results showed that high concentration of CTAB resulted in high glucose conversion. The highest glucose conversion of 60% represented in 40 CTAB/MW- TiO_2 . It can conclude that high concentration of CTAB toward high surface area and low agglomeration of TiO_2 , resulting in the highest glucose conversion (**Fig. 3**). The product yields of glucose conversion are shown in **Fig. 4**. There are 4 products of glucose conversion; gluconic acid, arabinose, xylitol, and formic acid. It was observed that the yields of all products tended to increase with increasing irradiation time. The highest conversion of 60% after 120 min showed the yield of gluconic acid, arabinose, xylitol, and formic acid of 5%, 26%, 3% and 25%, respectively. From the yields of products, it indicated that use of CTAB tended to give high yields of arabinose (**Fig. 3**).

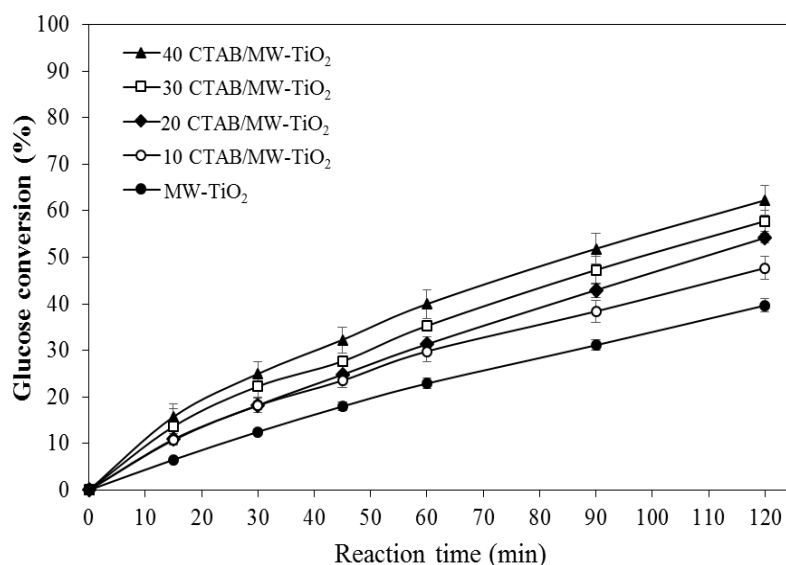


Fig. 3. Photocatalytic conversions of glucose with TiO₂ synthesized with different concentrations of CTAB in MW.

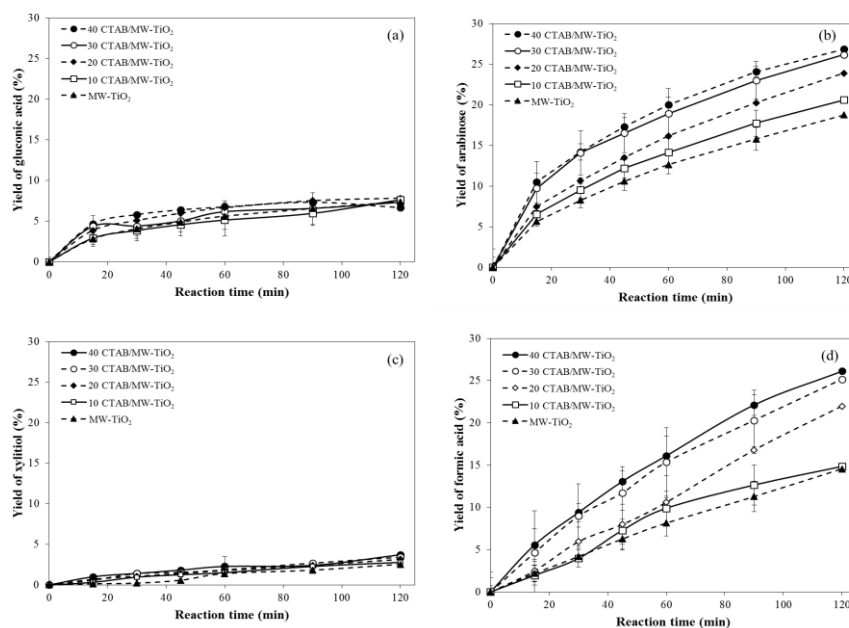


Fig. 4. Product yields of photocatalytic conversion of glucose with TiO₂ photocatalysts synthesized by different concentrations of CTAB.

As mentioned above, high surface area can enhance photocatalytic activity. So, the use of support materials is of interest for modification of TiO₂. The supports are expected to decrease agglomeration of TiO₂ and increase selectivity of photocatalytic reactions. From the group of supports, zeolites have been reported to delocalize band gap excited electrons of TiO₂ and thereby minimize electron-hole recombination to favor photoinduced electron-transfer reactions. SEM images show that surface morphology of zeolite changed after TiO₂ loading. It was found that the TiO₂ particles were coated on the surface (see **Fig. 5**) compared

with pristine zeolite. The TiO_2 coated on surface of zeolite showed well distribution. This caused the reduction of the agglomeration of TiO_2 nanoparticles synthesized with conventional process without zeolite. The catalyst size was increase when the amount of TiO_2 increased. Therefore, it was found that the specific surface area of TiO_2/ZeY increase compared with pure TiO_2 .

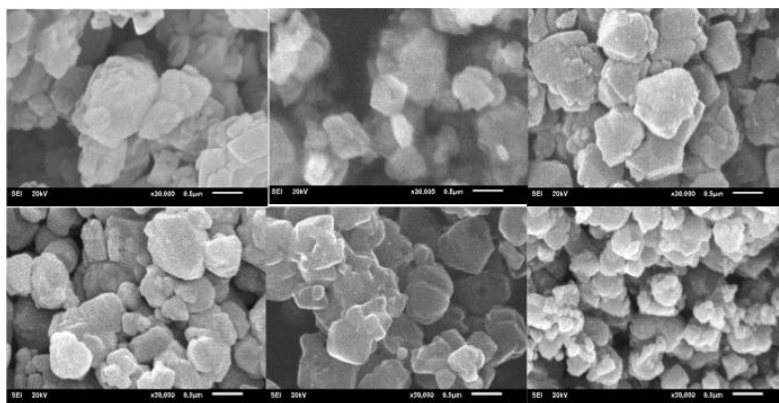


Fig. 5. SEM images (30000x) of ZeY, $\text{TiO}_2(5\%)/\text{ZeY}(95\%)$, $\text{TiO}_2(15\%)/\text{ZeY}(85\%)$, $\text{TiO}_2(30\%)/\text{ZeY}(70\%)$, $\text{TiO}_2(45\%)/\text{ZeY}(55\%)$, and TiO_2 .

The glucose conversion and organic compound yields increased with long irradiation time and reached a maximum value at 120 min. The results showed that zeolite supported TiO_2 (TiO_2/ZeY) represented higher photocatalytic conversion of glucose than pristine TiO_2 (**Fig. 6**). However, it is distinct that the conversion rates did not increase linearly with increasing TiO_2 content. Certainly, the highest glucose conversion was achieved at a medium loading of 15% TiO_2 (75%) (Wang, C.C. *et al.* 2008). The yields of gluconic acid, arabinose, xylitol, and formic acid were 8.0, 29, 3, and 37%, respectively.

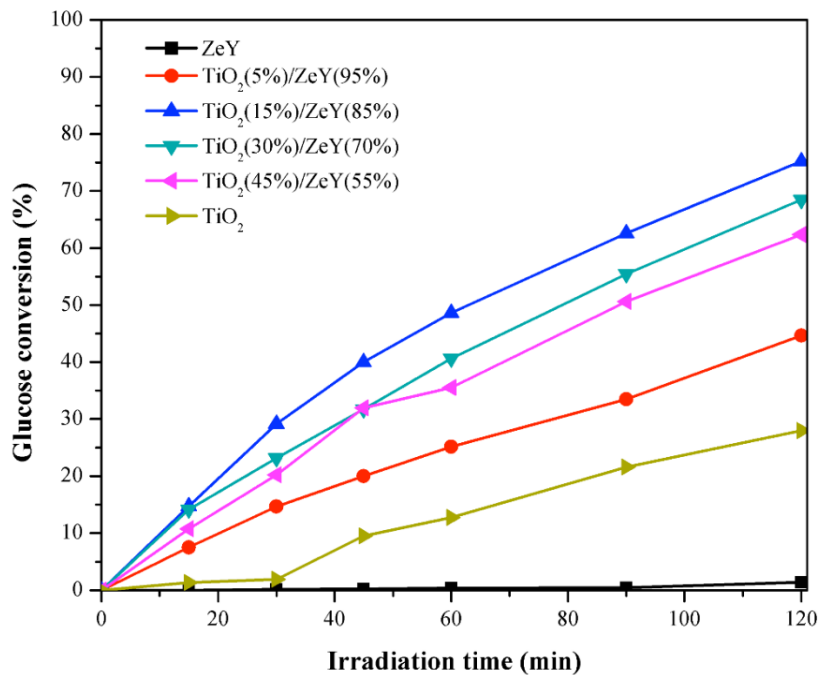


Fig. 6. Photocatalytic conversions of glucose under UV irradiation for 120 min with ZeY, TiO₂/ZeY (5, 15, 30, and 45 %wt), and TiO₂.

1.3.3 Modification of photocatalyst by non-metal doping

The doping TiO₂ photocatalysts was synthesized by sol gel method. The precursors as boric acid, glucose, and ammonia were performed in order to presence the dopant of boron (B), carbon (C), and nitrogen (N), respectively. In this study, the amount of dopants are based on mole ratio of titanium, which varying ratio of dopant:Ti is 0.02:1 mole.

1.3.3.1 Characterization of bare-TiO₂ and non-metal doped TiO₂

SEM image of obtained photocatalyst sample are illustrated in **Fig. 7**. In this part, the morphology appearance of bare-TiO₂ and B,N-TiO₂ particles were compared. It could be observed that both samples have a large distribution of particle sizes. This could be described that the agglomeration from the synthesis in form of nanoparticles. Although, this phenomenon indicated that the non-spherical shape of photocatalyst. The dopant was no substantial alteration on the morphology appearance of photocatalyst.

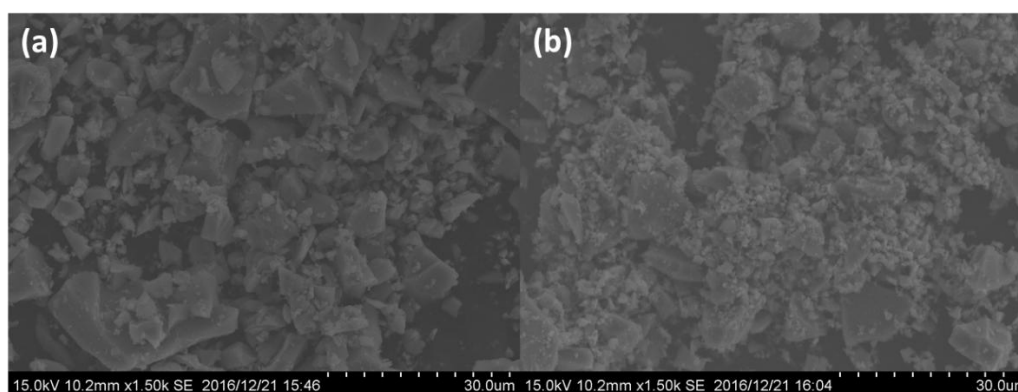


Fig. 7. SEM images of photocatalyst: (a) Bare-TiO₂, and (b) B,N-TiO₂

The surface area of modified TiO₂ with non-metal are shown in **Table 1**. The surface area remarkably increases with the presence of C, B, N, and BN, respectively. These results were corresponded with the performance on glucose conversion. The pore volume was also slightly increasing with the presence of dopant. Particularly, the presence of co-doping (B,N) gave the highest surface area with 227.69 m²/g. Thus, high surface area indicating to improve the active site on photocatalyst resulted in enhance of photocatalytic activity as the results in glucose conversion.

Table 1. The specific surface areas of non-metal doped on TiO₂

Samples	Pore size (nm)	Pore volume (cm ³ /g)	Surface area (m ² /g)
Bare TiO ₂	5.55	0.11	77.92
B-doped TiO ₂	3.99	0.15	147.37
C-doped TiO ₂	4.37	0.12	109.20
N-doped TiO ₂	5.47	0.21	153.04
B,N-dopedTiO ₂	5.56	0.32	227.69

In addition, the increasing of conversion and productivity was also corresponded with the results of PL measurement as shown in **Fig. 8**. Typically, the photoluminescence spectra have been widely studied to investigate the change in the surface state and the efficient of charge trapping, immigration and transferring in semiconductor nanoparticles [Shamaila, et al., 2010]. It was found that doping of non-metal on TiO₂ resulted in decrease the intensity on PL measurement. This could be described that the effective inhibited the recombination of electron and hole. This lead to increase the possibility of chemical reaction between radical and reactant resulting in achieve the performance on photocatalytic process [Srisasiwimon, et al., 2018].

UV- vis diffuse absorbance was demonstrated the optical properties of obtained photocatalysts (**Fig. 9**). It was found that bare-TiO₂ showed the lowest light absorption in the

visible region (400-700 nm). The presence of dopant on TiO_2 presented a slightly shift of light absorption. Based on Tauc plots (Fig. 10), the band gap energies of bare- TiO_2 was calculated with approximate 3.18 eV which corresponded to the typical band gap of anatase TiO_2 . Further, the narrow band gap energies of doping C, B, N, and BN on TiO_2 were observed. A wide absorption region led to increase the excited electron under light irradiation resulted in high performance on glucose conversion [Liu, et al., 2011].

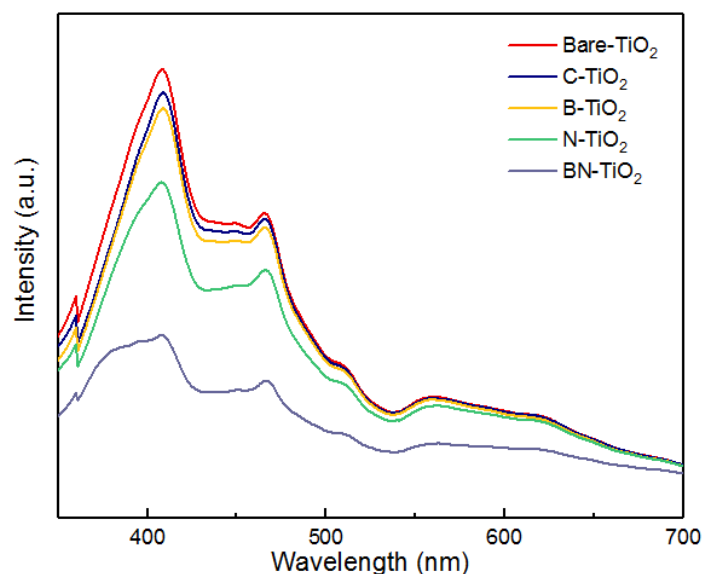


Fig. 8. Photoluminescence spectra of non-metals doped TiO_2

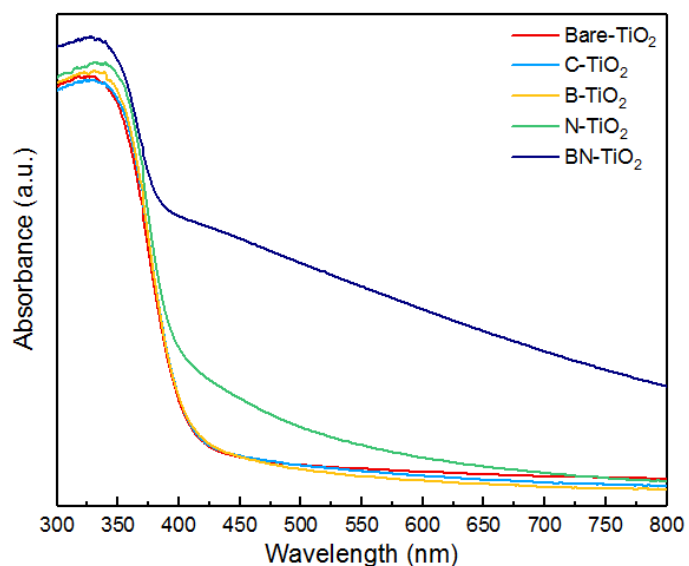


Fig. 9. UV-vis diffuse absorbance spectra of non-metal doped TiO_2

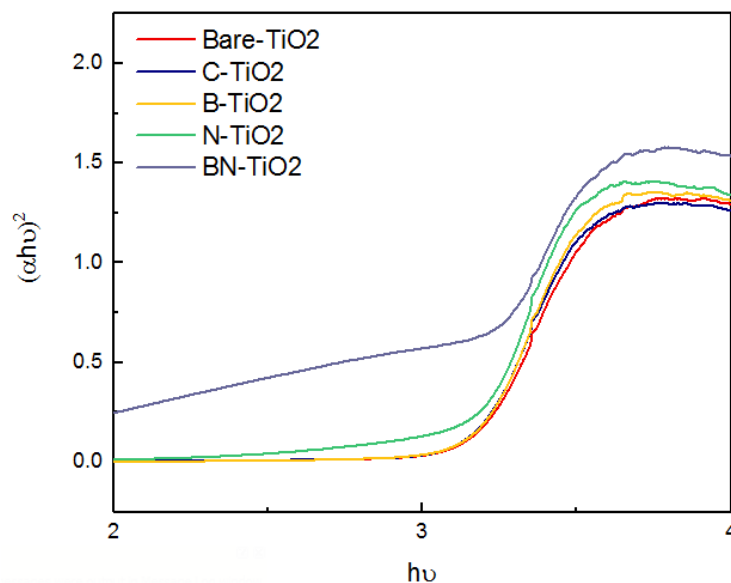


Fig. 10. Optical properties of non-metal doped TiO₂ based on Tauc plots equation

Typically, the different crystal phase affects the photocatalytic activity. Among them, anatase phase have been reported with high performance of photocatalyst. In this research, the non-metal doping on TiO₂ nanoparticles was carried out at 400 °C for 2 hours. The phase characterization of photocatalyst was measured by XRD techniques and the patterns are shown in **Fig. 11**. As the results, all of samples consist of anatase form as a unique phase. It was found that the strong peak was observed with (1 0 1) plane at $2\theta = 25.4^\circ$ as anatase phase reflection. Therefore, the average crystalline sizes of all samples were calculated by well-known Scherrer formula as shown in **Table 2**. The crystalline size of non-metal doping was smaller compared to bare-TiO₂. This could be ascribed that introducing of dopant would be affected a little distortion in the crystalline structure [Fu, et al., 2016].

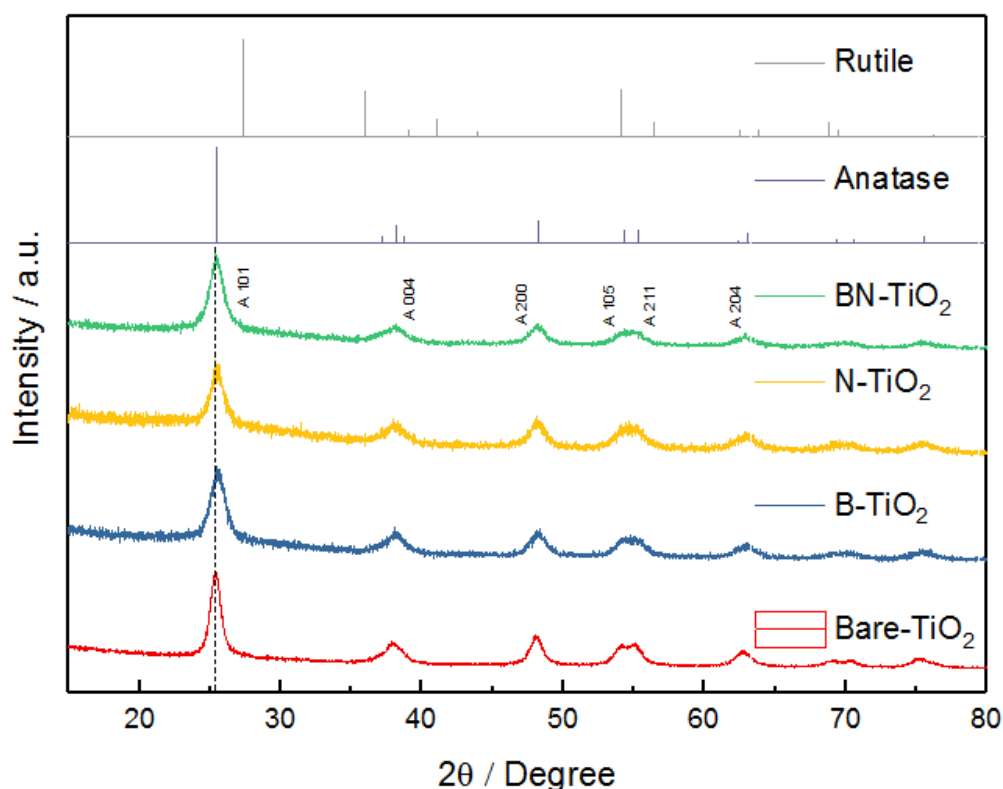


Fig. 11. XRD diffraction patterns of bare-TiO₂ and non-metal doped TiO₂

Table 2. The crystalline sizes of non-metal doped TiO₂

Photocatalysts	Crystal phase (%)		Crystallite size (nm)
	Anatase	Rutile	
Bare-TiO ₂	100	-	9.59
B-TiO ₂	100	-	7.31
N-TiO ₂	100	-	7.56
B,N-TiO ₂	100	-	7.35

1.3.3.2 The performance of non-metal doped TiO₂ on glucose conversion

The glucose conversion of non-metal doped TiO₂ is shown in **Fig. 12**. Bare-TiO₂ showed the conversion with 24.9% under UV-light. According to the results, the presence of non-metal doping (B, C, and N) could be enhance glucose conversion compared with benchmark. The single doping of nitrogen on TiO₂ was improved the glucose conversion with 60.3%. In addition, modified TiO₂ with co-doping of boron and nitrogen showed the highest glucose conversion up to 93.1% for 180 min (**Fig. 13**). The products yield of gluconic acid, arabinose, xylitol, and formic acid were 9.0, 30.5, 8.9 and 47.6%, respectively. However, time course-change of product profile was almost the same for all photocatalyst.

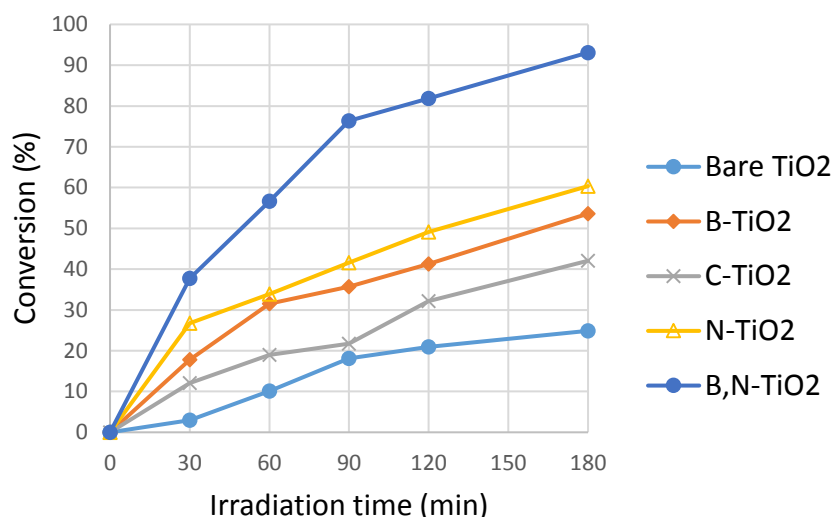


Fig. 12. Photocatalytic conversion of glucose under UV irradiation for 180 min in the presence of non-metal doping on TiO₂

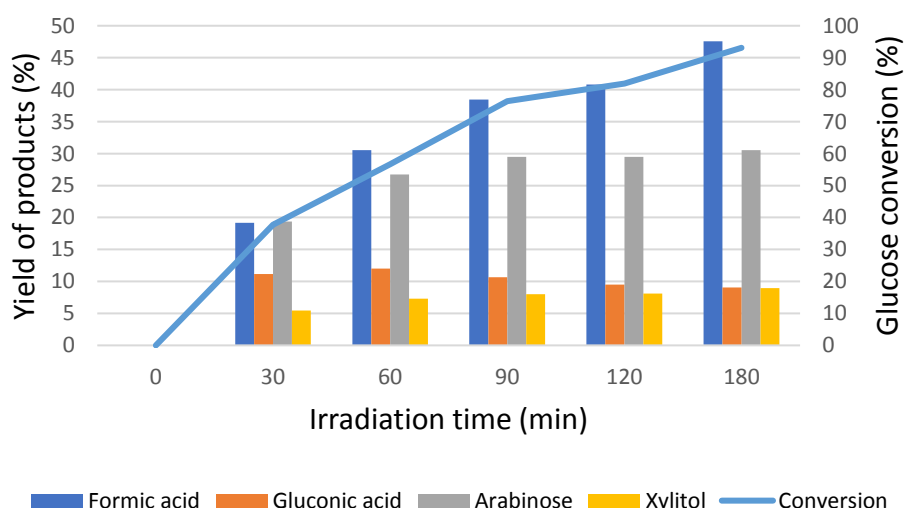


Fig. 13. The time-course products distribution profile of glucose conversion under UV irradiation for 180 min B,N doped TiO₂

1.3.3.3 Rate of reaction on photocatalytic glucose conversion

Table 3. demonstrate the reaction rate of photocatalytic glucose conversion. It could be seen that the bare-TiO₂ showed a slight increasing of reaction rate, until retention time of 90 min gave the highest rate of 0.9 mmol L⁻¹ h⁻¹. On the other hand, the doping photocatalyst could be enhance the performance on glucose conversion with short reaction time. The rapid reaction was occurred within 90 min and then slightly lower until final reaction time. For example, B,N-TiO₂ showed the highest reaction rate at 30 min with 3.5 mmol L⁻¹ h⁻¹. The derived products of all photocatalysts were presented in different reaction rate. However, performed in batch processing showed the same characteristic of products in term of

selectivity for all photocatalysts as previously proposed the reaction pathway of glucose conversion [Payormhorm, et al., 2017]. Further research, the reaction will be carried out in photocatalytic bio-flow reactor in order to study the kinetic reaction for improving the selectivity and yield of derived products.

Table 3. Reaction rates of non-metal doped TiO₂ nanoparticles

Catalyst	Time (min)	Reaction rate (mmol L ⁻¹ h ⁻¹)	Products rate (mmol L ⁻¹ h ⁻¹)			
			Gluconic acid	Arabinose	Xylitol	Formic acid
Bare-TiO ₂	30	0.3	0.00	0.29	0.06	1.34
	60	0.8	0.29	0.18	0.07	0.48
	90	0.9	0.17	0.22	0.04	0.44
	120	0.3	0.12	0.16	0.05	0.55
	180	0.2	0.02	0.03	0.05	0.48
B-TiO ₂	30	1.9	0.35	0.86	0.15	2.38
	60	1.5	0.07	0.45	0.21	1.28
	90	0.4	0.08	0.58	0.14	1.40
	120	0.6	0.06	0.43	0.12	1.36
	180	0.7	-0.04	0.21	0.05	0.95
N-TiO ₂	30	2.8	0.37	1.10	0.24	3.16
	60	0.8	0.18	0.68	0.20	2.05
	90	0.8	0.06	0.48	0.11	1.64
	120	0.8	0.05	0.29	0.05	1.31
	180	0.6	-0.07	0.25	0.07	1.26
B,N-TiO ₂	30	3.5	0.92	2.09	0.58	6.74
	60	1.7	0.07	0.79	0.20	4.00
	90	1.8	-0.11	0.30	0.07	2.77
	120	0.5	-0.10	0.00	0.01	0.83
	180	0.5	-0.02	0.06	0.04	1.19

1.3.4 Further extension of the catalyst design (1): Preparation of B,N-TiO₂ nanofibers and hollow nanoribbons and Ag-loaded TiO₂ nanofibers

In the above section of 1.3.3, nonmetal B,N-doped TiO₂ resulted in the highest catalytic activity for conversion of glucose (**Fig. 12**). In this context, we newly prepared B,N-doped TiO₂ nanofibers and B,N doped TiO₂ hollow nanoribbons by electrospinning technique in order to improve the catalytic activity through increment of the specific surface area (*viz.* active site) of the catalyst. Further characterization and evaluations of the catalytic activity for conversion of glucose under the illumination of the light are still underway.

1.3.4.1 Characterization of bare-TiO₂ and non-metal doped TiO₂ nanofiber and hollow nanoribbon

The morphologies appearance of electrospinning technique of TiO₂ nanofibers and hollow-nanofibers by SEM method are illustrated in **Fig. 14**. The first synthesized photocatalyst in form of nanofiber was showed in **Fig. 14 (a and b)**. Although the nanofiber showed a smooth

morphology of fiber, however, a slight distribution of sizes in both of pristine and doped TiO_2 were observed. The average diameter of B,N doped TiO_2 was approximately $150 \mu\text{m}$. Further, the hollow-nanofiber of TiO_2 and doped TiO_2 was studied by coaxial nozzle electrospinning technique as illustrated in **Fig. 14 (c and d)**. However, the obtained fiber was found in form of hollow-nanoribbon for both samples. Despite, the good morphologies of hollow-nanoribbons were obtained (smooth and uniform in the distribution of size). This could be further study the suitable condition in term of flow rate to obtain the hollow-nanofibers.

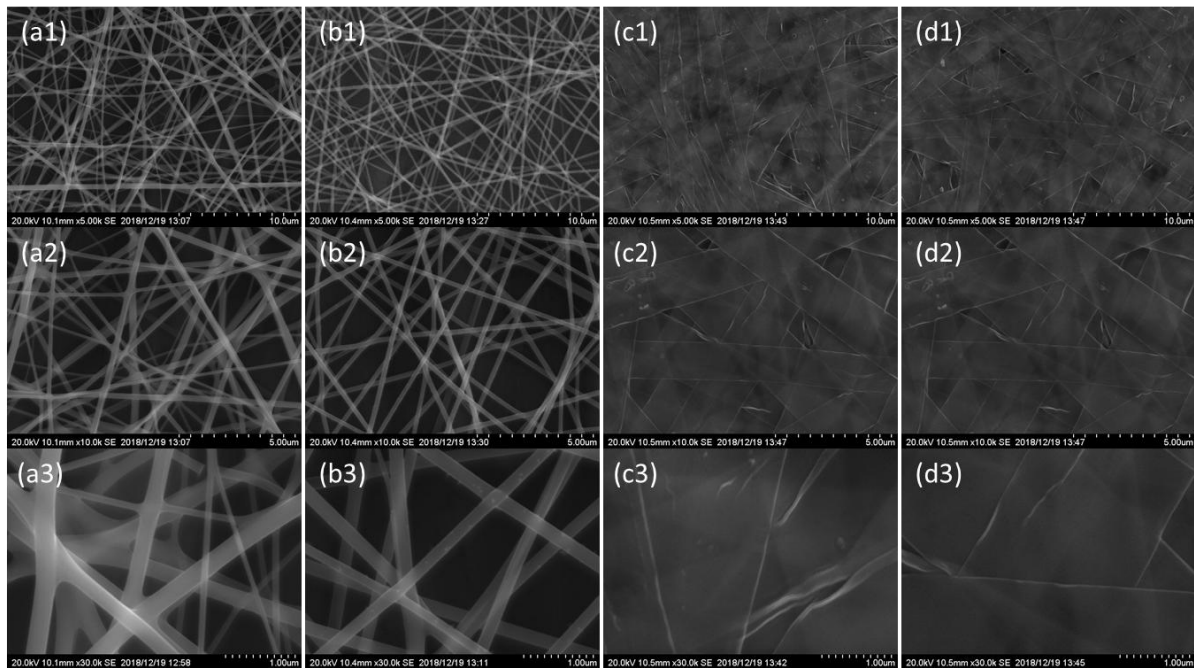


Fig. 14. SEM images of (a) TiO_2 nanofibers, (b) BN doped TiO_2 nanofiber, (c) TiO_2 nanoribbon, and (d) BN doped TiO_2 nanoribbon. The scale bar in figures with suffix “1” is $10 \mu\text{m}$, “2” is $5 \mu\text{m}$, and “3” is $1 \mu\text{m}$.

Fig. 15 shows the photoluminescence spectra comparison of TiO_2 and B,N doped TiO_2 nanofibers. The modified photocatalyst expressed the lower PL intensity resulting in decrease in the recombination of electron and holes (**Fig. 15a**). However, the comparison of PL pattern of hollow nanoribbon was no substantial alteration (**Fig. 15b**).

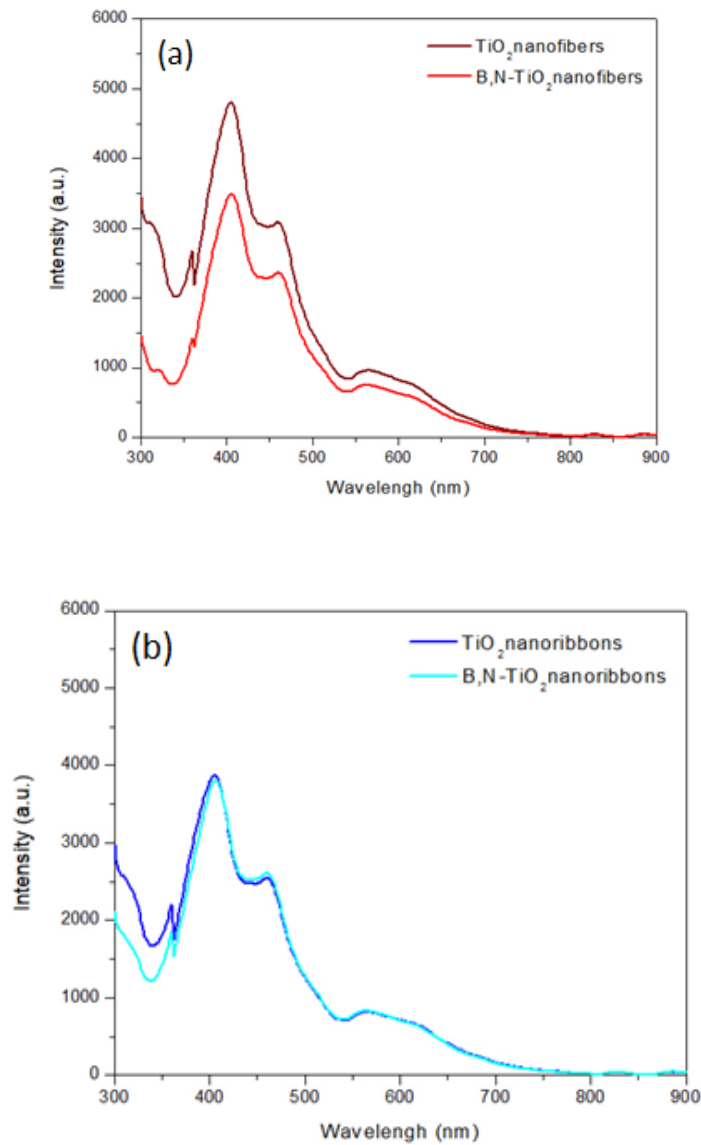


Fig. 15. Photoluminescence spectra of bare- TiO_2 and B, N doped TiO_2 (a) nanofiber and (b) hollow-nanoribbon.

Fig. 16 shows the XRD patterns of the nanofiber and hollow nanoribbon. The structural features obtained from XRD are summarized in **Table 4**. All samples showed very broad peaks with the (1 0 1) plane at $2\theta = 25.4^\circ$ indicating anatase phase reflection. As a result, the lower crystalline size of doped TiO_2 both nanofiber and nanoribbon was observed. This could be ascribed to the substitution of B and N in the crystalline of TiO_2 [Fu, et al., 2016].

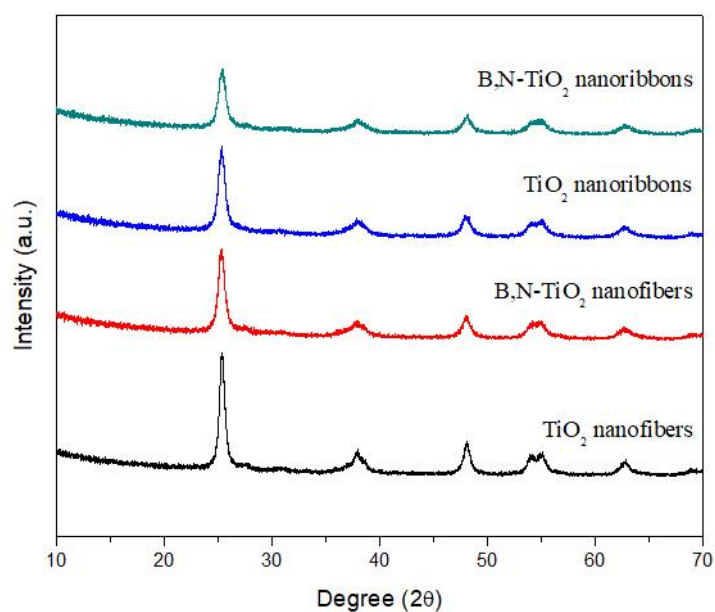


Fig. 16. XRD diffraction patterns of nanofibers and nanoribbons

Table 4. The crystalline sizes of nanofibers and nanoribbons

Photocatalysts	Crystal phase (%)		Crystallite size (nm)
	Anatase	Rutile	
TiO ₂ nanofiber	100	-	12.79
B,N-TiO ₂ nanofiber	100	-	10.66
TiO ₂ nanoribbon	100	-	10.34
B,N-TiO ₂ nanoribbon	100	-	9.77

1.3.4.2 The performance of fibrous TiO₂ on glucose conversion

Particularly, Ag-loaded TiO₂ nanofibers were also prepared and applied them for photoconversion of glucose. Although it has not yet been optimized the conditions for preparation of the Ag-loaded TiO₂ nanofibers in terms of the photocatalytic activity, in situ preparation in N₂ resulted in the highest activity (**Fig. 17**).

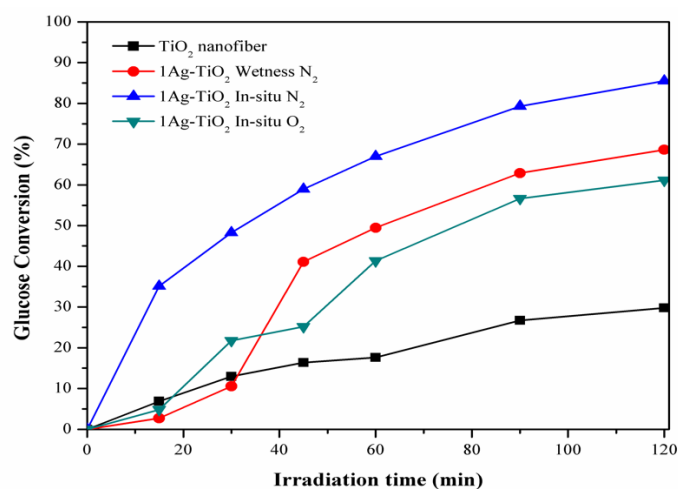


Fig. 17. Time-course conversion of glucose under UV irradiation for 2 h with Ag-loaded TiO₂ nanofibers prepared by different techniques.

1.3.5 Modification of photocatalyst by metal doping

The doping TiO₂ photocatalysts was synthesized by sol gel method. The several precursors were performed in order to presence the metal dopant on titanium dioxide. In this study, the amount of dopants are based on mole ratio of titanium, which varying ratio of dopant:Ti is 0.02:1 mole.

1.3.5.1 Characterization of bare-TiO₂ and metal doped TiO₂

According to the results in **Fig. 18**, It was found that the photocatalyst in form of nanoparticles showed a large distribution of particles sizes due to the agglomeration of nanoparticles **Fig. 18a**. For example, the agglomeration also found in modified photocatalyst (**Fig. 18b**). However, the dopant was no substantial effect on the morphology appearance.

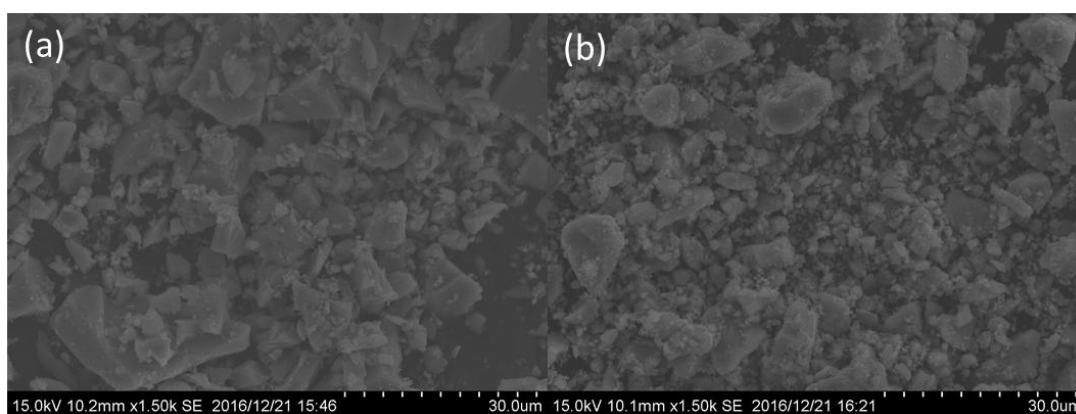


Fig. 18. SEM images of photocatalyst: (a) Bare-TiO₂, and (b) Sr-TiO₂

The surface area of modified TiO₂ with metal are shown in **Table 5**. All modified photocatalysts with metal dopant led to an increase of specific surface area and pore volume, while a slightly decreasing of pore size was observed. This could be found that the decreasing

of crystalline size was corresponding with a smaller crystalline size in XRD method. As the results, the presence of Sr-TiO₂ gave the highest surface area with 210.60 m²/g. This indicated the increasing of active site for improving the performance on photocatalytic activity [Payormhorm, et al., 2017].

Table 5. The specific surface areas of metal doped on TiO₂

Samples	Pore size (nm)	Pore volume (cm ³ /g)	Surface area (m ² /g)
Bare-TiO ₂	5.55	0.11	77.92
Sr doped TiO ₂	4.55	0.24	210.60
In doped TiO ₂	3.75	0.19	202.77
Ag doped TiO ₂	3.76	0.11	114.95
Cr doped TiO ₂	3.78	0.12	125.31
Cu doped TiO ₂	3.96	0.12	124.07
Ni doped TiO ₂	4.53	0.17	147.75

UV-vis diffuse absorbance was demonstrated the optical properties of obtained photocatalysts (**Fig. 19**). It could be observed that Sr-TiO₂ and In-TiO₂ showed the lower light absorption in the visible legion (400-700 nm) compared to bare-TiO₂ as benchmark. In contrast, the presence of Ag, Cr, Cu, and Ni on TiO₂ presented a broadly shift of light absorption in visible region. The results demonstrated the potential of photocatalyst for further applied in solar irradiation.

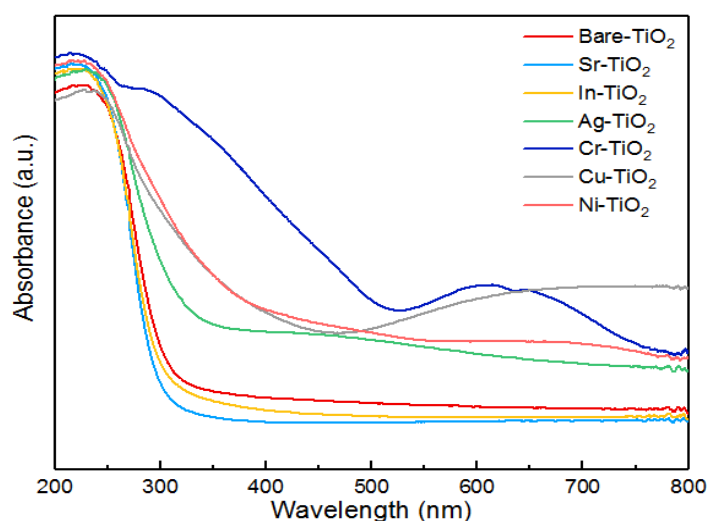


Fig. 19. UV-vis diffuse absorbance spectra of metal doped TiO₂

The photoluminescence spectra of metal doped TiO₂ are demonstrated in **Fig. 20**. The PL measurement was examined to investigate the change in the surface state and the efficient of charge trapping, immigration and transferring in semiconductor nanoparticles [Shamaila, et al., 2010]. It could be observed that the intensity spectra of all samples were corresponded

with the results of the ability of light absorption. According to the results, the presence of Ag, Cr, Cu, and Ni on TiO_2 led to decrease the intensity of PL spectra, whereas an increase in PL intensity with Sr and In doped on TiO_2 were observed. Typically, the decreasing an intensity of PL spectra indicated significantly high separation of charge carriers. In this study, the presence of metal on TiO_2 was no substantial correlation with the results on glucose conversion. However, the proper physio-chemical properties of photocatalyst should be determined with the combination of several techniques.

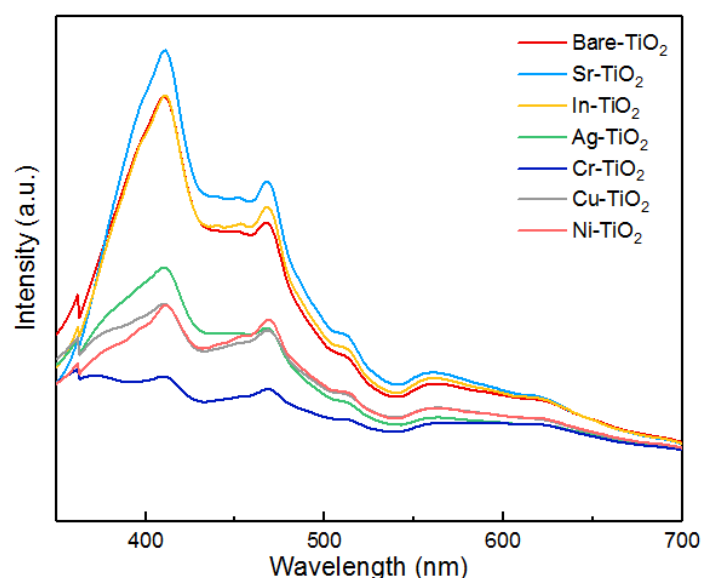


Fig. 20. Photoluminescence spectra of metals doped TiO_2

The phase characterization of photocatalyst was measured by XRD techniques and the patterns are shown in **Fig. 21**. Previous reported have been demonstrated that anatase phase TiO_2 was a proper form for an efficient in photocatalytic reaction [Kadam, et al., 2017]. In this study, all of samples consist of anatase form as a unique phase. It was found that the strong peak was observed with (1 0 1) plane at $2\theta = 25.4^\circ$ as anatase phase reflection. Therefore, the average crystalline sizes of all samples were calculated by well-known Scherrer formula as shown in **Table 6**. The providing value of Full-Width-at-Half-Maximum (FWHM) of Ag, In and Sr were 1.4546, 1.4209, and 1.1382, respectively. According to the results, the wider FWHM was corresponded to a decrease of crystalline size. Therefore, the presence of metal dopant showed a smaller crystalline size than those of bare- TiO_2 . This could be ascribed that introducing of dopant would be affected a little distortion in the crystalline structure [Fu, et al., 2016].

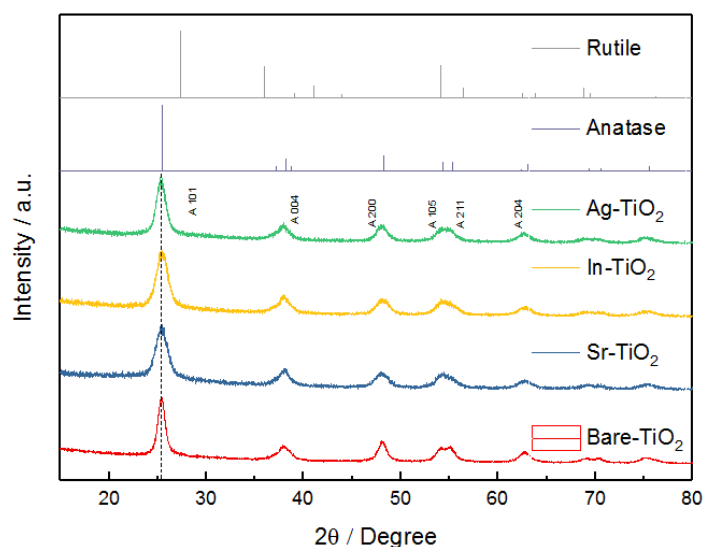


Fig. 21. XRD diffraction patterns of bare-TiO₂ and metal doped TiO₂

Table 6. The crystalline sizes of metal doped TiO₂

Photocatalysts	Crystal phase (%)		Crystallite size (nm)
	Anatase	Rutile	
Bare-TiO ₂	100	-	9.59
Sr-TiO ₂	100	-	5.81
In-TiO ₂	100	-	6.10
Ag-TiO ₂	100	-	7.41

1.3.5.2 The performance of metal doped TiO₂ on glucose conversion

The glucose conversion of metal doped TiO₂ is shown in **Fig. 22**. The Bare-TiO₂ was used as benchmark with glucose conversion of 24.9%. The modified photocatalyst with metal doping led to improve the efficiency except Cr-TiO₂. The highest glucose conversion was obtained in the presence of Sr-TiO₂ (87.5%). The product profile of Sr-TiO₂ is shown in **Fig. 23**. The products yield of gluconic acid, arabinose, xylitol, and formic acid were 6.7, 33.7, 8.2 and 37.4%, respectively. However, time course-change of product profile was almost the same for all metal doped photocatalyst.

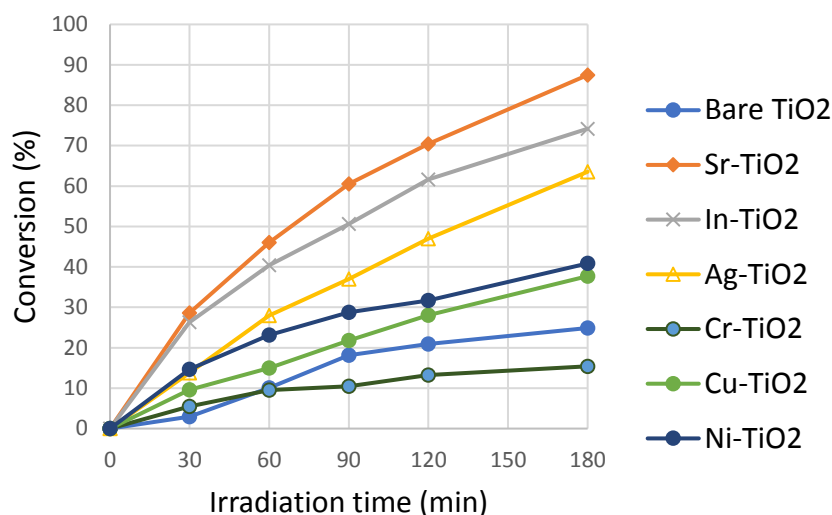


Fig. 22. Photocatalytic conversions of glucose under UV irradiation for 180 min in the presence of metal doping on TiO₂

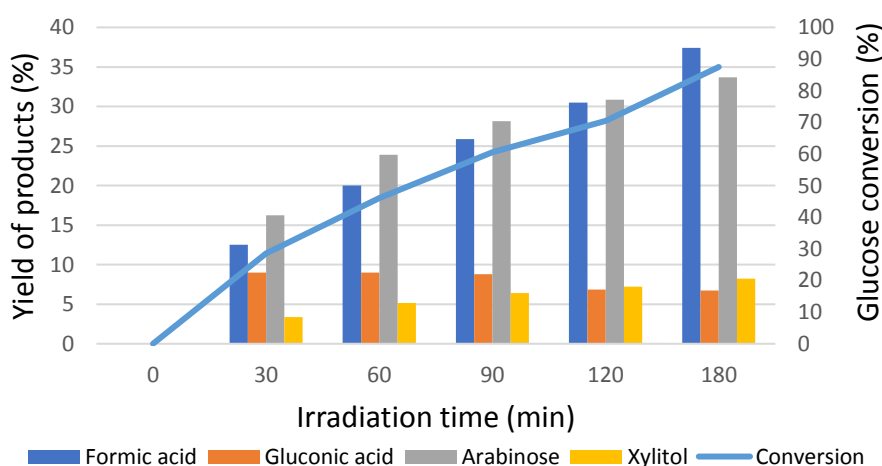


Fig. 23. The time-course products distribution profile of glucose conversion under UV irradiation for 180 min Sr doped TiO₂

1.3.6 Modification of photocatalyst by synergistic effects of metal/nonmetal doping

The modification of photocatalyst in the concept of synergistic was investigated to improve the performance of photocatalysts on glucose conversion. According to previous results, a single of nonmetal doping as nitrogen showed the good photocatalyst properties for single nonmetal doping resulted in the highest glucose conversion. Thus, the nitrogen dopant is a representative for efficient nonmetal doping on TiO₂. In this part, the synergistic effects of various metals/nonmetal (nitrogen) on the physio-chemical properties were studied. The doped TiO₂ photocatalysts were synthesized by sol gel method. Several precursors were studied in order to modify the metal/nonmetal dopant on titanium dioxide. In this study, the

amount of dopants are based on mole ratio of titanium, which varying ratio of dopant:Ti was 0.02:1 mole.

1.3.6.1 Characterization of bare-TiO₂ and synergistic metal/nonmetal doped TiO₂

The synergistic effects of metal/nonmetal doping on physio-chemical properties were studied. SEM image of obtained photocatalyst sample are illustrated in **Fig. 24**. The morphology appearance of metal/nonmetal doped TiO₂ particles (Ag,N-TiO₂, and Cr,N-TiO₂) were compared with bare-TiO₂. It could be observed that all photocatalyst samples showed the same morphology with a random arrangement of particle sizes. According to result, the large distribution in form of nanoparticle enhanced the agglomeration of samples. Although, this phenomenon indicated that the non-spherical shape of photocatalyst. The dopant was shown to have no substantial effect on alteration on the morphology appearance of photocatalyst.

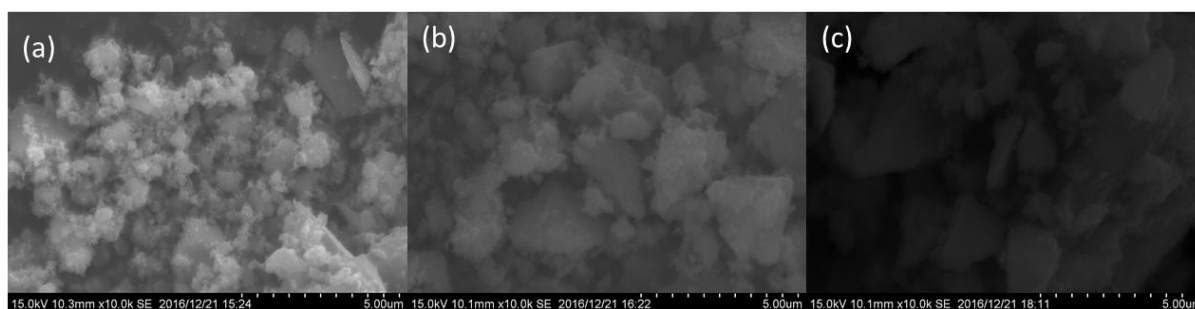


Fig. 24. SEM image of photocatalyst: (a) Bare-TiO₂, (b) Ag,N-TiO₂ and (c) Cr,N-TiO₂.

Pore size, pore volume, and surface areas of metal/nonmetal doped TiO₂ are shown in **Table 7**. It was observed that the surface area of bare-TiO₂ was 77.92 m²/g. The surface area was remarkably increased in the presence of metal/nonmetal dopant. Among the synthesized catalysts, the Sr,N-TiO₂, In,N-TiO₂, and B,N-TiO₂ showed the relative high surface area with 251.97, 242.34, and 227.69 m²/g, respectively. All modified photocatalyst showed a slightly increasing of pore size and pore volume compared with bare-TiO₂. However, a similar trend of pore size and pore volume for doping samples were observed. In this study, the high surface area is the main criteria which led to improved activity of the photocatalytic conversion.

Table 7. The specific surface areas of metal doping on TiO₂

Samples	Pore size (nm)	Pore volume (cm ³ /g)	Surface area (m ² /g)
Bare-TiO ₂	5.55	0.11	77.92
B,N doped TiO ₂	5.56	0.32	227.69
Ag,N doped TiO ₂	6.73	0.26	152.42

In,N doped TiO ₂	5.74	0.35	242.34
Sr,N doped TiO ₂	5.39	0.34	251.97
Cr,N doped TiO ₂	5.70	0.25	174.91
Cu,N doped TiO ₂	8.79	0.24	110.19
Ni,N doped TiO ₂	5.28	0.21	150.98

UV-vis diffuse absorbance was studied to demonstrate the optical properties of the obtained photocatalysts (**Fig. 25**). It was found that the bare-TiO₂ showed no significant absorption in the visible-light region (400-700 nm) due to a large band gap. All metal/nonmetal photocatalyst showed remarkable generate of light absorption in visible region. This notable increase in absorbance reflected the synergism for In,N-TiO₂ and Sr,N-TiO₂ on property of light absorption characteristic of TiO₂. Further increasing with two region absorption for Cr,N-TiO₂ and Cu,N-TiO₂ were observed. Based on Tauc plots (**Fig. 26**), the band gap energies of bare-TiO₂ was calculated with approximate 3.18 eV which corresponded to the typical band gap of anatase TiO₂. Narrower band gap energies of metal/nonmetal doped TiO₂ were observed. A narrow band gap led to the increase in the excited electron under light irradiation, resulting in improved performance of photocatalyst (Liu et al., 2011).

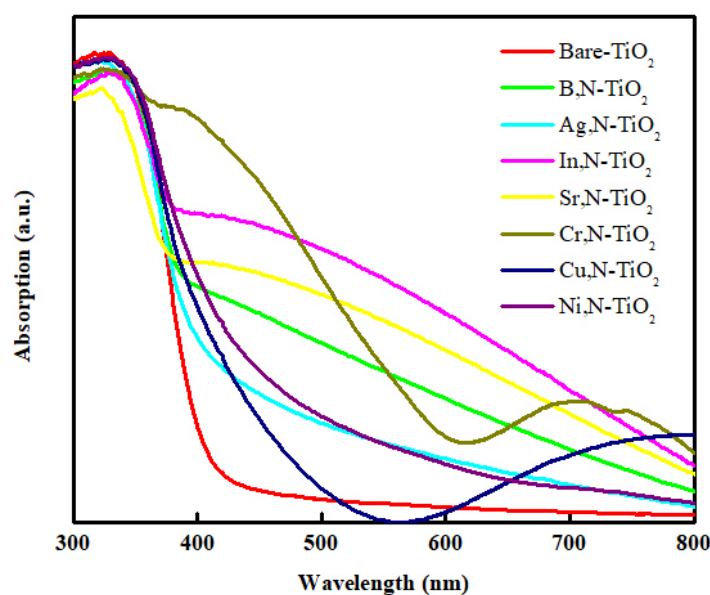


Fig. 25. UV-vis diffuse absorbance spectra of metal/nonmetal doped TiO₂.

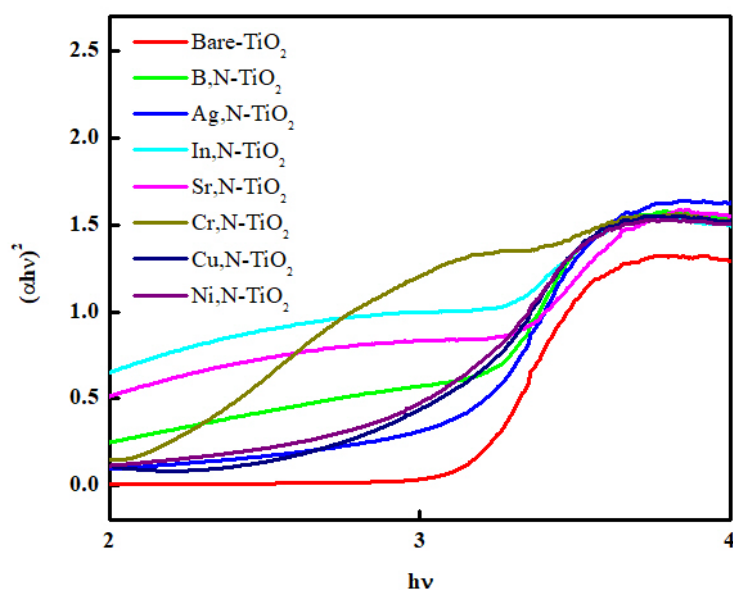


Fig. 26. Optical properties of metal/nonmetal doped TiO₂ based on Tauc plot equation.

The photoluminescence spectra of metal doped TiO₂ with the excitation wavelength of 270 nm are demonstrated in **Fig. 27**. The PL measurement was examined to investigate the change in the surface state and the efficient of charge trapping, immigration and transferring in semiconductor nanoparticles (Shamaila *et al.*, 2010). As the results, doping of metal/nonmetal on TiO₂ remarkable decrease on PL intensity in comparison to bare-TiO₂. This implied that a decrease in the PL intensity could be enhance the effective of charge separation.

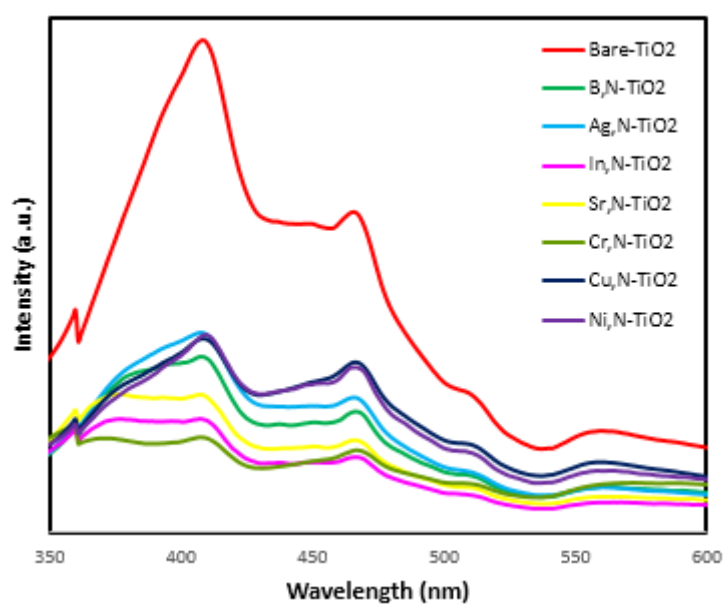


Fig. 27. Photoluminescence spectra of metal/nonmetal doped TiO₂.

In this part, the synergistic of metal/nonmetal doping on TiO₂ nanoparticles was carried out at 400 °C for 2 h. The phase characteristics of the photocatalysts were studied by XRD and the patterns are shown in **Fig. 28**. It was found that all samples were consisted of anatase form as a unique phase. It was found that the diffraction peak for all photocatalyst samples could be assign to TiO₂ anatase phase. The specific peak of all metal dopant could not be found in the photocatalyst sample. This could be ascribed with well dispersion of dopant on the surface of TiO₂ including small amount of dopant loading (2% mole of Ti) and its small size. The average crystalline sizes of all samples were calculated by well-known Scherrer formula as shown in **Table 8**. The crystalline size of the doped TiO₂ was smaller compared with the bare-TiO₂. According to the results, the wider FWHM was corresponded to a decrease of crystalline size. This could be due to the slight distortion in the crystalline structure resulted from the dopants (Fu et al., 2016). No change in the 25.4° degrees was observed between the bare and doped TiO₂.

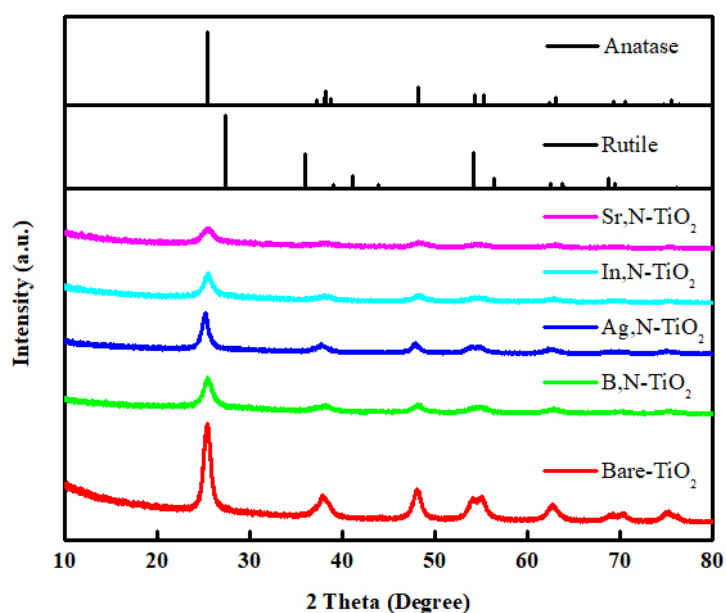


Fig. 28. XRD diffraction patterns of bare-TiO₂ and metal doped TiO₂.

Table 8. The crystalline sizes of metal doped TiO₂

Photocatalysts	Crystal phase (%)		Crystallite size (nm)
	Anatase	Rutile	
Bare-TiO ₂	100	-	9.59
B,N-TiO ₂	100	-	7.35

Sr,N-TiO ₂	100	-	6.03
In,N-TiO ₂	100	-	7.45
Ag,N-TiO ₂	100	-	7.63

1.3.6.2 The performance of synergistic effects metal/nonmetal doped TiO₂ on glucose conversion

The aim of this part is to investigate the synergistic effects of metal/nonmetal doped TiO₂ on the performance of glucose conversion in comparison with the efficiency of single doped TiO₂ (nonmetal or metal) in previous results. The efficiency of single doped TiO₂ on glucose conversion are illustrated in **Fig. 29**. As the results, a nitrogen doped TiO₂ was selected as nonmetal doping with highest performance on glucose conversion (60.3%). Then, various metal (B, Ag, In, Sr, Cr, Cu, Ni) was applied as co-catalyst with nonmetal (nitrogen) to study the synergistic effect on glucose conversion. The performance of synergistic photocatalysts are shown in **Fig. 30**. However, this study showed the conversion results of photocatalyst which gave the performance over 50%. It was found that Sr,N-TiO₂ and In,N-TiO₂ demonstrated a decreasing on glucose conversion compared to its single doping. This indicating no significant effect of synergistic was observed. On the other hand, the presence of B,N-TiO₂ and Ag,N-TiO₂ showed a good synergistic to greatly enhance on glucose conversion which were equivalent to 93.1 and 97.7%, respectively. However, the characteristic of products consists mainly of gluconic acid, arabinose, xylitol, and formic acid for all photocatalysts (**Fig. 31**). Moreover, the time course-change of product profile was almost the same for the reaction using all synergistic photocatalysts.

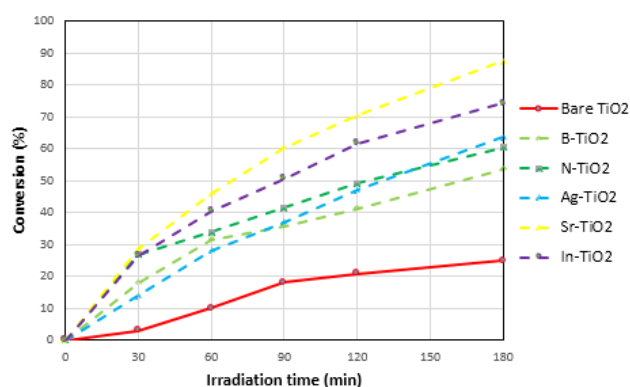


Fig. 29. Photocatalytic conversions of glucose under UV irradiation for 180 min in the presence of single doping on TiO₂.

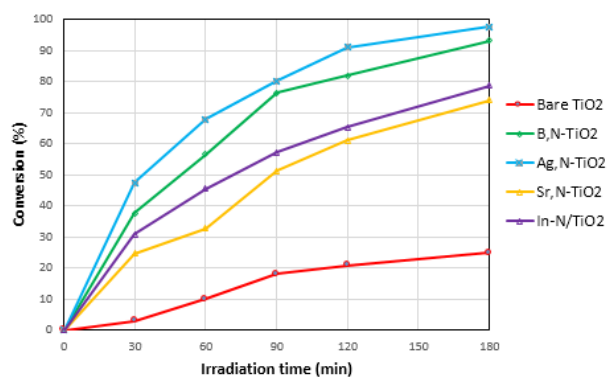


Fig. 30. Photocatalytic conversions of glucose under UV irradiation for 180 min in the presence of synergistic metal/nonmetal doping on TiO₂.

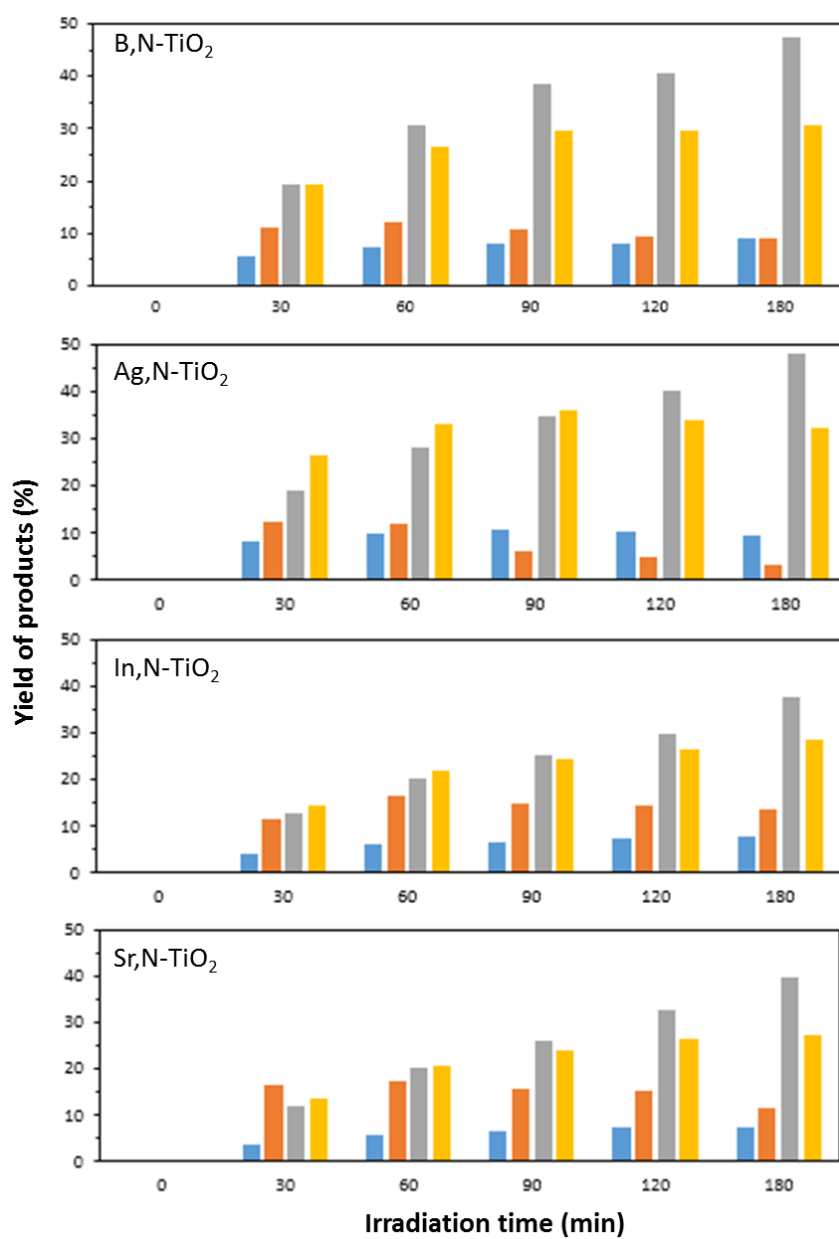


Fig. 31. The time-course products distribution profile of glucose conversion under UV irradiation for 180 min in the presence of synergistic metal/nonmetal doping on TiO₂.

1.3.7 Photocatalytic conversion of glucose under visible light

In this study, the modified photocatalyst were performed under 450 W Xenon lamp equipped with sharp cut-off filter $\lambda > 380$ nm. The commercial of TiO₂ (P25) was used as benchmark (**Fig. 32**). The highest glucose conversion of P25 was observed at 9 h with 62%. The main products were arabinose, formic acid, gluconic and xylitol with the yield of 26.08%, 23.36%, 10.92% and 10.42%, respectively. Further, applied material as graphitic carbon nitride (g-C₃N₄) is a special characteristic on photocatalytic conversion in term of productivity and selectivity (**Fig. 33**). The g-C₃N₄ could be enhance the conversion of 77% at 12 h. Interestingly, the different main products were gluconic acid and formic acid comparing with benchmark (P25). The yield of gluconic acid, formic acid, arabinose, and xylitol were 35.2, 29.7, 8.9 and 4.4%, respectively. However, others synthesized quantum-compound including ZAIS, AIS, CuO, and V₂O₅ were no substantial effect on the photocatalytic performance (data not shown). The fabricated photocatalyst will be further study on glucose conversion in order to compare the performance with photocatalysts nanoparticles.

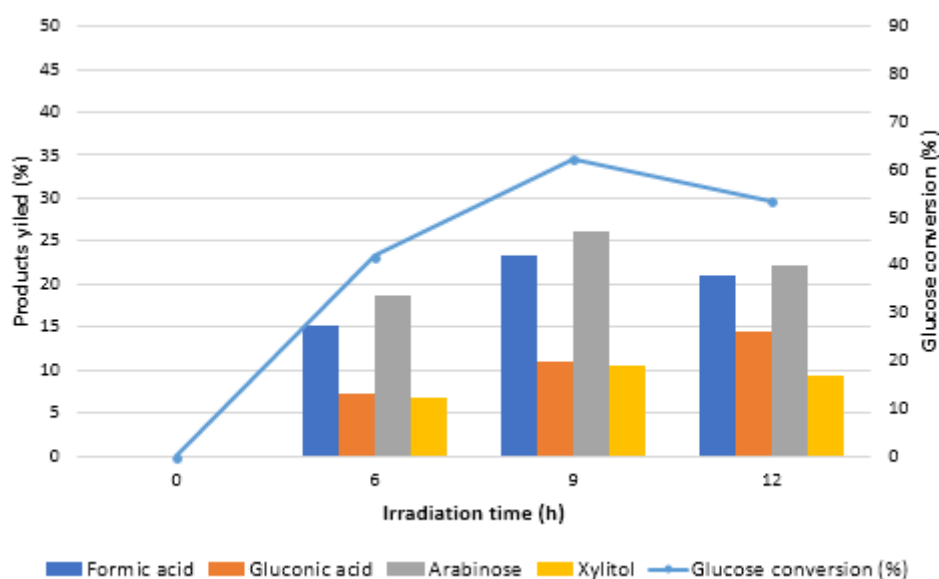


Fig. 32. Photocatalytic conversions of glucose under visible light irradiation in the presence of TiO₂ (P25)

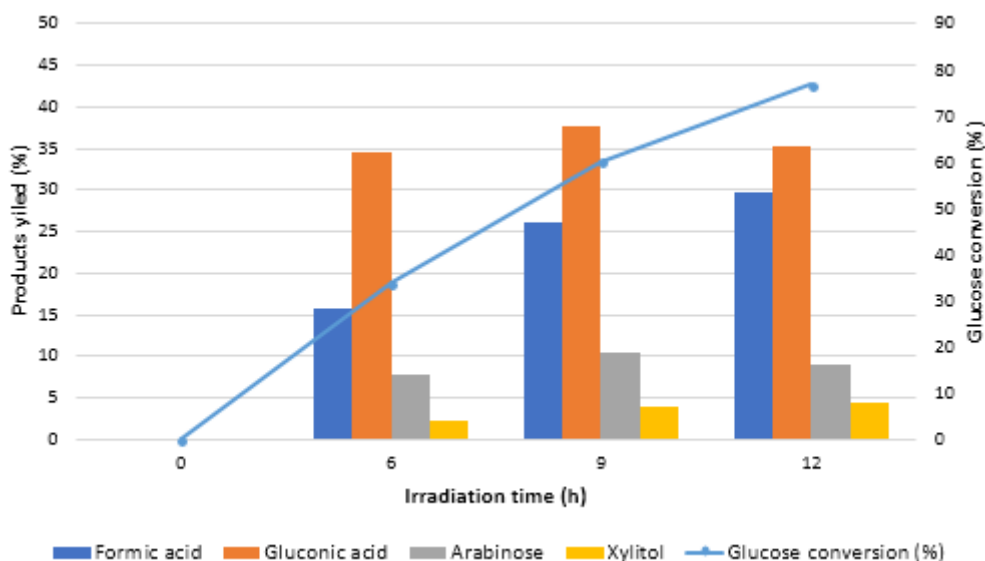


Fig. 33. Photocatalytic conversions of glucose under visible light irradiation in the presence of graphitic carbon nitride (g-C₃N₄)

1.3.8 Effect of Metal (Ag, and bimetallic (Ag and Cu) loading on 30%TiO₂/ZeY

In the previous section, it was found that the TiO₂ coated on surface of zeolite (TiO₂/ZeY) showed well distribution. This was caused by reduction of the agglomeration of synthesized TiO₂ nanoparticles which led to increasing photocatalytic performance of TiO₂. In this section, TiO₂/ZeY was further modified with Ag, Cu, and Ag-Cu bimetallic for improvement of TiO₂ properties and photocatalytic glucose conversion.

1.3.8.1 Characterization of Ag-TiO₂/ZeY photocatalyst

Fig. 34 (A, B, C, and D) showed the SEM images of 30%TiO₂/ZeY, and 0.5, 1, and 3wt.% Ag loading 30%TiO₂/ZeY. The SEM images showed that surface morphology of 30%TiO₂/ZeY was changed after Ag loading but the presence of Ag nanoparticle on the surface of TiO₂/ZeY was not clearly observed by SEM. The Ag content contained on catalyst surface of Ag-TiO₂ (30%)/ZeY sample was determined by EDS analysis. The peaks of Ag were observed at 3 keV (**Fig. 35**), which can confirm that Ag nanoparticles had been deposited onto the surface of TiO₂. The EDS analyses of all catalysts are presented in **Table 9**. From these data, the amount of metal was not equal to the actual loading because EDS analysis represents only surface concentration. This can be caused by other factors such as layer thickness, metal cluster size, and surface coverage, which are strongly influence on EDS analysis. So, the metal content analyzed by EDS was different from the absolute metal concentrations of the samples. However, the Ag content increased when Ag loading was increased in the catalyst preparation step. XRD patterns of TiO₂ (30%)/ZeY (undoped) and 0.5%, 1, 3, and 5wt.% Ag loading on TiO₂ (30%)/ZeY are illustrates in **Fig. 36**. All of the photocatalysts presented the strong diffraction peaks of anatase at 25.4°. The characteristic peak of Ag could not be observed on the XRD

patterns. This phenomenon may be ascribed to the loading of Ag which was below the detection limit of the instrument or high dispersion of metals on the surface of TiO_2/ZeY (Hlekelele et al. 2018). From **Table 10**, it was observed that the crystallite size of anatase decreased after Ag was loaded on $\text{TiO}_2(30\%)/\text{ZeY}$. This can indicate that Ag loading can lead to the increase anatase in TiO_2 . The rearrangement of titanium and oxygen ions in anatase grain boundaries would be disturbed by the silver ions. The transferring of material in anatase grains could lead to increasing energy for the movement of anatase grain boundary, resulting in slower grain growth. However, at 5wt% Ag loaded, the crystallite size was larger than that of the undoped. It could be explained that the greater Ag content over TiO_2/ZeY surface could enhance the growth of the crystallite size. So, the crystalline size increased with the higher Ag content (Jaafar et al. 2015).

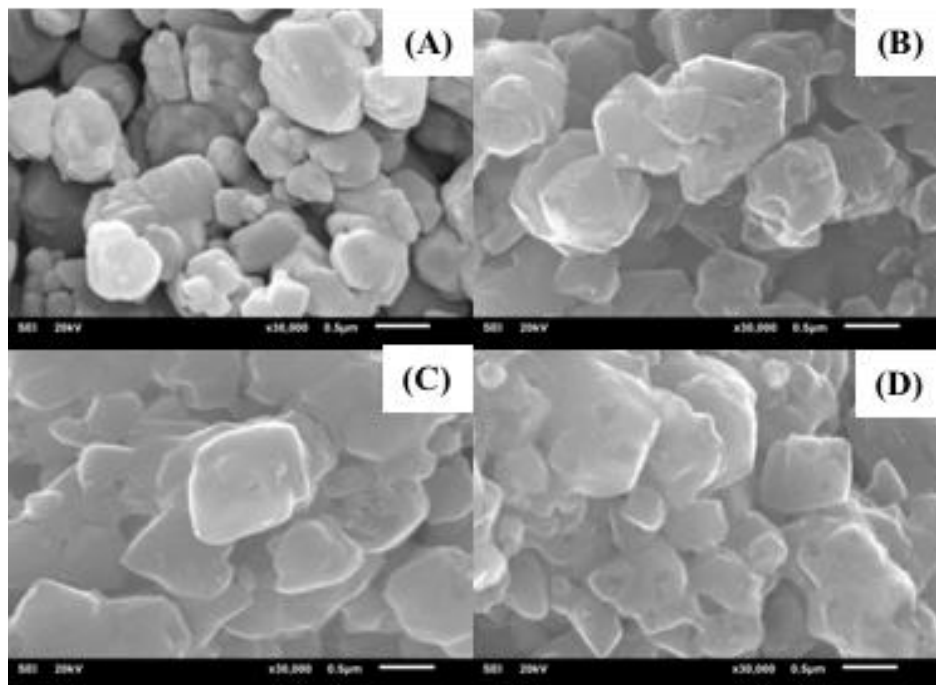


Fig. 34. SEM images (30000x) of (A) $\text{TiO}_2(30\%)/\text{ZeY}$ (B) 0.5wt.% $\text{Ag-TiO}_2(30\%)/\text{ZeY}$, (C) 1wt.% $\text{Ag-TiO}_2(30\%)/\text{ZeY}$, and (D) 3wt.% $\text{Ag-TiO}_2(30\%)/\text{ZeY}$ prepared by wetness impregnation with MW.

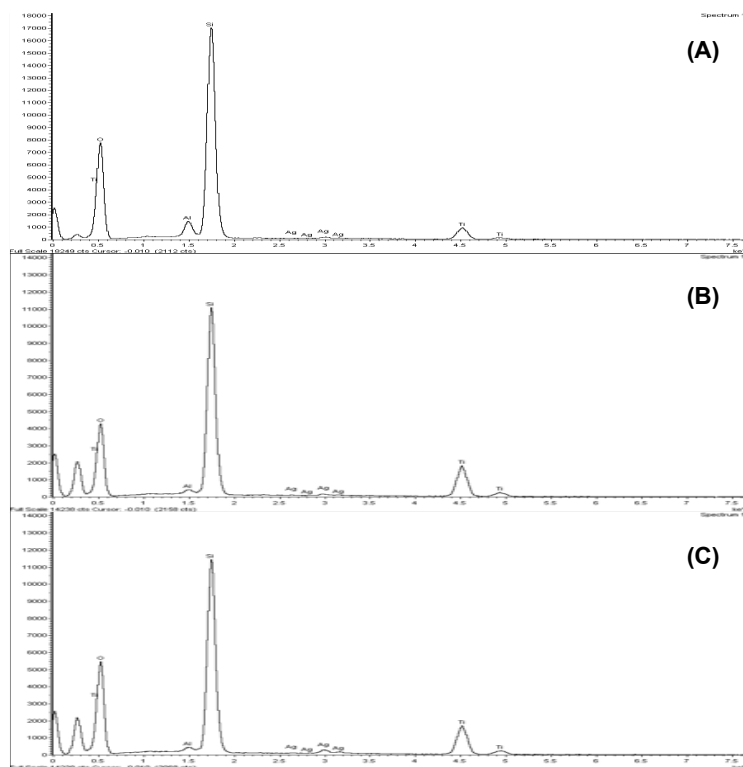


Fig. 35. EDS analyses of (A) 0.5wt.% Ag-TiO₂(30%)/ZeY, (B) 1wt.% Ag-TiO₂(30%)/ZeY, and (C) 3wt.% Ag-TiO₂(30%)/ZeY prepared by wetness impregnation with MW.

Table 9. Atomic ratios (wt.%) of three Ag-TiO₂ catalysts.

Catalyst	Intended metal loading (wt.%)	Atomic ratio (wt.%)				
		Ag	Ti	Al	Si	O
0.5wt.%Ag-TiO ₂ (30%)/ZeY	0.5	0.75	4.02	2.15	31.67	61.41
1wt.%Ag-TiO ₂ (30%)/ZeY	1	0.81	10.99	0.58	29.05	58.57
3wt.%Ag-TiO ₂ (30%)/ZeY	3	1.76	9.21	0.54	26.74	61.75

The specific surface area, and pore volumes of TiO₂/ZeY, 1 wt.%Ag-TiO₂/ZeY, and 3 wt.%Ag-TiO₂/ZeY are shown in **Table 11**. The specific surface area was slightly decreased (from 494.57 to 480.41 m²/g) after the loading of Ag ion. It could be explained by the successful loading of Ag through the wetness impregnation method on the surface of TiO₂/ZeY. The pore volume of samples was increased with increasing Ag content due to the high dispersion of Ag on the surface of TiO₂/ZeY. The effects of Ag doping content on the absorption threshold and the band gap energy of TiO₂ were also examined by UV-Visible Diffuse Reflectance

spectroscopy. The optical absorbance spectra of pure $\text{TiO}_2(30\%)/\text{ZeY}$, 0.5wt.%Ag- $\text{TiO}_2(30\%)/\text{ZeY}$, 1wt.%Ag- $\text{TiO}_2(30\%)/\text{ZeY}$, and 3wt.%Ag- $\text{TiO}_2(30\%)/\text{ZeY}$ are shown in **Fig. 37**. The absorption edge of 0.5wt.% Ag- $\text{TiO}_2(30\%)/\text{ZeY}$, 1wt.%Ag- $\text{TiO}_2(30\%)/\text{ZeY}$, and 3wt.%Ag- $\text{TiO}_2(30\%)/\text{ZeY}$ shifted to longer wavelength in the UV-vis region, indicating that Ag doped TiO_2/ZeY with broadened the absorption edge of TiO_2 . The band gap energy (E_g) of $\text{TiO}_2(30\%)/\text{ZeY}$, 0.5wt.%Ag- $\text{TiO}_2(30\%)/\text{ZeY}$, 1wt.%Ag- $\text{TiO}_2(40\%)/\text{ZeY}$, and 3wt.%Ag- $\text{TiO}_2(30\%)/\text{ZeY}$ were 3.12, 3.08 and 3.05 eV, respectively, as shown in **Table 12**. It implied that when Ag doping content increased, the absorption edge shifted towards a longer wavelength, which affected the decrease of the band gap. The shortening of band gap induced TiO_2/ZeY more photocatalytic activity, due to the decrease in the yield of photogenerated electron-hole pairs and the increase in the photocatalytic activity of TiO_2/ZeY (Rengaraj and Li 2006).

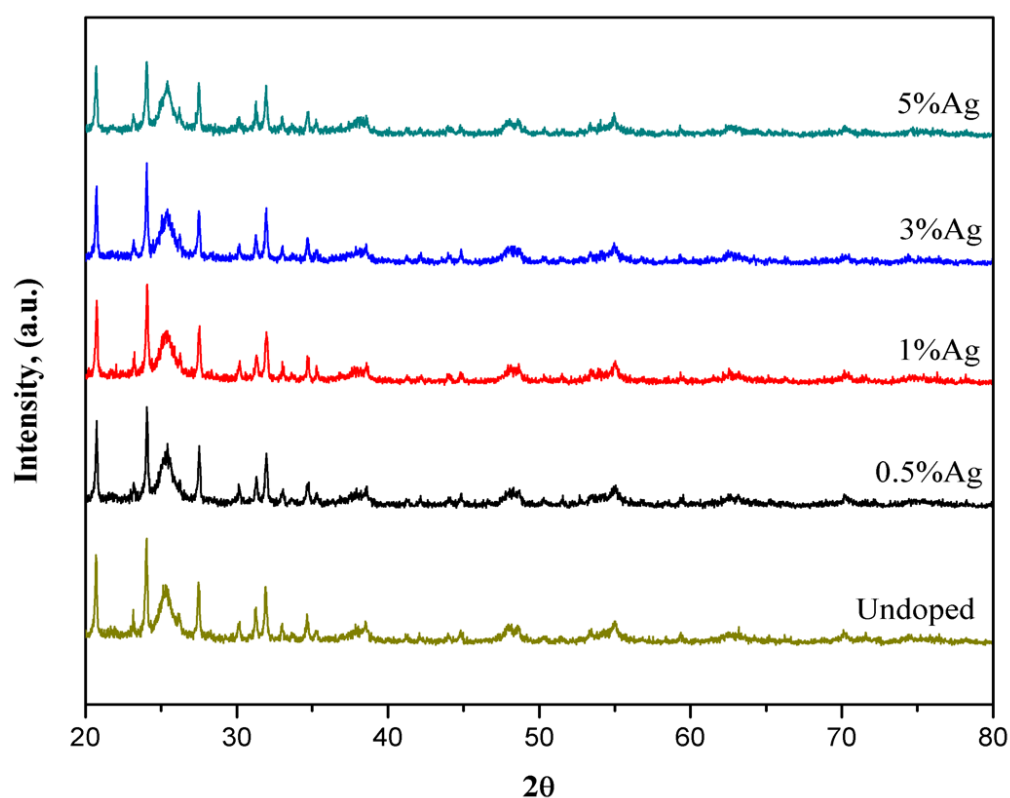


Fig. 36. XRD patterns of doped Ag (0.5%,1%,3%, and 5%) on $\text{TiO}_2(30\%)/\text{ZeY}$.

Table 10. Summary of crystal phases and crystallite sizes of Ag- loaded $\text{TiO}_2(30\%)/\text{ZeY}$ synthesized by wetness impregnation with MW (A = anatase, R = rutile).

Photocatalyst	Crystal phase (%)	Crystallite size (nm)
---------------	-------------------	-----------------------

Undoped	A(38)/R(62)	A(15.14)
0.5% Ag	A(40)/R(60)	A(11.80)
1% Ag	A(42)/R(58)	A(11.81)
3%Ag	A(44)/R(56)	A(13.31)
5% Ag	A(45)/R(55)	A(21.33)

Table 11. Specific surface areas (S_{BET}), pore volumes (V_p), and pore diameters of (1% and 3%) Ag-loaded on TiO_2 (30%)/ZeY.

Photocatalyst	N_2 isotherms		
	S_{BET} (m^2/g)	V_p (mL/g)	Pore diameter (nm)
Undoped	494.57	0.30	3.68
1% Ag	487.53	0.33	3.69
3%Ag	480.41	0.32	3.70

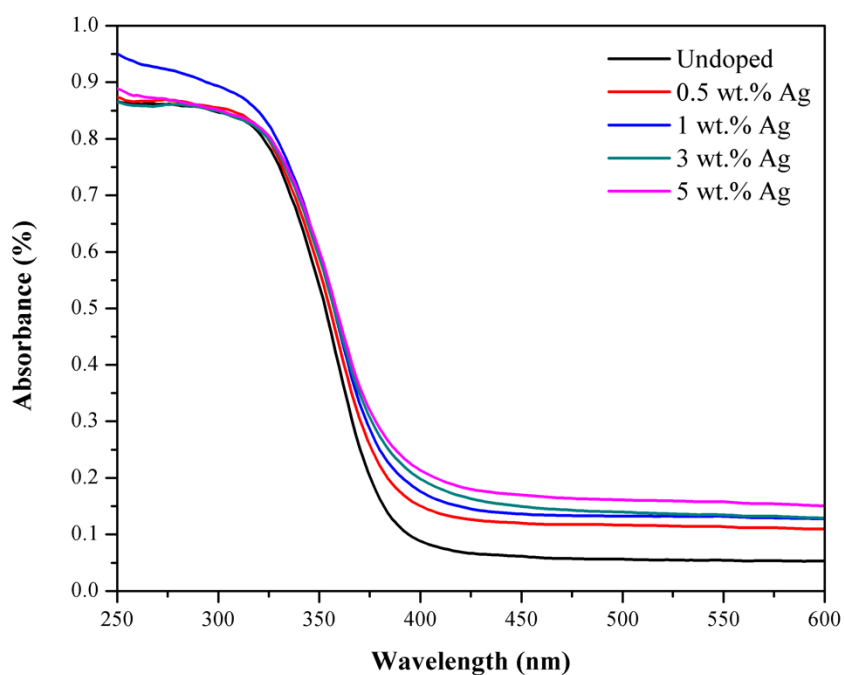


Fig. 37. UV-vis diffuse reflectance spectra of Ag-loaded on TiO_2 (30%)/ZeY.

Table 12. Summary of characteristics of Ag-loaded TiO₂ (30%)/ZeY catalyst prepared by wetness impregnation with MW techniques obtained from UV-vis diffuse reflectance spectra.

Photocatalyst	Wavelength (nm)	E _g
Undoped	386	3.21
0.5 wt.% Ag	389	3.19
1 wt.% Ag	392	3.16
3 wt.% Ag	394	3.15
5 wt.% Ag	395	3.14

1.3.8.2 Photocatalytic conversion of glucose

The glucose conversion on the Ag-TiO₂/ZeY base catalyst was carried out for 120 min. The photocatalytic activity of TiO₂/ZeY and Ag-TiO₂/ZeY catalysts with Ag loading content 0.5, 1, 3, and 5 wt.% are shown in **Fig. 38** and the maximum yields of products are shown in **Fig. 39**. The result indicated that after 120 min irradiation time, four organic compounds were produced: xylitol, gluconic acid, arabinose and formic acid. The highest glucose conversion of 96.90% and the yield of gluconic acid, arabinose, xylitol and formic acid are 3.43%, 9.97%, 11.87% and 57.79% were obtained from 1wt.%Ag-TiO₂(30%)/ZeY. It indicated that with the high surface area (487.53 m²/g), mixed phase of anatase and rutile (42% of anatase : 58% of rutile), small crystallite size (11.81 nm) and small band gap (3.08 eV) of 1wt.%Ag-TiO₂(30%)/ZeY could promote high photocatalytic activity. The small band gap facilitated yield of photogenerated electron-hole pairs increase, and electrons easily transferred ([Rengaraj and Li 2006](#)). It was reported that Ag dopant could insert into TiO₂ lattice as Ag impurity state, over the valance band and below the conduction band of TiO₂, forms in its optical band gap. For photocatalytic reaction of glucose under mercury lamp irradiation, electrons in valence band were excited to Ag impurity state, left holes in valence band, and after that these electrons were transferred from impurity state to conduction band. Doping of Ag could led to the formation of an intermediate band that the electron can transiently stay before transfer to the conduction band. This could facilitate the photoactivity in the visible light region ([Sun et al. 2010](#)). On the other hand, 5wt.% TiO₂(30%)/ZeY enhanced the lowest glucose conversion because the high Ag loading might close active site of catalyst which resulted in low photocatalytic activity. Furthermore, Ag might defect into the TiO₂ lattice resulting in too many oxygen vacancies in the lattice. Oxygen vacancies acted as recombination centers of generated electron-hole pairs, resulting decreased photocatalytic activity ([Lv et al. 2014](#)).

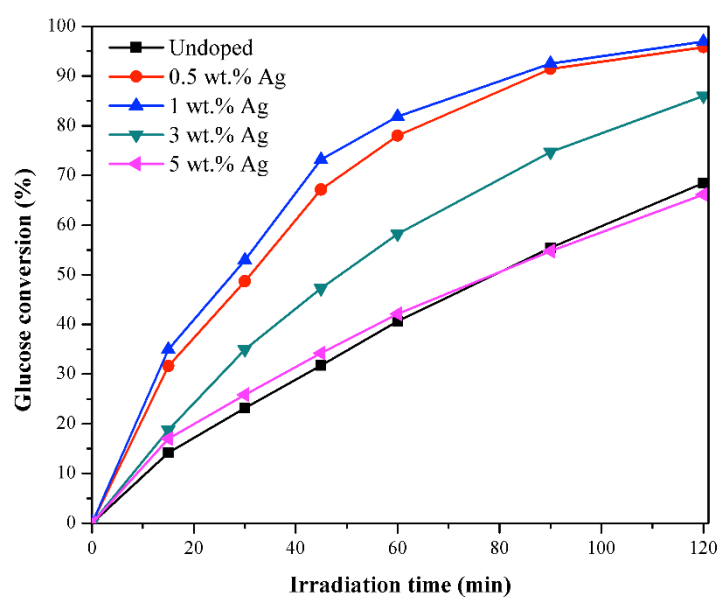


Fig. 38. Photocatalytic conversions of glucose under UV irradiation for 120 min with Ag-loaded on $\text{TiO}_2(30\%)/\text{ZeY}$ catalyst prepared by wetness impregnation with MW techniques.

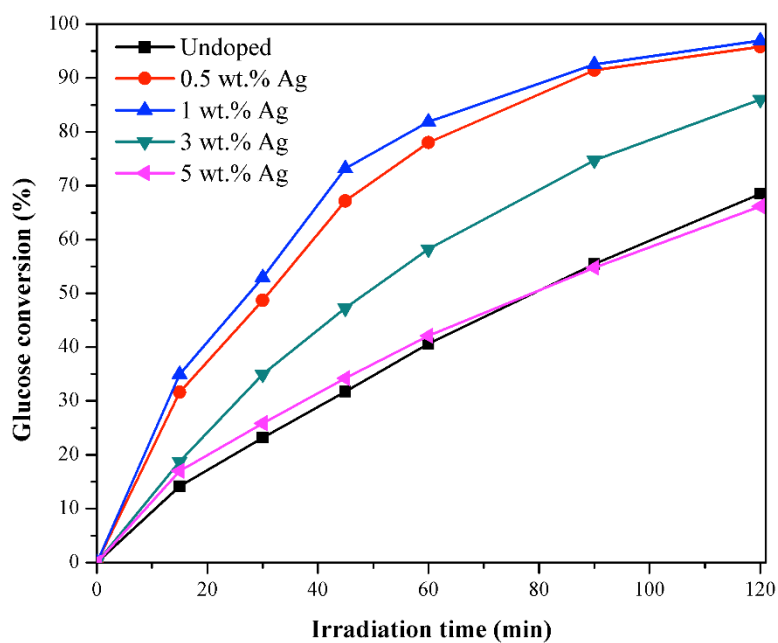


Fig. 39. Product yields of formic acid, gluconic acid, arabinose, and xylitol at 120 min with Ag-loaded on $\text{TiO}_2(30\%)/\text{ZeY}$ catalyst prepared by wetness impregnation with MW techniques.

1.3.8.3 Characterization of Cu and Ag-Cu bimetallic loading TiO_2/ZeY photocatalyst

Cu is one of the transition metals that was found to be an effective dopant for TiO_2 which could enhance the photocatalytic activity. The Cu doped TiO_2/ZeY affected the crystal phase and the crystallite size of anatase. The comparison of XRD patterns of 1 wt.%Cu doped TiO_2/ZeY and 1 wt.%Ag-Cu doped TiO_2/ZeY , 1 wt.% Ag doped TiO_2/ZeY and undoped prepared by wetness impregnation technique are shown in **Fig. 40**. The phase identification and crystallite size of the photocatalyst from XRD analysis are shown in **Table 13**. All of photocatalysts presented diffraction peaks of anatase but it could not observe neither the characteristic peaks of Cu nor those of Ag as shown in Figure 60. In addition, both of Cu-doped TiO_2/ZeY and Ag-Cu-doped TiO_2/ZeY increased crystal phase of anatase. It indicated that Cu and Ag-Cu bimetallic dopant inhibited phase transformation from anatase to rutile. The phenomena occurred due to the incorporation of Cu and Ag-Cu bimetallic into the TiO_2 lattice. Cu^{2+} (0.73\AA) and Ti^{4+} (0.64\AA) have similarity in the ionic radius, so, the Cu ions can substitutional to replace Ti ions in TiO_2 lattice and might exist in the form of Ti-O-Cu three elements around the anatase crystallites which possibly inhibited the transformation to rutile phase (Francisco et al, 2002). Moreover, the crystallites size of anatase increased after Cu and Ag doped TiO_2/ZeY . It can be explained by metal ions doped into TiO_2 lattice, which tended to present in the grain boundary regions or on the surface of particles which could inhibit the growth of TiO_2 crystallites size (Christoforidis and Fernández-García 2016).

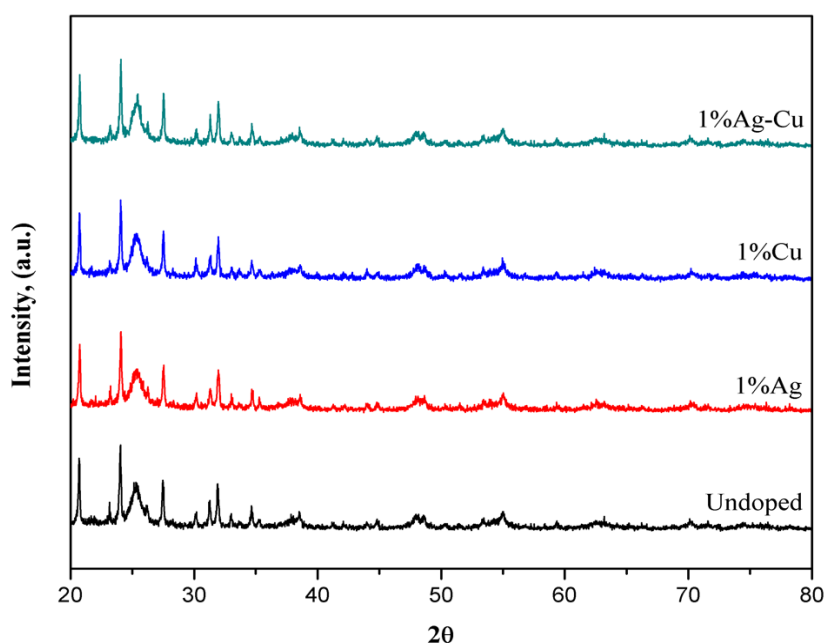


Fig. 40. XRD patterns of doped Cu (1%) and bimetallic (1% Ag-Cu) compared with 1% Ag on TiO_2 (30%)ZeY and undoped.

Table 13. Summary of crystal phases and crystallite sizes of 1% Ag, 1%Cu, and 1% Ag-Cu loaded TiO₂ (30%)/ZeY (70%) (A = anatase, R = rutile).

Photocatalyst	Crystal phase (%)	Crystallite size (nm)
Undoped	A(38)/R(62)	A(15.14)
1% Ag	A(42)/R(58)	A(11.81)
1% Cu	A(40)/R(60)	A(11.79)
1% Ag-Cu	A(44)/R(56)	A(21.29)

The Cu-doped TiO₂/ZeY and Ag-Cu doped TiO₂/ZeY on the absorption threshold and the band gap energy were also examined by UV-Visible Diffuse Reflectance spectroscopic. The UV-visible diffuse reflectance spectra of undoped TiO₂/ZeY, 1wt.% Ag- TiO₂/ZeY, 1wt.% Cu- TiO₂/ZeY, and 1wt.% Ag-Cu- TiO₂/ZeY are shown in **Fig. 41**. The absorption spectrum for Cu, Ag and Ag-Cu doped TiO₂/ZeY shifted to an energy region lower than the undoped TiO₂/ZeY and the red shift of the absorbance edge toward longer wavelengths of Cu, Ag and Ag-Cu doped TiO₂/ZeY which promoted the decrease in band gap energy of TiO₂/ZeY. Hence, the values of Eg for TiO₂/ZeY, 1wt.% Ag- TiO₂/ZeY, 1wt.% Cu- TiO₂/ZeY, and 1wt.% Ag-Cu- TiO₂/ZeY were 3.18, 3.08, 3.04, and 3.13 eV, respectively as shown in **Table 14**. It indicated that Eg values decreased with loading metal. The electron could be easily transferred when Cu- TiO₂/ZeY, Ag-Cu- TiO₂/ZeY have low band gap energy (Francisco and Mastelaro 2002). In addition, the inducing impurity energy level by doping metal (Cu, and Ag) led to separation of electron-hole pair. As the valence band of Cu²⁺ ion is less than Ti⁴⁺, so Cu doped TiO₂ could induce oxygen vacancies, which acted as the active sites and could also capture the holes to restrain the recombination of hole–electron pairs. Hence, this resulted in high photocatalytic performance of TiO₂/ZeY.

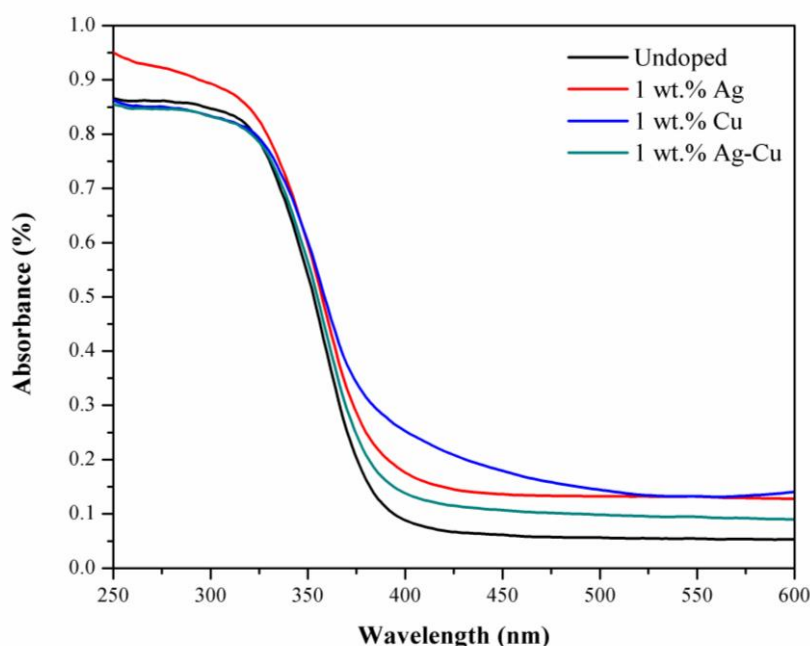


Fig. 41. UV-vis diffuse reflectance spectra of 1% Ag, 1% Cu, and 1% Ag-Cu-loaded on $\text{TiO}_2(30\%)/\text{ZeY}(70\%)$.

Table 14. Summary of characteristics of 1% Ag, 1% Cu, and 1% Ag-Cu-loaded $\text{TiO}_2(30\%)/\text{ZeY}(70\%)$ catalyst prepared by wetness impregnation with MW techniques obtained from UV-vis diffuse reflectance spectra.

Photocatalyst	Wavelength (nm)	Eg
Undoped	386	3.21
1% Ag	392	3.16
1% Cu	389	3.19
1% Ag-Cu	390	3.18

1.3.8.4 Photocatalytic conversion of glucose

The photocatalytic activity of Ag-Cu- TiO_2 compared to Ag- TiO_2 and Cu- TiO_2 catalysts are shown in **Fig. 42**. It was found that glucose conversion with 1wt.% Ag- TiO_2/ZeY , 1wt.% Cu- TiO_2/ZeY and 1wt.% Ag-Cu- TiO_2/ZeY achieved by 96.90, 94.71, and 82.23%, respectively. Among them, 1wt.% Cu- TiO_2/ZeY achieved lowest glucose conversion. The maximum yield of products: xylitol, gluconic acid, arabinose and formic acid are 12.93%, 5.92%, 20.49% and 59.73% respectively. But when compared with undoped ($\text{TiO}_2(30\%)/\text{ZeY}$), 1wt.% Cu- TiO_2 present higher

glucose conversion because Cu have smaller band gap than TiO_2/ZeY , so the electron can transfer from the conduction band of TiO_2/ZeY to metallic copper ion. This could facilitate the charge separation, and hence enhances the photocatalytic performance of TiO_2/ZeY . The bimetallic Ag/Cu were studied for the purpose of increasing the efficiency of photoconversion of glucose. In conclusion, the bimetallic 1 wt.% Ag-Cu doped TiO_2/ZeY present higher glucose conversion than 1 wt.% Cu doped TiO_2/ZeY . It can indicate that metallic Ag can promote the increased efficiency of Cu. The conversion efficiency by 1 wt.% Ag-Cu doped TiO_2/ZeY achieved 94.71% and the yield of gluconic acid, arabinose, xylitol and formic acid are 5.91%, 20.49%, 12.93%, and 59.73% respectively (**Fig. 43**). Moreover, the bimetallic Ag-Cu doped TiO_2/ZeY enhanced the highest xylitol yield of 12.93% and selectivity of 13.65%.

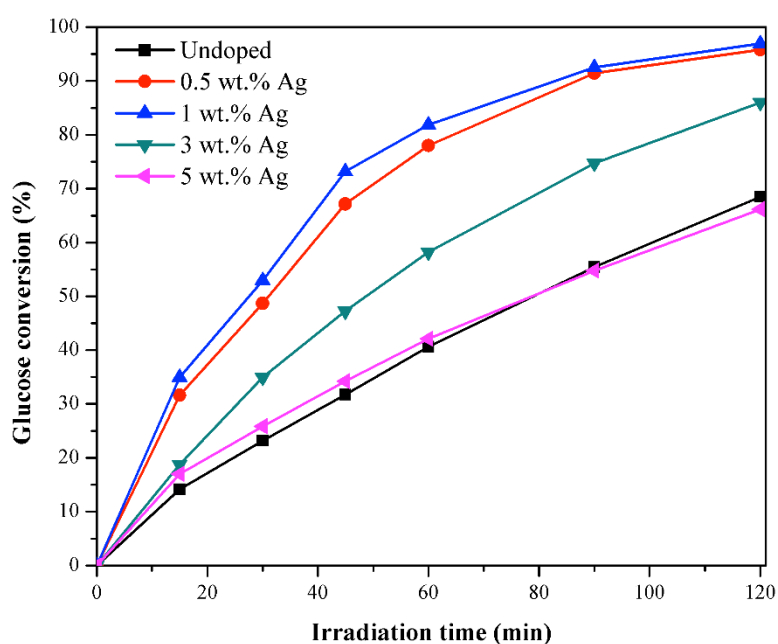


Fig. 42. Photocatalytic conversions of glucose under UV irradiation for 120 min with 1% Ag, 1%Cu and 1%Ag-Cu-loaded on TiO_2 (30%)/ZeY catalyst prepared by wetness impregnation with MW techniques.

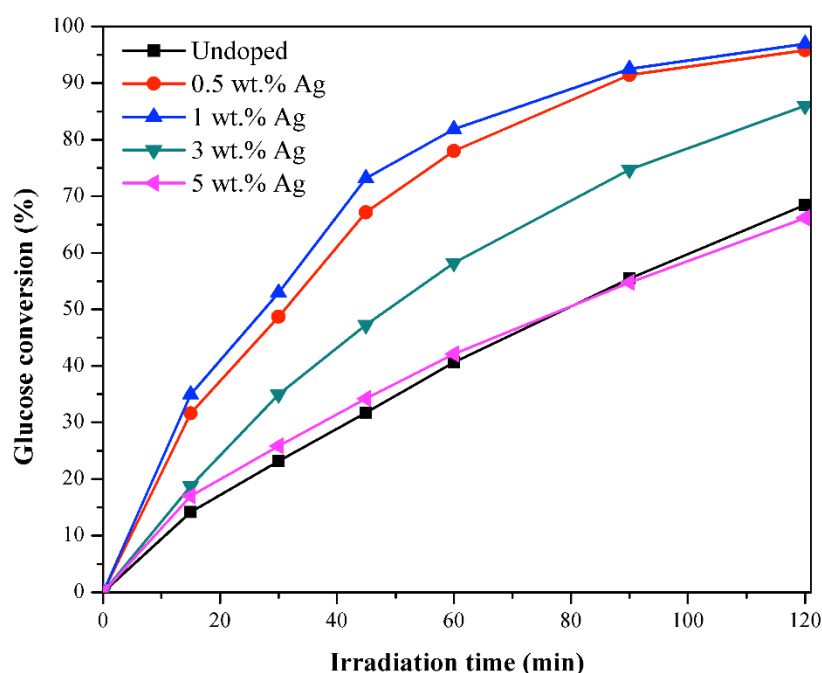


Fig. 43. Product yields of formic acid, gluconic acid, arabinose, and xylitol at 120 min with 1% Ag, 1%Cu and 1%Ag-Cu-loaded on TiO₂ (30%)/ZeY compared with TiO₂ (30%)/ZeY.

1.3.9 Photocatalytic performance in photo bio-flow reactor

In this work, TiO₂ was coated on supporter (such as glass bead, ceramic, and alumina ball) and used as photocatalyst in photo-bio flow reactor. Among our photocatalysts, it was found that Ag-N/TiO₂ nanoparticles present high performance of photocatalytic glucose conversion. Several methods have been reported to prepare TiO₂ coatings, including sol gel (Ranjitha et al., 2013; Liang et al., 2018), chemical vapor deposition (Quesada-González et al., 2016), thermal spraying (Mauer et al., 2013), and impregnation (Huang et al., 2011). According to coating methods, sol gel and impregnation method have several advantages including coating on complicated surface, simple operation and low temperature. So, this work was focused on coating methods which base on sol gel and impregnation technique.

1.3.9.1 Type of supporter

In this work, ceramic and alumina balls were selected as supporter to investigate the suitable material for coating. Ag-N/TiO₂ coated on supporter were prepared by dip coating method. The field emission scanning electron microscope (FE-SEM) was used to determine the surface morphology, catalyst morphology, and particles size. According to results (Fig. 44a and 44b), coated on ceramic ball exhibit rough surface morphology than coated alumina ball. This indicates the agglomeration of Ag-N/TiO₂ nanoparticles on surface. The Ag-N/TiO₂ on ceramic ball show a smaller particles size (376 nm), while higher dispersion due to roughness surface

of ceramic ball compared to alumina ball. It can conclude that the ceramic ball is suitable supporter for coating.

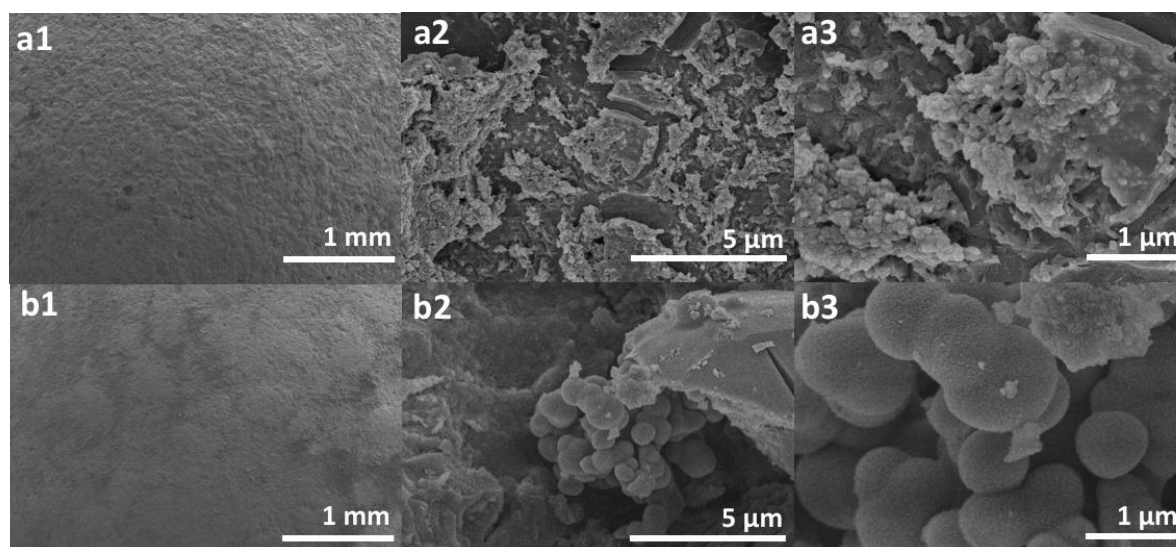


Fig. 44. SEM images of (a) Ag-N/TiO₂ nanoparticles coated on ceramic ball, and (b) Ag-N/TiO₂ nanoparticles coated on alumina ball. Numbers 1, 2, 3 refer to image magnifications of 35 (scale bar = 1mm), 10.0k (scale bar = 5 μm), and 30k (scale bar = 1 μm), respectively.

1.3.9.2 Comparison of various coating techniques

According to the previous section, ceramic balls were selected as supporter for finding the suitable coating method. In this part, Ag-N/TiO₂ were coated on ceramic ball by various techniques (dip coating, dip coating with binder (PVA), impregnation, aging, and evaporation). **Fig. 45** shows the SEM images of the catalyst surface with different coating method. The result showed that the surface of ceramic in different method were covered with Ag-N/TiO₂ nanoparticles. Dip coating method showed small particles size and some agglomeration of Ag-N/TiO₂ (**Fig. 45A**). Further, dip coating with binder showed a uniform of thin film with large thickness because the use PVA as binder (**Fig. 45B**) ([Conradi, M., et al. 2020](#)). However, Ag-N/TiO₂ nanoparticles coated on ceramic ball by dip coating with binder was found with no complete covering on the surface. Impregnation method showed a well coating with high agglomeration of Ag-N/TiO₂ on the surface of ceramic ball (**Fig. 45C**) compared with dip coating method. It was found that aging method showed a uniform of thin film with large thickness (**Fig. 45D**), however, cracks formation was observed due to high temperature during hydrothermal process. For evaporation method, a rough of surface and some aggregation of catalyst were also observed. From the discussion, it can be concluded that dip coating and impregnation are the good condition for coating because of the small particles size, and well packed on surface, This morphology led to high efficiency and stability of modified photocatalyst.

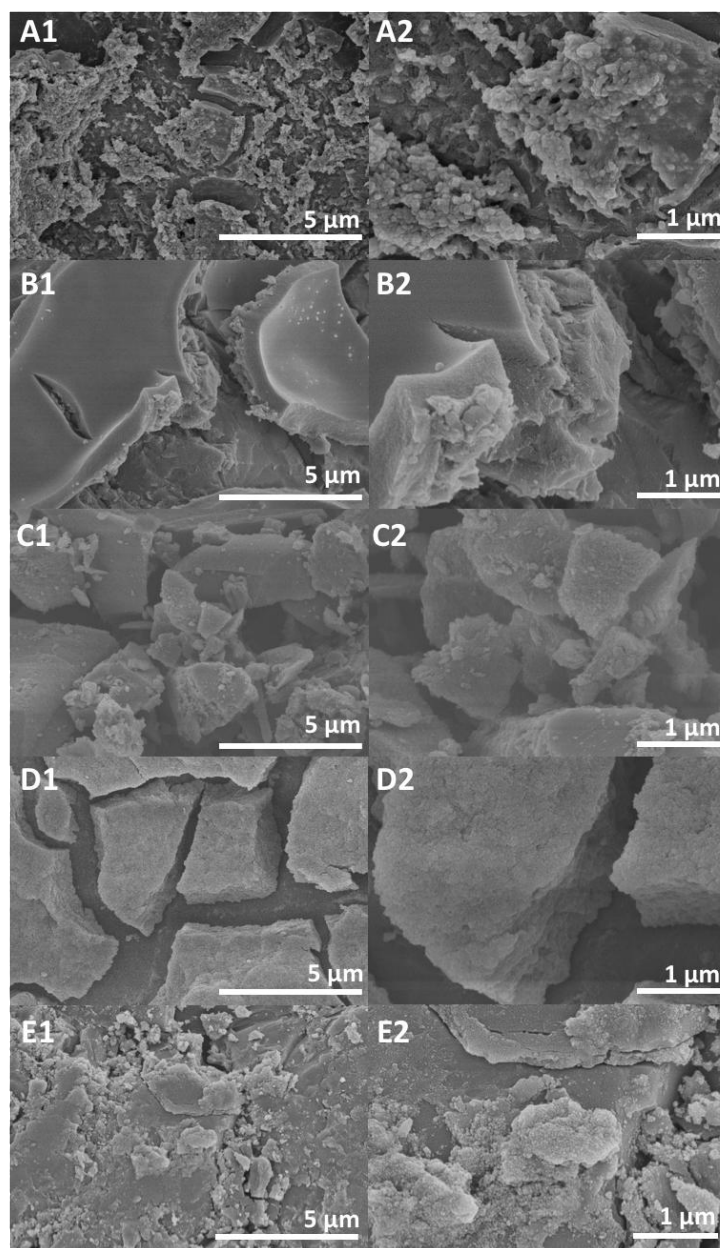


Fig. 45. SEM images of Ag-N/TiO₂ nanoparticles coated on ceramic ball by (A) dip coating (B) dip coating with PVA, (C) impregnation, (D) aging, and (E) evaporation. Numbers 1 and 2 refer to image magnifications of 10.0k (scale bar = 5 μm), and 30k (scale bar = 1 μm), respectively.

1.3.9.3 Photocatalytic degradation of MB

The photocatalytic performance of Ag- N/ TiO₂ immobilized on ceramic balls with different coating method was evaluated by the degradation of methylene blue under UVC light irradiation. To reach the adsorption equilibrium, the MB solution and photocatalyst (Ag- N/ TiO₂ immobilized on ceramic balls) were continually stirred in dark condition for 30 min. The standard experiment (supporter without photocatalyst and photolysis) was also carried out under the same conditions. The standard experiment showed that the concentration of methylene blue solution remained almost the same for the whole processing. This indicates the stable of methylene blue under irradiation (**Fig. 46**). According to **Fig. 47**, it can be clearly seen that Ag- N/ TiO₂ immobilized on ceramic balls prepared by dip coating, and impregnation

led to achieve performance of photocatalytic degradation of MB. Both of dip coating and impregnation could enhanced the degradation of MB nearly 90% for 360 min. The impregnation method showed a high degradation of MB at 120 min and remain constant until 360 min. The high performance could be described that well packed and high dispersion of photocatalyst on ceramic ball. The excellent photocatalytic degradation of Ag-N/TiO₂ prepared by dip coating and impregnation will be further proposed for photocatalytic glucose conversion.

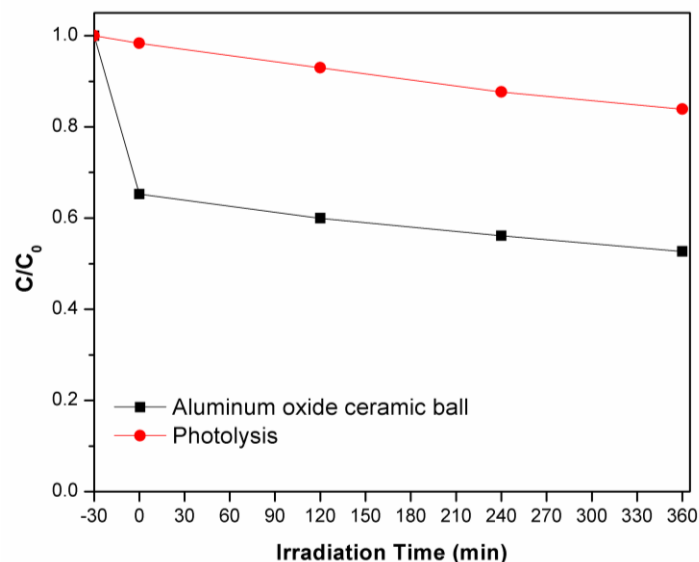


Fig. 46. Photocatalytic degradation curves of methylene blue (5 ppm) without photocatalyst under UVC.

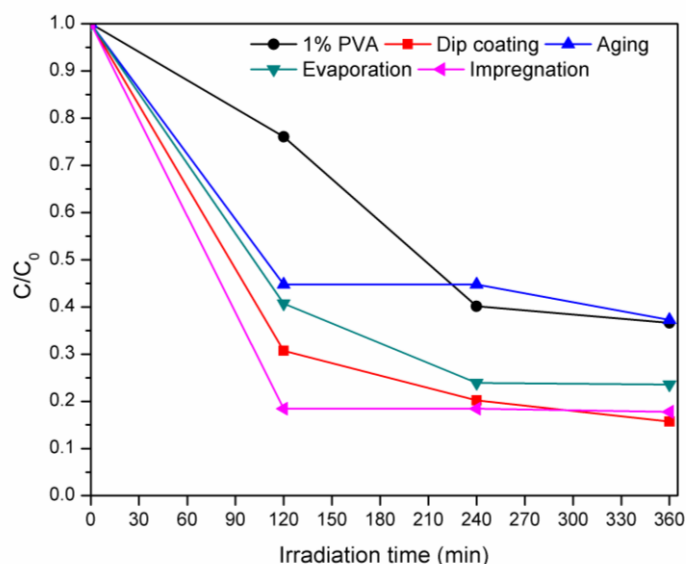


Fig. 47. Photocatalytic degradation curves of methylene blue (5 ppm) over Ag/N-TiO₂ nanoparticles coated on ceramic ball under UVC.

1.3.9.4 Photocatalytic glucose conversion under various solvent mixture

The photocatalytic performance of Ag-N/TiO₂ immobilized on ceramic balls was further evaluated on photocatalytic glucose conversion. The initial aqueous glucose concentration was 1 g/L. The photocatalyst (Ag-N/TiO₂ immobilized on ceramic balls) were continue stirred in glucose solution under dark condition for 30 min to achieve the adsorption equilibrium. The solvent ratio of DI water and acetonitrile was firstly studied to optimize the best condition for glucose conversion and product yields. It was found that the solvent mixture of 10% H₂O/90% ACN showed the performance of photocatalytic glucose conversion of 16%, which achieved 4 times compared with pure DI water (**Fig. 48a**). The results in this study seems to be similar to the previous reported by other researchers ([Colmenares, J. C., et al 2013](#); [Payormhorm et al., 2017](#)). For product distribution at 180 min (**Fig. 48b**), it was found that the modified photocatalyst in solvent mixture of 10% H₂O/90% ACN gave the yield of gluconic acid, arabinose, xylitol, and formic of 2.7%, 6.9%, 0.6%, and 3.6%, respectively. Arabinose is the main product in this reaction. On the other hand, the product distribution of pure water showed the highest yield of gluconic acid, which equivalent to 2.6%. Thus, the best solvent ratio for enhance high photocatalytic glucose conversion and product yield is 10% H₂O/90% ACN.

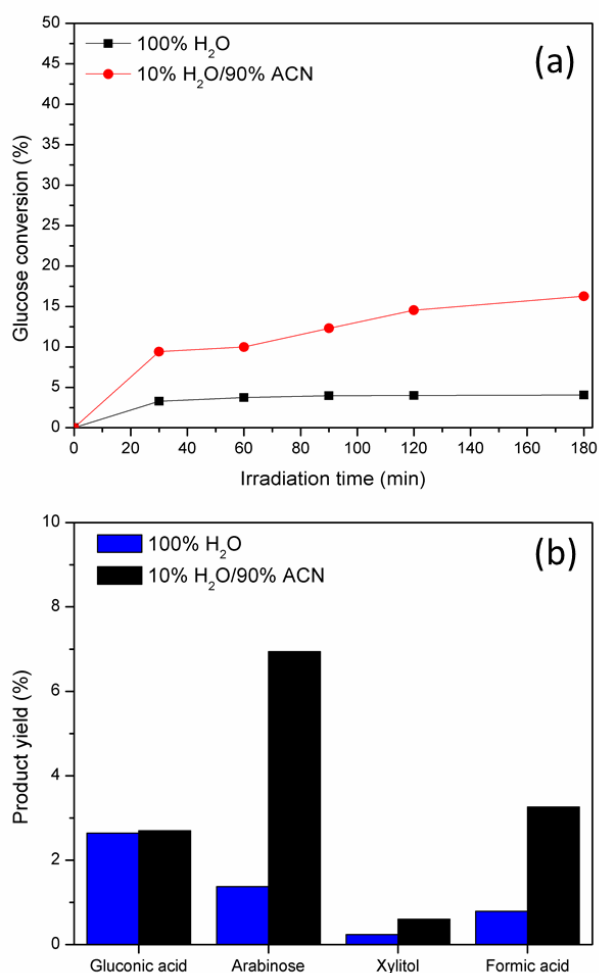


Fig. 48. Photocatalytic conversions of glucose (a) and product yields distribution (b) with Ag-N/TiO₂ immobilized on ceramic balls in different two solvents.

1.3.9.5 Photocatalytic glucose conversion with different coating technique

The photocatalytic performance of Ag-N/TiO₂ immobilized on ceramic balls with different coating method (dip coating and impregnation) were investigated by the glucose conversion under UVC light illumination for 360 min. The initial aqueous glucose concentration was 1 g/L in a mixture of 10% H₂O/90% ACN. The experiment was also carried out under the same conditions that mention before. The photocatalytic glucose conversion over Ag-N/TiO₂ immobilized on ceramic balls prepared by dip coating and impregnation method are demonstrated in **Fig. 49**. It was observed that the impregnation method led to higher performance of photocatalytic activity than dip coating. The impregnation method could achieve the glucose conversion of 24% for 360 min (**Fig. 49a**). Both coating methods showed a similar trend of product yield. Arabinose and gluconic acid were the main product in this reaction (**Fig. 49b**). The highest yield of gluconic acid, arabinose, xylitol, and formic acid were 8.6%, 12.0%, 1.0%, and 7.6% respectively.

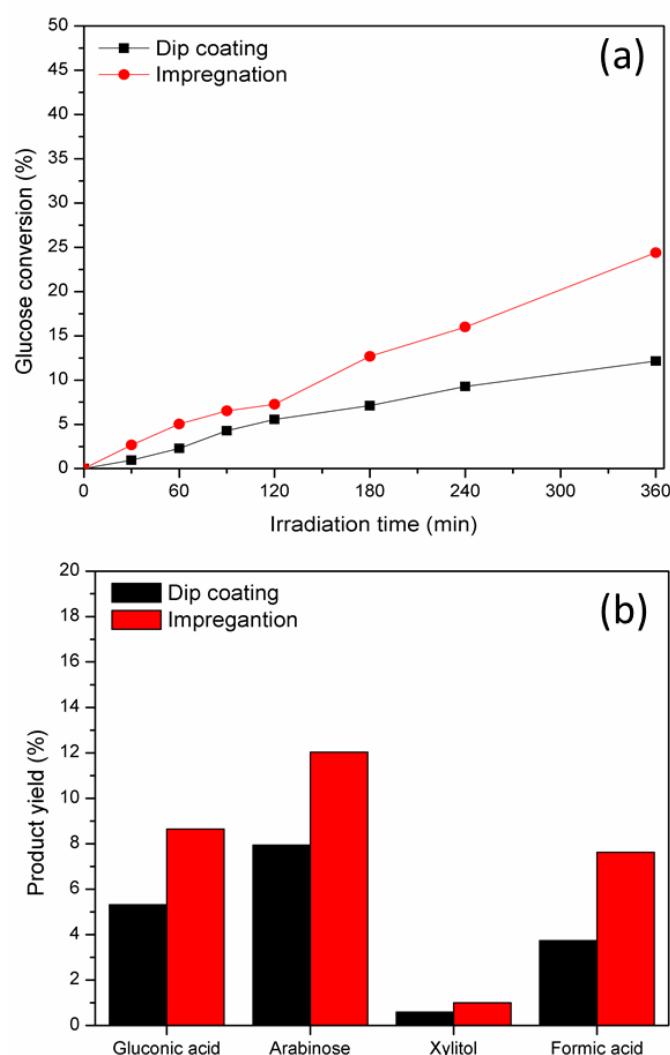


Fig. 49. Photocatalytic conversions of glucose (a) and yields of the products (b) with Ag-N/TiO₂ immobilized on ceramic balls coated by different methods.

1.3.9.6 Recyclability

The recyclability of catalysts is needed to find the stability and the reusability of the catalyst. To achieve up-scaling applications, the photocatalytic activity was repeated for three consecutive batch. **Fig. 50** showed the recycling process and the ability to degrade the MB over Ag/N-TiO₂ prepared by three coating methods (dip coating, dip coating with binder, and impregnation). After recycling, impregnation method showed the same performance in MB degradation, while a slightly decrease of dip coating with binder was observed. This clearly indicates that Ag-N-TiO₂ nanoparticles coated on ceramic balls by impregnation was selected for further using in photo bio-flow reactor.

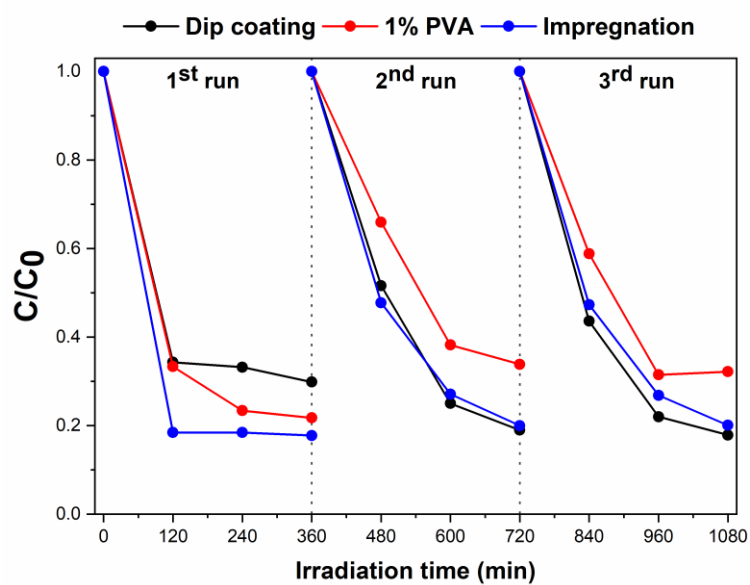


Fig. 50. Recyclability of Ag/N-TiO₂ nanoparticles coated on aluminum ball in photocatalytic degradation of methylene blue (5 ppm) using UVC as light source.

1.3.9.7 Design and assembly of photo-bio flow reactor

The work involves design and assembly of the photo-bio flow prototype for up-scaling on sugar conversion by photocatalytic reaction. In this study, the photo-bio flow reactor was designed based on the overall results in lab-scale in term of process characteristic, yield and selectivity of the products, and reaction kinetics. The 3D sketch of photo-bio flow reactor is illustrated in **Fig. 51a**. According to **Fig. 51b**, a piping and instrument diagram is equipped with storage tank, magnetic pump, metering pump, photo reactor, chiller, and controls and sensors equipment. The photocatalytic reactor design is shown in **Fig. 52**. The reactor is equipped with light source inside covered by quartz glass. The available space in the reactor is used for packing of photocatalyst with cooling jacket to control the temperature of reaction.

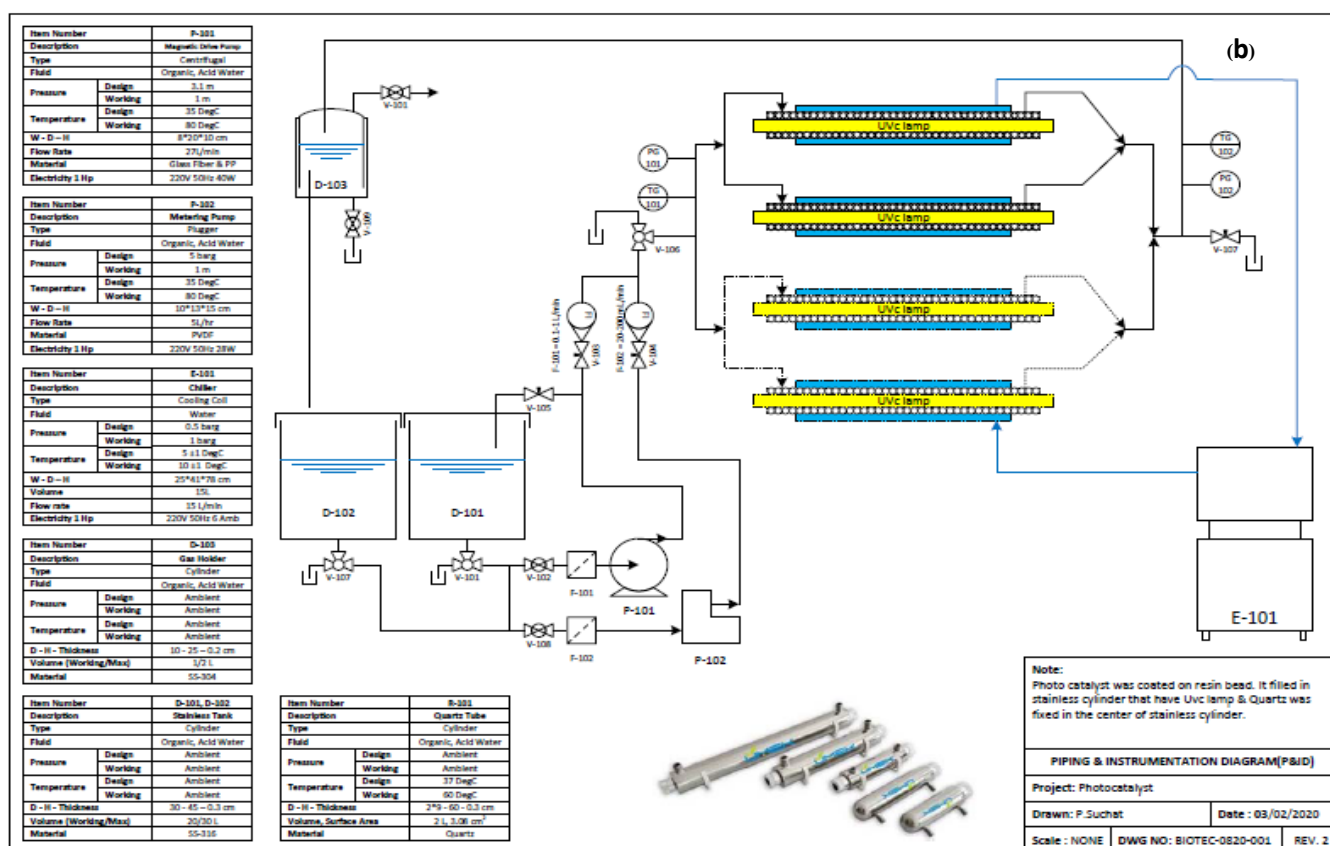
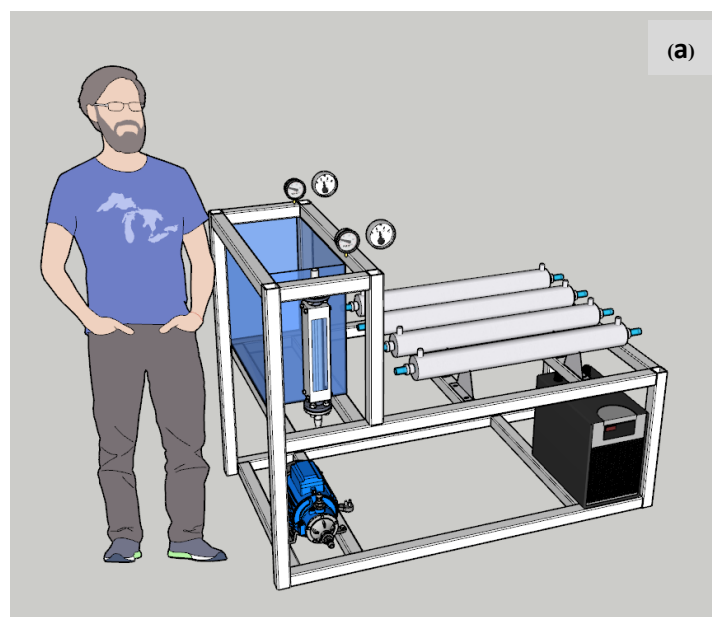


Fig. 51. Design of photo-bio flow reactor: (a) 3D sketch and (b) P&ID diagram



Fig. 53. Accessory equipment for the photo-bio flow reactor

(2) Support equipment

According to the progress work of each equipment shown in **Table 15**, the photo bio-flow reactor was expected to finish in July 2020 and will be test run in Q4 fiscal year 2020.

Table 15 Progress work in design and assembly of the prototype photo-bio flow reactor

List of Equipment	Equipment status				Summary
	Step 1: Specification /Quotation	Step 2: Testing	Step 3: Purchasing process	Step 4: Finish	
Photo reactor	√	√	√	√	Finished
Chiller	√	√	√	√	Finished
Magnetic pump	√	√	√	√	Finished
Metering pump	√	√	√	√	Finished
Lamp and power control	√	√	√	√	Finished
Storage tank	√	√	√	√	Finished

Control and sensor equipment	√	√	√	√	Finished
Fitting	√	√	√	√	Finished
Structure (Aluminum profile)	√	√	√	√	Finished
Chemicals	√	√	√	√	Finished

1.3.9.9 Assembly of photo-bio flow reactor

All equipment was assembled for prototype photo-bio flow reactor as illustrated in

Fig. 54



Fig. 54. Photo-bio flow reactor prototype.

1.3.10 Photocatalytic conversion of lignin to high value fuels and chemicals

Cellulose is the main component of lignocellulosic, while lignin is the second abundant composition. So, lignin has high potential for production of chemicals. There are many techniques to convert lignin to value added chemical, such as pyrolysis, gasification, and depolymerization. These technologies use high temperature and high energy consumption. So, photocatalytic is an interesting process. The photocatalytic conversion of kraft lignin catalyzed by P25 TiO₂ under UV irradiation present various products. The main products from lignin conversion are 2-methyl-naphthalene, 4-hydroxy-benzaldehyde, and vanillin (Fig. 55 and Table 16).

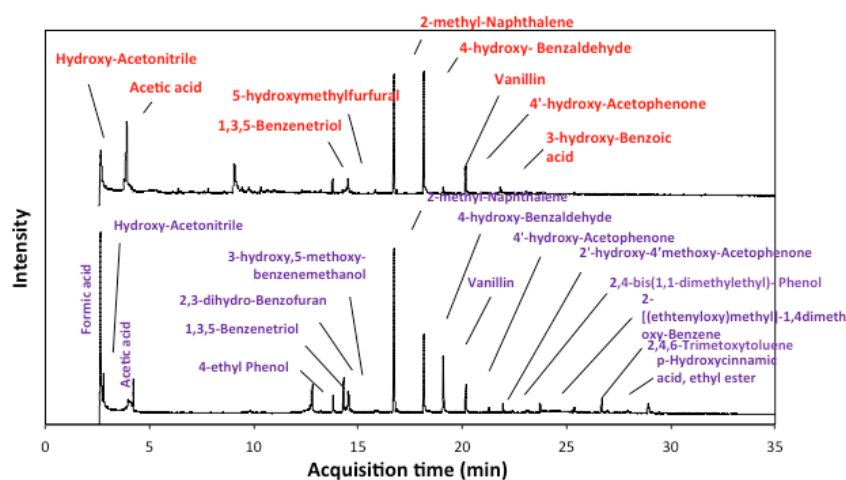


Fig. 55. GC-MS spectra of hydrocarbon compounds derived from photocatalytic conversion of kraft lignin catalyzed by P25 TiO₂ under UV irradiation for 2 h and 5 h.

Table 16. Products Obtained from Photocatalytic Lignin Conversion of Pristine TiO₂ and TiO₂/Lignin Composite Photocatalysts (Identified by GC/MS)

Entry	Compounds identified	Structure	Entry	Compounds identified	Structure
1	Butanedinitrile		7	4-Hydroxy-3-methoxy acetophenone (Apocynin, Acetovanillone)	
2	Benzoic acid		8	3-Ethoxy-benzoic acid	
3	1,3-Bis(1,1-dimethyl ethyl) benzene		9	Butylated hydroxytoluene (BHT)	
4	4-Hydroxybenzaldehyde		10	3-Hydroxy-4-methoxy benzoic acid (Isovanillic acid)	
5	3-Ethoxy-4-methoxy phenol		11	4-Hydroxy-3-methoxy propiophenone (Propiovanillone)	
6	4-Hydroxy-3-methoxy benzaldehyde (Vanillin)		12	4-Hydroxy-3-methoxy cinnamaldehyde (Coniferyl aldehyde)	

1.3.11 Combination of photocatalysis to conventional processes for enhancement of biomass pretreatment/hydrolysis

The pretreatment of biomass using photocatalytic process catalyzed P25 TiO₂ under UV irradiation for 24 h was preliminary carried out. The result showed that the amounts of individual sugar, as well as the total sugar yields, were low in the cases of no catalyst and no UV irradiation. TiO₂ photocatalysts could accelerate the separation of biomass compositions. Thus, a lot of products (native) were produced much compared with the photolysis (**Fig. 56**).

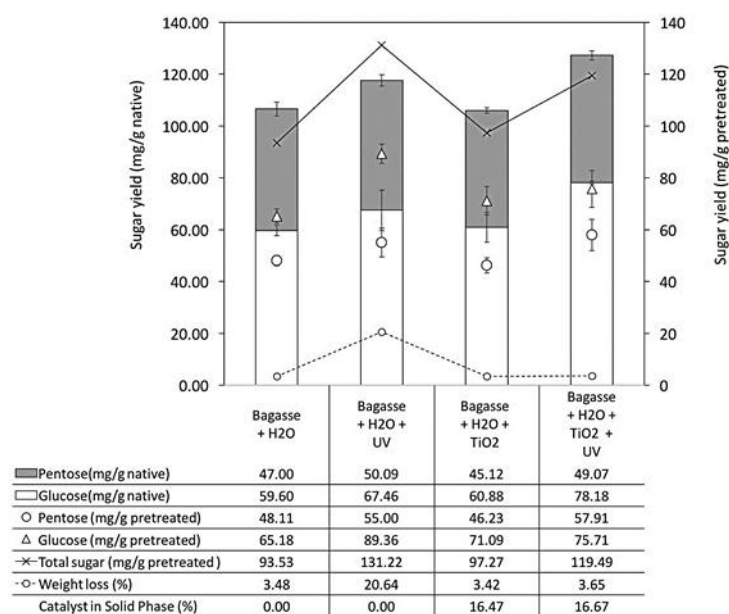


Fig. 56. Sugar digestibility yields in photocatalytic pretreatment (solvent = water) compared with blanks (no catalyst and/or no UV irradiation).

1.3.12 Further extension of the catalyst design: Preparation of molecularly imprinted TiO_2 hollow nanofibers

According to the procedures confirmed by Roongraung *et al.* in 2016, we prepared TiO_2 hollow nanofibers by electrospinning technique. SEM and TEM images of electrospun TiO_2 hollow nanofibers are indicated in **Fig. 57**.

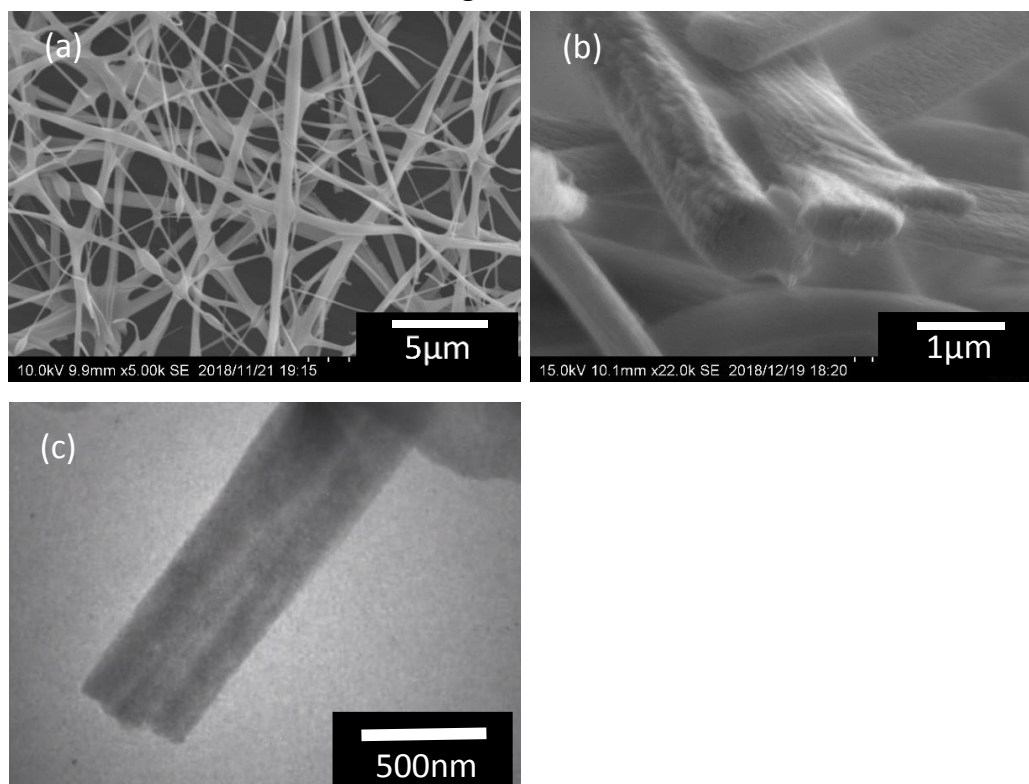


Fig. 57. SEM (a, b) and TEM (c) images of electrospun TiO_2 hollow nanofibers.

Photodegradation of methyl orange (MO) with TiO₂ hollow nanofibers under the irradiation of uv-vis light with 500 W Xe lamp was performed. Pseudo first order kinetic constant (*k*) for degradation of MO was estimated from the time course changes of the absorption peak at 508 nm. It was found that TiO₂ hollow nanofibers has the highest catalytic activity [*k* = (1.57±0.03)×10⁻² min⁻¹] as compared with those of TiO₂ single nanofibers [(1.20±0.03)×10⁻² min⁻¹] or TiO₂ (P25) nanoparticles [(8.60±0.70)×10⁻³ min⁻¹]. Furthermore, methyl red (MR)-based molecularly imprinted TiO₂ hollow nanofibers were also prepared as follows: Polymerizable target molecule for imprinting was initially prepared with chlorotitanium (IV) triisopropoxide and methyl red in methanol. Thereafter, polyvinylpyrrolidone, acetylacetone, and titanium (IV) butoxide were mixed with the above solution of the polymerizable target molecule to prepare the precursor solution for shell part of the spinning. While mineral oil was used for core part. Electrospinning was performed with coaxial needles under 15 kV biased conditions. Soaking in n-octane for 6h and washing with 1 % NH₃ aqueous solution for 3h followed by the desiccation at 60 °C for 1d and calcination with raising the temperature with 10 °C min⁻¹ ramping from room temperature to 600 °C and hold for 3h at 600 °C in air. Optical images of the obtained fiber mats after soaking in n-octane, washing with 1% NH₃, and calcination process were shown in **Fig. 58**.

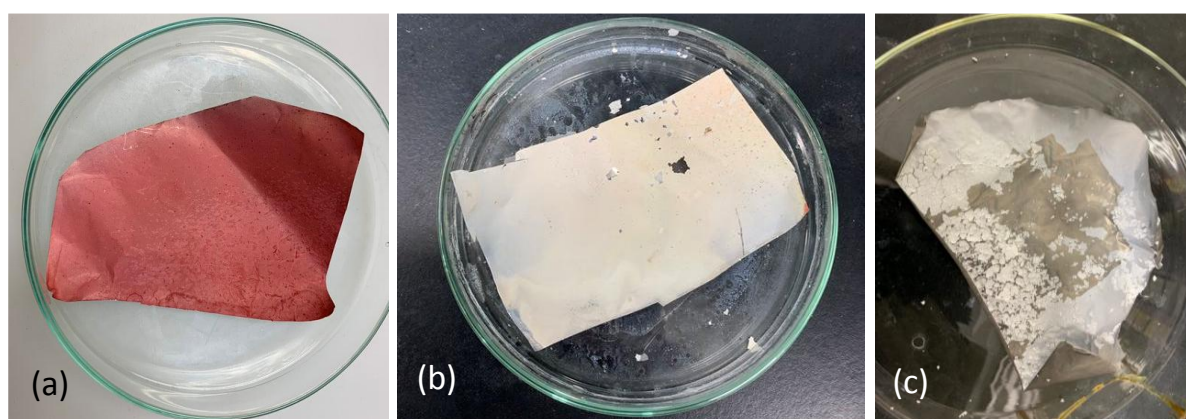


Fig. 58. Optical images of the obtained fiber mats after soaking in n-octane (a), washing with 1% NH₃ (b), and calcination (c).

Table 17. Specific surface area and porosity of TiO₂ nanoparticles (NPs), nanofibers (NFs), hollow nanofibers (HNFs), and MR-based molecularly imprinted hollow nanofibers (MIHNFs).

TiO ₂	Specific surface area (m ² g ⁻¹)	Averaged pore diameter (nm)
NPs	45.3	9.68
NFs	63.5	9.70
HNFs	133.4	9.71
MIHNFs	123.8	9.64

Characterization of the specific surface area and porosity of those materials are summarized in **Table 17**. Each of four samples of NPs, NFs, HNFs, and MIHNFs indicated predominant XRD patterns of anatase crystalline phase. The evaluations of the photocatalytic activity for degradation of MO or MR are summarized in **Table 18**.

Table 18. Pseudo first order rate constants (k) for photodegradations of MO or MR with TiO₂ NPs, NFs, HNFs, and MR-based MIHNFs.

TiO ₂	k (min ⁻¹) for MO photodegradation	k (min ⁻¹) for MR photodegradation
NPs	$(8.60 \pm 0.70) \times 10^{-3}$	$(1.82 \pm 0.07) \times 10^{-2}$
NFs	$(1.20 \pm 0.03) \times 10^{-2}$	$(2.60 \pm 0.04) \times 10^{-2}$
HNFs	$(1.57 \pm 0.03) \times 10^{-2}$	$(3.09 \pm 0.07) \times 10^{-2}$
MIHNFs	$(1.69 \pm 0.06) \times 10^{-2}$	$(3.93 \pm 0.09) \times 10^{-2}$

In spite of similar chemical structures of MO and MR, MR-based MIHNFs shows higher enhancement of photodegradation activity as compared with that of HNFs without molecular imprinting. Therefore, molecular imprinting is effective way for formation of selective recognition sites against the target template of MR on the HNFs TiO₂ catalyst.

1.4 Conclusions

Development of biomass conversion system in the combination with utilization of solar energy is an important issue to realize sustainable energy systems. That system is going to be constructed as “*photo-bio flow reactor*”. The collaborative work will provide strong platform technology for alternative environmentally friendly approach on conversion of biomass-derived intermediates to value-added chemicals in integrative biorefinery. According to the results, the photocatalytic reaction could convert glucose to a mixture of value-added chemical such as gluconic acid, arabinose, xylitol and formic acid under UV-light. The surface modification of TiO₂ by CTAB and zeolite could improve the photocatalytic activity of the photocatalyst. Furthermore, modification of the photocatalyst by non-metals and metals also enhanced the performance in terms of yield and selectivity. The fabrication technique was studied for improving the properties of photocatalyst. This led to the high conversion yield of 93.1% achieved by non-metal modified TiO₂ in the form of B,N-dopedTiO₂. The yields of products obtained (gluconic acid, arabinose, xylitol, and formic acid) were 9.0, 30.5, 8.9 and 47.6%, respectively. Compared with previous works, the yields of high value products, i.e. gluconic acid and xylitol, in this work (9.0 and 8.9%, respectively) were higher than our previous report (7.83 and 4.72%, respectively). The synergistic effects of metal/nonmetal doped TiO₂ were systematically investigated. It was observed that Ag,N-TiO₂ showed the best synergistic effects in photocatalysis compared with the single doped samples. The presence of Ag,N-TiO₂ gave the highest glucose conversion with 97.7%. The photocatalysts in the forms of modified-TiO₂ and quantum-dot composite especially graphitic carbon nitride showed potential on

glucose conversion under visible-light as an alternative energy source. However, with lower glucose conversion yield (77% at 12 h) compared to that achieved using the UV light. In addition, the modification of TiO₂/ZeY with metal loading were prepared by wetness impregnation assisted MW could lead to improved photocatalytic activity. The highest glucose conversion of 96.9 % were obtained from 1 wt.% Ag-TiO₂(30%)/ZeY. 1wt.% Ag- TiO₂(30%)/ZeY showed the smallest anatase crystallite size (11.81 nm), the highest S_{BET} (487.5 m²/g), and relatively small band gap (3.08 eV). The use of bimetallic 1 wt.% Ag-Cu-TiO₂/ZeY led to higher glucose conversion (94.71%) than 1 wt.% Cu doped TO₂/ZeY (82.23%). In addition, the bimetallic Ag-Cu- TiO₂/ZeY presented the highest of xylitol yield of 12.93% when compared with other samples. The photo bio-flow reactor has already been designed and assembled as a packed-bed reactor for immobilized photocatalyst which will be combined with the circulating system for controlling flow of reactant solution for further studies on kinetic of the reaction in order to improve the selectivities of the derived products.

1.5 Project Outputs

1.5.1 Publications Publications (The publications 1-6 did not acknowledge JST. Papers 7-12 had already been cited JST.)

1. Navaporn Kaerkittha, Surawut Chuangchote, and Takashi Sagawa (2016) "Control of physical properties of carbon nanofibers obtained from coaxial electrospinning of PMMA and PAN with adjustable inner/outer nozzle-ends," *Nanoscale Research Letters*, 11(1), 1-9.
2. Witchaya Arpavate, Surawut Chuangchote, Navadol Laosiripojana, Jatuphorn Wootthikanokkhan, and Takashi Sagawa (2016) "ZnO Nanorod Arrays Fabricated by Hydrothermal Method Using Different Thicknesses of Seed Layers for Applications in Hybrid Photovoltaic Cells," *Sensors and Materials*, 28(5), 403-408.
3. Kamonchanok Roongraun, Navadol Laosiripojana, Surawut Chuangchote (2016) "Development of Photocatalytic Conversion of Glucose to Value-added Chemicals by Supported-TiO₂ Photocatalysts," *Applied Mechanics and Materials*, 839, 39-43.
4. Mathana Wongaree, Siriluk Chiarakorn, Surawut Chuangchote, and Takashi Sagawa (2016) "Photocatalytic Performance of Electrospun CNT/TiO₂ Nanofibers in a Simulated Air Purifier under Visible Light Irradiation," *Environmental Science and Pollution Research*, 23, 21395-21406.
5. Navaporn Kaerkittha, Surawut Chuangchote, Kan Hachiya, and Takashi Sagawa (2017) "Influence of the Viscosity Ratio of Polyacrylonitrile/Poly(methyl methacrylate) Solutions on Core-Shell Fibers Prepared by Coaxial Electrospinning", *Polymer Journal*, 49, 497-502.
6. Jiraporn Payormhorm, Surawut Chuangchote, Kunlanan Kiatkittipong, Siriluk Chiarakorn, and Navadol Laosiripojana (2017) "Xylitol and Gluconic Acid Productions via Photocatalytic-Glucose Conversion Using TiO₂ Fabricated by Surfactant-Assisted Techniques: Effects of Structural and Textural Properties", *Materials Chemistry and Physics*, 196, 29-36.

7. Jiraporn Payormhorm, Surawut Chuangchote, and Navadol Laosiripojana (2017) "CTAB-Assisted Sol-microwave Method for Fast Synthesis of Mesoporous TiO₂ Photocatalysts for Photocatalytic Conversion of Glucose to Value-added Sugars", Materials Research Bulletin, 95, 546-555.
8. Nutsanun Klueb-arb, Surawut Chuangchote, Kamonchanok Roongraung, Navadol Laosiripojana, and Takashi Sagawa (2017) "Fabrication of Several Metal-Doped TiO₂ Nanoparticles and Their Physical Properties for Photocatalysis in Energy and Environmental Applications", Journal of Sustainable Energy & Environment, accepted.
9. Puangphen Hongdilokkul, Surawut Chuangchote, Navadol Laosiripojana, and Takashi Sagawa (2017) "Conversion of Lignin via Photocatalysis Using Synthesized Ag-TiO₂ Photocatalysts Sintered under Different Atmospheres", Journal of Sustainable Energy & Environment, accepted.
10. Nattida Srisasiwimon, Surawut Chuangchote, Navadol Laosiripojana, and Takashi Sagawa (2018) "TiO₂/lignin-based carbon composited photocatalysts for enhanced photocatalytic conversion of lignin to high value chemicals", ACS Sustainable Chemistry & Engineering, 6, 13968-13976.
11. Kamonchanok Roongraung, Surawut Chuangchote, Navadol Laosiripojana, and Takashi Sagawa (2020) "Electrospun Ag-TiO₂ Nanofibers for Photocatalytic Glucose Conversion to High-Value Chemicals", ACS Omega, 5, 11, 5862-5872.
12. Nopparat Suriyachai, Surawut Chuangchote, Navadol Laosiripojana, Verawat Champreda, and Takashi Sagawa "Synergistic Effects of Co-doping on Photocatalytic Activity of Titanium Dioxide on Glucose Conversion to Value-added Chemicals", ACS Omega, accepted.

1.5.2 Conference Proceeding

1. Navaporn Kaerkitcha, Surawut Chuangchote, Takashi Sagawa, Control of the physical properties of carbon nanofibers obtained from coaxial electrospinning of PAN and PMMA with adjustable inner/outer nozzle ends, EMN Hong Kong Meeting, Hong Kong, PRC, 2016/12/10.
2. Navaporn Kaerkitcha, Surawut Chuangchote, Takashi Sagawa, Control of the physical properties of carbon nanofibers obtained from coaxial electrospinning of PAN and PMMA with adjustable inner/outer nozzle ends, Ajou – Kyoto University Joint Symposium 2016, Swon, South Korea, 2016/1/28.
3. Navaporn Kaerkitcha, Surawut Chuangchote, Kan Hachiya, Takashi Sagawa, "Suitable outer/inner viscosity ratio of polymer solutions for fabrication of core-shell fibers by coaxial electrospinning," The 11th SPSJ International Polymer Conference (IPC2016), Fukuoka, 2016/12/16.

4. Kamonchanok Roongraun, Navadol Laosiripojana, and Surawut Chuangchote, 2015, "Development of Photocatalytic Conversion of Glucose to Value-added Chemicals by Supported-TiO₂ Photocatalysts," World Future Alternatives (Naresuan University, Phitsanulok, November 30-December 2), School of Renewable Energy Technology.
5. Jiraporn Payormhorm, Xiaobo Li, Thomas Maschmeyer, Navadol Laosiripojana, and Surawut Chuangchote, 2016 "The Study of Photocatalytic Oxidation of Benzyl Alcohol with g-C₃N₄ under Visible Light: Effect of pH and Salt," 2016 5th International Conference on Material Science and Engineering Technology (ICMSET 2016) (Tokyo, Japan, October 29-31), University of Tokyo.
6. Patcha Pattanapibul, Surawut Chuangchote, Navadol Laosiripojana, Verawat Champreda, Jerawut Kaewsane, 2017 "Enhancement of Enzymatic Hydrolysis and Lignin Removal of Bagasse Using Photocatalytic Pretreatment," The 3rd International Conference on Renewable Energy Technologies (ICRET2017) (Thammasat University, Bangkok, Thailand, January 22-24), ICRET Organization.
7. Surawut Chuangchote, 2017 "Electrospun TiO₂ Nanofibers Composed of Bundle of Aligned Nanofibrils: Fabrication, Structural and Photoluminescent Properties," 11th South East Asian Technical University Consortium (Ho Chi Minh City University of Technology (HCMUT), Vietnam, March 13-15), Ho Chi Minh City University of Technology.
8. Puangphen Hongdilokkul, Surawut Chuangchote, Navadol Laosiripojana, Takashi Sagawa, 2017 "Effects of Sintering Conditions in Ag-TiO₂ Nanoparticles on Photocatalytic Degradation of Lignin," International Conference on Materials Processing Technology 2017 (MAPT 2017) (Ramada Plaza Bangkok Menam Riverside, Bangkok, November 30-December 1), King Mongkut's University of Technology Thonburi, NM_01.
9. Nutsanun Klueb-arb, Surawut Chuangchote, Navadol Laosiripojana, Takashi Sagawa 2017 "Modifications of TiO₂ Nanoparticle Catalysts by Dopes with Transition Metals (Ag and Cu) or Alkali Metal (Rb)," International Conference on Materials Processing Technology 2017 (MAPT 2017) (Ramada Plaza Bangkok Menam Riverside, Bangkok, November 30-December 1), King Mongkut's University of Technology Thonburi, NM_01.
10. Nattida Srisasiwimon, Surawut Chuangchote, Navadol Laosiripojana, Takashi Sagawa (2018) "Carbon/TiO₂ Composite Photocatalysts and Their Applications for Lignin Conversion under Visible Light Irradiation," 2018 International Conference on Engineering, Technology, and Applied Science-Summer Session (ICETA-Summer 2018) (Sapporo Convention Center, Sapporo, Hokkaido, Japan, August 17-19), Setsunan University, ISSN 2411-9318, pp. 125-132.
11. Oranoot Sittipunsakda, Surawut Chuangchote, Navadol Laosiripojana, Verawat Champreda, Takashi Sagawa (2018) "Sr-Modified TiO₂ Photocatalyst for Photocatalytic Hydrogen Production from Urine," 2018 International Conference on Engineering, Technology, and Applied Science-Summer Session (ICETA-Summer 2018) (Sapporo

Convention Center, Sapporo, Hokkaido, Japan, August 17-19), Setsunan University, ISSN 2411-9318, pp.118-123.

12. Kamonchanok Roongraung, Surawut Chuangchote, Navadol Laosiripojana, and Takashi Sagawa (2018) "TiO₂ Hollow Nanofibers Fabricated by Coaxial Electrospinning for Photocatalytic Glucose Conversion to High Value Chemicals," 2018 International Conference on Engineering, Technology, and Applied Science-Summer Session (ICETA-Summer 2018) (Sapporo Convention Center, Sapporo, Hokkaido, Japan, August 17-19), Setsunan University, ISSN 2411-9318, pp. 104-109.
13. Kamonchanok Roongraung, Surawut Chuangchote, and Navadol Laosiripojana (2018) "Development of Green Synthesis of Value-added Chemicals using Photocatalytic Conversion of Glucose with TiO₂/Supporter," The International Conference on Advanced and Applied Petroleum, Petrochemicals, and Polymers 2018 (ICAPPP 2018) (Chulalongkorn University, Bangkok, Thailand, December 18-20), The Petroleum and Petrochemical College, pp. 58 (#O-ACC-4).

1.5.3 Award

1. The Best Presentation Award in The 3rd International Conference on Renewable Energy Technologies (ICRET2017) (Ms. Patcha Pattanapibul).

1.5.4 Exchange Researches

Table 1. Exchange researches in JASTIP

Name	Exchange Period	Research Topic
Ms. Kamonchanok Roongraung	18 Feb 2016 - 19 July 2016	Nano-scaled Photocatalysts for Energy Applications
Mr. Suriyachai Nopparat	28 Sep 2016 - 31 May 2017	Modification of Visible Light Photocatalytic Activity for Biomass Conversion to Value-added Chemicals
Ms. Nutsanun Klueb-arb	14 Nov 2016 - 23 Dec 2016	A Study of Reaction Pathways in Photocatalytic Conversion of Sugars to High-Value Fuels and Chemicals
Ms. Puangphen Hongdilokkul	14 Nov 2016 - 23 Dec 2016	Photocatalytic Upgrading of Lignin to High Value Products by Nanostructured Catalysts
Ms. Kanyanee Sanglee	6 Feb 2017 - 17 Mar 2017	Development of Visible-Light Irradiation Responded Metal Oxide for Photocatalytic and Photovoltaic Applications
Ms. Nattida Srisasiwimon	29 May 2017 - 29 June 2017	Modification of Photocatalysts for Lignin Conversion
Ms. Oranoot Sittipunsakda	29 May 2017 - 29 June 2017	Development of Metal-doped Photocatalysts for Hydrogen Evolution

Ms. Nattakarn Sakarapunthip	09 Oct 2018 - 27 Oct 2018	Perovskite Materials for Photovoltaic Applications
Ms. Tunnapat Worarutariyachai	09 Oct 2018 - 27 Oct 2018	Fabrication of Carbon Fibers from Bio-resource Materials
Mr. Surachet Soontontaweesub	18 Nov 2018 - 22 Dec 2018	Preparation of B,N-containing TiO ₂ Hollow Nanoribbons

1.6 References

- Awungacha, L. C., Hild, J., Czermak, P., and Herrenbauer, M. (2014). Photocatalytic active coatings for lignin degradation in a continuous packed bed reactor, **International Journal of Photoenergy**, 2014.
- Bahadur, N., Jain, K., Pasricha, R., and Chand, S. (2011), Selective gas sensing response from different loading of Ag in sol-gel mesoporous titania powders, **Sensors and Actuators B: Chemical**, 159, 1, 112-120.
- Chaudhary, V., Srivastava, A.K., and Kumar, J. (2011), On the Sol-gel Synthesis and Characterization of Titanium Oxide Nanoparticles, **Materials Research Society**, 1352.
- Cheng, G., Akhtar, M.S., Yang, O.B., and Stadler, F.J. (2013), Structure modification of anatase TiO₂ nanomaterials-based photoanodes for efficient dye-sensitized solar cells, **Electrochimica acta**, 113, 527-535.
- Christoforidis, K. C., & Fernández-García, M., (2016). Photoactivity and charge trapping sites in copper and vanadium doped anatase TiO₂ nano-materials. **Catal. Sci. Technol.**, 6(4), 1094-1105.
- Colmenares J.C., Magdziarz A., and Bielejewska A. (2011), High-value chemicals obtained from selective photo-oxidation of glucose in the presence of nanostructured titanium photocatalysts, **Bioresource Technology**, 102, 11254-11257.
- Colmenares, J. C., & Magdziarz, A. (2013). Room temperature versatile conversion of biomass-derived compounds by means of supported TiO₂ photocatalysts. **Journal of Molecular Catalysis A: Chemical**, 366, 156-162.
- Conradi, M., Kocijan, A., Kosec, T., & Podgornik, B. 2020. Manipulation of TiO₂ Nanoparticle/Polymer Coatings Wettability and Friction in Different Environments. **Materials**. 13 (7), pp. 1702.
- Fan, H. X., Li, H. P., Liu, Z. H., Yang, F., and Li, G. (2015). Production of fine chemicals by integrated photocatalytical degradation of alkali lignin solution in corrugated plate reactor and cyclic extraction technology, **Industrial Crops and Products**, 74, 497-504.
- Fu, D., Gong, Y., Wu, Y., Liu, J., Zhang, Z., Li, C., and Niu, L., (2016). Photocatalytic enhancement of TiO₂ by B and Zr co-doping and modulation of microstructure. **Applied Surface Science**. 379, 83-90.
- Francisco, M.S.P., Mastelaro, V.R., (2002). Inhibition of the Anatase-Rutile Phase Transformation with Addition of CeO₂ to CuO-TiO₂ System: Raman Spectroscopy, X-ray Diffraction, and Textural Studies, **Chem. Mater.**, 14, 2514-2518.

Gomathisankar, P., Yamamoto, D., Katsumata, H., Suzuki, T., and Kaneco, S. (2013), Photocatalytic hydrogen production with aid of simultaneous metal deposition using titanium dioxide from aqueous glucose solution, **International Journal of Hydrogen Energy**, 38, 5517-5524.

Gong, Y., Fu, C., Ting, L., Chenu, J., Zhao, Q., and Li, C., (2015) Exploring the effect of boron and tantalum codoping on the enhanced photocatalytic activity of TiO₂. **Applied Surface Science**, 351, 746–752.

Hlekelele, L., Franklyn, P.J., Dziike, F., & Durbach, S. H., (2018). Novel synthesis of Ag decorated TiO₂ anchored on zeolites derived from coal fly ash for the photodegradation of bisphenol-A. **New Journal of Chemistry**, 42(3), 1902-1912.

Huang, D., Miyamoto, Y., Matsumoto, T., Tojo, T., Fan, T., Ding, J., & Zhang, D. 2011. Preparation and characterization of high-surface-area TiO₂/activated carbon by low-temperature impregnation. **Separation and Purification Technology**. 78 (1), pp. 9-15.

Hwang, K.J., Lee, J.W., Shim, W.G., Jang, H.D., Lee, S.I., and Yoo, S.J. (2012), Adsorption and photocatalysis of nanocrystalline TiO₂ particles prepared by sol-gel method for methylene blue degradation, **Advance Powder Technology**. 23, 414-418.

Jaafar, N. F., Jalil, A. A., Triwahyono, S., Efendi, J., Mukti, R. R., Jusoh, R., & Suendo, V., (2015). Direct in situ activation of AgO nanoparticles in synthesis of Ag/TiO₂ and its photoactivity. **Applied Surface Science**, 338, 75-84.

Jaimy, K. B., Vidya, K., Saraswathy, H. U. N., Hebalkar, N. Y., and Warriar, K. G. K. (2014), Dopant-free anatase titanium dioxide as visible-light catalyst: Facile sol-gel microwave approach, **Journal of Environmental Chemical Engineering**.

Kadam, A.; Dhabbe, R.; Shin, D. S.; Garadkar, K.; Park, J. (2017), Sunlight Driven High Photocatalytic Activity of Sn Doped N-TiO₂ nanoparticles Synthesized by a Microwave Assisted Method. **Ceram. Int.** 43, 5164–5172.

Kameyama, T., et al., (2015), Controlling the Electronic Energy Structure of ZnS–AgInS₂ Solid Solution Nanocrystals for Photoluminescence and Photocatalytic Hydrogen Evolution. **J. Phys. Chem. C** 119, 24740–24749.

Liang, Y., Sun, S., Deng, T., Ding, H., Chen, W., & Chen, Y. 2018. The preparation of TiO₂ film by the sol-gel method and evaluation of its self-cleaning property. **Materials**. 11 (3), pp. 450.

Li, H., Lei, Z., Liu, C., Zhang, Z., and Lu, B. (2015). Photocatalytic degradation of lignin on synthesized Ag-AgCl/ZnO nanorods under solar light and preliminary trials for methane fermentation, **Bioresource Technology**. 175, 494-501.

Liu, J., Han, R., Zhao, Y., Wang, H., Lu, W., Yu, T., and Zhang, Y., (2011), Enhanced Photoactivity of V-N Codoped TiO₂ Derived from a Two-Step Hydrothermal Procedure for the Degradation of PCP-Na under Visible Light Irradiation. **J. Phys. Chem. C**. 115, 4507-4515.

Lv, Y., Liu, Y., Zhu, Y., & Zhu, Y., (2014) Surface oxygen vacancy induced photocatalytic performance enhancement of a BiPO₄ nanorod. **J. Mater. Chem. A**, 2(4), 1174-1182.

Mauer, G., Guignard, A., & Vaßen, R. 2013. Plasma spraying of efficient photoactive TiO₂ coatings. **Surface and Coatings Technology**. 220, pp. 40-43.

Mozia S., Heciak A., and Morawski A.W. (2011), Photocatalytic acetic acid decomposition leading to the production of hydrocarbons and hydrogen on Fe-modified TiO₂, **Catalysis Today**, 161, 189-195.

Murugan, K., Subasri, R., Rao, T.N., Gandhi, A.S., and Murty, B.S. (2013), Synthesis, characterization and demonstration of self-cleaning TiO₂ coatings on glass and glazed ceramic tiles, **Progress in Organic Coatings**, 76, 1756-1760.

Mutuma, B. K., Shao, G. N., Kim, W. D., and Kim, H. T. (2015), Sol-gel synthesis of mesoporous anatase-brookite and anatase-brookite-rutile TiO₂ nanoparticles and their photocatalytic properties, **Journal of colloid and interface science**, 442, 1-7.

Nasralla, N., Yeganeh, M., Astuti, Y., Piticharoenphuna, S., Shahtahmasebi, N., Kompany, A., Karimipour, M., Mendis, B.G., Poolton, N.R.J., Siller, L., (2013), "Structural and spectroscopic study of Fe-doped TiO₂ nanoparticles prepared by sol-gel method", **Scientia Iranica**. 20, 1018-1022.

Oh, J. K., Lee, J. K., Kim, S. J., and Park, K. W. (2009), Synthesis of phase- and shape-controlled TiO₂ nanoparticles via hydrothermal process, **Journal of Industrial and Engineering Chemistry**, 15, 2, pp. 270-274.

Ong, W.J., Tan, L.L., Ng, Y.H., Yong, S.T., and Chai, S.P., (2016), Graphitic carbon nitride (g-C₃N₄)-based photocatalysts for artificial photosynthesis and environmental remediation: Are we step closer to achieving sustainability?. **Chem. Rev.** 116, 7159-7329.

Payormporn, J., Chuangchote, S., Kiatkittipong, K., Chiarakorn, S., and Laosiripojana, N., (2017), Xylitol and gluconic acid productions via photocatalytic-glucose conversion using TiO₂ fabricated by surfactant-assisted techniques: Effects of structural and textural properties. **Materials Chemistry and Physics**. 196, 29-36.

Prado, R., Erdocia, X., and Labidi, J. (2013). Effect of the photocatalytic activity of TiO₂ on lignin depolymerization, **Chemosphere**, 91, 1355-1361.

Park, J.Y., Yun, J.J., Hwang, C.H., and Lee, I.H. (2010), Influence of silver doping on the phase transformation and crystallite growth of electrospun TiO₂ nanofibers, **Materials Letters**. 64, 2692-2695.

Pelaez, M., et al., (2012), A review on the visible light active titanium dioxide photocatalysts for environmental applications. **Applied Catalysis B: Environmental**. 125, 331-349.

Quesada-González, M., Boscher, N. D., Carmalt, C. J., & Parkin, I. P. 2016. Interstitial boron-doped TiO₂ thin films: the significant effect of boron on TiO₂ coatings grown by atmospheric pressure chemical vapor deposition. **ACS applied materials & interfaces**. 8 (38), 25024-25029.

Rengaraj, S., and Li, X.Z. (2006), Enhanced photocatalytic activity of TiO₂ by doping with Ag for degradation of 2,4,6-trichlorophenol in aqueous suspension, **Journal of Molecule Catalysis. A: Chemica**, 243, 60-67.

Ranjitha, A., Muthukumarasamy, N., Thambidurai, M., Balasundaraprabhu, R., & Agilan, S. 2013. Effect of annealing temperature on nanocrystalline TiO₂ thin films prepared by sol-gel dip coating method. **Optik**. 124 (23), 6201-6204.

Shamaila, S., Sajjad, A.K.L., Chen, F., Zhang, J., (2010), Study on highly visible light active Bi₂O₃ loaded ordered mesoporous titania. **Appl. Catal. B: Environ**. 94, 272-280.

Shen, X., Zhang, J., and Tian, B. (2011), Microemulsion-mediated solvothermal synthesis and photocatalytic properties of crystalline titania with controllable phases of anatase and rutile, **Journal of hazardous materials**, 192, 651-657.

Shi, J., & Wang, X. (2011). Growth of rutile titanium dioxide nanowires by pulsed chemical vapor deposition. **Crystal Growth & Design**, 11, 949-954.

Shojaie, A.F., and Loghmani, M.H. (2010), La³⁺ and Zr⁴⁺ co-doped anatase nano TiO₂ by sol-microwave, **Chemical Engineering Journal**, 157, 263-269.

Song, S., Yang, T., Li, Y., Pang, Z., Lin, L., Lv, M., and Han, S. (2009), Structural, electrical and optical properties of ITO films with a thin TiO₂ seed layer prepared by RF magnetron sputtering, **Vacuum**, 83, 1091-1094.

Srisasiwimon, N., Chuangchote, S., Laosiripojana, N., Sagawa, T., (2018), TiO₂/Lignin-Based Carbon composited photocatalysts for enhanced photocatalytic conversion of lignin to high value chemicals. **ACS Sustainable Chem. Eng**. 6, 13968-13976.

Su, C., Hong, B.Y., and Tseng, C.M. (2004), Sol-gel preparation and photocatalysis of titanium dioxide, **Catalysis today**, 96, 119-126.

Sun A., Li Z., Li M., Xu G., Li Y., and Cui P. (2010), Room temperature synthesis of spherical mesoporous titania, **Powder Technology**, 201, 130-137.

Suwarnkar, M. B., Dhabbe, R. S., Kadam, A. N., & Garadkar, K. M. (2014). Enhanced photocatalytic activity of Ag doped TiO₂ nanoparticles synthesized by a microwave assisted method. **Ceramics International**, 40, 5489-5496.

Tahir, A.A., Peiris, T.A., and Wijayantha, K.G. (2012), Enhancement of Photoelectrochemical Performance of AACVD-produced TiO₂ Electrodes by Microwave Irradiation while Preserving the Nanostructure, **Chemical Vapor Deposition**, 18, 107-111.

Tanaka, Y., Sakai, H., Tsuke, T., Uesugi, Y., Sakai, Y., and Nakamura, K. (2011), Influence of coil current modulation on TiO₂ nanoparticle synthesis using pulse-modulated induction thermal plasmas, **Thin Solid Films**, 519, 7100-7105.

Tobaldi, D. M., Škapin, A. S., Pullar, R. C., Seabra, M. P., & Labrincha, J. A. (2013). Titanium dioxide modified with transition metals and rare earth elements: phase composition, optical properties, and photocatalytic activity. **Ceramics International**. 39, 2619-2629.

Torimoto, T., Adachi, T., Okazaki, K., Sakuraoaka, M., Shibayama, T., Ohtani, B., Kudo, A., and Kuwabata, S., (2007), Facile Synthesis of ZnS-AgInS₂ Solid Solution Nanoparticles for a Color-Adjustable Luminophore. **J. AM. CHEM. SOC.** 129, 12388-12389.

Vijayalakshmi, R., and Rajendran, V. (2012), Synthesis and characterization of nano-TiO₂ via different methods, **Arch App Sci Res**, 4, 2, 1183-1190.

Xu, G., Zeng, S., Zhang, B., Swihart, M.T., Yong, K.T., and Prasad, P.N., (2016), New Generation Cadmium-Free Quantum Dots for Biophotonics and Nanomedicine. **Chem Rev.** 116, 12234-12327.

Zhang, Y., Zheng, H., Liu, G., and Battaglia, V. (2009), Synthesis and electrochemical studies of a layered spheric TiO₂ through low temperature solvothermal method, **Electrochimica Acta**, 54, 16, 4079-4083.

Zhao, Y., Li, C., Liu, X., Gu, F., Jiang, H., Shao, W., and He, Y. (2007), Synthesis and optical properties of TiO₂ nanoparticles, **Materials Letters**, 61, 1, 79-83.

Nanocarbon Materials for Sustainable Production and Storage of Green Fuels and Platform Chemicals

Nanocarbon Materials for Sustainable Production and Storage of Green Fuels and Platform Chemicals

1. Research team

Prof.Dr. Noriaki Sano, Kyoto University (PI, Japan side)
Dr. Kajornsak Faungnawakij, NANOTEC, NSTDA (PI, Thailand side)
Dr. Sanchai Kuboon, NANOTEC, NSTDA
Dr. Pongkarn Chakthranont, NANOTEC, NSTDA
Miss. Sutarat Thongratkaew, NANOTEC, NSTDA
Dr. Supawadee Namuangruk, NANOTEC, NSTDA
Dr. Chompoonut Rungnim, ThaiSC, NSTDA
Dr. Pussana Hirunsit, NANOTEC, NSTDA
Dr. Manaschai Kunaseth, ThaiSC, NSTDA
Assoc. Prof. Tawatchai Charinpanitkul, Chulalongkorn University
Dr. Chompoopitch Termvidchakorn, Chulalongkorn University
Dr. Sareeya Bureekaew, VISTEC
Asst. Prof. Thongthai Witoon, Kasetsart University

2. Purpose of Collaborative Research

The effects of climate change caused by the anthropogenic CO₂ emission has increased the average global temperature by 1 °C above the pre-industrial level. If this current trend is continued, the average global temperature is expected to inevitably elevate by 4-5 °C by 2100. To slow down this global crisis, the greenhouse gas emission must be drastically reduced towards zero emission within this century. These need has led to the blossom of green technological concepts including biorefinery and bio-energy devices where renewable resources replace the need for fossil fuel in the future. The catalytic productions of carbon-based materials, biofuels, and biochemicals are at the heart of biorefinery industry. The collaborative researches carried out by the groups in NANOTEC/NSTDA (Faungnawakij's team) and Kyoto University (Sano's team) aim to develop new and innovative knowledge on biomass conversion to useful materials and development of bio-energy devices.

In this year, 3 major research activities have been done as follows.

- ☐ Influence of hydrogen spillover on Pt- decorated carbon nanocones for enhancing hydrogen storage capacity: A DFT mechanistic study
- ☐ DFT study of catalytic CO₂ hydrogenation over Pt- decorated carbon nanocones: H₂ dissociation combined with the spillover mechanism
- ☐ Doped- Carbon Nanohorns catalysts for efficient electrosynthesis of H₂O₂ from O₂ reduction

3. Research Outcome

3.1 Influence of hydrogen spillover on Pt-decorated carbon nanocones for enhancing hydrogen storage capacity: A DFT mechanistic study

Nuttapon Yodsin,¹ Chompoonut Runnim,^{2,*} Vinich Promarak,³ Supawadee Namuangruk,² Nawee Kungwan,^{4,5} Rattanawalee Rattanawan¹ and Siriporn Jungsuttiwong^{1,*}

¹Center for Organic Electronic and Alternative Energy, Department of Chemistry and Center for Innovation in Chemistry, Faculty of Science, Ubon Ratchathani University, Ubon Ratchathani 34190, Thailand

² National Nanotechnology Center, National Science and Technology Development Agency, Pathum Thani 12120, Thailand

³School of Molecular Science and Engineering, Vidyasirimedhi Institute of Science and Technology, Wangchan, Rayong 21210, Thailand

⁴Departments of Chemistry, Faculty of Science, Chiang Mai University, Chiang Mai 50200, Thailand

⁵Center of Excellence in Materials Science and Technology, Chiang Mai University, Thailand

Reproduced from N. Yodsin, C. Runnim, V. Promarak, S. Namuangruk, N. Kungwan, R. Rattanawan and S. Jungsuttiwong, *Phys. Chem. Chem. Phys.*, 2018, 20, 21194 with permission from the PCCP Owner Societies.

Abstract

We used density functional theory (DFT) to investigate hydrogen adsorption and diffusion on platinum-decorated Carbon nanocone (Pt-CNC). The curvature presented in the conical section of CNC materials effect Pt binding stability. The role of Pt atom as an active catalyst for H₂ adsorption and dissociation has been investigated in perfect Pt-4CNC and defect Pt-v4CNC systems. Then, the spillover mechanism of dissociated hydrogen atom in Pt-v4CNC is explored via two reaction steps i) H-migration from Pt to carbon atoms and ii) H-diffusion over C-C route thought out the CNC surface. Our results show that the presence of hydrogen atom on Pt catalyst can efficiently induced H-diffusion process through C-C surface, the Pt-H significantly facilitates the H-migration from C-H bonds near by the active Pt catalyst to its adjacent carbon atom with energy barrier < 0.5 eV under ambient conditions. Altogether, the theoretical results support the concept of spillover mechanism as a key role for enhancing hydrogen storage capacity of metal-decorated CNC. These results improve our understanding about hydrogen spillover mechanism and the catalytic reactions which are very important for the development of high efficient hydrogen storage material.

Keywords: spillover mechanism, H-migration, hydrogen storage material, carbon nanocone, DFT

1. Introduction

Energy demand increases with population size. Most of the energy we use comes from nonrenewable sources, such as coal, oil shale, oil sand, crude oil, gasoline, and natural gas. Use of these resources raises environmental issues, such as toxic gas and waste emissions, and aquatic pollution. Associated issues include: greenhouse gas emissions, acid rain, climate change, and our dependency on depleting supplies of fossil fuels. Alternative renewable energy sources such as wind, water, sunlight, geothermal and biomass have received attention in recent decades. In the future, hydrogen could join electricity as an important energy source for the fuel cell.¹ Hydrogen energy offers an alternative technology to petrochemicals, such as gasoline. Utilization of hydrogen as an energy storage technology to serve as fuel requires innovation in many areas such as delivery, production, conversion, storage, and end-use. Hydrogen can be generated by chemical reaction and stored in liquid and gas forms, such as compressed fuel storage,² liquid hydrogen storage, and solid-state conformable storage.³ Compressed fuel cylinders use high-pressure, heavy equipment and offer low efficiencies for hydrogen storage.

Carbon-based nanomaterial is one of promising materials for hydrogen storage systems.⁴⁻
³¹ Carbon nanohorn (CNH) is a carbon-based materials synthesized by using arc-discharge methods without the need for a catalyst.³² CNH have two main key advantages over carbon nanotubes: (i) the absence of toxic metal catalyst in synthesis procedure, and (ii) the mass production can occur at room temperature.³³ The structure, synthesis, and topology of CNH as well as its chemistry and applications are reviewed by N. Karousis et al.³³ CNH is a novel form of carbon which can provide a suitable support for various metals to form new carbon-metal nano-composite materials. Such composites have many potential applications, including supercapacitors³⁴, drug delivery³⁵⁻³⁶, lithium ion batteries,³⁷ biofuel cells³⁸, energy storage^{7, 8, 12, 17-19}, and solar cells³⁹. In terms of structural geometry, CNH is an aggregated in spherical form of carbon nanocones (CNCs). The CNC is describing as conical nanocarbon. The shape of CNC is defined by declination angle of $n(\pi/3)$ where n is the number of pentagon at the cone tip,³³ as shown in Figure 1. We note that each cone tip of CNH typically has declination angle 19° or five pentagon rings at the cone tips, as suggested from the TME image and theoretical study.^{33, 40, 41}

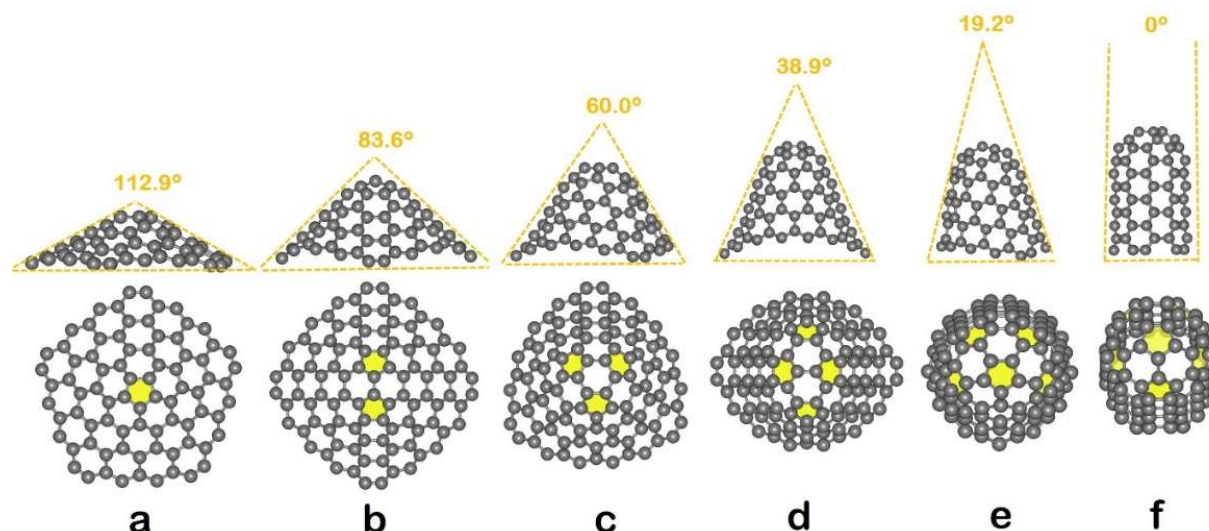


Figure 1. Representation of CNC with (a) single, (b) two, (c) three, (d) four, (e) five, and (f) six pentagon at cone tips, respectively.

The physical properties of CNCs as novel substrates for hydrogen storage applications have attracted a great deal of interest in recent years.^{8, 12, 17-19, 42-44} For example, Gotzias et al.⁸ investigated hydrogen adsorption on CNCs with five different cone angles by applying the grand canonical Monte Carlo method. Wang et al.⁴⁵ performed hydrogen storage capacity of AlN nanostructures, including AlN-CNC, by using gradient-corrected density functional theory (DFT) and suggested that AlN nanostructure are proper for hydrogen storage under ambient conditions. In 2012, Ming-Liang Liao⁴⁶ explored the confinement of CNC toward hydrogen physisorption behaviors on open- tip CNCs by using molecular dynamics simulations. The hydrogen chemisorption on CNC can be promoted by using hydrogen dissociation catalysts, such as transition metals. For example, A. S. Shalabi et al.¹⁸ studied hydrogen storage reactions on Ti decorated CNC, the results showed that Ti atoms preferentially bind with CNC at bridging sites between two hexagonal rings and the system can bind up to 6 hydrogen molecules, with adsorption energies of -1.73, -0.74, -0.57, -0.45, -0.42, and -0.35 eV per hydrogen molecule. In addition, Valencia et al.²² reported hydrogen activation by 3d transition metal functionalized graphene and (8,0) single-walled carbon nanotubes (SWCNT) by using DFT calculations. They found that two expected coordination modes of H₂ were identified; dissociated dihydride (D) and molecular Kubas coordination (K).

Enhanced hydrogen storage capacity on an adsorbent support arises by a process of hydrogen dissociation, followed by spillover. Hydrogen spillover has occurred as one of the most promising techniques for the accomplishment of high hydrogen capacity under lightweight materials at ambient conditions. Spillover can be defined as ‘the transport of active species that have sorbed or formed on a first surface, migrated onto another surface that does not sorb or form active species under the same conditions’⁴⁷. The spillover mechanism is crucial in adsorption process and as a mechanistic step in heterogeneous catalysis⁴⁸⁻⁵¹. It has been proposed that hydrogen spillover mechanism accounts for enhanced hydrogen storage capacity⁵²⁻⁵⁴. The hydrogen spillover mechanism comprises several steps. Initially, a hydrogen molecule

coordinates on a transition metal catalyst, such as Pt, in close contact with a carbon-based nanomaterial. The hydrogen molecule dissociates to form two ligated hydrogen atoms, which then migrate from the metal onto the substrate. The evidence of catalytic dissociation of hydrogen molecules by metal nanoparticles and spillover of atomic hydrogen onto CNC was observed by using inelastic neutron scattering measurements in an experimental study from Liu et al.¹². Additionally, Sano et al.¹⁷ synthesized single-walled carbon nanohorns containing Pd–Ni alloy nanoparticles (Pd–Ni/SWCNHs) for hydrogen storage applications by using a gas-injected arc-in-water method. They found that Pd–Ni alloy nanoparticles on CNHs can catalyze H₂ dissociation and remarkable absorption occurs via the spillover effect. Even many experimental studies propose that the spillover effect is the key mechanism for H₂ storage, the detail of the mechanism is still under discussion, especially for CNHs and CNCs.

Therefore, the aim of this work is to investigate hydrogen spillover mechanism on Pt-decorated CNCs. We utilize DFT calculations to explore dissociative adsorption, migration and diffusion of 1 to 3 adsorbed H₂ molecules. The details of spillover mechanism are provided via the hydrogen migration from metal to carbon support and hydrogen diffusion over C–C route. We anticipate that these observations improve our understanding about hydrogen spillover mechanism and catalytic reactions which are very important for the development of high efficient hydrogen storage material.

2. Computational details

All calculation at ground state were performed in Gaussian09 software suite. Firstly, all structures were optimized using Becke's three parameter gradient-corrected exchange potential combined with the Lee-Yang-Parr gradient-corrected correlation potential (B3LYP)^{55–57} with the 6-31G(d,p) basis set for C and H atoms and LANL2DZ basis set for Pt atom. Then, energies of all structures were corrected by single point calculation using B3LYP functional including Grimme's D3 dispersion correction (B3LYP-D3)⁵⁸ with 6-311G(d,p) basis set for C and H atoms and cc-pVTZ-PP basis set for Pt atom. The details of method validation are provided in supplementary data.

Suggesting from the CNC construction of N. Karousis et al.³³, we created six CNCs with different numbers of pentagons named as xCNC where x is number of pentagon rings (x = 1 to 6). All models were hydrogen-free CNC edges which successfully applied in the studies related to H₂ adsorption on CNC based material^{18, 44}. The xCNC's tips sharpen when increase numbers of pentagons, as shown in Figure 1. After fully optimizations, we measured cone declination angles (see Table S1) and obtain values in the same range with Karousis et al.³³ who calculate the declination angle by $n(\pi/3)$ with $0 \leq n \leq 5$, where n is the number of pentagons. After that, the stability of Pt on xCNC has been investigated. The Pt binding energy (E_{bind}) is calculated following the equation (1).

$$E_{\text{bind}} = E_{\text{Pt-xCNC}} - E_{\text{Pt}} - E_{\text{xCNC}} \quad (1)$$

where $E_{\text{Pt-xCNC}}$ is a total energy of xCNC with a Pt atom, E_{Pt} and E_{xCNC} represents the total energy of free single Pt atom and an isolated xCNC, respectively. The E_{bind} of Pt on defective-CNC (Pt-

vxCNC) is calculated in the same manner. Then, the H₂ adsorption is explored. The H₂ adsorption energy (E_{ads}) is calculated by

$$E_{\text{ads}} = E_{n\text{H}_2/\text{substrate}} - nE_{\text{H}_2} - E_{\text{substrate}} \quad (2)$$

where $E_{\text{H}_2/\text{surface}}$ is the total energy of hydrogen molecule adsorbed on Pt-xCNC or Pt-vxCNC substrate, $E_{\text{substrate}}$ represents the total energy of Pt-xCNC or Pt-vxCNC, E_{H_2} is total energy of hydrogen molecule and n is the number of H₂ adsorbed on the substrate. The average H₂ adsorption energy or E_{ads} per H₂ molecule is calculated by divide the E_{ads} with number of adsorbed H₂ molecules.

The H-spillover mechanism is divided in three steps; *i*) dissociative adsorption of H on Pt atom, *ii*) H-migration from Pt to an adjacent C atom and *iii*) H-diffusion from C to C atoms. Here, all steps of spillover mechanism are explored step by step and all transition states during reaction pathway are verified by vibrational frequency analysis. All atomic charges are obtained from Mulliken population analysis.

3. Results and discussion

3.1 Stability of Pt on carbon nanocone

We investigated all possible adsorption sites for Pt binding on top of CNC with difference cone shape, Pt-xCNC structures ($x = 1$ to 6). The sites of interest are consisted of bridge positions (B: above a C-C bond), hollow positions (Hh: above a hexagon and Hp: a pentagon) and top positions (T: above a C atom), as illustrated in Figure S1 of the supplementary data. From geometry optimization at B3LYP/6-31G(d,p), LANL2DZ, we found that the most stable Pt binding site on each xCNC is located at the B site, as shown in Figure S2. From the optimized geometries, we recalculate the Pt binding energies from the most stable structure of each CNC model using single point calculation at B3LYP-D3/6-311G(d,p), cc-pVTZ-PP level of theory as presented in Figure 2. The Pt binding energies of all six xCNC models (-3.33 to -2.67 eV) are noticeable stronger than those of graphene (-1.86 eV). Among all Pt-xCNC structures, Pt-4CNC has the strongest Pt binding energy (-2.83 eV) which corresponds to its curvature effect suggested from high pyramidalization angle (ϑ_P) of the carbon atoms. See more detail about the π -orbital axis vector (POAV) analysis for ϑ_P calculation in the supplementary data.

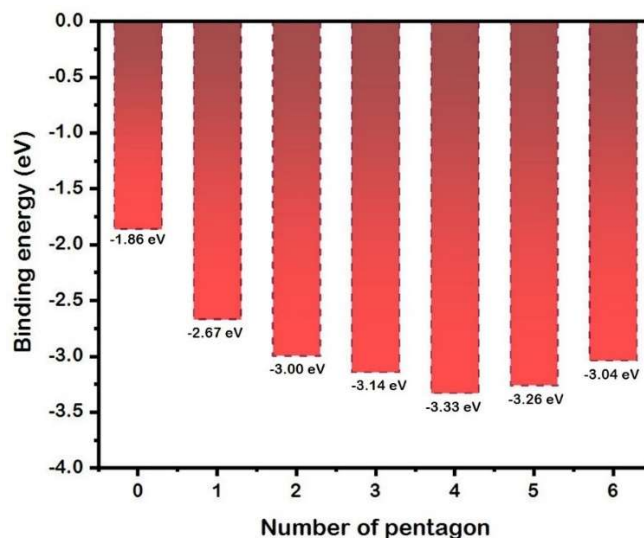


Figure 2. Pt binding energy diagram of Pt-xCNC structures (x = number of pentagon on the CNC tip).

The structural properties of the most stable Pt-xCNC complexes are shown in Table S3 of the supplementary data. The Pt atomic charges are in the range of $0.10e$ to $0.22e$ while those of the nearest neighbor C atom detected around $-0.31e$ to $-0.21e$. The results suggest that Pt transfers electrons to its conjugated carbon atoms. The similar phenomena was detected in Ti-CNC system from shalabi et al.,¹⁸ who explain the overlap between Ti d -orbital with sp^2 orbitals of the C-C bonds to create mixed sp^2d hybridization. These charge transfer can induce Lewis acid characteristics of Pt leading to an active site for hydrogen adsorption.

Since the Pt-4CNC shows the strongest Pt binding energy, we generated the monovacancy on 4CNC called as Pt-v4CNC and calculated the Pt binding energy at this vacancy site. We found that the Pt binding energy in Pt-v4CNC is -7.35 eV that is much stronger than the binding in Pt-4CNC (-3.33 eV). The Pt atom in Pt-v4CNC firmly settles down at the vacancy site with Pt-C bond length around 1.9 Å, as depicted in Figure 3b. The Pt binding energy at the vacancy site is greater than the Pt cohesive energy (-5.84 eV/atom)⁵⁹. Thus, Pt binding at this vacancy site tends to prevent the metallic aggregation or formation of large metal cluster.

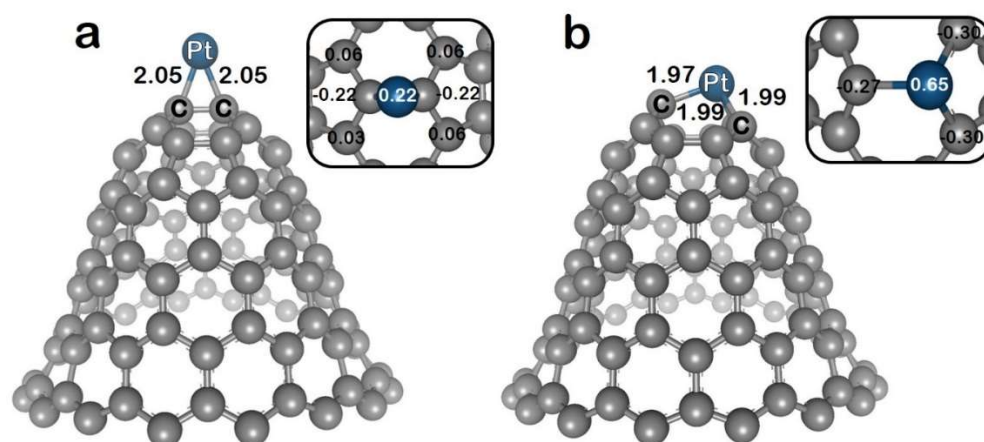


Figure 3. Geometrically optimized structures of (a) Pt-4CNC, (b) Pt-v4CNC. Mulliken charges are showed in box. Bond distances are in Å

3.2 H₂ Adsorption on Pt-4CNC and Pt-v4CNC

The H₂ adsorption on Pt-4CNC is explored since it is a model with the strongest Pt binding energy among the six Pt-xCNC. In comparison, the H₂ adsorption on Pt-v4CNC is also performed. In general, there are typically two modes of H₂ adsorption, i. e., D-mode (dissociated dihydride) and K-mode (Kubas mode) bonding. The D-mode is a η^1 bonding while the K-mode identified by Kubas⁶⁰ occurs via η^2 coordination from H₂ to a metallic center with the H-H bond length of 1.0-1.4 Å, or approximately 20% longer than its equilibrium distance of 0.74 Å.

In this work, we found that a preferable mode for H₂ molecule adsorption on Pt-4CNC is the K-mode rather than the D-mode. As shown in Table 1, the E_{ads} for H₂ adsorption in K-mode is -1.02 eV with H-H bond length of 0.87 Å, while those of D-mode is -0.94 eV with H-H bond length of 1.44 Å. This result agrees well with characteristic of H₂ adsorption of group 10 transition metal such as the Ni-doped graphene and carbon nanotube.²² In order to find maximum H₂ adsorption in K-mode, the adsorption capacity is investigated by increasing number of H₂ molecules, as shown in Figure 4. We found that the Pt-4CNC reaches its saturation after two adsorbed H₂ molecules because the third H₂ molecule cannot adsorb on Pt atom indicated from Pt-H distance of 3.16 Å. After the Pt-4CNC is saturated with two H₂ molecules, the E_{ads} is steady at -1.39 eV or -0.70 eV/H₂.

For Pt-v4CNC, the system reaches its maximum H₂ adsorption capacity after the first H₂ molecule in K-mode. The second and third H₂ molecules cannot adsorb on Pt atom and the E_{ads} is steady at -0.41 eV after the first H₂ adsorption. For the adsorption in D-mode, its E_{ads} (-0.36 eV) is weaker than that of the adsorption in K-mode (-0.41 eV). Therefore, the K-mode adsorption is preferable either for Pt-4CNC or Pt-v4CNC. On the top of that, the E_{ads} values of saturated Pt-4CNC and Pt-v4CNC is in energy window of 0.2–0.6 eV/H₂ that is suited energy for reversible hydrogen storage at near standard conditions.⁶¹

However, in this work we focus on the enhancement of the hydrogen adsorption by assuming spillover mechanism. In this mechanism, the hydrogen molecules are first adsorbed

and dissociated on the surface of the metallic nanoparticles, and are next transported onto the surface of CNC. Therefore, we are interested in the adsorption of H_2 dissociated mode (D-mode). Interestingly, after the H_2 adsorption (D-mode) on the perfect Pt-4CNC, the Pt-C bond is significantly elongated to be 2.22 Å. In this case, the Pt atoms may diffuse on the carbon surface leads to the metallic aggregation along with dramatic decrease of the hydrogen adsorption rate. In order to solve this problem, the defect Pt-v4CNC has been used, we found that Pt-C bond in the defect Pt-v4CNC decrease to 1.92 Å after the H_2 adsorption in the D-mode, see Figure 4. Therefore, Pt aggregation on Pt-v4CNC is prevented due to the hydrogen saturated Pt complex is firmly settle down at the vacancy site of the v4CNC model.

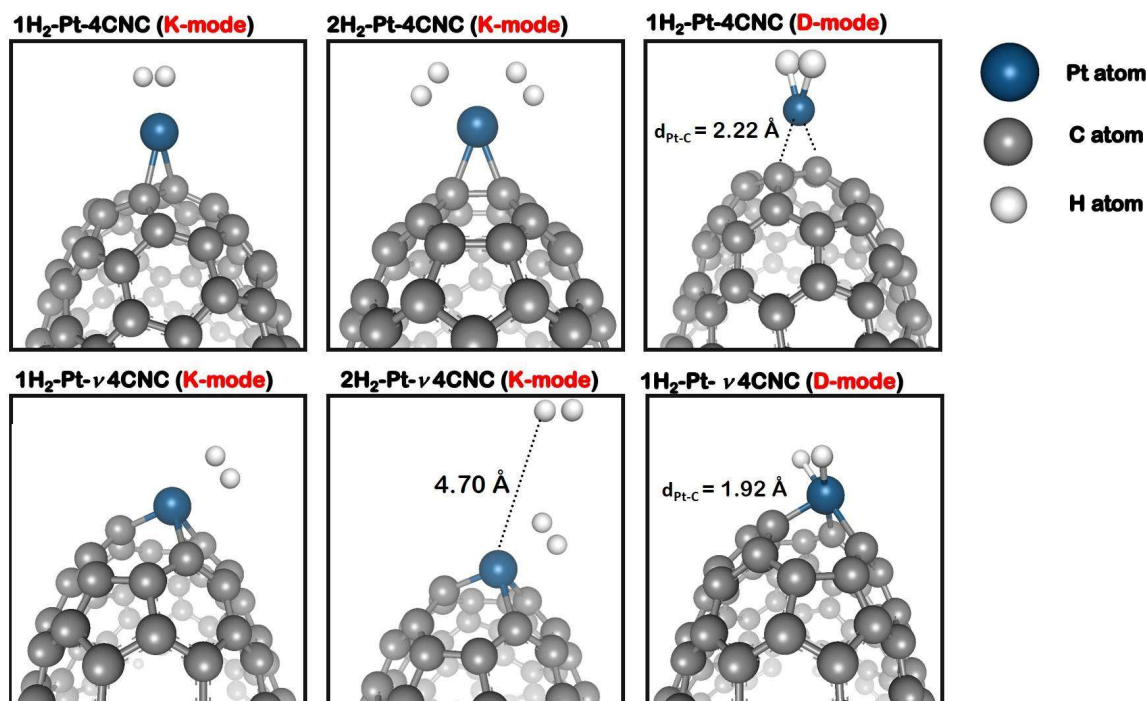


Figure 4 Optimized hydrogen adsorption geometries on Pt-4CNC and Pt-v4CNC (K- and D-mode of adsorptions). Carbon, platinum, and hydrogen are displayed in gray, blue, and white, respectively.

Table 1 Structural properties of hydrogen adsorption on CNC: H₂ adsorbed on Pt-4CNC and Pt-v4CNC. Adsorption energy (E_{ads}), bond distance between Pt atom and C atom on Pt-v4CNC tips ($d_{\text{Pt-C}}$) in Å, distance between the Pt atom and hydrogen molecules ($d_{\text{Pt-H}_2}$) in Å, and H₂ bond length ($d_{\text{H-H}}$) in Å

Substrate	H ₂ adsorption	<i>E</i> _{ads} (eV)	<i>d</i> _{Pt-C}	<i>d</i> _{Pt-H2}	<i>d</i> _{H-H}	
Pt-4CNC	H ₂	K-mode	-1.02	2.12	1.73	0.87
		D-mode	-0.94	2.22	1.56	1.44
	2H ₂ (K-mode)	-1.39	2.09	1.84 (1), 1.84 (2)	0.81 (1), 0.81 (2)	
	3H ₂ (K-mode)	-1.44	2.09	1.84 (1), 1.84 (2), 3.16 (3)	0.81 (1), 0.81 (2), 0.74 (3)	
	Pt-v4CNC	H ₂	K-mode	-0.41	1.98, 2.03, 2.00	1.94
D-mode			-0.36	1.92, 2.08, 2.08	1.64	2.22
2H ₂ (K-mode)		-0.42	1.95, 2.02, 2.02	1.98 (1), 4.79 (2)	0.79 (1), 0.74 (2)	
3H ₂ (K-mode)		-0.42	1.95, 2.02, 2.02	1.98 (1), 4.91 (2), 5.13 (3)	0.79 (1), 0.74 (2), 0.74 (3)	

3.3 H₂ spillover mechanism

3.3.1 H₂/Pt-v4CNC: hydrogen migration

To maximize hydrogen storage capacity, metal clustering should be avoided. In Pt-v4CNC, the Pt strongly binds to the dangling carbons with binding energy of approximately -7.35 eV. In addition, after reach the maximum H₂ adsorption, hydrogen-saturated Pt complex remain depositing at the vacancy site. For that reason, we examined spillover mechanism only in the Pt-v4CNC

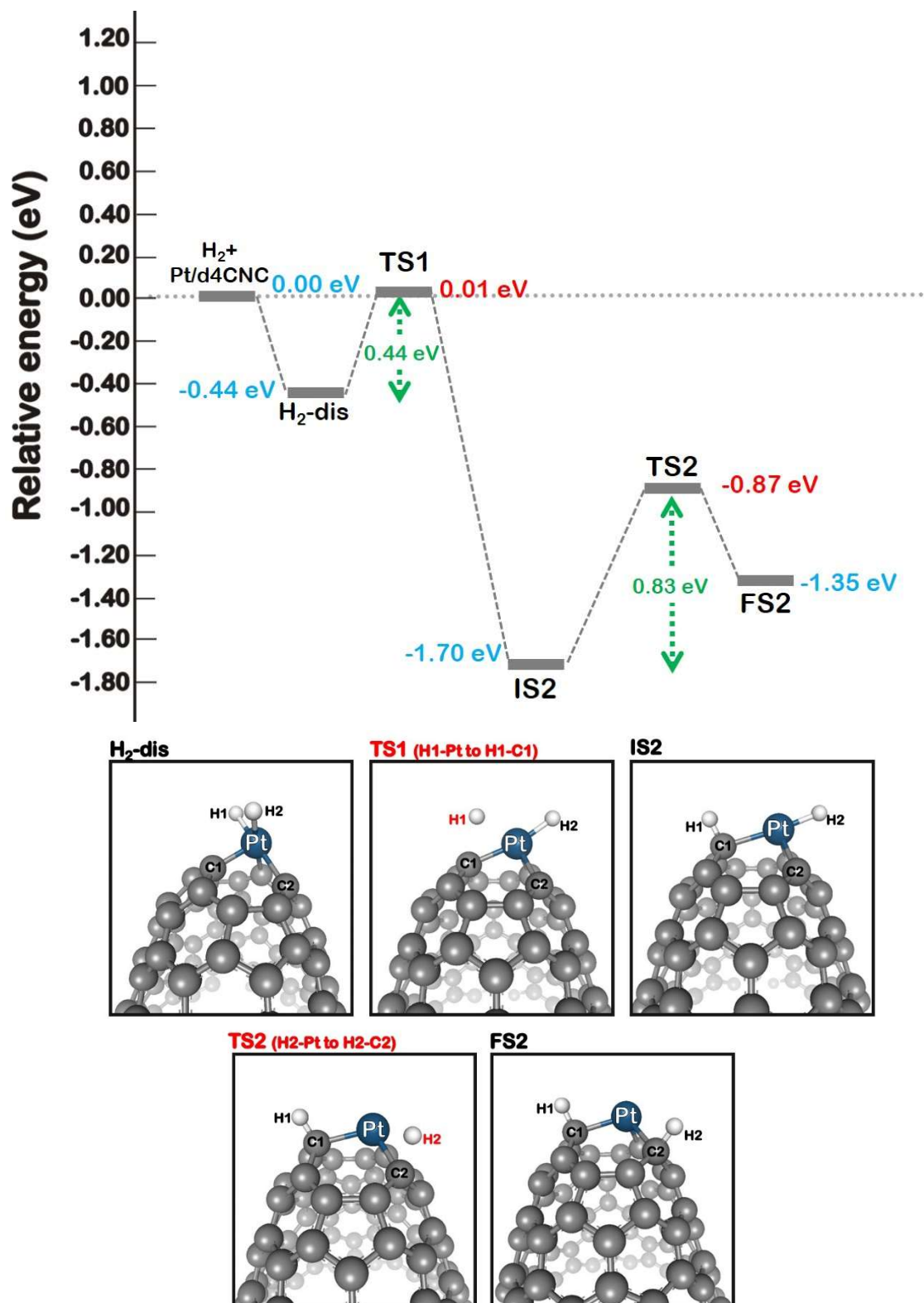


Figure 5 Migration reaction pathway and energy profile of H_2 /Pt-v4CNC

The hydrogen spillover process involves dissociative adsorption of H atoms on Pt-based nanoparticles, followed by H-migration to an adjacent carbon receptor. The reaction pathway for the spillover of the first H₂ over Pt-v4CNC is shown in Figure 5. Our calculated activation barrier, E_a , for H1-migration from Pt to C1 of the CNC surface is around 0.44 eV (TS1, Figure 5). This energy barrier is smaller than that reported for graphene (2.72 eV)¹¹. The calculated imaginary frequency for TS1 is -1023.86 cm⁻¹. At the TS1 transition state, hydrogen spillover distances of H1-Pt and H1-C1 are 1.81 and 1.82 Å, respectively. The final energy state after the first H-migration (IS2) is at -1.70 eV with H1-C1 bond of 1.10 Å. After H1 is completely migrated, the E_a for TS2 or the migration of the second hydrogen atom (H2 atom) is 0.83 eV (imaginary frequency of -1014.14 cm⁻¹) with the distance of H2-Pt and H2-C2 of 1.74 and 1.53 Å, respectively. The final step of the migrations (FS2) with both hydrogen atoms separately adsorbed to the carbon atoms of the CNC surface gains reaction energy of around -1.35 eV. Further structural parameters of each reaction step is provided in Table S4 in the supplementary data.

3.3.2 H₂/Pt-v4CNC: hydrogen diffusion

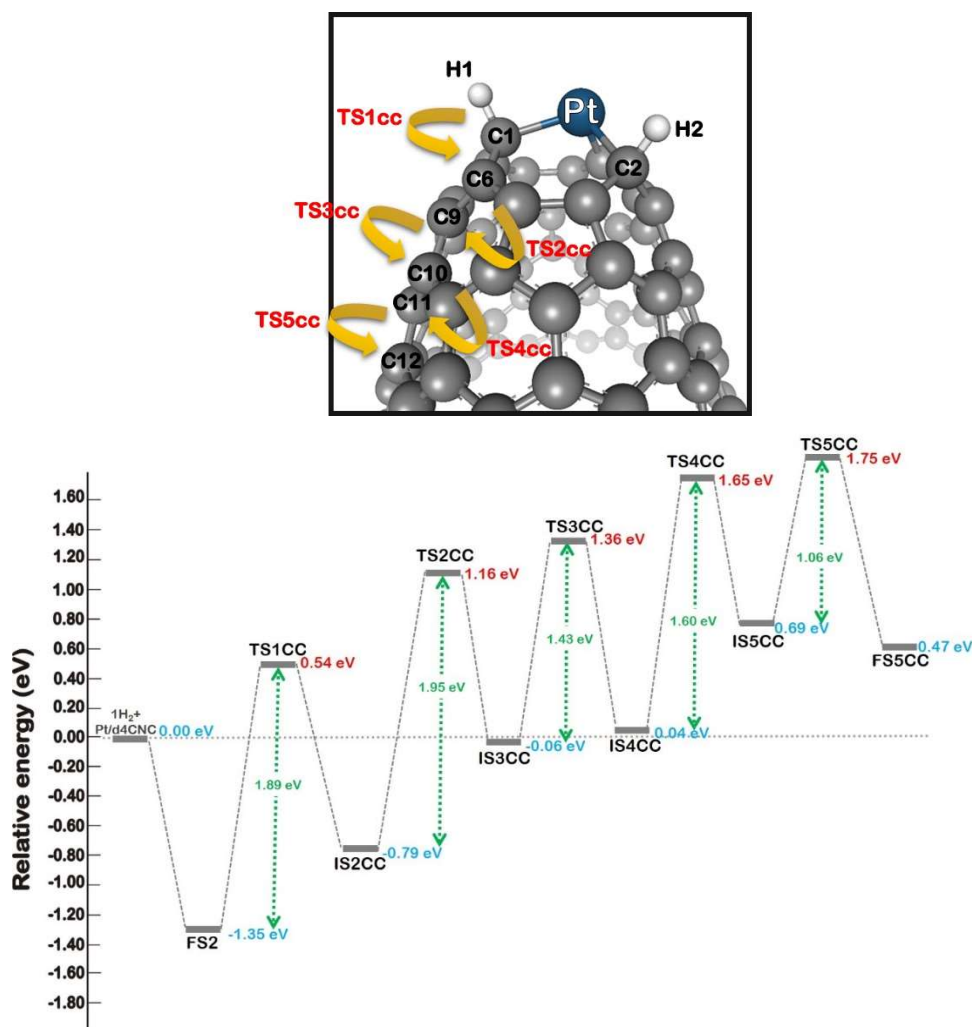


Figure 6 The H-diffusion reaction pathway through C-C route of Pt-v4CNC

Normally, the spillover process consists of two steps⁶². Firstly, H atoms migrate from the Pt catalyst to the nearest carbon atoms. The second is a diffusion of the migrated H atoms throughout the carbon support. The H-diffusion through possible C-C route of a carbon nanocone material surface is proposed in Figure 6 and the optimized structures at each step are shown in the Figure S4 of the supplementary data. The H-diffusion process via C-C route starts from FS2 configuration. Then, the H1 atom diffuses from C1 to C6 via TS1cc with E_a of 1.89 eV. Next, the H1 atom migrates from C6 to C9 with E_a at TS2CC of 1.94 eV and an imaginary frequency of -1420.79 cm^{-1} . As shown in Figure 6, the calculated E_a for diffusion from C9 to C10, C10 to C11 and C11 to C12 are 1.43, 1.60 and 1.06 eV, respectively. The E_a values are smaller when the H1 is diffused to the area having low curvature. Therefore, the H-diffusion on C1, C6 and C9, which tend to possess more character of sp^3 -like hybridization, are more difficult compared with the H-diffusion on planar carbon or sp^2 -like carbon atoms (C9-12). This phenomena is in line with the study from Liang Chen et al.⁶² who investigated the H-migration on graphene and carbon nanotube. They reported that the E_a for H-migration is depending on stability of the adsorbed H. The weaker of hydrogen adsorption, the smaller of the E_{ads} of H-migration. In this work, the H-adsorption on carbon atoms located near CNC cone tip (e.g. C1 and C6) is stronger than the H-adsorption over CNC side wall (e.g. C10 and C11) as a result of its curvature. Thus, it indicates that the first H_2 molecule is likely to be allocated on the nearest adjacent carbons of Pt because the strong hydrogen adsorption at the cone tip area make it difficult to diffuse H atom to the side wall of the CNC.

3.3.3 Hydrogen migration and diffusion in $2H_2$ /Pt-v4CNC

To examine the effect of spillover mechanism, we investigate the adsorption of the second adsorbed H_2 molecule by adding a new H_2 molecule to the system called as $2H_2$ /Pt-v4CNC. As shown in Figure 7, the adsorption on the new H_2 (IS3) has E_{ads} of -0.90 eV . The spillover process of the second H_2 begins with dissociation of H_2 ($H3$ - $H4$). The migration of H3 from Pt to the C3 atom that is an adjacent atom of Pt occurred via TS3 with a calculated activation barrier of 0.45 eV and an imaginary frequency of -1060.38 cm^{-1} . Details of structural parameters are disclosed in Table S4.

For the H4-migration, there are two possible pathways, i.e., A- and B- route as shown in Figure 7. The A-route is the H4-migration from Pt to C4 that is not directly bonded to Pt (Pt-C4 distance of 3.29 Å). The A-route occurs through TS4A with energy barrier of 1.34 eV and an imaginary frequency of -1435.35 cm^{-1} . In the B-route, the H4 migrates from Pt to C1 that is the adjacent carbon atom of Pt atom. In order to regenerate an available site on the C1, the H1 is diffused to other carbon atom (C6) via TS4B transition state with E_a of 1.03 eV . Compared with the H1 migration to C6 via TS1CC (1.89 eV) of the system with single H_2 adsorption (H_2 /Pt-v4CNC) in Figure 6, the energy barrier for H-diffusion to C6 via the TS4B is significantly smaller. The data suggest that the second H_2 molecule adsorption on Pt-v4CNC acts as an assistant to help H1 atom spill over into other C atom more easily. Then, the H4 is migrated from Pt to C1 with Pt-C1 bond distance of 1.95 Å via TS5B transition state with small E_a of 0.23 eV . After the H4-migration through the B-route, the product (FS5B) containing four migrated H atoms is a final product and the reaction is exothermic with the energy of -1.18 eV .

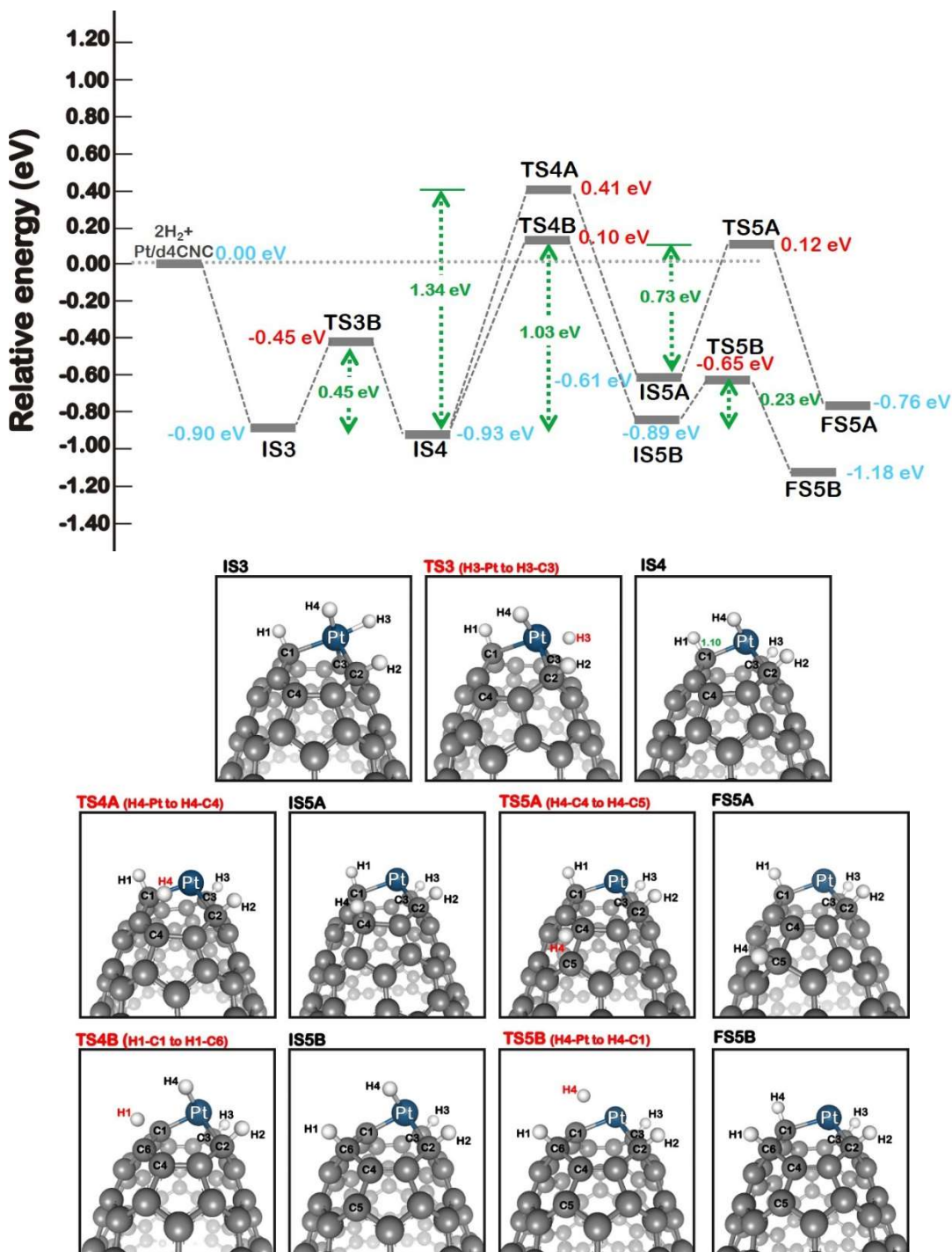


Figure 7 Spillover reaction pathway and energy profile of $2\text{H}_2/\text{Pt-v4CNC}$

From these results, we found two important points. The first one is that the H4-migration via B-route is more preferable than A-route or one can say that the H-migration from Pt to its adjacent carbon atom is easier than the migration to other carbon atoms. The second point is that in the presence of H4 on Pt atom as shown in IS4 make the H1-migration over C-C bond near

Pt catalyst more easily. The adjacent carbon atoms of Pt are re-available (C1) for an upcoming H-migration after the diffusion of prior migrated hydrogen. It is also imply that H atom sticking on Pt catalyst facilitating H-diffusion throughout CNC surface.

3.3.4 Hydrogen migration and diffusion in 3H₂/Pt-v4CNC

We investigated the hydrogen migration process of the system with three hydrogen molecules (3H₂/Pt-v4CNC) by adding new H₂ adsorption on Pt atom of the FS5B structure. As shown in Figure 8, adsorption of the third hydrogen molecule is name as IS6 with adsorption energy of -0.76 eV. As all three carbon adjacent (C1, C2 and C3) to Pt atom is already full with hydrogen adsorptions, the spillover process of the third adsorbed H₂ starts with H-diffusion through C-C bonds. The first step of this pathway is the H4 atom migration from C1 to C7 atom via TS6 with energy barrier of 0.48 eV and an imaginary frequency of -1177.17 cm⁻¹. At the TS6 transition state, we also investigated the physical properties as demonstrated in Table S4. The H4-C1 and H4-C7 distances are 1.41 and 1.29 Å, respectively. Next, migration of the third adsorbed H₂ (H5-H6) is begun with the H5- migration from Pt to C1 atom via TS7 with a simulated energy barrier of 0.12 eV and an imaginary frequency of -819.49 cm⁻¹. The H5-migration is exothermic step with an energy release of -1.05 eV. Likewise, by following the reaction pathway shown in Figure 8, the migrations of H6 come through TS8 and TS9 with energy barriers of 0.82 eV (-1376.51 cm⁻¹) and 0.14 eV (-411.83 cm⁻¹), respectively. For the structural and electronic properties of each transition state are showed in Table S4. The interesting point from this data is that the energy barriers for H-migration from Pt to C atom (TS7 and TS9) are very smaller (< 0.2 eV). Furthermore, the H-diffusions trough C-C surface (TS6 and TS8) are easier compared to the H-diffusion in the other systems such as H₂/Pt-v4CNC and 2H₂/Pt-v4CNC. Taken together, our results show that adsorption of the new H₂ molecules induce the H-migration from Pt to C and H-diffusion through C-C surface in the Pt-v4CNC. Altogether, the theoretical results support the concept of spillover mechanism as a key role for enhancing hydrogen storage capacity of metal-decorated CNC.

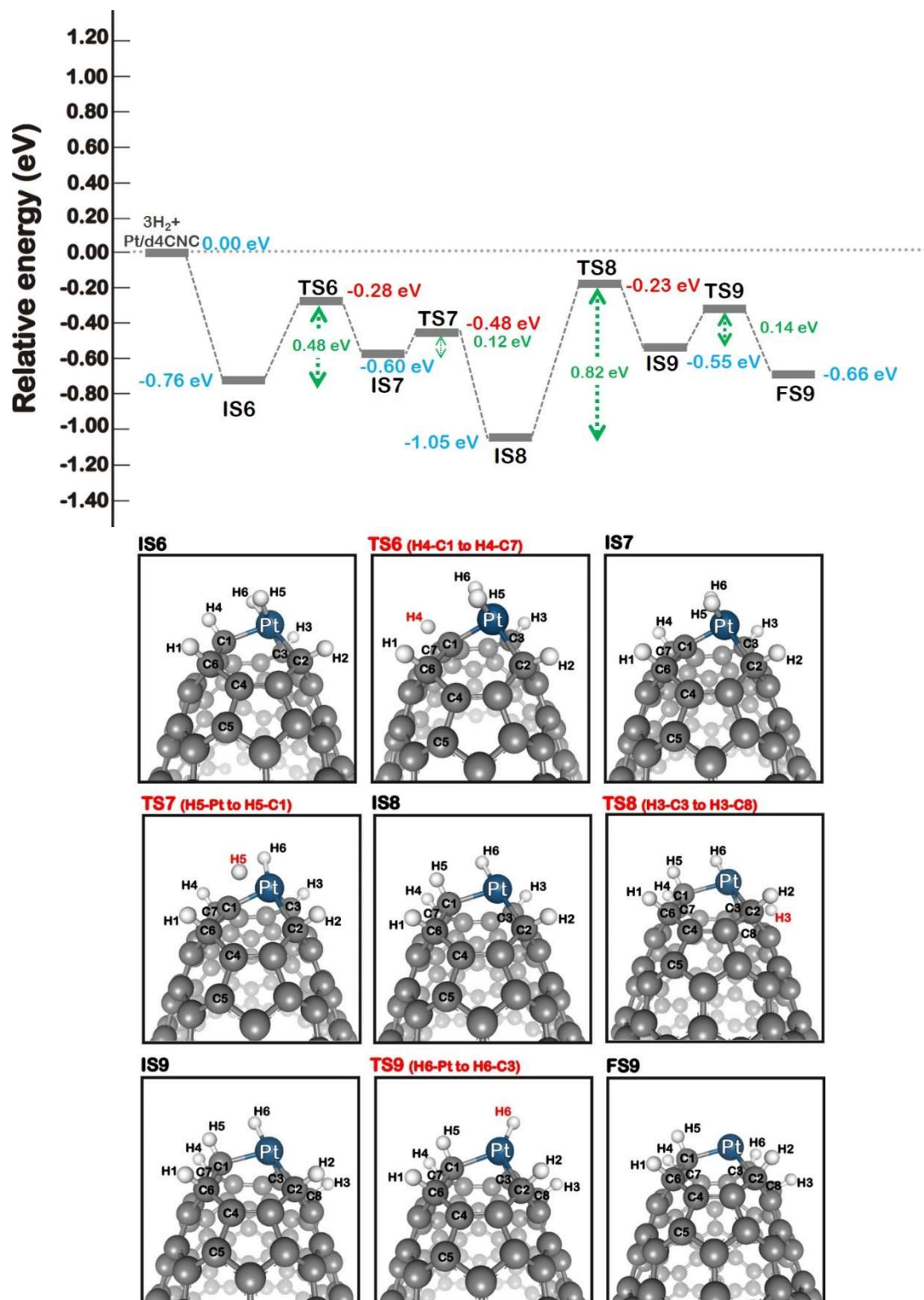


Figure 8 Spillover reaction pathway and energy profile of 3H₂Pt-v4CNC

4. Conclusions

In summary, we investigated six standard cone shaped CNCs and calculated cone angles for several different configurations. We performed DFT studies of platinum decorated CNC and of the H₂ adsorption characteristics of these complexes. Our calculations reveal that the most stable position for a Pt atom deposited locates at pentagonal bridge sites. Due to the 4-pentagon complex offers the greatest stability, we generate a v4CNC model with single vacancy and compare the Pt binding stability and H₂ adsorption with the non-defective 4CNC system. We found that the Pt atom is the active site for H₂ adsorption. The average hydrogen adsorption energy in K-mode bonding is -0.47 eV/H₂ for Pt-4CNC and -0.56 eV/H₂ for Pt-v4CNC. The spillover mechanism provides a significant improvement in hydrogen adsorption capacity for Pt-v4CNC, by first dissociating hydrogen molecules into atomic hydrogen, which then migrates and diffuses into the CNC substrate. The H-migrations of the first two-dissociated H atoms are spontaneous while the next H-migrations are trigger by the adsorption of new H₂ at the Pt active site. The preferable sites for H-migration from Pt are the three neighboring C atoms connected to the metal. Those preferable sites for H-migration are re-available via H-diffusion from C to other C atoms. Our result suggest that spillover mechanism can increases the maximum number of hydrogen adsorption at least three H₂ molecules at ambient conditions.

Acknowledgement

The authors are grateful to sources of financial support: the department of chemistry at Ubon Ratchathani University, Thailand Research Fund (RTA6080005), and the Human Resource Development in Science Project Science Achievement Scholarship of Thailand (SAST). The Center of Excellence for Innovation in Chemistry (PERCH-CIC), the office of the Higher Education Commission, and the Ministry of Education are gratefully acknowledged. The research has been also supported by Japan-ASEAN Science, Technology and Innovation Platform (JASTIP) and National Nanotechnology Center (NANOTEC), Thailand.

5. References

1. L. Schlapbach and A. Züttel, *Nature*, 2001, 414, 353.
2. D. Mori and K. Hirose, *International Journal of Hydrogen Energy*, 2009, 34, 4569-4574.
3. A. Züttel, *Materials Today*, 2003, 6, 24-33.
4. A. Züttel, P. Sudan, P. Mauron, T. Kiyobayashi, C. Emmenegger and L. Schlapbach, *International Journal of Hydrogen Energy*, 2002, 27, 203-212.
5. B. Panella, M. Hirscher and S. Roth, *Carbon*, 2005, 43, 2209-2214.
6. H. Lee, J. Ihm, M. L. Cohen and S. G. Louie, *Physical Review B*, 2009, 80, 115412.
7. G. Chen, Q. Peng, H. Mizuseki and Y. Kawazoe, *Computational Materials Science*, 2010, 49, S378-S382.
8. A. Gotzias, H. Heiberg-Andersen, M. Kainourgiakis and T. Steriotis, *Carbon*, 2011, 49, 2715-2724.
9. I. López-Corral, E. Germán, A. Juan, M. A. Volpe and G. P. Brizuela, *The Journal of Physical Chemistry C*, 2011, 115, 4315-4323.
10. A. Reyhani, S. Z. Mortazavi, S. Mirershadi, A. Z. Moshfegh, P. Parvin and A. N. Golikand, *The Journal of Physical Chemistry C*, 2011, 115, 6994-7001.

11. H.-Y. Wu, X. Fan, J.-L. Kuo and W.-Q. Deng, *The Journal of Physical Chemistry C*, 2011, 115, 9241-9249.
12. Y. Liu, C. M. Brown, D. A. Neumann, D. B. Geohegan, A. A. Puretzky, C. M. Rouleau, H. Hu, D. Styers-Barnett, P. O. Krasnov and B. I. Yakobson, *Carbon*, 2012, 50, 4953-4964.
13. I. López-Corral, J. de Celis, A. Juan and B. Irigoyen, *International Journal of Hydrogen Energy*, 2012, 37, 10156-10164.
14. H. Soleymanabadi and J. Kakemam, *Physica E: Low-dimensional Systems and Nanostructures*, 2013, 54, 115-117.
15. S. Jalili, F. Molani, M. Akhavan and J. Schofield, *Physica E: Low-dimensional Systems and Nanostructures*, 2014, 56, 48-54.
16. L. Ma, J. - M. Zhang, K. - W. Xu and V. Ji, *Physica E: Low-dimensional Systems and Nanostructures*, 2014, 63, 45-51.
17. N. Sano, K. Taniguchi and H. Tamon, *The Journal of Physical Chemistry C*, 2014, 118, 3402-3408.
18. A. S. Shalabi, H. O. Taha, K. A. Soliman and S. Abeld Aal, *Journal of Power Sources*, 2014, 271, 32-41.
19. S. A. Aal and K. A. S. A. S. Shalabi, *Journal of Quantum Information Science*, 2015, Vol.05No.04, 16.
20. M. Mananghaya, *Int J Hydrogen Energy*, 2015, 40, 9352-9358.
21. D. Rao, Y. Wang, Z. Meng, S. Yao, X. Chen, X. Shen and R. Lu, *Int J Hydrogen Energy*, 2015, 40, 14154-14162.
22. H. Valencia, A. Gil and G. Frapper, *The Journal of Physical Chemistry C*, 2015, 119, 5506-5522.
23. A. Ariharan, B. Viswanathan and V. Nandhakumar, *International Journal of Hydrogen Energy*, 2016, 41, 3527-3536.
24. M. Blanco-Rey, J. I. Juaristi, M. Alducin, M. J. López and J. A. Alonso, *The Journal of Physical Chemistry C*, 2016, 120, 17357-17364.
25. M. Gallouze, A. Kellou and M. Drir, *International Journal of Hydrogen Energy*, 2016, 41, 5522-5530.
26. C. Kaewkhonkaen and V. Ruangpornvisuti, *Molecular Physics*, 2016, 114, 3508-3517.
27. I. López-Corral, S. Piriz, R. Faccio, A. Juan and M. Avena, *Applied Surface Science*, 2016, 382, 80-87.
28. F. Molani, S. Jalili and J. Schofield, *International Journal of Hydrogen Energy*, 2016, 41, 7431-7437.
29. C. Zhou, J. A. Szpunar and X. Cui, *ACS Applied Materials & Interfaces*, 2016, 8, 15232-15241.
30. O. Faye, J. A. Szpunar, B. Szpunar and A. C. Beye, *Applied Surface Science*, 2017, 392, 362-374.
31. C. M. Ramos-Castillo, J. U. Reveles, M. E. Cifuentes-Quintal, R. R. Zope and R. de Coss, *The Journal of Physical Chemistry C*, 2016, 120, 5001-5009.
32. P. J. F. Harris, S. C. Tsang, J. B. Claridge and M. L. H. Green, *Journal of the Chemical Society, Faraday Transactions*, 1994, 90, 2799-2802.
33. N. Karousis, I. Suarez-Martinez, C. P. Ewels and N. Tagmatarchis, *Chemical Reviews*, 2016, 116, 4850-4883.

34. P. Hiralal, H. Wang, H. E. Unalan, Y. Liu, M. Rouvala, D. Wei, P. Andrew and G. A. J. Amaratunga, *Journal of Materials Chemistry*, 2011, 21, 17810-17815.
35. J. Xu, M. Yudasaka, S. Kouraba, M. Sekido, Y. Yamamoto and S. Iijima, *Chemical Physics Letters*, 2008, 461, 189-192.
36. K. Ajima, M. Yudasaka, T. Murakami, A. Maigné, K. Shiba and S. Iijima, *Molecular Pharmaceutics*, 2005, 2, 475-480.
37. R. Yuge, N. Tamura, T. Manako, K. Nakano and K. Nakahara, *Journal of Power Sources*, 2014, 266, 471-474.
38. D. Wen, L. Deng, M. Zhou, S. Guo, L. Shang, G. Xu and S. Dong, *Biosensors and Bioelectronics*, 2010, 25, 1544-1547.
39. F. Loder Meyer, R. D. Costa, R. Casillas, F. T. U. Kohler, P. Wasserscheid, M. Prato and D. M. Guldi, *Energy & Environmental Science*, 2015, 8, 241-246.
40. C. Ming, Z.-Z. Lin, R.-G. Cao, W.-F. Yu and X.-J. Ning, *Carbon*, 2012, 50, 2651-2656.
41. S. Zhu and G. Xu, *Nanoscale*, 2010, 2, 2538-2549.
42. X. Yu, M. Tverdal, S. Raaen, G. Helgesen and K. D. Knudsen, *Applied Surface Science*, 2008, 255, 1906-1910.
43. X. Yu and S. Raaen, *Applied Surface Science*, 2013, 270, 364-369.
44. A. S. Shalabi, K. A. Soliman and H. O. Taha, *Physical Chemistry Chemical Physics*, 2014, 16, 19333-19339.
45. Q. Wang, Q. Sun, P. Jena and Y. Kawazoe, *ACS Nano*, 2009, 3, 621-626.
46. M.-L. Liao, *Journal of Nanoparticle Research*, 2012, 14, 837.
47. L. Jeloica and V. Sidis, *Chem. Phys. Lett.*, 1999, 300, 157.
48. Y. Ferro, F. Marinelli and A. Allouche, *J. Chem. Phys.*, 2002, 116, 8124.
49. Y. Ferro, F. Marinelli and A. Allouche, *Chem. Phys. Lett.*, 2003, 368, 609.
50. M. Volpe and F. Cleri, *Surf. Sci.*, 2003, 544, 24.
51. A. J. Lachawiec, G. Qi and R. T. Yang, *Langmuir*, 2005, 21, 11418.
52. A. Lueking and R. T. Yang, *Journal of Catalysis*, 2002, 206, 165-168.
53. A. Lueking and R. T. Yang, *AIChE Journal*, 2003, 49, 1556-1568.
54. A. D. Lueking and R. T. Yang, *Applied Catalysis A: General*, 2004, 265, 259-268.
55. S. H. Vosko, L. Wilk and M. Nusair, *Canadian Journal of Physics*, 1980, 58, 1200-1211.
56. A. D. Becke, *Physical Review A*, 1988, 38, 3098-3100.
57. C. Lee, W. Yang and R. G. Parr, *Physical Review B*, 1988, 37, 785-789.
58. S. Grimme, J. Antony, S. Ehrlich and H. Krieg, *The Journal of chemical physics*, 2010, 132, 154104.
59. C. Kittel, *Introduction to Solid State Physics*, Wiley, 2004.
60. G. J. Kubas, R. R. Ryan, B. I. Swanson, P. J. Vergamini and H. J. Wasserman, *Journal of the American Chemical Society*, 1984, 106, 451-452.
61. Y.-H. Kim, Y. Zhao, A. Williamson, M. J. Heben and S. B. Zhang, *Physical Review Letters*, 2006, 96, 016102.
62. L. Chen, A. C. Cooper, G. P. Pez and H. Cheng, *The Journal of Physical Chemistry C*, 2007, 111, 18995-19000.

3.2 DFT study of catalytic CO₂ hydrogenation over Pt-decorated carbon nanocones: H₂ dissociation combined with the spillover mechanism

Nuttapon Yodsin¹, Chompoonut Runnim^{2,*}, Supawadee Namuangruk², and

Siriporn Jungsuttiwong^{1,*}

¹ Center for Organic Electronic and Alternative Energy, Department of Chemistry and Center for Innovation in Chemistry, Faculty of Science, Ubon Ratchathani University, Ubon Ratchathani 34190, Thailand

² National Nanotechnology Center, 130Thailand Science Park, Klong Luang, Pathumthani 12120, Thailand

Reprinted with permission from Yodsin, N. ; Runnim, C. ; Tungkamani, S. ; Promarak, V. ; Namuangruk, S. ; Jungsuttiwong, J. Phys. Chem. C 2020, 124 (3), 1941–1949. Copyright 2020 American Chemical Society.

Abstract

Carbon dioxide (CO₂), a greenhouse gas is one of the most prominent pollutants that must be resolved immediately. Among the CO₂ chemical conversion, formic acid (FA) is an interesting value-added product used in numerous applications. For the catalytic conversion of CO₂, carbon nanocones (CNC) are one of the most interesting materials for CO₂ hydrogenation to FA. In this work, we addressed the potential catalytic role of platinum decorated on defective CNC (Pt-dCNC) in CO₂ hydrogenation reaction to FA following equation; CO₂ + H₂ → HCOOH, by density functional theory (DFT) approach. We illustrate that the combination of highly reactive Pt atoms and defective CNC makes the Pt- dCNC a reactive mono- dispersed atomic catalyst for CO₂ hydrogenation reaction. We propose three possible reaction pathways which are i) co-adsorption pathway, ii) H₂-dissociation pathway and iii) H₂-dissociation together with H-spillover pathway. The CO₂ hydrogenation reaction via co-adsorption of CO₂ and H₂ is not a favorable pathway because of a high activation energy (1.49 eV) at the rate determining step. For the H₂-dissociation pathway, the H-H dissociation over Pt/dCNC to generate Pt-H atoms easily undergoes with energy barrier only 0.09 eV and the activation energy for FA formation via Pt-formate intermediate is lower than the reaction processes through the Pt-carboxylate intermediate. In the H₂-dissociation together with H-spillover pathway, the reaction mechanism starts with H₂ dissociation and follow by a spillover of the dissociated H atom to the CNC surface before the CO₂ adsorption and hydrogenation through the formate intermediate. Then, this Pt-formate specie can be converted to FA by the H₂-dissociation of a new H₂ molecule. The reaction in this H₂-dissociation together with H-spillover pathway is energetically favorable with a small activation energy (0.76 eV) at the rate determining step. Our results demonstrated that the rate of FA production is controlled by the H₂ amount. The Pt- dCNC would be a promising candidate catalytic material for the CO₂ hydrogenation reaction to FA when the system has high H₂ concentration.

Keywords: Density functional theory (DFT); CO₂ hydrogenation reaction; Formic acid (FA); Carbon nanocone (CNC); Platinum (Pt); Hydrogen spillover

1. Introduction

At present, the increased population, rapid development of cities, industrial activities and transportation have resulted in raising the level of greenhouse gases in the Earth's atmosphere. Most of the current energy utilization comes from fossil fuels such as coal, crude oil, gasoline, and natural gas. The main disadvantages of these fossil fuels are toxic gas emission, pollution and toxic wastes which are principal contributors to global warming and climate change. Carbon dioxide (CO₂) is the main greenhouse gas and one of the most prominent pollutants that must be resolved instantaneously. Elevated technologies have been applied to reduce CO₂ such as carbon capture storage (CCS) and carbon capture utilization (CCU) by conversion into a value-added product. The most important challenge for the CCU process is to find reactive and cost-effective catalysts. Therefore, a lot of effort has been made for the design and development of new inexpensive catalysts with high stability and efficiency for the CO₂ conversion into valuable products such as formic acid, methane, and methanol. Hence, the indispensable key benefit of the CO₂ conversion is not only to decrease the amount of greenhouse gas but also to reduce fossil utilization in the petrochemical industry.

Formic acid (FA) is widely used as a principle reagent for chemical applications and also received considerable attention because it is related in numerous industrial application.¹⁻⁶ Nowadays, there are many experimental and theoretical studies have investigated the chemical and CO₂ conversion to FA⁷⁻²⁴. Recent catalytic materials for CO₂ hydrogenation to FA are highly toxic material, expensive, easy to explore and low efficiency of CO₂ conversion.^{1,9,17,25} Therefore, exploring and developing a more cost-effective catalyst for CO₂ conversion to FA is really crucial.

Here, we are interested in carbon-based nanomaterial as a catalytic supporter because of its low cost, high purity, and high surface area. Carbon nanocones (CNCs) is a novel form of carbon which could act as a suitable support for various metal to form new carbon-metal nanocomposites.²⁶⁻²⁷ These composites could be used in several applications, including supercapacitors²⁸, drug delivery²⁹⁻³⁰, lithium ion batteries³¹, biofuel cells³², conversion and storage of energy³³⁻³⁴, and solar cells³⁵. The CNCs as a new substrate for CCU application has attracted a great deal of interest in recent years. Therefore, CNCs have been selected for investigating the catalytic reaction of CO₂ conversion to FA. The perfective CNCs, there are many advantages, but it is inert and low efficiency to be useful for catalytic CO₂ hydrogenation reaction. Therefore, to enhance CO₂ conversion to FA, carbon nanomaterial surfaces should be decoration with transition metals.

After 10 years later from the first observed, high purity single-walled carbon nanohorns (SWCNHs) by using the arc-discharge study to produce materials directly used a pulsed arc-discharge.³⁶ From the synthesis, the researchers found that the arc-discharge method can synthesize high purity of SWNHs reached higher than 90%. For the CO₂ hydrogenation by using metal surface, there are many kinds of transition metals have been used for CO₂ hydrogenation such as the group 11 element.³⁷⁻⁴⁰ The experimental study of Cu-metal surface have been used to be an active catalyst for CO₂ conversion to FA.^{37,39-41} Due to the reaction mechanisms and the

support effects remain unclear. Theoretical calculations can help to understand fundamental processes, the structures of reactants and transition state along with the catalytic path. For example, the mechanisms of CO₂ hydrogenation catalyzed by copper was reported by using DFT calculations.⁴¹ Recently, due to metal catalysts are toxic material and more expensive, the theoretical study reported that the atomic copper deposited into the organic linker of the MOF-5 can catalyze the CO₂ hydrogenation to produce FA to reduce metal amount¹¹. Sirijaraensre and Limtrakul¹⁴, Esrafil, M. D., et al.⁸, and Nguyen, L. T. M., et al.¹³ showed that carbon-based catalyst could efficiently catalyze the hydrogenation reaction of CO₂ to FA. Moreover, experimental and theoretical studies of other metal were also considered. The Pt-metal and Ni-metal surface for CO₂ hydrogenation reaction were investigated.^{9, 25, 42} Concerning the cost of pure metal, the Pt- and Ni- doped on defective graphene for formic production were studied through CO₂ hydrogenation reaction.⁸ Interestingly, in 2018, Pt nanoparticle- loaded carbon nanohorns (Pt/CNHs) materials were synthesized by using FA as a reducing agent at the mild condition. Comparing with commercial Pt/C, the small size of Pt nanoparticle on Pt/CNHs nanocomposites showed higher catalytic activity, electrocatalytic activity and durability in FA oxidation reactions.⁴³ Very recently, M. Melchionna and coworker²¹ successfully synthesized inorganic Pd@TiO₂/carbon nanohorn electrocatalysts to convert CO₂ to FA directly at thermodynamic equilibrium. From their study, the CNHs with transition metal can be used as a promising catalytic supporter for hydrogenation reaction of CO₂ to FA.

In this work, the adsorption of CO₂ and its subsequent hydrogenation reduction to FA are studied over Pt-doped defective CNC (Pt/dCNC) using DFT calculations. The geometry, electronic structure and the catalytic activity of Pt/dCNC studied and compared with other reported carbon-based materials in details. To the best of our knowledge, this is the first report on the hydrogenation reaction of CO₂ molecule to FA over Pt/dCNC material. Our simulated results illustrated that the spillover mechanism on CNC can be helpful for increasing of the active site of Pt/dCNC material. Our results of this study could clarify the chemical and catalytic properties of metal-doped dCNC material and in designing highly efficient carbon-based catalysts for the conversion of CO₂ to useful chemicals. In facts, this study could be helpful for environment cleanly.

2. Computational methodology

All DFT calculations were investigated by using the Gaussian 09 programs package. The optimized geometries and the frequency calculation of all complexes were performed with Becke's three parameters gradient-corrected exchange potential combined with the Lee-Yang-Parr gradient-corrected correlation potential (B3LYP)⁴⁴⁻⁴⁶. In DFT calculations, all-atom on our systems were calculated with the 6-31G (d, p) basis set except for the Pt atom using the LANL2DZ basis set. Then, energies of all structures were corrected by single point calculation using B3LYP functional including Grimme's D3 dispersion correction (B3LYP-D3)⁴⁷ with 6-311G(d,p) basis set for C, O and H atoms and cc-pVTZ-PP basis set for Pt atom.

In this work, the CNC cluster model consists of 112 carbon atoms with four pentagon rings at the cone tip and hydrogen termination at the cone edge as suggested from our previous study.³⁴ The defective carbon nanocones (dCNC) complexes were created by removing one

carbon atom at the top of the cone tip. Then, a Pt atom was placed at the vacancy of dCNC called as Pt/dCNC substrate. The stability of the Pt atom on the dCNC support was calculated by the following equation

$$E_{bind} = E_{Pt/dCNC} - E_{Pt} - E_{dCNC}$$

where $E_{Pt/dCNC}$, E_{Pt} , and E_{dCNC} are the total energies of Pt/dCNC, Pt atom (Pt) and dCNC substrate, respectively.

The gas adsorption on Pt/ dCNC was monitored via adsorption energy (E_{ads}) which calculated in Eq.

$$E_{ads} = E_{gas-Pt/dCNC} - E_{Pt/dCNC} - E_{gas}$$

where $E_{gas-Pt/dCNC}$, $E_{Pt/dCNC}$, and E_{gas} correspond to total energies of the adsorbed gas over Pt/dCNC, the bare Pt/dCNC and the isolated gas, respectively.

In the CO₂ hydrogenation mechanism over Pt/ dCNC, three possible mechanisms are proposed. The transition state of each sequence of step was confirmed by frequency calculation, which showed only one imaginary frequency. The activation energy (E_a) of each step is defined in Eq.

$$E_a = E_{transition} - E_{reactant}$$

where $E_{transition}$ and $E_{reactant}$ represent total energies of the transition state and reactant prior to the transition state, respectively.

3. Results and discussion

To understand the catalytic material behavior, the electronic, structural, energetic properties of Pt/dCNC are investigated and discussed in detail. From the optimized structure of Pt/dCNC, the metal atom is located preferably on top of the single vacancy site of the pentagon on the cone to form covalent bonds with three coordinated carbon atoms, as demonstrated in Figure S1. The binding energy of Pt on dCNC is about -6.60 eV with Pt-C bond length around 1.9 Å, which is corresponding to our reported value^{34, 48}. Comparing with Pt cohesive energy (5.84 eV/atom)⁴⁹, the strength of Pt binding on vacancy site tend to prevent the aggregation and formation of Pt metal cluster. According to the Mulliken charge population analysis, the Pt metal atom has a positive charge of 0.618e and net charge of the dCNC is negative as a result of electron transferred from a Pt metal to the carbon support. Additionally, there is a strong hybridization of Pt and dCNC in the lowest occupied molecular orbital (LUMO), see more details in Figure S2 of the supplementary data. Therefore, the Pt atom behaves like Lewis acid and it is expected to get a strong interaction toward CO₂ hydrogenation with the adsorption mode corresponded to the LUMO orbital.

In the next part, the adsorption of CO₂ and H₂ over Pt/ dCNC together with possible catalytic mechanisms for hydrogenation reaction to convert CO₂ into FA will be focused.

3.1. Adsorption of CO₂ and H₂ molecules on Pt/dCNC

To understand the mechanism of CO₂ conversion to FA, we first consider the adsorption of individual CO₂ and H₂ molecules on Pt/dCNC surfaces. The position and orientation of the two gases are varied in order to find the most stable adsorption mode. The most energetically favorable configuration of CO₂, H₂ and CO₂/H₂ co-adsorptions is demonstrated in Figure 1.

The adsorption energy of CO₂ over Pt/dCNC is -0.40 eV which is stronger than its adsorption energy on the perfect surface of CNC (-0.13 eV). The Pt-O intermolecular bond distance is around 2.68 Å as shown in Figure 1. Compared with the Pt decorated on single vacancy graphene ($E_{\text{ads}} = -0.33 \text{ eV}^8, -0.23 \text{ eV}^{50}$), the CO₂ adsorption energy on Pt/dCNC is slightly stronger. For the H₂ adsorption, the H₂ molecule adsorbed on the Pt metal atom with an adsorption energies Pt/dCNC of -0.44 eV. By comparison with CO₂ adsorption on the Pt/dCNC, the H₂ adsorption is more favorable than the CO₂.

Additionally, we also investigated the co-adsorption of the two gas molecules. As depicted in Figure 1, the CO₂ and H₂ can be co-adsorbed on the Pd/dCNC but the Pt-O and Pt-H bonds are slightly weaker than those of individual adsorption modes. The Pt-O bond distance in the co-adsorption mode is prolonged by 0.33 Å (from 2.68 to 3.01 Å). Considering on adsorption energy in this co-adsorption mode, the CO₂ and H₂ adsorption energies are -0.28 and -0.38 eV, respectively. The result implies that both gas molecules can cover on the metal surface when a CO₂/H₂ mixture has flowed as the reaction gas. To confirm the gas adsorption, the analysis of frontier orbitals of gas-Pt/dCNC is investigated. As shown in Figure S3, the hybridizations between gas adsorbent and Pt/dCNC substrate mainly correspond to the Pt-O and Pt-H bonds, confirming the strong interaction of the Pt towards CO₂ and H₂ molecules.

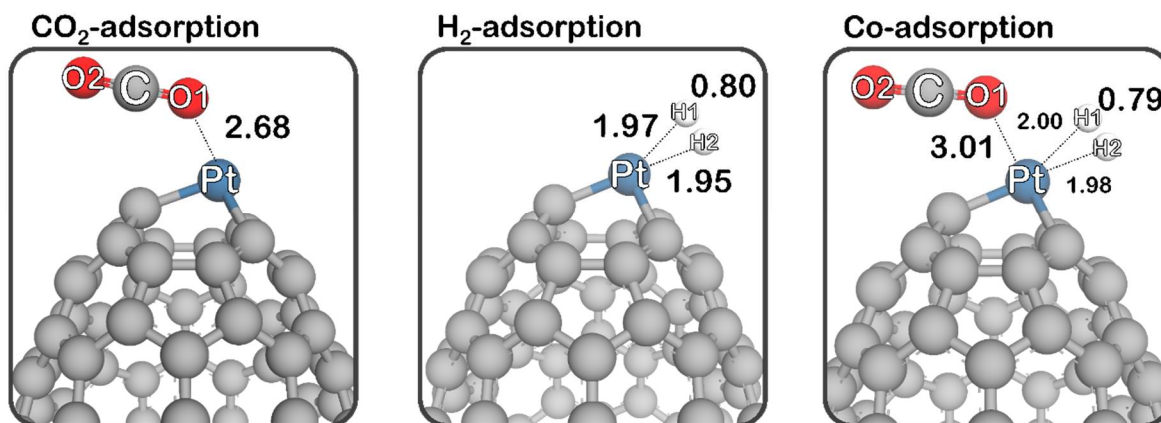


Figure 1. Optimized configurations of the gas adsorption on the Pt/dCNC surface: CO₂, H₂, and CO₂/H₂ co-adsorption complexes. Bond distances are in Å.

3.2. Reaction mechanism of CO₂ Hydrogenation on Pt-dCNC surface

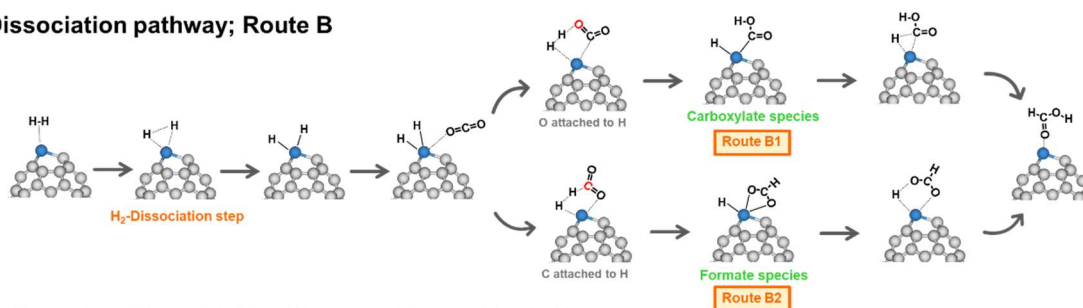
In this section, the reaction mechanism of CO₂ hydrogenation to FA is proposed and investigated with three possible reaction pathways. The first pathway is the co-adsorption

pathway (route A). Secondly, hydrogen dissociation pathways are studied called a hydrogen dissociation pathway (route B). Lastly, to gain more active site, the pathway with hydrogen spillover after hydrogen dissociation is considered (route C). All possible mechanisms of CO₂ hydrogenation to FA illustrate in Figure 2.

a. Co-adsorption pathway; Route A



b. H₂-Dissociation pathway; Route B



c. H-Spillover together with H-spillover pathway ; Route BS

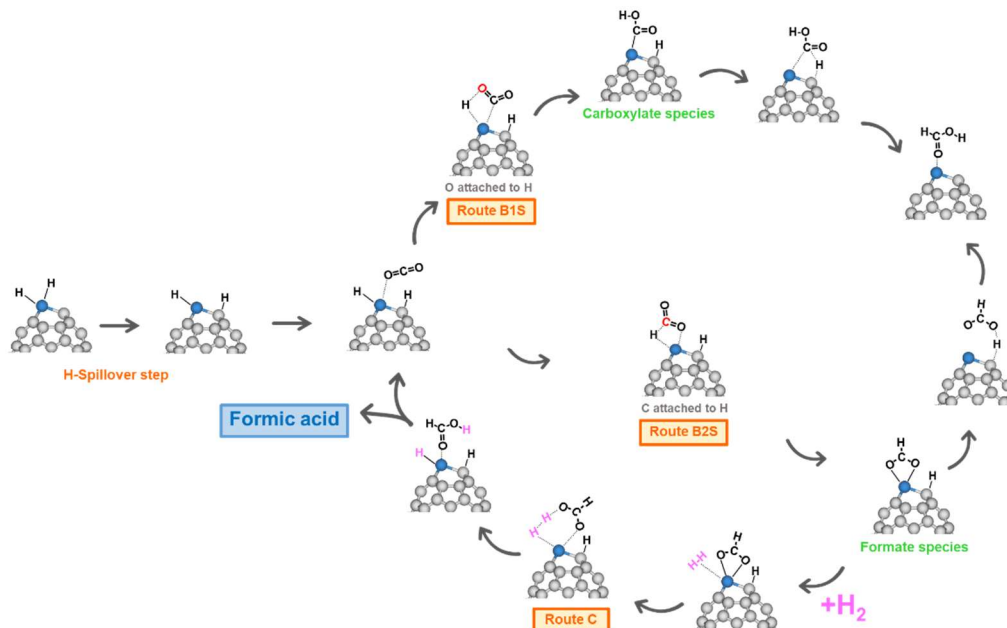
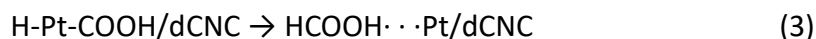
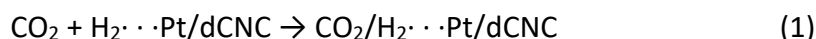


Figure 2. All possible reaction pathways of CO₂ hydrogenation to FA.

3.2.1 CO₂ hydrogenation reaction on Pt-dCNC surface via CO₂ and H₂ co-adsorption pathway

We endeavor to propose the CO₂ hydrogenation reaction through the co-adsorption pathway (route A). After the co-adsorption of CO₂ and H₂, the CO₂ hydrogenation could convert

CO₂ molecules into FA through carboxylate intermediate as can be seen the sequence of a step following equation (1)-(3)



The optimized structures and catalytic pathway with the conversion CO₂ to FA via route A are demonstrated in Figure 3. At the first transition state of route A or TS1-Route A, the CO₂ molecule is hydrogenated at oxygen atom (O1-atom) to generate –COOH ligand (carboxylate-intermediate). At the same time, the hydrogen molecule is dissociated and the bond distance between H1-H2 is elongated from 0.79 to 0.95 Å. The H1 atom is located at the middle of O1 atom of CO₂ and H2 atom with the distance of 1.34 and 0.95 Å, correspondingly. The calculated activation energy barrier (E_a) for carboxyl functional group (–COOH) formation at the TS1-Route A, is around 1.49 eV with a single imaginary frequency around -1425.17 cm⁻¹. The obtained energy barrier is in line with a value of 1.50 eV for Cu deposited graphene surface¹⁴, but it is smaller than the reaction on Ni/Graphene material⁸ (2.08 eV) by similar DFT calculations. After the TS1-Route A step, the carboxylate intermediate or H-Pt-COOH (INT1-Route A) is formed with relative energy around -0.69 eV. Then, the H2 atom is transferred from Pt catalyst to the –COOH ligand via TS2-Route A transition state with an energy barrier of 0.78 eV and single imaginary frequency of -559.23 cm⁻¹. At the TS2-Route A, the distance between C atom of –COOH ligand and H2 atom is decreased to form HCOOH over Pt/dCNC surface. Finally, the FA is produced on Pt/dCNC complex with an adsorption energy of -0.95 eV. Remarkably, the rate determining step for the CO₂ and H₂ co-adsorption pathway is the formation of carboxylate intermediate at the TS1-Route A, as represented in Figure 3.

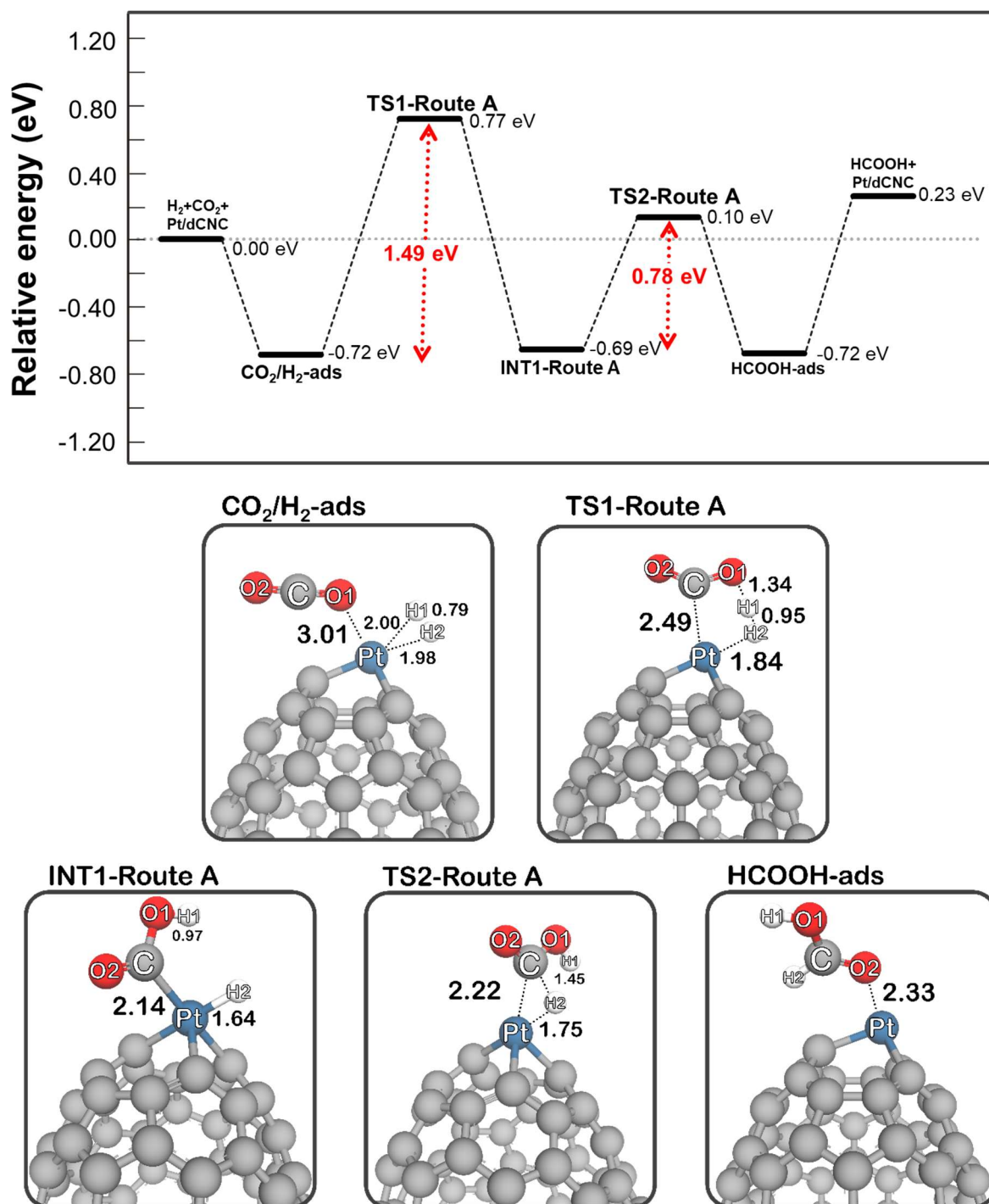
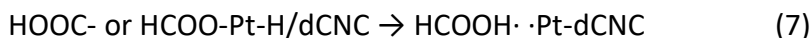
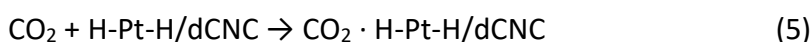


Figure 3. Catalytic reaction pathways (eV) of the Pt/dCNC for the CO₂ hydrogenation to FA via CO₂ and H₂ co-adsorption pathway (route A). Distances are in Å.

3.2.2 CO₂ hydrogenation reaction on Pt/dCNC surface via H₂-dissociation pathway

From the early section, we observed that the H₂ adsorption on Pt/dCNC is slightly favorable than the adsorption of CO₂. In addition, the H-H bond of the hydrogen molecule is a strong covalent bond with bond-dissociation energy (BDE) of 4.51 eV¹⁴. However, the hydrogen bond can be easily dissociated over Pt/dCNC complex with small energy barrier (0.09 eV). Compared to hydrogen dissociation on other material, the H₂ molecules dissociations hardly process over Pt-Gr (0.29 eV) as shown in Figure S6, Cu-Gr (1.31 eV)¹⁴, CoN3-Gr (0.95 eV)²⁰, which is similar to the results of CO₂ hydrogenation over other surfaces.^{11, 14, 20, 51} Hence, the CO₂ hydrogenation reaction on Pt/dCNC surface via hydrogen dissociation pathway (called Route B) is very attractive. In this pathway, we found that there are two possible pathways. The first one is pathway with carboxylate intermediate (-COOH; Route B1) and another one occurs via formate intermediate (-OOCH; Route B2) as disclosed in the following equations. These possible mechanisms are also reported in the CO₂ hydrogenation over Cu-alkoxide-functionalized MOF¹¹, alkali metal zeolites⁵², Cu-graphene¹⁴.



As shown in Figure 4, the CO₂ hydrogenation through the Route B pathway starts with hydrogen molecule adsorption over the Pt atom on Pt/dCNC. So, this configuration is set as the initial state (H₂-Pt/dCNC). Next, the hydrogen molecule is dissociated via the TS1-Route B transition state which is an almost barrierless reaction (0.09 eV) with a single imaginary frequency of -953.83 cm⁻¹. After hydrogen dissociation step, the bond distance between the hydrogen atoms of H₂ is noticeably increased from 0.80 to 2.18 Å at the INT1-Route B intermediate. Afterward, the CO₂ is subsequently adsorbed on the platinum hydride species over CNC surface named as CO₂-INT1-Route B.

In the Route B1 or carboxylate intermediate, the CO₂ molecule bend to interact with H1 atom and form the carboxylate- species via TS2-Route B1. The formation of carboxylate-intermediate requires a high energy barrier of 2.91 eV. Subsequently, the H₂ is transferred from Pt to the carbon of the -COOH moiety through the TS3-Route B1 with an activation energy of 0.78 eV. The observed TS2-Route B1 and TS3-Route B1 are confirmed by the frequency analysis with one imaginary frequency of -1,765.73 and -559.23 cm⁻¹, respectively. From this result, the CO₂ hydrogenation on Pt/dCNC hardly occur through carboxylate intermediate in the hydrogen dissociation pathway.

In formate intermediate or Route B2, the formate intermediate (-OOCH) is generated through the TS2-Route B2 transition state with an activation energy of 0.66 eV. Frequency

calculation demonstrates one imaginary frequency at -106.55 cm^{-1} in the direction related to the movement along the reaction coordinate. At transition state, the C-H1 is formed simultaneously with the bond distance of C-H1 and Pt-H1 around 1.37 and 1.84 Å , respectively. Finally, the FA is formed via TS3-Route B2 with an energy barrier of 1.15 eV . Therefore, the CO_2 hydrogenation reaction over Pt/dCNC catalyst via formate intermediate is more favorable than carboxylate intermediate, which is in good agreement with the CO_2 hydrogenation reaction on Faujasite-supported Ir_4 Clusters²³.

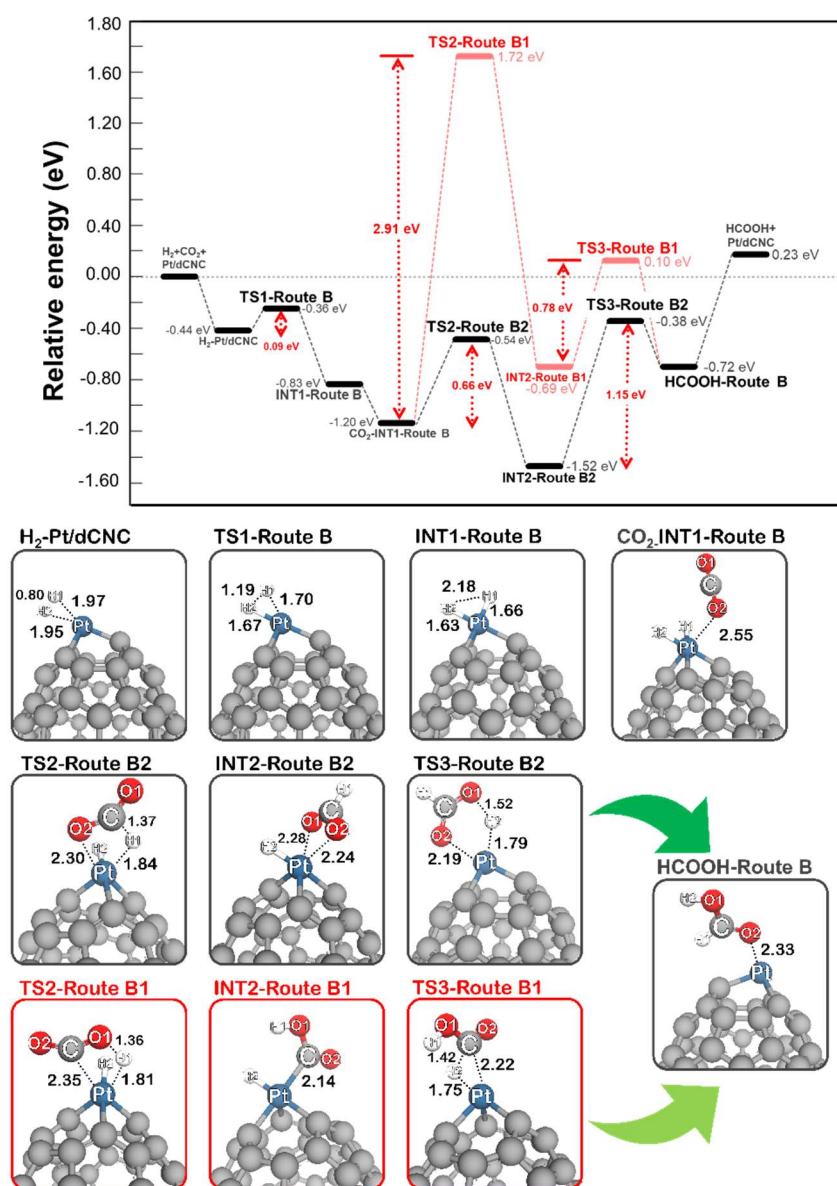
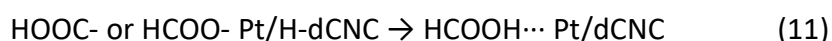
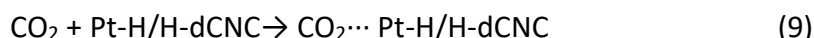


Figure 4. The energy profile, optimized geometries of the initial states, transition states, and final state (FS) for CO_2 hydrogenation reaction on Pt/dCNC surface via H_2 -dissociation pathway (route B). All distances are in Å.

3.2.3 CO₂ hydrogenation reaction on Pt/dCNC surface via H₂-dissociation together with H-spillover pathway

Another pathway for CO₂ hydrogenation reaction to FA over Pt/dCNC surface is carried out by considering the hydrogen spillover mechanism suggested from our previous work³⁴. The energetic profile of this mechanism was investigated as presented in Figure 6. Following introductory reaction step proposed by J. Sirijaraensre and J. Limtrakul in 2016¹⁴, the CO₂ hydrogenation to FA over Pt/ dCNC complex through the H₂- activated intermediate is demonstrated in the following equations:



The hydrogen molecule can be dissociated over Pt/dCNC material and generated a metal-hydride in the INT1-Route B intermediate, as mention earlier. After the hydrogen dissociation step, the hydrogen spillover from the Pt to three neighbor carbons (marked as 'C1', 'C2' and "C3" in Figure S4) is explored. From our calculations, the energy barrier for H-spillover to C1, C2, and C3 are 0.76, 0.92 and 0.92 eV, respectively. Thus, the H-spillover to C1 via TS2-Route BS transition state is selected for further reaction step. After the H-spillover, the C-H is formed on dCNC called as INT2-Route BS.

Then, the CO₂ is adsorbed to the complex system named as CO₂-INT2-Route BS with the adsorption energy of -0.45 eV. Following the formic reaction partway, the CO₂ hydrogenation is proposed through the -OOCH intermediate. At the TS3-Route B2S transition state, the H2 atom on metal hydride is elongated from 1.63 to 1.79 Å and form a covalent bond with the carbon atom of the CO₂ molecule. The activation energy of -OOCH formation was 0.64 eV as illustrated in Figure 6. Moreover, the single imaginary frequency of this transition state was calculated, which is -584.76 cm⁻¹. After that, the format intermediated (INT3-Route B2S) is created. Comparing with CO₂ hydrogenation without H spillover step, the activation energy for the formation of format intermediate slightly decreases from 0.66 eV to 0.64 eV.

This evidence suggests that hydrogen spillover mechanism can facilitate the CO₂ hydrogenation. Further details corresponding to the adsorption property of CO₂ gas as depicted in Figure 5 and Table 1.

Considering of the effect of hydrogen spillover mechanism for CO₂ adsorption reaction, the results show that the first hydrogen spillover into the dCNC surface can increase adsorption energy of CO₂ molecule from -0.37 eV to -0.45 eV. Supported by Pt-O distance, the Pt-O bond distance of CO₂-INT1-Route BS structure is 2.52 Å, while the Pt-O distance of CO₂-INT1-Route B is 2.55 Å that is a little bit larger than CO₂-INT1-Route BS intermediate. The strong interaction between gas adsorbed on the substrate can reduce the energy barrier of formate intermediate

formation. From the best of our knowledge, we can conclude that Pt/dCNC is increased active site by spillover one hydrogen atom into the CNC surface after hydrogen molecule dissociation for CO₂ hydrogenation reaction.

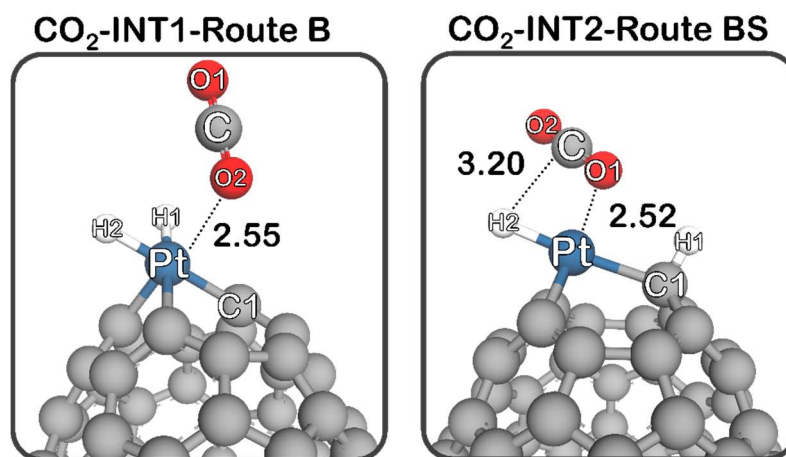


Figure 5. CO₂ adsorption properties of with and without hydrogen spillover mechanism over the Pt/dCNC surface. Distances are in Å.

Table 1. The effect of hydrogen spillover mechanism for CO₂ adsorption

System	CO ₂ -INT1-Route B structure	CO ₂ -INT1-Route BS structure
E_{ads} (eV)	-0.37	-0.45
E_a (eV)	0.66	0.64
d(Pt-O)	2.55	2.52
d(C-H)	2.99	3.20

Note: Distances are in Å; Energy barrier of formate formation (E_a)

At the INT3- Route B2S intermediate, the format intermediate arranges in bidentate orientation with the distances between Pt-O1 and Pt-O2 of 2.27 and 2.26 Å, respectively. The format intermediate in the INT3-Route B2S is quite stable with relative energy of -2.49 eV. For the formic formation from the INT3- Route B2S intermediate, two possible pathways are proposed as demonstrated in Figure 6-8.

The first one is the FA formation via the protonation from C-H1 on dCNC to an oxygen atom of HCOO⁻ ligand via TS4-Route B2S. The bond distance between H1 atom and C1 atom on the surface is elongated from 1.10 to 1.55 Å and H1 atom interacted with O1 atom of -OOCH intermediated with a distance of 1.14 Å. The transition state has one imaginary frequency of -949.95 cm⁻¹. We found that the barrier of TS4-Route B2S transition step is 2.24 eV, which is the rate-determining step of the CO₂ hydrogenation reaction in the Route B2S.

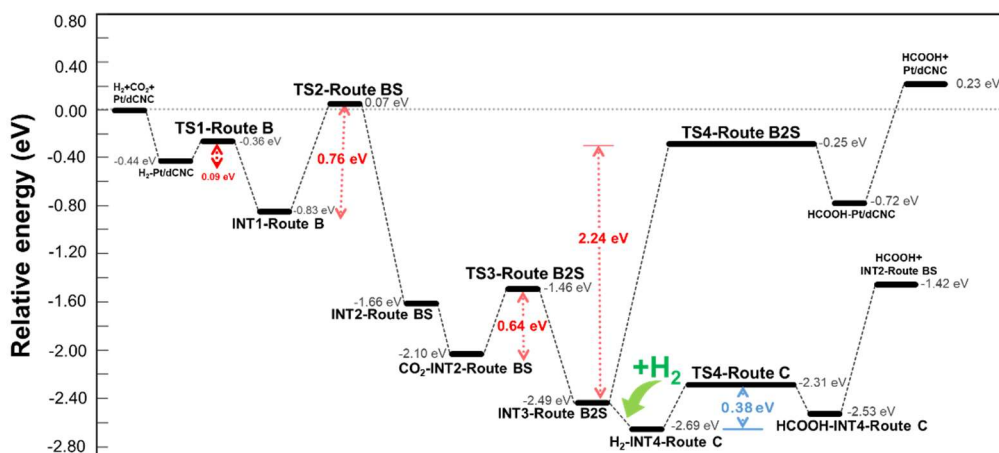


Figure 6. Energetic profile in eV of the Pt/dCNC surface for the CO₂ hydrogenation to FA through route B2S and C pathways. Distances are in Å.

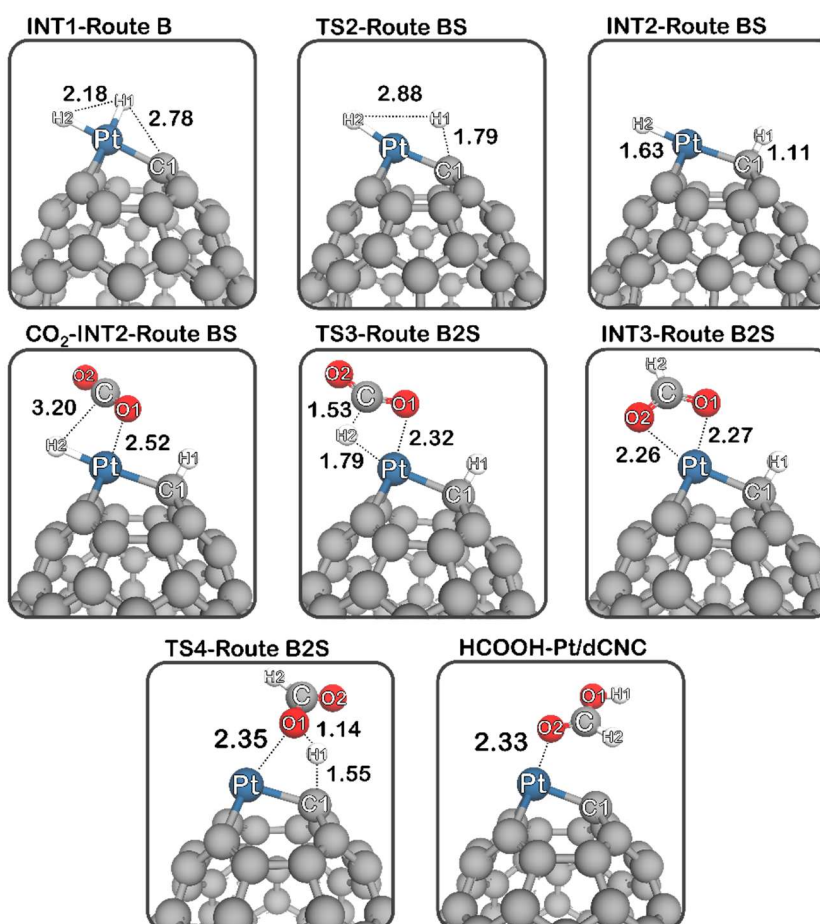


Figure 7. Structural properties of hydrogen dissociation and spill over on the Pt/dCNC for formic production by using the CO₂ hydrogenation reaction via route BS mechanism. Distances are in Å.

To reduce the rate-determining step, a new pathway for the FA formation is proposed by adding the second hydrogen molecule (Route C) with the following sequence of reaction steps:



After hydrogen spillover step and the formate intermediate formation, the Pt on Pt/dCNC is available for the approach of the second hydrogen molecule. As shown in Figure 8, the second hydrogen molecule is weakly adsorbed with –OOCH group on Pt-dCNC complex (-0.20 eV). At the TS4-Route C transition state, the H3-H4 bond length is elongated from 0.75 to 0.90 Å, while the intermolecular of H3-O1 and Pt-H4 distances are decreased to 1.44 and 1.87 Å, respectively. The data confirms a dissociation of the second hydrogen and a forming of FA with a single imaginary frequency of -499.68 cm^{-1} at the transition state. As illustrated in Figure 6, the activation energy of TS4-Route C is 0.38 eV. The energy barrier via the TS4-Route C transition state is much lower than the calculated barrier from the direct hydrogenation of formate over the Cu(1 1 1) surface ($E_a = 0.91 \text{ eV}$)¹⁷, over the Cu-MOF-5 ($E_a = 0.79 \text{ eV}$)¹¹ and over the Cu doped graphene ($E_a = 0.50 \text{ eV}$)¹⁴.

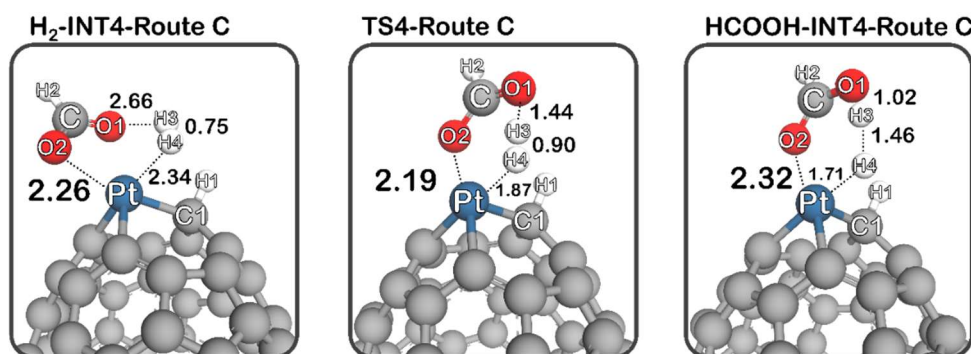


Figure 8. Structural properties of FA production on the Pt/dCNC by using the CO₂ hydrogenation reaction via route C mechanism. Distances are in Å.

From these results, we can suggest that the FA production on Pt/dCNC would be generated through the second hydrogen dissociation on HCOO-Pt/dCNC rather than direct H-transfer from the hydrogenated dCNC surface (H1 atom). When the FA is released, the catalyst component (Pt-H/H-dCNC) is similar to the INT2-Route BS complex, which is suddenly used as a catalytic active site for CO₂ hydrogenation to FA in the next cycle. Our results demonstrated that the rate of FA production is controlled by H₂ amount. At the high H₂ ratio, the FA is accelerate produced via second H₂ dissociation through TS4-Route C transition state requiring activation energy only 0.38 eV. For the next cycle of FA production, the rate-determining step is formate production step via route B2S having activation energy only 0.64 eV, see the catalytic cycle in Figure 2. From our calculated results, the Pt/dCNC is a reactive catalyst for the CO₂ hydrogenation to FA via the proposed reaction pathway.

4. Conclusion

The Pt decorated over defective 4 pentagon carbon nanocone (Pt/dCNC) is a candidate catalytic material for CO₂ transformation to FA. The reaction in CO₂ and H₂ co-adsorption pathway has a high energy barrier of 1.49 eV. Interestingly, we found that the hydrogen dissociation generating metal hydride easily occurs with an energy barrier only 0.09 eV. Therefore, the hydrogen dissociation over Pt/dCNC before the CO₂ hydrogenation are investigated. Our calculations show that the CO₂ hydrogenation in hydrogen dissociation pathway through formate intermediate is more favorable than the carboxylate intermediate. However, the rate-determining step of CO₂ hydrogenation in hydrogen dissociation pathway with formate intermediate requires a high activation energy of 1.15 eV. To reduce such high activation energy of the reaction, the hydrogen dissociation together with hydrogen spillover is considered as alternative reaction pathway. In this new pathway, the dissociated hydrogen is spillover to the carbon surface of dCNC and promotes the CO₂ hydrogenation via the formate intermediate. The insertion of the second hydrogen molecule significantly facilitates the FA formation in this new pathway with a small activation energy of 0.38 eV. Taken together, the Pt/dCNC catalyst is a reactive catalyst for the FA production when the reaction process via the hydrogen dissociation together with hydrogen spillover mechanism.

References

1. Álvarez, A.; Bansode, A.; Urakawa, A.; Bavykina, A. V.; Wezendonk, T. A.; Makkee, M.; Gascon, J.; Kapteijn, F., Challenges in the Greener Production of Formates/Formic Acid, Methanol, and DME by Heterogeneously Catalyzed CO₂ Hydrogenation Processes. *Chemical Reviews* 2017, 117 (14), 9804-9838.
2. Jeong, K.-J.; Miesse, C. M.; Choi, J.-H.; Lee, J.; Han, J.; Yoon, S. P.; Nam, S. W.; Lim, T.-H.; Lee, T. G., Fuel crossover in direct formic acid fuel cells. *Journal of Power Sources* 2007, 168 (1), 119-125.
3. Grasemann, M.; Laurenczy, G., Formic acid as a hydrogen source – recent developments and future trends. *Energy & Environmental Science* 2012, 5 (8), 8171-8181.
4. Mellmann, D.; Sponholz, P.; Junge, H.; Beller, M., Formic acid as a hydrogen storage material – development of homogeneous catalysts for selective hydrogen release. *Chemical Society Reviews* 2016, 45 (14), 3954-3988.
5. Dong, Q.; Yin, T.; Wan, H.; Zhu, G.; Yu, G.; Guo, C., Self-assembly of Pd nanoparticles on anatase titanium dioxide and their application in formic acid fuel cells. *Int J Electrochem Sci* 2016, 11 (1), 804.
6. Hao, C.; Wang, S.; Li, M.; Kang, L.; Ma, X., Hydrogenation of CO₂ to formic acid on supported ruthenium catalysts. *Catalysis Today* 2011, 160 (1), 184-190.
7. Upadhyay, P.; Srivastava, V., Carbon Sequestration: Hydrogenation of CO₂ to Formic Acid. In *Present Environment and Sustainable Development*, 2016; Vol. 10, p 13.
8. Esrafil, M. D.; Sharifi, F.; Dinparast, L., Catalytic hydrogenation of CO₂ over Pt- and Ni-doped graphene: A comparative DFT study. *Journal of Molecular Graphics and Modelling* 2017, 77 (Supplement C), 143-152.

9. Peng, G.; Sibener, S. J.; Schatz, G. C.; Ceyer, S. T.; Mavrikakis, M., CO₂ Hydrogenation to Formic Acid on Ni(111). *The Journal of Physical Chemistry C* 2012, **116** (4), 3001-3006.
10. Wu, S.-Y.; Ho, J.-J., Adsorption, Dissociation, and Hydrogenation of CO₂ on WC(0001) and WC-Co Alloy Surfaces Investigated with Theoretical Calculations. *The Journal of Physical Chemistry C* 2012, **116** (24), 13202-13209.
11. Maihom, T.; Wannakao, S.; Boekfa, B.; Limtrakul, J., Production of Formic Acid via Hydrogenation of CO₂ over a Copper-Alkoxide-Functionalized MOF: A Mechanistic Study. *The Journal of Physical Chemistry C* 2013, **117** (34), 17650-17658.
12. Moret, S.; Dyson, P. J.; Laurenczy, G., Direct synthesis of formic acid from carbon dioxide by hydrogenation in acidic media. *Nature Communications* 2014, **5**, 4017.
13. Nguyen, L. T. M.; Park, H.; Banu, M.; Kim, J. Y.; Youn, D. H.; Magesh, G.; Kim, W. Y.; Lee, J. S., Catalytic CO₂ hydrogenation to formic acid over carbon nanotube-graphene supported PdNi alloy catalysts. *RSC Advances* 2015, **5** (128), 105560-105566.
14. Sirijaraensre, J.; Limtrakul, J., Hydrogenation of CO₂ to formic acid over a Cu-embedded graphene: A DFT study. *Applied Surface Science* 2016, **364** (Supplement C), 241-248.
15. Gassner, F.; Leitner, W., Hydrogenation of carbon dioxide to formic acid using water-soluble rhodium catalysts. *Journal of the Chemical Society, Chemical Communications* 1993, (19), 1465-1466.
16. Chorkendorff, I.; Taylor, P. A.; Rasmussen, P. B., Synthesis and hydrogenation of formate on Cu(100) at high pressures. *Journal of Vacuum Science & Technology A: Vacuum, Surfaces, and Films* 1992, **10** (4), 2277-2281.
17. Fujitani, T.; Choi, Y.; Sano, M.; Kushida, Y.; Nakamura, J., Scanning Tunneling Microscopy Study of Formate Species Synthesized from CO₂ Hydrogenation and Prepared by Adsorption of Formic Acid over Cu(111). *The Journal of Physical Chemistry B* 2000, **104** (6), 1235-1240.
18. Sredojević, D. N.; Šljivančanin, Ž.; Brothers, E. N.; Belić, M. R., Formic Acid Synthesis by CO₂ Hydrogenation over Single-Atom Catalysts Based on Ru and Cu Embedded in Graphene. *ChemistrySelect* 2018, **3** (9), 2631-2637.
19. Thongnuam, W.; Maihom, T.; Choomwattana, S.; Injongkol, Y.; Boekfa, B.; Treesukol, P.; Limtrakul, J., Theoretical study of CO₂ hydrogenation into formic acid on Lewis acid zeolites. *Physical Chemistry Chemical Physics* 2018, **20** (39), 25179-25185.
20. Esrafil, M. D.; Nejadebrahimi, B., Theoretical insights into hydrogenation of CO₂ to formic acid over a single Co atom incorporated nitrogen-doped graphene: A DFT study. *Applied Surface Science* 2019, **475**, 363-371.
21. Melchionna, M.; Bracamonte, M. V.; Giuliani, A.; Nasi, L.; Montini, T.; Tavagnacco, C.; Bonchio, M.; Fornasiero, P.; Prato, M., Pd@TiO₂/ carbon nanohorn electrocatalysts: reversible CO₂ hydrogenation to formic acid. *Energy & Environmental Science* 2018, **11** (6), 1571-1580.
22. Esrafil, M. D.; Dinparast, L., A DFT study on the catalytic hydrogenation of CO₂ to formic acid over Ti-doped graphene nanoflake. *Chemical Physics Letters* 2017, **682**, 49-54.
23. Szyja, B. M.; Smykowski, D.; Szczygieł, J.; Hensen, E. J. M.; Pidko, E. A., A DFT Study of CO₂ Hydrogenation on Faujasite-Supported Ir₄ Clusters: on the Role of Water for Selectivity Control. *ChemCatChem* 2016, **8** (15), 2500-2507.

24. Motokura, K.; Kashiwame, D.; Miyaji, A.; Baba, T., Copper-Catalyzed Formic Acid Synthesis from CO₂ with Hydrosilanes and H₂O. *Organic Letters* 2012, 14 (10), 2642-2645.
25. Vesselli, E.; Rogatis, L. D.; Ding, X.; Baraldi, A.; Savio, L.; Vattuone, L.; Rocca, M.; Fornasiero, P.; Peressi, M.; Baldereschi, A.; Rosei, R.; Comelli, G., Carbon Dioxide Hydrogenation on Ni(110). *Journal of the American Chemical Society* 2008, 130 (34), 11417-11422.
26. Karousis, N.; Suarez-Martinez, I.; Ewels, C. P.; Tagmatarchis, N., Structure, properties, functionalization, and applications of carbon nanohorns. *Chemical reviews* 2016, 116 (8), 4850-4883.
27. Harris, P. J.; Tsang, S. C.; Claridge, J. B.; Green, M. L., High-resolution electron microscopy studies of a microporous carbon produced by arc-evaporation. *Journal of the Chemical Society, Faraday Transactions* 1994, 90 (18), 2799-2802.
28. Hiralal, P.; Wang, H.; Unalan, H. E.; Liu, Y.; Rouvala, M.; Wei, D.; Andrew, P.; Amaratunga, G. A., Enhanced supercapacitors from hierarchical carbon nanotube and nanohorn architectures. *Journal of Materials Chemistry* 2011, 21 (44), 17810-17815.
29. Xu, J.; Yudasaka, M.; Kouraba, S.; Sekido, M.; Yamamoto, Y.; Iijima, S., Single wall carbon nanohorn as a drug carrier for controlled release. *Chemical Physics Letters* 2008, 461 (4-6), 189-192.
30. Ajima, K.; Yudasaka, M.; Murakami, T.; Maigné, A.; Shiba, K.; Iijima, S., Carbon nanohorns as anticancer drug carriers. *Molecular pharmaceutics* 2005, 2 (6), 475-480.
31. Yuge, R.; Tamura, N.; Manako, T.; Nakano, K.; Nakahara, K., High-rate charge/discharge properties of Li-ion battery using carbon-coated composites of graphites, vapor grown carbon fibers, and carbon nanohorns. *Journal of Power Sources* 2014, 266, 471-474.
32. Wen, D.; Deng, L.; Zhou, M.; Guo, S.; Shang, L.; Xu, G.; Dong, S., A biofuel cell with a single-walled carbon nanohorn-based bioanode operating at physiological condition. *Biosensors and Bioelectronics* 2010, 25 (6), 1544-1547.
33. Liu, Y.; Brown, C. M.; Neumann, D. A.; Geohegan, D. B.; Paretzky, A. A.; Rouleau, C. M.; Hu, H.; Styers-Barnett, D.; Krasnov, P. O.; Yakobson, B. I., Metal-assisted hydrogen storage on Pt-decorated single-walled carbon nanohorns. *Carbon* 2012, 50 (13), 4953-4964.
34. Yodsin, N.; Rungnim, C.; Promarak, V.; Namuangruk, S.; Kungwan, N.; Rattanawan, R.; Jungsuttiwong, S., Influence of hydrogen spillover on Pt-decorated carbon nanocones for enhancing hydrogen storage capacity: A DFT mechanistic study. *Physical Chemistry Chemical Physics* 2018, 20 (32), 21194-21203.
35. Lodermeier, F.; Costa, R. D.; Casillas, R.; Kohler, F. T.; Wasserscheid, P.; Prato, M.; Guldi, D. M., Carbon nanohorn-based electrolyte for dye-sensitized solar cells. *Energy & Environmental Science* 2015, 8 (1), 241-246.
36. Yamaguchi, T.; Bandow, S.; Iijima, S., Synthesis of carbon nanohorn particles by simple pulsed arc discharge ignited between pre-heated carbon rods. *Chemical physics letters* 2004, 389 (1-3), 181-185.
37. Chorkendorff, I.; Taylor, P.; Rasmussen, P., Synthesis and hydrogenation of formate on Cu (100) at high pressures. *Journal of Vacuum Science & Technology A: Vacuum, Surfaces, and Films* 1992, 10 (4), 2277-2281.

38. Rasmussen, P.; Holmblad, P.; Askgaard, T.; Ovesen, C.; Stoltze, P.; Nørskov, J.; Chorkendorff, I., Methanol synthesis on Cu (100) from a binary gas mixture of CO₂ and H₂. *Catalysis Letters* 1994, 26 (3-4), 373-381.
39. Fujitani, T.; Choi, Y.; Sano, M.; Kushida, Y.; Nakamura, J., Scanning tunneling microscopy study of formate species synthesized from CO₂ hydrogenation and prepared by adsorption of formic acid over Cu (111). *The Journal of Physical Chemistry B* 2000, 104 (6), 1235-1240.
40. Gokhale, A. A.; Dumesic, J. A.; Mavrikakis, M., On the Mechanism of Low-Temperature Water Gas Shift Reaction on Copper. *Journal of the American Chemical Society* 2008, 130 (4), 1402-1414.
41. Rasmussen, P. B.; Holmblad, P. M.; Askgaard, T.; Ovesen, C. V.; Stoltze, P.; Nørskov, J. K.; Chorkendorff, I., Methanol synthesis on Cu(100) from a binary gas mixture of CO₂ and H₂. *Catalysis Letters* 1994, 26 (3), 373-381.
42. Grabow, L. C.; Gokhale, A. A.; Evans, S. T.; Dumesic, J. A.; Mavrikakis, M., Mechanism of the Water Gas Shift Reaction on Pt: First Principles, Experiments, and Microkinetic Modeling. *The Journal of Physical Chemistry C* 2008, 112 (12), 4608-4617.
43. Zhu, C.; Liu, D.; Chen, Z.; Li, L.; You, T., Superior catalytic activity of Pt/carbon nanohorns nanocomposites toward methanol and formic acid oxidation reactions. *Journal of Colloid and Interface Science* 2018, 511, 77-83.
44. Vosko, S. H.; Wilk, L.; Nusair, M., Accurate spin-dependent electron liquid correlation energies for local spin density calculations: a critical analysis. *Canadian Journal of physics* 1980, 58 (8), 1200-1211.
45. Becke, A. D., Density-functional exchange-energy approximation with correct asymptotic behavior. *Physical Review A* 1988, 38 (6), 3098-3100.
46. Lee, C.; Yang, W.; Parr, R. G., Development of the Colle-Salvetti correlation-energy formula into a functional of the electron density. *Physical review B* 1988, 37 (2), 785.
47. Grimme, S.; Antony, J.; Ehrlich, S.; Krieg, H., A consistent and accurate ab initio parametrization of density functional dispersion correction (DFT-D) for the 94 elements H-Pu. *The Journal of chemical physics* 2010, 132 (15), 154104.
48. Rungnim, C.; Faungnawakij, K.; Sano, N.; Kungwan, N.; Namuangruk, S., Hydrogen storage performance of platinum supported carbon nanohorns: A DFT study of reaction mechanisms, thermodynamics, and kinetics. *International Journal of Hydrogen Energy* 2018, 43 (52), 23336-23345.
49. Kittel, C., *Introduction to Solid State Physics*. Wiley: 2004.
50. Tawfik, S. A.; Cui, X. Y.; Ringer, S. P.; Stampfl, C., Multiple CO₂ capture in stable metal-doped graphene: a theoretical trend study. *RSC Advances* 2015, 5 (63), 50975-50982.
51. Vesselli, E.; Rizzi, M.; De Rogatis, L.; Ding, X.; Baraldi, A.; Comelli, G.; Savio, L.; Vattuone, L.; Rocca, M.; Fornasiero, P.; Baldereschi, A.; Peressi, M., Hydrogen-Assisted Transformation of CO₂ on Nickel: The Role of Formate and Carbon Monoxide. *The Journal of Physical Chemistry Letters* 2010, 1 (1), 402-406.
52. Chan, B.; Radom, L., Zeolite-Catalyzed Hydrogenation of Carbon Dioxide and Ethene. *Journal of the American Chemical Society* 2008, 130 (30), 9790-9799.

3.3 Doped-Carbon Nanohorns catalysts for efficient electrosynthesis of H_2O_2 from O_2 reduction

Pongkarn Chakthranont^{*1}, Sakvarit Nitrathorn¹, Sutarat Thongratkaew¹, Pongtanawat Khemthong¹, Kajornsak Faungenawakij¹, Noriaki Sano²

¹ National Nanotechnology Center (NANOTEC), National Science and Technology Development Agency, Pathum Thani, Thailand

² Department of Chemical Engineering, Kyoto University, Kyoto, 615-8510, Japan

Abstract

Hydrogen peroxide (H_2O_2) is one of the most important oxidizing agents utilized worldwide in many industrial applications. The complexity of the anthraquinone process, which is the current method of industrial H_2O_2 production, and the instability of H_2O_2 limit the use of this chemical in remote areas. An electrosynthesis process is a promising method for decentralized production of H_2O_2 , enabling on-site generation from the two-electron reduction reaction of O_2 . To achieve an economically-viable process, an active, stable, scalable, and selective electrocatalyst is required. Carbon-based catalysts are promising for this reaction due to their high selectivity, low cost, and highly tunable surface properties. Among the reported carbon-based catalysts, carbon nanohorns (CNH) catalyst exhibits superior selectivity and activity, as well as exceptional stability in wide range of pH. While the chemical modification seems to play an important role in enhancing the selectivity, the effects of O and N dopants in CNH catalysts are not well understood. Herein, we present a highly active and selective catalyst for O_2 reduction reaction (ORR) to H_2O_2 based on CNH, synthesized by gas-injected arc-in-water (GI-AIW) method. The effects of O and N dopants by chemical modifications of CNH are investigated. Using x-ray photoelectron spectroscopy (XPS) and Near-edge x-ray absorption fine structure (NEXAFS), the dopant species were identified, shedding insights onto the active sites for H_2O_2 production on CNH catalysts.

Keywords: Hydrogen Peroxide, Oxygen reduction reaction, Carbon Nanohorns, Surface modification, Electrosynthesis

Introduction

Hydrogen peroxide (H_2O_2) is one of the most important chemicals produced worldwide with a global market of 4.5 million metric tons per year in 2014.¹ H_2O_2 is a strong oxidizing agent and is employed as an oxidizer or a bleaching agent in many industrial applications such as pulp paper mill, textiles, pharmaceutical manufacturing and healthcare, paint and polymer production, and semiconductors. The current method for production of H_2O_2 is the anthraquinone process, which is highly energy-consuming and limited to large-scale facilities. The complexity of the anthraquinone process and the instability of H_2O_2 limit the use of H_2O_2 in remote areas. Hence, there is an increasing interest in a small-scale decentralized production process of H_2O_2 .²

One promising method for decentralized H₂O₂ production is an electrochemical reduction process in which H₂O₂ can be generated on-site from the two-electron reduction reaction of O₂ (eq. 1). In order to lower the energy intensity of the system, an active, stable, and scalable electrocatalyst that is also selective towards two-electron reduction over a four-electron reduction product (eq. 2) is required.³



The reaction for H₂O₂ production is an intermediate reaction step of the four-electron transfer process. The sole reaction intermediate of the H₂O₂ production is *OOH species, which can be oxidized further to form *O and *OH intermediates for the four-electron transfer process. It was theoretically postulated that the *OOH preferentially binds to a top site of a Pt atom, while *O would bind to a hollow site between two Pt atoms. This idea was experimentally confirmed with a PtHg₄ material, in which Pt atoms are physically isolated by inert Hg atoms, making it less favorable for *O to form. As a result, the catalyst exhibited the highest selectivity of 96% at 50 mV overpotential.⁴ Several other catalysts such as Pt-Au, Pt-Sn, and Ag₃Pt were designed using a similar concept and demonstrated good activity and selectivity for H₂O₂ production. However, all of the high performing catalysts contain noble metals, which is less industrially scalable from a cost perspective.

Another class of material that is promising for electrochemical H₂O₂ production from O₂ is carbon-based catalysts, especially those with mesoporous structures and doped with N or O.^{5–9} For example, commercial carbon black and carbon cloths have been reported previously to have moderate activity and selectivity for the electrochemical reduction reaction of O₂ to H₂O₂.^{6,10} Recently, Chen et al. investigated the effects of the pore size of the carbon catalysts and found that mesoporous carbon showed higher activity compared to the microporous carbon catalyst. They suspected that higher activity was potentially caused by better mass transport of the reactant and the product in a bigger pore size. Interestingly, both micro and mesoporous carbon exhibit highest activity in strong alkaline electrolyte but require over 400 mV higher overpotential to drive the same rate of reaction in acidic conditions. Additionally, the activity of the carbon catalyst is governed by the nature of its defects and so far quaternary nitrogen, pyrrolic nitrogen, vacancy or edge sites, and the surface oxygen-containing functional groups were identified as promising candidates.⁷ N-doped mesoporous carbon exhibits high selectivity and moderate activity.⁸ It was also demonstrated that the activity of carbon nanotubes increases drastically with the amount of oxidized sites.⁹ Recently, N-doped carbon nanohorn catalyst was shown to have comparable activity and selectivity to noble metal catalysts. However, the H₂O₂ production was deactivated after 5 hours of continuous production.¹¹

Despite the promising selectivity and scalability nature of doped-mesoporous carbon, the activity of this class of catalyst remains subpar to that of noble metal catalysts. Designing a highly active catalyst requires that the effects of morphology and dopant on catalytic performance are well understood. Herein, we present highly active and selective H₂O₂ production catalysts based

on carbon nanohorns. The effects of O and N contents in the catalysts have been investigated. We found that the presence of moderate amount of N content results in high selectivity towards 2-electron reduction, while high N content lead to 4-electron pathway. On the other hand, O content introduced by oxidation increases the surface area and onset of ORR drastically, making it suitable to be used in a H_2O_2 generation device.

Experimental Methods

CNH Catalyst Preparation

Carbon nanohorns (CNH) were synthesized using the gas-injected arc-in-water (GI-AIW) method. As shown in Figure 1 a set of graphite anode and cathode was submerged in de-ionized water contained in a beaker. Direct electrical current of 80 amperes was supplied from a power source for generating arc discharge between both electrodes. The anode was moved toward the inner surface of the cathode hole by a step motor with a speed of 5.25 mm/s. A graphite rod with a diameter of 6 mm and a length of 75 mm (99.9995% purity) was used as anodes. A graphite rod with a diameter of 20 mm and a length of 55 mm was used as a cathode. Typically, CNH samples were synthesized in a N_2 environment. However, to avoid the introduction of N dopant, Ar gas were employed instead of N_2 , resulting in a N-free CNH sample, denoted CNH(Ar). The synthesized products were collected after being dried in an oven set at 90 °C overnight.

Oxygen-doped CNH catalyst (O-CNH), O-CNH, was synthesized by immersing a mixture of CNH and KOH with 1:4 weight ratio in water for 8 hours. The mixture was dried in an oven at 80 °C overnight, followed by heating in air with a heating rate of 3 °C/min ramp and hold at 600 °C for 1 hour. The catalyst was washed and dried again at 90 °C overnight.

Nitrogen-doped CNH catalyst (N-CNH), was synthesized by immersing a mixture of CNH and melamine with 1:6 weight ratio in 80% ethanol-water for 5 hours. The mixture was dried in an oven at 105 °C overnight, followed by heating in N_2 atmosphere using a ramp rate of 10 °C/min ramp and hold at the 850 °C for 2 hours.

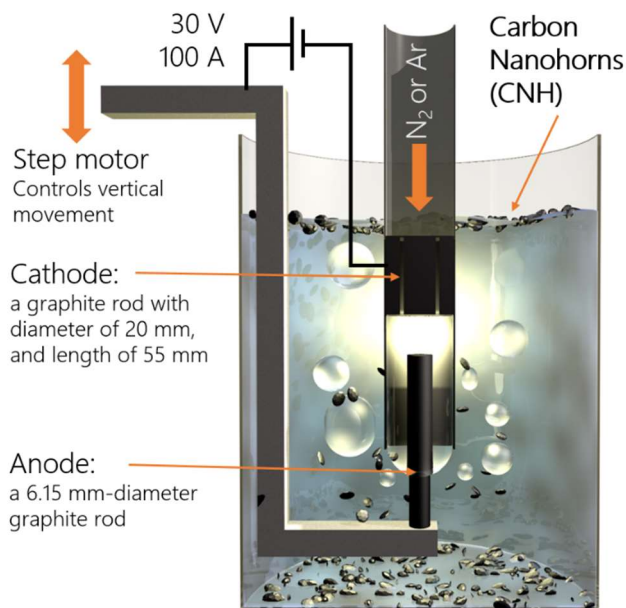


Figure 1. Gas-injected arc-in-water (GI-AIW) method for CNH synthesis.

Characterizations

Crystallographic identification of each typical catalyst was performed by X-ray diffractometry (XRD, Bruker, D8 advance) using CuK α radiation operated at 40 kV and 100 mA with a scanning step of 0.03°/min in a range of 10–80°. Samples were prepared using Si low background as a sample holder. Raman microscope spectroscopy (HORIBA Scientific/LabRAM HR Revolution) was used to determine ID/IG ratio of catalysts. Morphology of each catalyst sample were investigated by transmission electron microscope (TEM, JEOL, JEM-2100Plus). BET surface area of each carbonaceous support material and catalyst samples was characterized by N₂ sorption. Surface areas were determined by Brunauer-Emmett-Teller (BET) method using Nova 2000e physisorption analyzer at liquid nitrogen temperature.

The chemical compositions of catalysts were analyzed by X-ray photoelectron spectroscopy (XPS) on a SHIMADZU KRATOS/AXIS SUPRA. C1s, O1s, and N1s spectra were collected for all carbon nanohorns samples. CasaXPS software was used for interpretation and the C1s peak was calibrated to be 284.8 eV. The near edge X-ray absorption fine structure (NEXAFS) spectroscopy was measured at BL3.2 of the Synchrotron Light Research Institute (SLRI), Thailand. The K-edge NEXAFS spectra of carbon, oxygen and nitrogen were obtained using energy resolution of 0.5 eV (FWHM) in the total electron yield mode.¹² The spectra were normalized using the clean Si(100) and were calibrated to their peak position by HOPG program.

Electrochemical Testing

Glassy carbon disks (geometrical surface area of 0.196 cm², single-side polished, Sigradur G HTW Hochttemperatur-Werkstoffe GmbH) were cleaned by sonication in acetone, isopropanol, and water for an hour each. Catalyst inks were prepared by mixing 5 mg of the CNH catalyst, 980 μ L of 200 proof ethanol, and 20 μ L of 5 wt% Nafion solution. The mixture was dispersed by

sonication for 1 hour. 10 μL of the ink solution was added to the 5 mm diameter glassy carbon disk and spin-dried at 300 rpm for at least 1 hour.

All electrochemical experiments were operated at ambient temperature and pressure and the measurements were conducted using PARSTAT MC multichannel potentiostat (PMC1000). The electrochemical O_2 reduction reaction (ORR) activity of each catalyst was measured using a rotating ring-disk electrode (RRDE) setup (Princeton Applied Research), which is a 4-electrode electrochemical system consisting of a carbon disk working electrode, a platinum ring working electrode, a platinum wire counter electrode, and a Ag/AgCl reference electrode. The ORR was performed in 0.1M KOH (99.99%, Sigma-Aldrich), which was continuously purged with 99.99% O_2 gas with a flow rate of 50 mL/min. The RRDE experiment was carried out by scanning the disk potential from 0.2 V and 1.1 V vs. the reversible hydrogen electrode (RHE) at 10 mV/s while holding the Pt ring at 1.2 V vs. RHE to oxidize H_2O_2 formed on the disk electrode. The rotating speed of the RRDE was 1600 rpm. The background capacitance was collected in a similar manner in an Ar (99.995%) saturated electrolyte. All potentials are reported with respect to RHE scale, calculated by the following equation:

$$E_{\text{RHE}} = E_{\text{Ag/AgCl}} + 0.0591 \times \text{pH} + 0.197 \text{ V}$$

The system's ring collection efficiency was determined using the reversible $[\text{Fe}(\text{CN})_6]^{4-}/3-$ redox couple. RRDE measurement using Pt disk and Pt ring was performed in 10 mM of $\text{K}_4\text{Fe}(\text{CN})_6$ in 0.1 M KOH at varying rotating speed (400, 900, 1600, 2500, 3600 rpm). The selectivity of H_2O_2 can be calculated as follow:

$$\text{H}_2\text{O}_2(\%) = 200 \frac{\frac{I_{\text{R}}}{N}}{I_{\text{D}} + \frac{I_{\text{R}}}{N}}$$

Where I_{R} is the ring current, I_{D} is the disk current, and N is the ring collection efficiency, which was found to be 25.38% in our experiment.

The ORR activity was measured by subtracting the current density of the catalyst measured in O_2 -purged electrolyte by current density measured in Ar-purged electrolyte. The CV was corrected for 100% ohmic loss, determined by potentiostatic impedance spectroscopy at the open circuit potential. Lastly the electrochemical active surface area (ECSA) was assessed by CV scans between -0.2 to 0.2 V vs. Ag/AgCl at varying scan rate (5, 10, 25, 50, 100 mV/s) in an Ar-purged electrolyte.

Result and Discussion

XRD patterns in Figure 2a demonstrate that all CNHs catalysts exhibit a characteristic peak at 2θ of 26.8 degree, representing the graphitic structure. The ratios between the area of D and G bands from Raman spectra in Figure 2b indicate the level of defects in the carbon materials. CNH and O-CNH appear to contain higher levels of defects compared to the N-CNH and CNH(Ar), implying higher degrees of broken sp^2 bonds due to the effects of dopants or vacancies. TEM images in Figure 3 show that the structure of pristine and doped CNH catalysts similar. The

nanohorn clusters with around 5 nm diameter and 20 nm in length can be easily observed in all samples, with an exception of O-CNH. In O-CNH, the nanohorns seem to be slightly collapsing, likely due to the microporous defects introduced by the oxidation process.

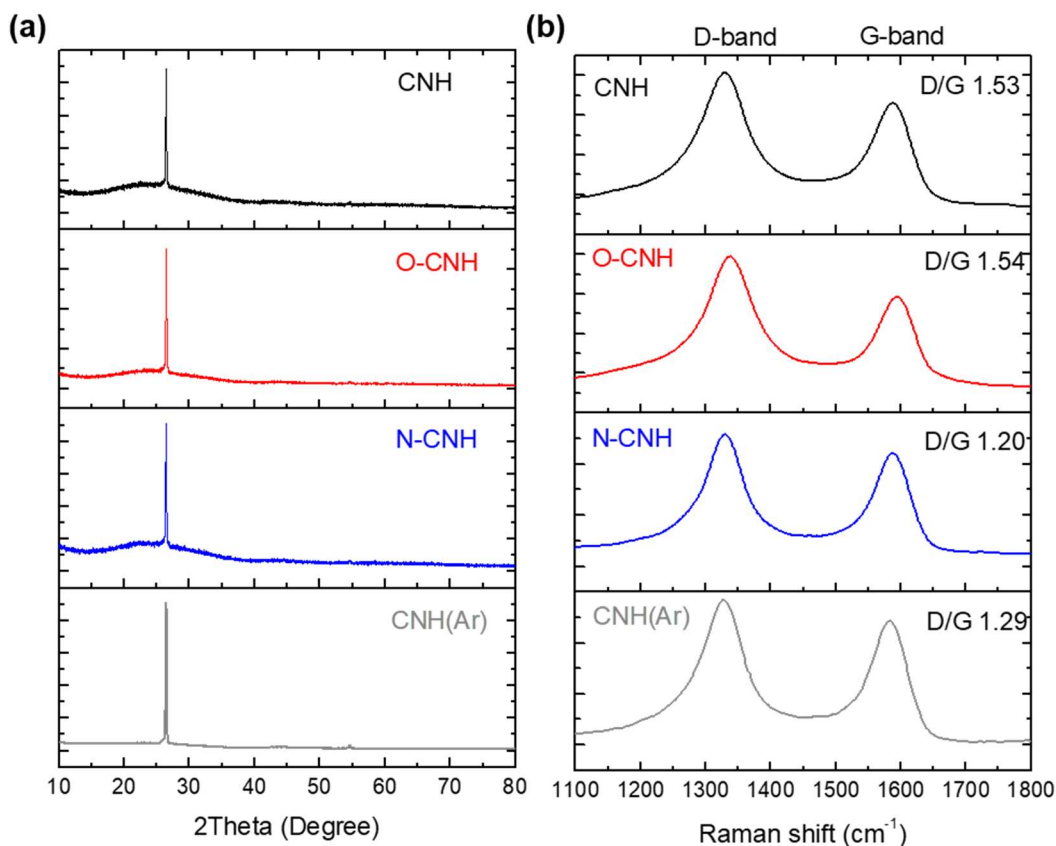


Figure 2. (a) X-ray diffraction patterns and (b) Raman spectra of all CNH catalysts

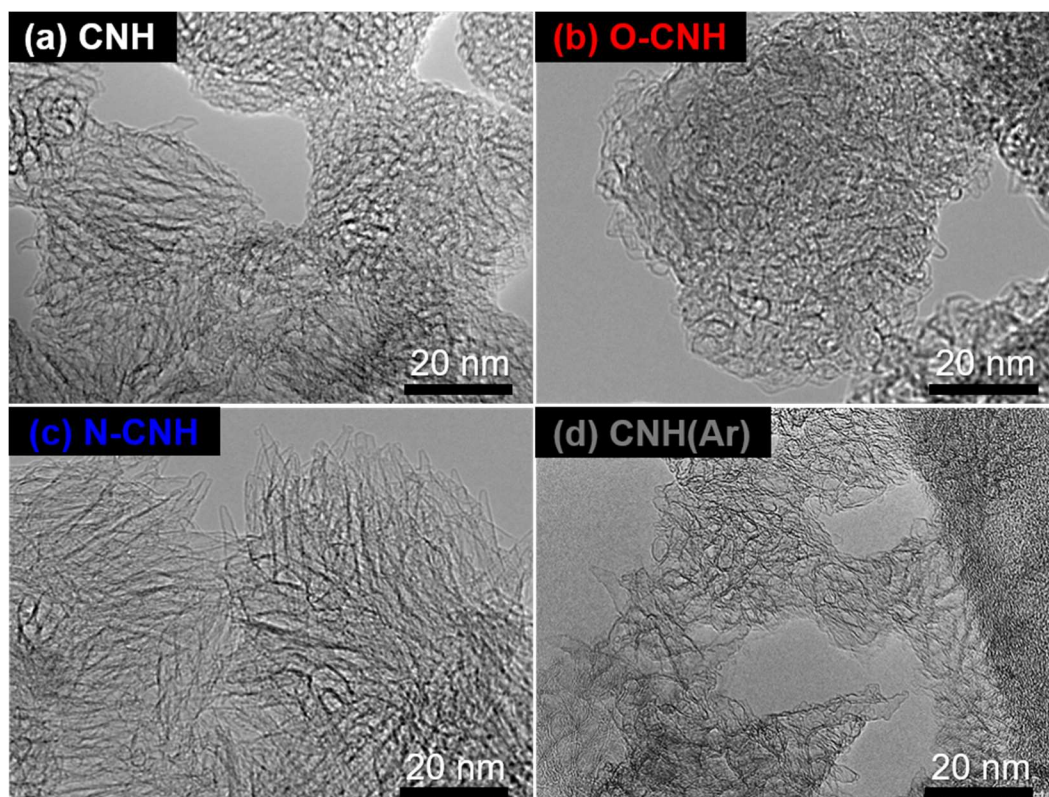


Figure 3. TEM images of CNHs with various surface treatments.

BET analysis of the CNH catalysts (Table 1) show that the as-prepared CNH in both N_2 and Ar were mesoporous in nature with surface area of 303 and 385 m^2/g respectively. The doping processes significantly increased the surface area of CNH. O-CNH exhibited microporous structure, likely due to the micro-windows opening on the side of the nanohorns, resulting in the BET surface area as high as 872 m^2/g . On the contrary, most of the pore sizes in N-CNH remained in the mesoporous range but the surface area was increased up to 469 m^2/g .

Table 1. BET measurement of CNH catalysts

Catalysts	Surface area (m^2/g)	Pore volume (cc/g)	Pore size (nm)
CNH	303	1.11	19.7
O-CNH	872	0.281	3.67
N-CNH	469	0.963	17.4
CNHs(Ar)	385	1.61	17.1

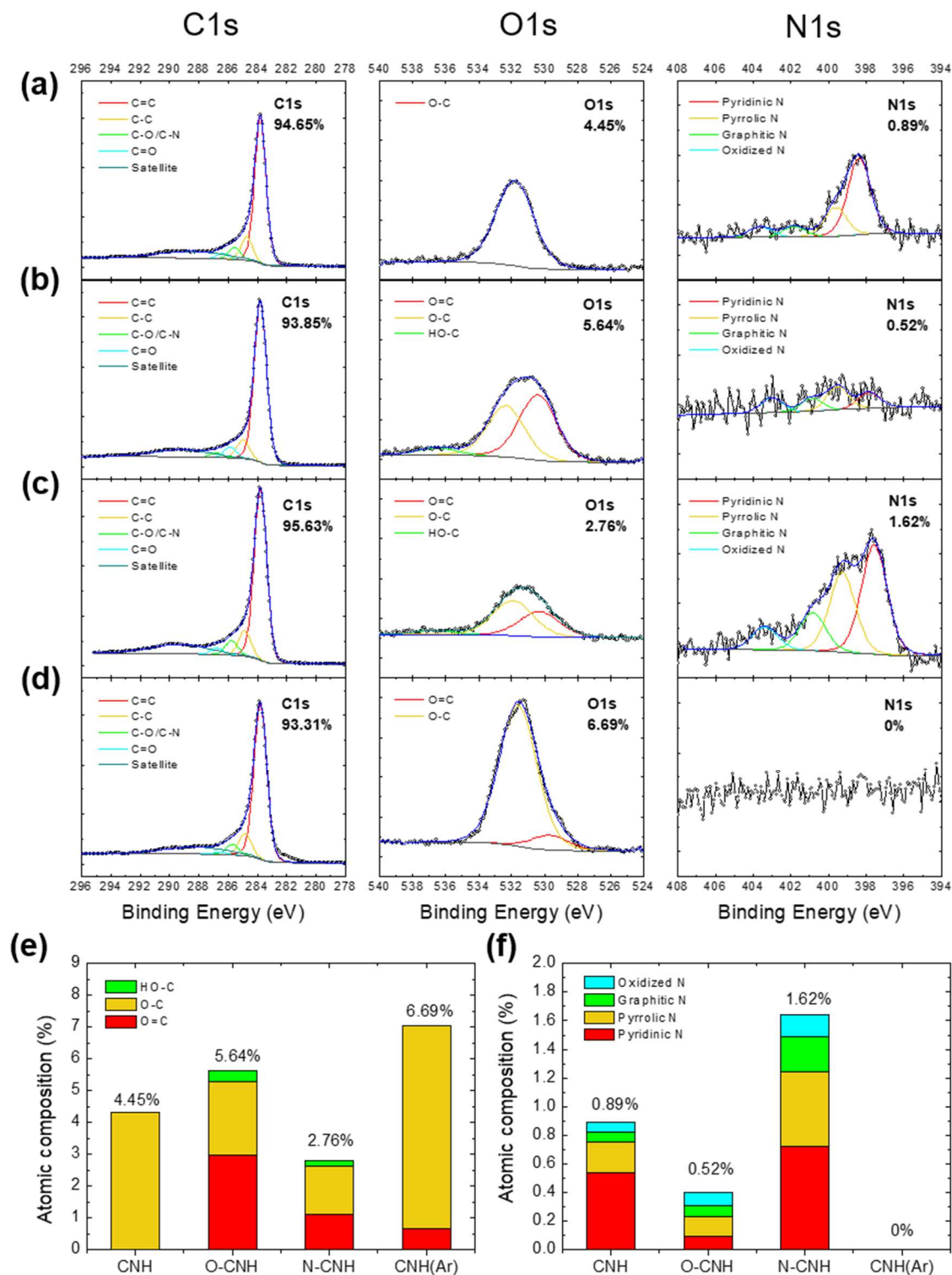


Figure 4. XPS spectra of C1s (left column), O1s (middle column), and N1s (right column) of (a) CNH, (b) O-CNH, (c) N-CNH, and (d) CNH(Ar). Atomic composition of (e) O1s species and (f) N1s species.

XPS spectra of the CNH prepared in N_2 atmosphere contained both O and N contents (Figure 4a), while no N1s was detected in CNH(Ar) sample (Figure 4d). These results confirm that N can be introduced into the structure of CNH during GI-AW synthesis process. Oxidation process of CNH introduce C=O into the structure and oxidized off some of the N dopants. N-CNH exhibit higher N1s content.

The characteristic peaks of C K-edge (Figure 5a) are mainly including unoccupied π^* and excited σ^* states. The fingerprint region from 282 - 290 eV is the π^* resonance that is due to electronic excitation from the C 1s level to the unoccupied orbital or conduction π^* states. A sharp excitonic transition $1s \rightarrow \sigma^*$ was also observed at the range between 290.5 - 294.5 eV which is assigned to the correlation effects of electron-hole pairs within the nanostructures. This is followed by broad transitions of mixed symmetry peaking at 297 - 310 eV. The difference between those spectra appears at 286-290 eV where an increase in the intensity of the absorption signal for CNHs is observed. The O K-edge NEXAFS (Figure 5b) confirm the existence of oxygen-containing functional groups in samples. Upon treatment with oxygen gas, the NEXAFS of O-CNHs provide a broad peak of $1s \rightarrow \pi^*$ transition, indicating the fruitful of carboxylic)530 eV(and quinone)531 eV(groups. However, the charge transfer peak between C and O from C=O and C-O was diminishing after treating with oxygen or nitrogen gasses. More importantly, NEXAFS N K-edge spectra (Figure 5c) of all samples are totally differences. The sample treated with Ar was not shown a characteristic peak of N species. It is very evident that the atmosphere plays an important role on the species of nitrogen incorporate in the CNHs.

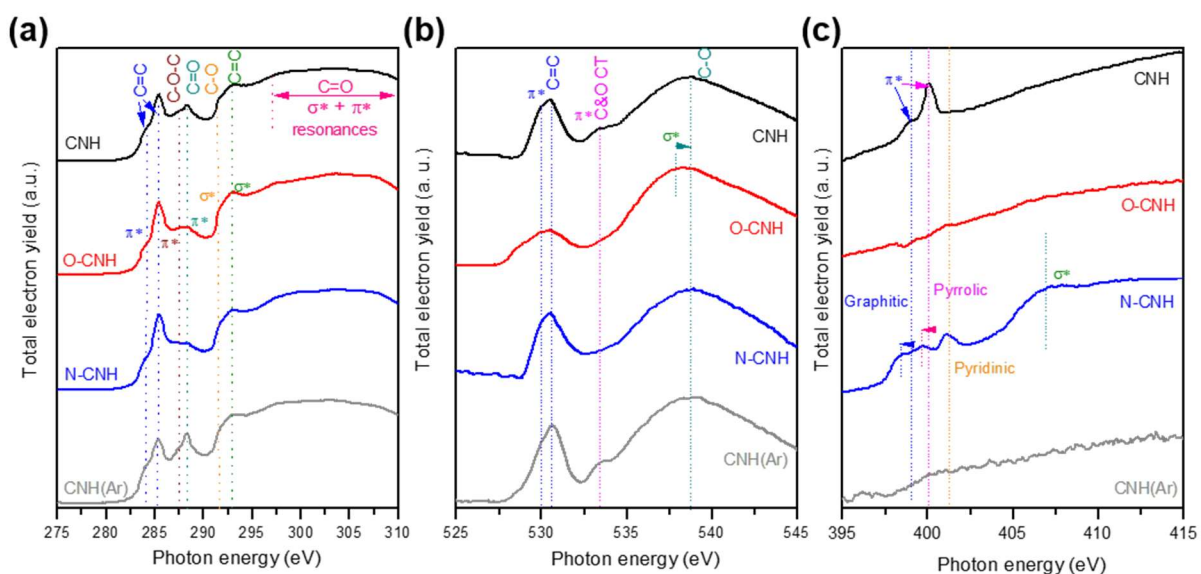


Figure 5. Normalized (a) C K-edge, (b) O K-edge, and (c) N K-edge NEXAFS spectra of all CNH catalysts.

Electrochemical measurements from the RRDE show that the CNHs catalyst and its derivatives are highly active for the ORR. Doping with O and N can drastically improve the current onset)at -0.1 mA/cm²(from 0.75 V vs. RHE to 0.81 and 0.83 for O-CNH and N-CNH respectively

) Figure 6a(. However, doping reduces the selectivity of CNH catalyst towards H_2O_2 . At 0.5 V vs. RHE, the selectivity towards H_2O_2 of CNH, O-CNH, N-CNH, and CNHs(Ar) are 88.06%, 85.03%, 54.43%, and 83.52% respectively) Figure 6b(.

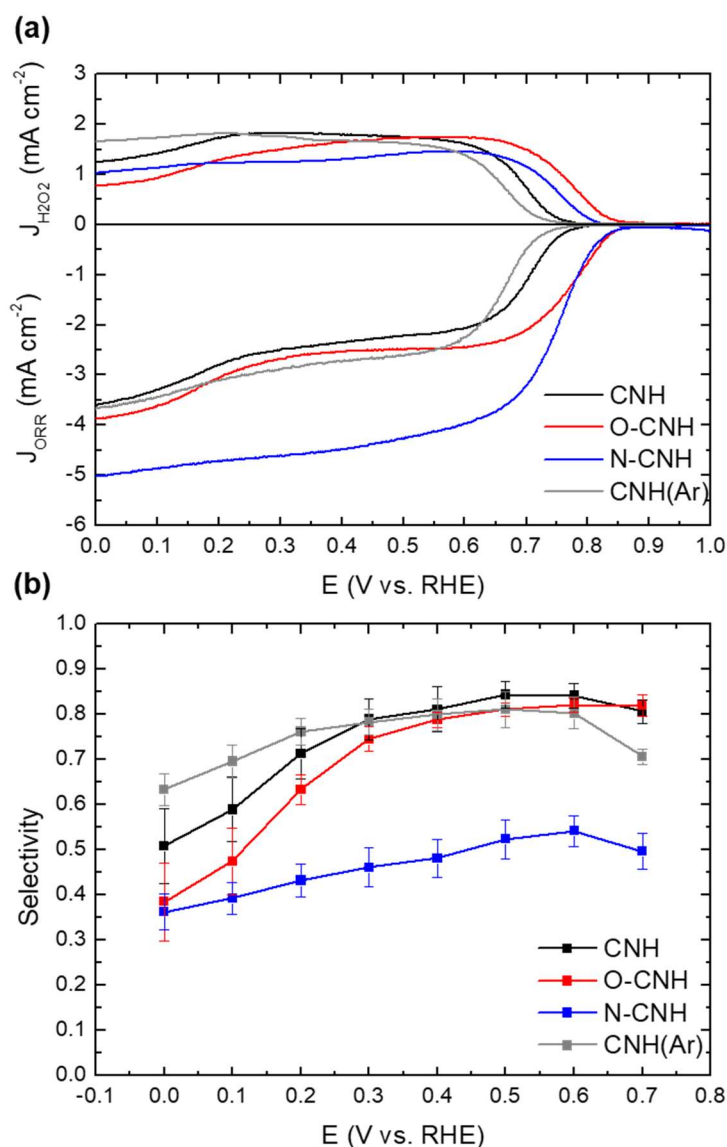


Figure 6. ORR activities of CNH catalysts; (a) current density of H_2O_2 production (anodic current) and current density of overall oxygen reduction (cathodic current), (b) selectivity towards H_2O_2 production at varying potentials.

References

- [1] R. Ciriminna, L. Albanese, F. Meneguzzo, M. Pagliaro, Hydrogen Peroxide: A Key Chemical for Today's Sustainable Development. *ChemSusChem* **2016**, 9, 3374–3381.
- [2] Z. Chen, S. Chen, S. Siahrostami, P. Chakthranont, C. Hahn, D. Nordlund, S. Dimosthenis, J. K. Nørskov, Z. Bao, T. F. Jaramillo, J. K. Nørskov, Z. Bao, T. F. Jaramillo, *React. Chem. Eng.* **2017**, 2, 239.
- [3] S. H. Vijapur, T. D. Hall, S. Snyder, M. Inman, E. J. Taylor, B. Skinn, *ECS Trans.* **2017**, 77, 947.
- [4] S. Siahrostami, A. Verdaguer-Casadevall, M. Karamad, D. Deiana, P. Malacrida, B. Wickman, M. Escudero-Escribano, E. A. Paoli, R. Frydendal, T. W. Hansen, I. Chorkendorff, I. E. L. Stephens, J. Rossmeisl, *Nat. Mater.* **2013**, 12, 1137.
- [5] J. F. Pérez, C. Saez, J. Llanos, P. Cañizares, C. López, M. A. Rodrigo, *Ind. Eng. Chem. Res.* **2017**, acs. iecr.7b02563.
- [6] M. A. Abdel Rahim, M. W. Khalil, M. A. Sultan, *Int. J. Electrochem. Sci.* **2017**, 12, 7890.
- [7] S. Chen, Z. Chen, S. Siahrostami, T. R. Kim, D. Nordlund, D. Sokaras, S. Nowak, J. W. F. To, D. Higgins, R. Sinclair, J. K. Nørskov, T. F. Jaramillo, Z. Bao, *ACS Sustain. Chem. Eng.* **2018**, 6, 311.
- [8] T. P. Feller, F. Hasché, P. Strasser, M. Antonietti, *J. Am. Chem. Soc.* **2012**, 134, 4072.
- [9] Z. Lu, G. Chen, S. Siahrostami, Z. Chen, K. Liu, J. Xie, L. Liao, T. Wu, D. Lin, Y. Liu, T. F. Jaramillo, J. K. Nørskov, Y. Cui, *Nat. Catal.* **2018**, 1, 156.
- [10] J. F. Pérez, A. Galia, M. A. Rodrigo, J. Llanos, S. Sabatino, C. Sáez, B. Schiavo, O. Scialdone, *Electrochim. Acta* **2017**, 248, 169.
- [11] D. Iglesias, A. Giuliani, M. Melchionna, S. Marchesan, A. Criado, L. Nasi, M. Bevilacqua, C. Tavagnacco, F. Vizza, M. Prato, P. Fornasiero, *Chem* **2018**, 4, 106.
- [12] H. Akasaka, S. Tunmee, U. Rittihong, M. Tomidokoro, C. Euaruksakul, S. Norizuki, R. Supruangnet, H. Nakajima, Y. Hirata, N. Ohtake, *Diam. Relat. Mater.* **2020**, 101, 107609.

4. Outputs

4.1 Publication

- Yodsin, N.; Rungnim, C.; Promarak, V.; Namuangruk, S.; Kungwan, N.; Rattanawan, R.; Jungsuttiwong, S. Influence of Hydrogen Spillover on Pt-Decorated Carbon Nanocones for Enhancing Hydrogen Storage Capacity: A DFT Mechanistic Study. *Phys. Chem. Chem. Phys.* **2018**, 20 (32), 21194–21203. <https://doi.org/10.1039/C8CP02976H>.
- Yodsin, N.; Rungnim, C.; Tungkamani, S.; Promarak, V.; Namuangruk, S.; Jungsuttiwong, S. DFT Study of Catalytic CO₂ Hydrogenation over Pt-Decorated Carbon Nanocones: H₂ Dissociation Combined with the Spillover Mechanism. *J. Phys. Chem. C* **2020**, 124 (3), 1941–1949. <https://doi.org/10.1021/acs.jpcc.9b08776>.
- Butburee, T.; Chakthranont, P.; Phawa, C.; Faungnawakij, K. Beyond Artificial Photosynthesis: Prospects on Photobiorefinery. *ChemCatChem* **2020**, cctc.201901856. <https://doi.org/10.1002/cctc.201901856>.

4.2 Conference and Forum

- **Japan–Thailand Joint Seminar under JASTIP Program 2019, NSTDA, 3rd September 2019**
Innovations in Biomass Application for Catalytic Material Synthesis and Energy Devices
- **Japan–Thailand Joint Seminar under JASTIP Program 2019, Kyoto University, 12th November 2019**

4.3 Book

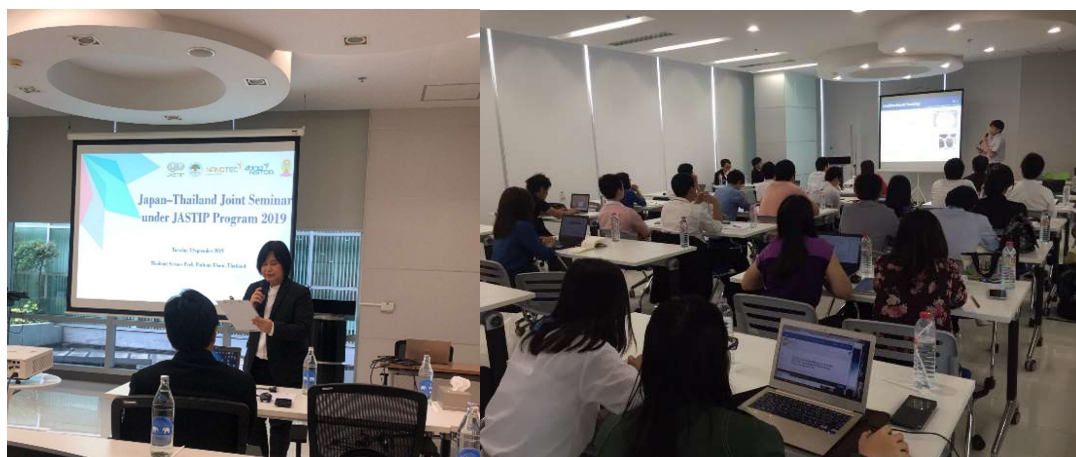
- P. Chakthranont, “Ch. 7 Photoelectrochemical Processes for Energy & Environmental Applications: Handbook of Nanotechnology Applications” Elsevier, *In prep*

4.4 Award

-

4.5 Exchange and Visitation

- Two JASTIP seminars of the project were held in 2019 at NANOTEC (Sep, 3: 6 Japanese members visited NANOTEC and at Kyoto university (Nov, 18: 5 Thai members visited Kyoto University.).



JASTIP seminar in Thailand



JASTIP seminar in Japan



Report of International Collaborative Research Program in Kyoto University under “Japan-ASEAN Science, Technology and Innovation Platform (JASTIP)”

Progress of collaborative research in the title of “Synthesis and characterization of new photocatalytic nano-materials”

Research team:

Prof. Dr. Keiichi N. Ishihara, Kyoto University (Project leader, Japan side)

Assoc. Prof. Dr. Wisanu Pecharapa, College of Nanotechnology, KMITL (Project leader, Thai side)

Asst. Prof. Dr. Wanichaya Mekprasart, College of Nanotechnology, KMITL

Asst. Prof. Dr. Sorapong Pavasupree, Faculty of Engineer, RMUTT

Dr. Chakkaphan Wattanawikkam, Faculty of Science, RMUTT

Mr. Thanaphon Kansa-ard, College of Nanotechnology, KMITL

1. Project Propose

This project is the collaborative research under JASTIP fund in Kyoto University cooperated with Prof. Dr. Keiichi Ishihara at Social-Environmental Energy Science, Graduate School of Energy Science and Assoc. Prof. Dr. Wisanu Pecharapa at Nanocomposite Material Research Laboratory, KMITL. Main topic in this research is focused on searching and sharing new photocatalytic nano-materials to apply in photodegradation application under solar light activation. Meanwhile, new knowledges of the best photocatalyst candidates are revealed in this project relating to the improvement of functionality of new functional materials. Moreover, the appropriate preparation and deep characterization of new nano-materials based on metal oxide have been investigated. The crucial properties especially in optical properties of new nano-materials and their mechanisms were analyzed and utilized as photocatalyst and luminescent materials.

In addition, this research project is the collaboration including both local and international academic institutes, i.e, Kyoto University, Japan, NSTDA, industrial sector and local communities. This cooperation will effectively lead to the research exchanges, characterized techniques and sharing specific equipment. The outcomes of this project will result in the novel knowledge in functional materials, multi-sector and multidisciplinary collaboration and practically commercialized applications. Moreover, the research relationship between Thailand and Japan will be stably for Lab connection. Meanwhile, the production of the world's highest level of wastewater filter, publishing the results and lab prototype will be proposed following this project.

2. Project progress

Research Topic 2.1: X-ray absorption spectroscopy analysis and magnetic properties of M-doped TiO₂ nanoparticles (M=Co, Mn, Ni and Zn) Prepared by co-precipitation method

Titanium dioxide (TiO₂)-based materials have been extensively studied and researched for decades because of their excellent potential chemical, electrical and optical properties. TiO₂ represents the high chemical, electrical and mechanical stability and ease of doping with active ions [1]. During recent decades, the exhibition of magnetic behavior on TiO₂ semiconductor materials by doping with a small percent of magnetic impurity ions have attracted great attention (as call dilute magnetic semiconductors; DMSs) with promising application for use in the spintronic and magnetoelectronic devices [2-4]. Numerous experiments and researches have been performed on DMSs of TiO₂-based materials doped with transition magnetic ions. Among these transition magnetic ions with high magnetic ions behavior such as Co, Mn and Ni are the most selected ions dopants [5-10] B. Choudry *et al.* [6] and A. Bouaine *et al.* [5] reported the ferromagnetic and paramagnetic properties of Co-doped TiO₂. The magnetism at room-temperature of transition metal ions (Mn and Co) doped TiO₂ was claimed by M. M. Rashad and colleague [11]. The mechanisms for the occurrence of magnetic behavior in DMSs still remain controversial. Many experimental investigations have claimed that the oxygen vacancy or the F-centers in a gap of host matrix played crucial roles on the ferromagnetic behaviors of DMSs [12]. A super-exchange mechanism between the 3d ions dopant associated to the oxygen vacancy is also the key factor for the magnetic properties of DMSs [13]. Furthermore, it had been reported that that the transition metal dopant is essential for paramagnetic and ferromagnetic behavior to the spurious phase such as the metal oxide or clusters [14].

The structural phase and effect of transition metal ions dopant on TiO₂ structure attracts interesting as well, herein, it is important to accurately understand local structure and the doping effectiveness. X-ray absorption spectroscopy (XAS) technique is a powerful technique which provides insight into the electronic structure and local order around a selected type of atom. XAS can be divided into two techniques, the X-ray absorption near edge spectroscopy (XANES) and extended X-ray absorption fine structure (EXAFS). XANES technique provides the information on oxidation state, coordination number and site symmetry of absorbing atoms [15]. Meanwhile, EXAFS region spectra offer short-order information on the crystal structure and local structure information of elements such as a number and type of coordinating atom, the distances to neighboring atom and distance order [16]. Some research reports revealed the XAS analysis for transition metal incorporated in TiO₂ matrix such as O. Yildirim *et al.* (2015) investigated a non-magnet-to-ferromagnet and the local structure of Mn⁺-implanted TiO₂ employing the XAS technique. [17].

However, there are few publications focusing on the local structure investigation for transition metal ion incorporated into TiO₂ nanoparticles. Thus, this work aims to investigate of structural phase and magnetic properties of TiO₂ nanoparticles doped with different transition metal ions at various dopant concentrations. The influence of transition metal ions doping on phase structure, physicochemical state and magnetic properties of TiO₂ samples have been evaluated using X-ray diffractometer (XRD), X-ray photoelectron microscopy (XPS), X-ray absorption near edge spectroscopy (XANES), and vibrating samples magnetometer (VSM). The effect of different

dopant ions with different doping concentrations on the structural phase and magnetic properties of TiO₂ nanoparticles were also discussed in this paper.

- ***Material and methods***

M-doped TiO₂ nanoparticles (M=Co, Mn, Ni and Zn) with doping concentrations of 0.5, 1, 3 and 5 mol% were synthesized by co-precipitation method. Titanium isopropoxide [Ti(OCH(CH₃)₂)₄] purchased from Nacalai tesque, was used as a precursor of Ti source. Cobalt nitrate hexahydrate (Co(NO₃)₂·6H₂O), manganese nitrate tetrahydrate (Mn(NO₃)₂·4H₂O), zinc nitrate hexahydrate (Zn(NO₃)₂·6H₂O) and nickel nitrate hexahydrate (Ni(NO₃)₂·6H₂O) purchased from Wako were used as precursors of Co, Mn, Zn and Ni source, respectively. Ammonium solution (NH₃) and absolute ethanol was employed as a precipitation agent and solvent, respectively.

The starting precursor of cobalt nitrate and titanium isopropoxide were weighed according to the required stoichiometric proportion and separately dissolved in absolute ethanol under magnetic stirring to form the starting precursor solution. The starting precursors were mixed together under magnetic stirring to form the homogeneous solution. The precipitation agent of NH₃ was slowly added in the homogeneous solution until the pH became 9. The mixing solution was constantly stirred for 3 h then the solution was aged for 12 h to obtain the precipitated product. After this stage, the precipitate was washed by DI water until the pH became neutral and then dried at 100°C for 12 h. Finally, the green powders were annealed at 500°C in atmosphere for 2 h.

The phase structure of M-TiO₂ samples was identified by XRD diffractometer model Rigaku Rint2100 CMJ with CuK_α radiation ($\lambda = 0.154$ nm) in the scan range from 20–60°. The X-ray absorption spectroscopy (XAS) technique was used to identify the chemical state of all samples. The chemical states of samples were investigated by X-ray photoelectron spectroscopy (XPS); JEOL Ltd. X-ray absorption near edge structure (XANES) of Ti K-edge in transmission mode and Co K-edge, Mn K-edge, Ni K-edge and Zn K-edge in fluorescent mode were recorded at room temperature using Ge(220) double crystal monochromator at Beamline-8, Synchrotron Light Research Institute (SLRI), Nakhonrachasima, Thailand. Reference standards of transition metal ions such as TiO₂, CoO, MnO, Mn₂O₃, MnO₂, NiO and ZnO which known decisive oxidation state were measured as well for comparison purpose. The magnetic behavior of all samples was observed at room temperature by vibrating samples magnetometer (VSM); Riken Denshi, BHV-50 model with the external applied magnetic field range of ± 10 kOe.

• Results and Discussion

XRD- X-ray diffraction pattern of undoped and TiO₂ nanoparticles doped with transition metal ions of Co, Mn, Ni and Zn at different concentration are shown in Fig. 1. All diffractogram peaks of undoped and doped samples exhibit main diffraction peaks of (101), (004), (200), (105) and (211) positioned at around 25.4°, 36.8°, 48.9° and 54.7°, respectively, which confirmed the tetragonal anatase phase of TiO₂. It is noteworthy that no diffraction peak corresponding to metal oxide dopant and any impurity peak, indicating that the transition metal ions dopants are well dispersed within the TiO₂ matrix.

XAS- To investigate the atomic structure of TiO₂ doped with Co, Mn, Ni and Zn, K-edge XANES data analysis for each ions was performed. The normalized Ti K-edge XANES spectra of TiO₂ reference standard and M-TiO₂ samples are shown in Fig. 2 (a)-(d). The Ti K-edges of M-TiO₂ samples represent the feature of spectra similar to TiO₂ reference standard comprising a triplet pre-edge peak. This major feature of pre-edge peak (A₁, A₂ and A₃) is a characteristic fingerprint to assign the coordination number of materials, which arises from the X-ray induced electronic transitions from the valence band to the conduction band. The pre-edge features were observed at ~4968 (A₁), ~4970 eV (A₂) and ~4972 eV (A₃). A₁ peak generally attributes to a quadrupole transition from 1s to 3d (t_{2g}) in the Ti absorber, A₂ peak arises from a dipole transition from 1s to hybridized p-d (t_{2g}) on the neighboring Ti atom and A₃ peak is dipole transition from 1s to hybridized p-d (e_g) on the Ti neighboring atom [18-21]. The shoulder B feature peak of XANES spectra may attribute to the interactions of the central Ti 4p orbital hybridized with the near Ti and O atom. For the post-edge spectrum, C feature (~4988 eV) can be assigned to 3s-np dipole-allowed transition [22-23]. From the pre-edge and post-edge feature data of all samples, it could be concluded that the Ti in Co-, Mn-, Ni- and Zn-TiO₂ samples contains six coordinated Ti⁴⁺ ions. In addition, a small change in proportion of A₁, A₂ and A₃ feature implies the substitution of Ti⁴⁺ ion in the samples by the transition metal ions dopant.

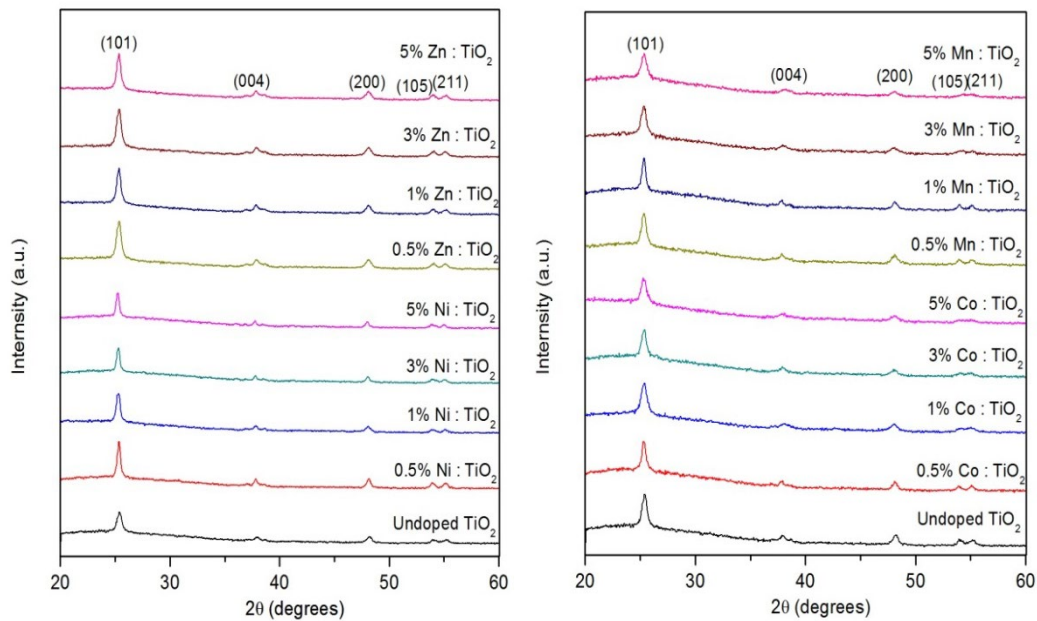


Fig. 1. XRD patterns of M-TiO₂ nanoparticles calcined at 500°C for 2 h.

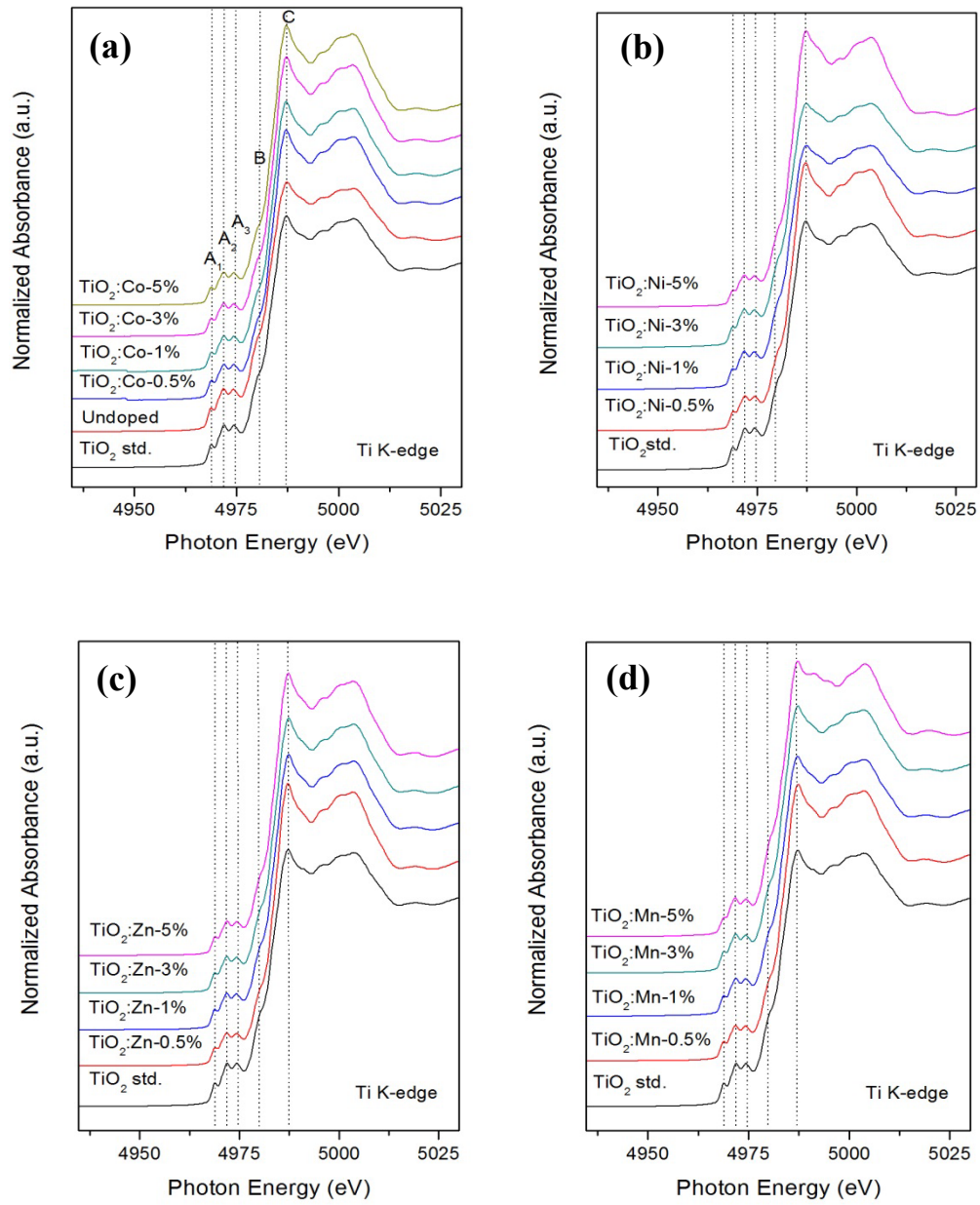


Fig. 2. Normalized XANES spectra of M-TiO₂ samples for Ti K-edge with (a) Co-TiO₂, (b) Ni-TiO₂, (c) Zn-TiO₂ and (d) Mn-TiO₂ samples.

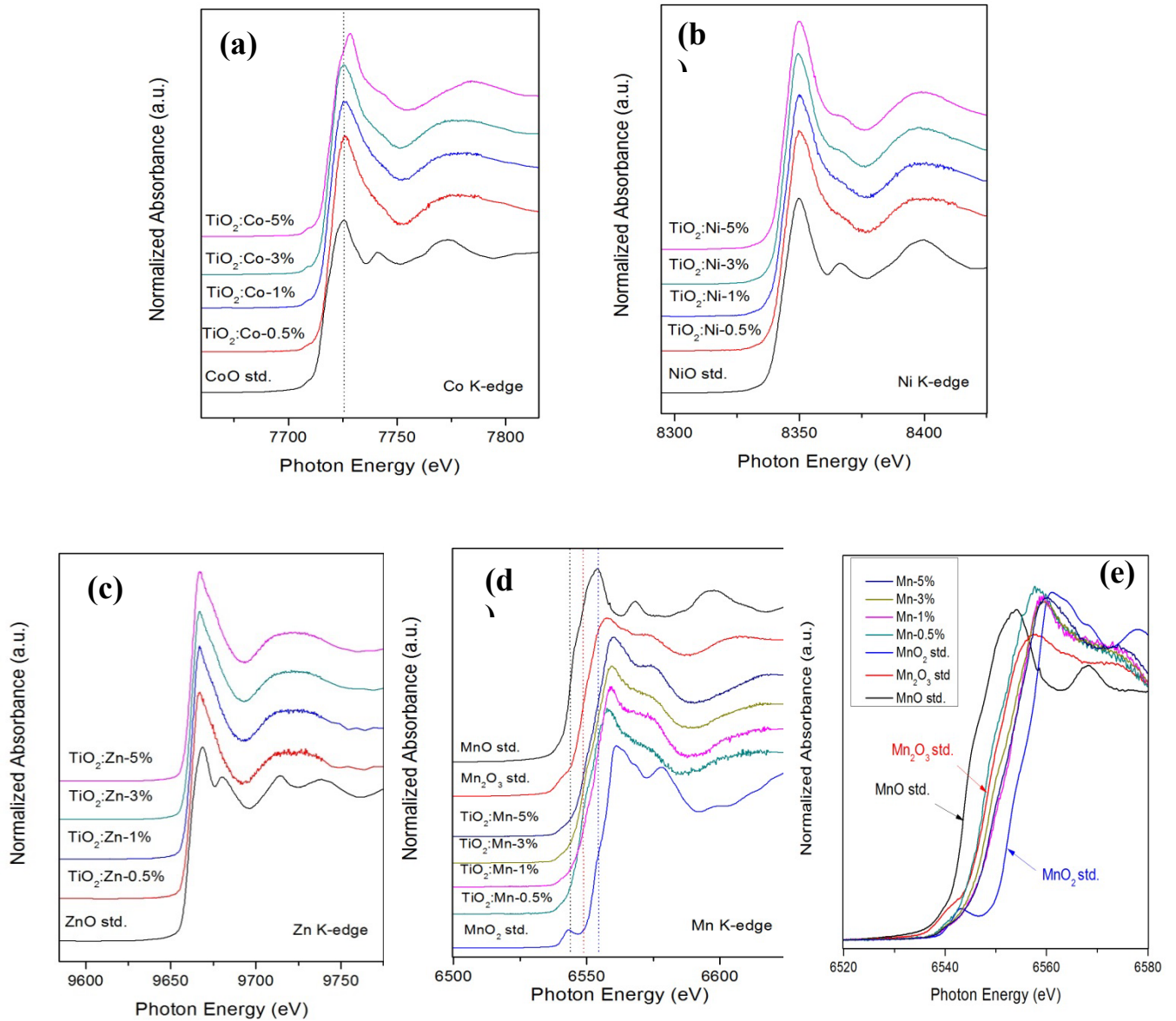


Fig. 3. Normalized XANES spectra of M-TiO₂ samples for (a) Co K-edge (b) Ni K-edge, (c) Zn K-edge, (d) Mn K-edge and (e) high resolution Mn K-edge.

The normalized X-ray absorption near edge structure (XANES) of Co-, Mn-, Ni- and Zn-doped TiO₂ nanoparticles including their reference standard in fluorescent mode are shown in Fig. 3 (a)-(d). Fig. 3(a) displays the Co K-edge for Co-TiO₂ nanoparticles with doping content of 0.5-5 mol%. It can be clearly seen that the position of absorption edge spectra is observed at ~7710 eV without pre-edge peak which similar to the CoO reference standard. This result suggests that the oxidation state of Co ions in Co-doped TiO₂ samples is 2+. When the Co concentration increases to 3 and 5 mol%, the XANES spectrum character shows small broaden peak around ~7745 eV situated at same location with CoO standard peak. This manner may originate from the beginning formation of CoO cluster in the samples. For Ni-doped TiO₂ samples, the XANES spectra are represented in Fig. 3(b). The absorption-pre-edge and post-edge spectra obviously exhibit the strong absorption energy of ~8336-8345 eV that is similar to NiO standard. These results confirm that it contains 2+ formal valence state of Ni ions for Ni-doped TiO₂ sample. At the higher Ni concentration, a small broaden peak around ~8365 eV is observed due to the NiO

phase formation in the sample. As seen in Fig. 3(c) displaying the XANES spectra of Zn K-edge, it is noticeable that there is the strong absorption edge around 9653 eV for all dopant concentrations, which corresponds to the oxidation state of 2+. In case of Mn-doped TiO₂ samples, the Mn K-edge XANES spectra are shown in Fig. 3(d). The spectra of all samples represent strong absorption energy edge in a range of ~6538-6553 eV between the standard spectrum of Mn₂O₃ and MnO₂, as clearly seen in Fig. 3(e). This tendency of data suggests the existence of mixture of Mn ions in different oxidation states in Mn-doped TiO₂ sample. Linear combination fitting (LCF) of Mn spectra was performed to confirm the oxidation states of Mn dopant in Mn-doped TiO₂ sample using MnO, Mn₂O₃ and MnO₂ as a reference model. The best LCF with three of reference standards suggests that the decrease of Mn³⁺ component and the increase of Mn⁴⁺ of oxidation state occurs when the Mn dopant concentration increases, as seen in Table 1.

XPS- X-ray photoelectron spectroscopy was employed to determine insight of oxidation states for titanium, oxygen and dopant metal cations in the samples and to ensure the chemical composition at surface layer of M-TiO₂ nanoparticles. The XPS survey scan (0-1300 eV) of 5mol% M-doped TiO₂ nanoparticles is shown in Fig. 4(a). The rough scanning spectra of each doped sample reveal the existence of each dopant ion, with main peaks coming from Mn, Co, Ni, Zn, O and Ti, confirming the chemical composition of major elements of M-doped TiO₂ samples. It is noticed that the splitting of Ti 2p_{3/2} and 2p_{1/2} binding energy located at ~458.6-458.8 and ~464.5-464.5 eV, respectively is observable for all samples. The separation of splitting binding energy of all samples is ~5.5-5.7 eV, demonstrating a normal state of Ti with 4+ of oxidation state, which is attributed to the spin-orbit splitting of Ti2p_{3/2} and 2p_{1/2} for Ti⁴⁺ in TiO₂. The binding energy of O1s for all samples could be deconvoluted into two constituents, corresponding to oxygen containing chemical bonds of water molecule (H-O-H) at ~531.4-531.8 eV and hydroxyl (Mn-O-H) at ~530.0-530.2 eV. The XPS core level spectra of Mn, Co, Ni and Zn ions in the TiO₂ matrix are illustrated in Fig.4. For the Mn-doped TiO₂ sample, Mn 2p_{3/2} and 2p_{1/2} peaks are observed at 642.0 and 653.6 eV, respectively, which correspond to those for Mn₂O₃ [21] as seen in Fig. 4(b). This result suggests that the surface of sample mainly contains Mn ion with a valency number 3+ of Mn. Fig. 4(c) demonstrates the binding energy values of Co2p_{3/2} and 2p_{1/2} positioned at 781.1 and 796.9 eV, indicating that the Co elements could be in 2+ state. For the Ni-doped TiO₂ sample, the XPS spectra show complex structure with binding

Table 1. Weight of component from XANES linear combination fitting in TiO₂ doped with Mn at various concentrations.

samples	Component		
	MnO	Mn ₂ O ₃	MnO ₂
TiO ₂ : Mn-0.5%	0.021	0.885	0.094
TiO ₂ : Mn-1%	0	0.613	0.387
TiO ₂ : Mn-3%	0	0.767	0.233
TiO ₂ : Mn-5%	0	0.591	0.409

energies of 855.9 and 862.4 eV for Ni 2p_{3/2} and 873.5 and 881.4 eV for Ni 2p_{1/2}, respectively. These can be suggested that the sample contains Ni with 2+ of valence state on the surface of sample. In case of Zn-doped TiO₂ sample, the XPS spectrum is shown in Fig. 4(e). The Zn 2p_{3/2} and 2p_{1/2} characteristic spectra are detected at 1022.2 and 1045.0 eV, which is close to the value of Zn²⁺ in ZnO. This feature implies that the Zn-doped TiO₂ sample contains Zn²⁺ on the surface of sample.

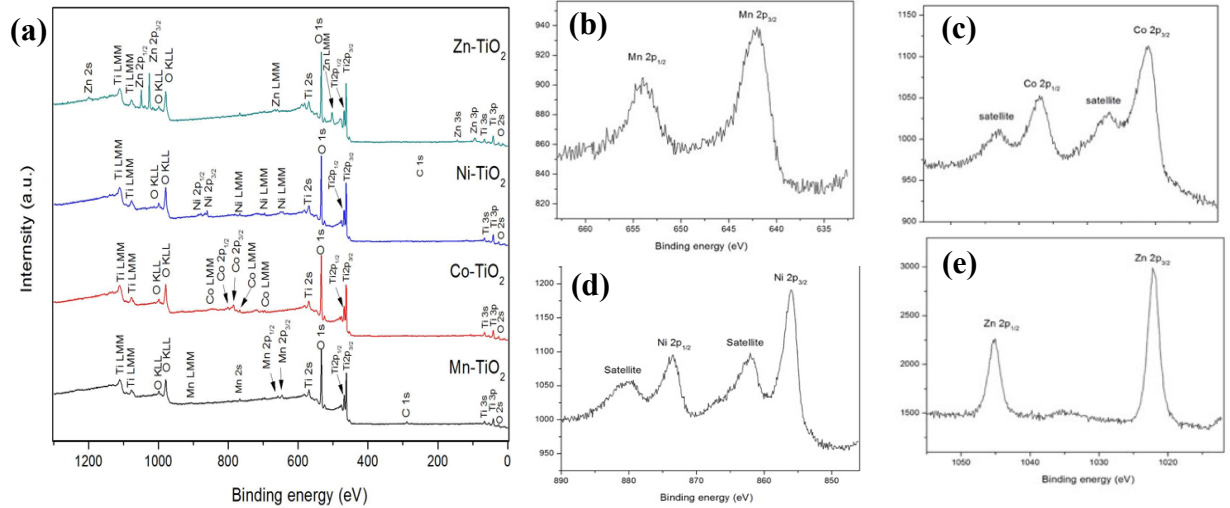


Fig. 4. (a) XPS survey spectra for M-doped TiO₂ samples and core level spectra of (b) Mn, (c) Co, (d) Ni and (e) Zn.

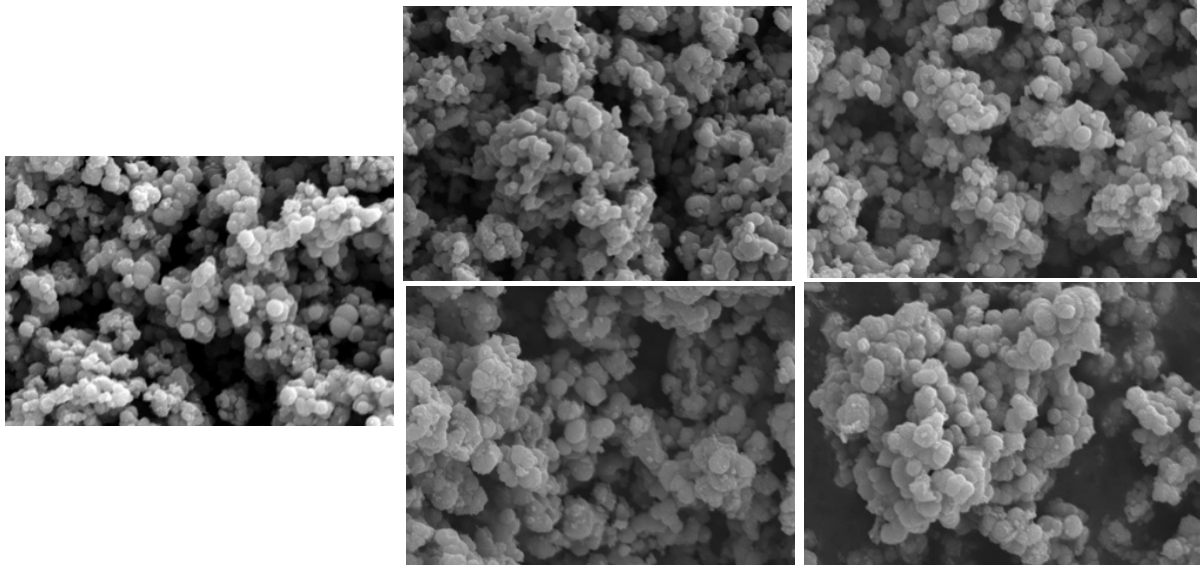


Fig. 5 FESEM images of undoped and M-doped TiO₂ nanoparticles.

Morphology- Fig. 5 represents the FESEM micrographs of the undoped and transition-metal-doped TiO₂ nanoparticles. As seen in micrographs, the powdered particle of undoped sample consists of clusters of nanosized spherical primary particles. The average particle size is around 330 nm. Meanwhile, the samples doped with different transition metal ions exhibit slightly smaller particle size at higher percentage of dopant and more agglomeration occurs with increasing doping content. The average particle size of doped samples slightly decreases with increasing doping concentration. A slight decrease in the particle size with increasing doping content could be due to the inhibition of the grain growth and lattice distortion of crystal structure with doping. The FESEM investigation suggests that the primary particle size could be responsible for the specific surface area of the powder. The BET surfaces of all samples were measured. The undoped sample shows BET surface area of 48 m²/g. For the doped samples, the Mn-, Co-, Ni- and Zn-doped TiO₂ show their BET surface areas are in a range of 54-64 m²/g, 53-58 m²/g, 60-67 m²/g and 51-57 m²/g, respectively. In overall, the doped samples represent the higher surface area compared with undoped samples. This may be originated from the fact that the transition metal dopant could provide the additional nucleation during the precipitation process and subsequent calcination step, leading to the solid materials with greater surface area. Overall, the transition-metal-doped TiO₂ exhibit higher BET surface area, that could result to the enhancement of photocatalytic behavior of the doped samples.

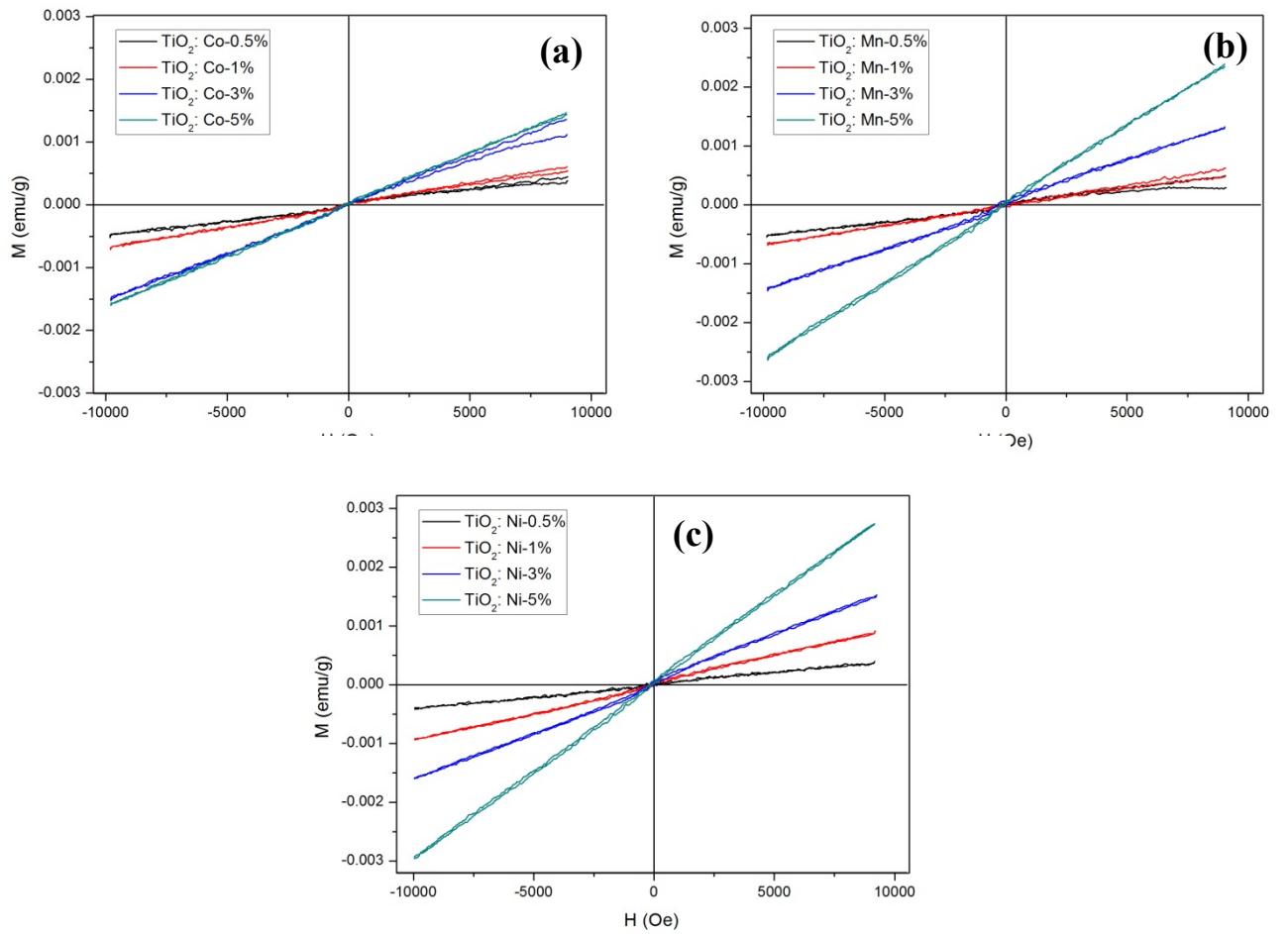


Fig. 6. The plot of M - H hysteresis loop at room temperature of M-TiO₂ samples with (a) Co-TiO₂, (b) Mn-TiO₂ and (c) Ni-TiO₂.

VSM- The magnetic properties of the samples were investigated by VSM for ± 10 kOe at room temperature. Fig. 6 shows the plot of magnetization; M and magnetic field; H curve recorded for Co-, Mn-, Ni- and Zn-doped TiO_2 samples. Pure TiO_2 sample presents the diamagnetic behavior. Meanwhile, all transition metal ion doped samples exhibit typical magnetization loop indicating paramagnetic behavior. The slope of linear paramagnetic increases with the increase of Co-, Mn-, Ni- doping concentration. The magnetic properties of the samples were investigated by VSM for ± 10 kOe at room temperature. Fig. 4(a)-(c) shows the plot of magnetization; M and magnetic field; H curve recorded for Co-, Mn- and Ni-doped TiO_2 samples. Pure TiO_2 sample presents the diamagnetic behavior. Meanwhile, all transition metal ion doped samples exhibit typical magnetization loop indicating paramagnetic behavior. The paramagnetism presented in prepared samples may be originated from the isolated transition metal dopant ions dispersed on the TiO_2 host matrix. This result is in harmony with the XANES results that indicate the existence of Co-, Mn- and Ni-dopant occurring as Co^{2+} , Ni^{2+} and $\text{Mn}^{3+,4+}$ insertion into the TiO_2 lattice [11]. In addition, the substitution of Ti^{4+} ions in TiO_2 by Co^{2+} , Ni^{2+} and $\text{Mn}^{3+,4+}$ will result in the creation of oxygen vacancies and charge carriers playing significant role for the magnetism origin in magnetic oxide.

• **Conclusions**

TiO_2 nanoparticles doped with different transition metal ions of Co, Mn, Ni and Zn at various concentrations were prepared by co-precipitation method and calcinations at 500°C for 2h. The XRD results confirm the structural phase belonging to tetragonal anatase TiO_2 phase for all samples without secondary phase of doped metal oxide phase. XANES results clearly show tripped pre-edge fingerprint of Ti with 4+ of valence state for Ti in all samples. The 2+ oxidation state was found in Co-, Ni- and Zn- doped samples. The mixing oxidation state of 3+ and 4+ was observed in the Mn-doped TiO_2 samples. Magnetic measurement on the samples indicates the existence of paramagnetic behavior at room temperature for Co- Mn- and Ni-doped samples, and diamagnetic behavior for undoped and Zn doped samples. Higher Co-, Mn- and Ni- concentration leads to greater magnetization value. The isolate magnetic ion of Co, Mn and Zn dispersed in the host oxide matrix is a key factor for magnetic behavior

• **References**

- [1] M. H. Henderson, A surface science perspective on TiO_2 photocatalysis. *Surf. Sci., Rep.* 66 (2011) 185-278.
- [2] S.A. Wolf, D.D. Awschalom, R.A. Buhrman, J.M. Daughton, S. V. Molnar, M.L. Roukes, A.Y. Chtchelkanova and D.M. Treger, Spintronics: a spin-based electronics vision for the future, *Science*. 294 (2001) 1488.
- [3] G.A. Prinz, Magnetoelectronics, *Science*. 282 (1998) 1660–1663.
- [4] J. M. Kikkawa, I. P. Smorchkova, N. Samarth and D.D. Awschalom, Room- temperature spin memory in two dimensional electron gases, *Science*. 277 (1997) 1284–1287.
- [5] A. Bouaine, G. Schmerber, D. Ihiawakrim, A. Derory, Structural, optical, and magnetic properties of polycrystalline Co-doped TiO_2 synthesized by solid-state method, *Matt. Sci. Eng. B* 177 (2012) 1618-1622.

- [6] B. Choudhury, A. Choudhury, A.K.M. Maidul Islam, P. Alagarsamy, M. Mukherjee, Effect of oxygen vacancy and dopant concentration on the magnetic properties of high spin Co^{2+} doped TiO_2 nanoparticles, *J. Magn. Magn. Mater.* 323 (2011) 440–446.
- [7] K. Karthik, S. K. Pandian, K. S. Kumar and N. V. Jaya, Influence of dopant level on structural, optical and magnetic properties of Co-doped anatase TiO_2 nanoparticles, *Appl. Surf. Sci.* 256 (2010) 4757–4760.
- [8] D. Vokoun, M. Svatuška, J. Olejníček, M. Kohout, J. Drahokoupil, M. Rameš, J. Vejpravová, A. Mantlíková, L. Fekete, J. Kopeček, L. Klimša and O. Heczko, Ni– TiO_2 nanocomposite films and their magnetic properties, *Physica B: Condensed Matter*. 503 (2016) 44–50.
- [9] B. Choudhury and A. Choudhury, Oxygen vacancy and dopant concentration dependent magnetic properties of Mn doped TiO_2 nanoparticle, *Curr. Appl. Phys.* 13 (2013) 1025e1031.
- [10] C.K. Sellers and E. G. Seebauer, Room temperature ferromagnetism in Mn-doped TiO_2 nanopillar matrices, *Mater. Lett.* 114 (2014) 44–47.
- [11] M.M. Rashad, E.M. Elsayed, M.S. Al-Kotb and A.E. Shalan, The structural, optical, magnetic and photocatalytic properties of transition metal ions doped TiO_2 nanoparticles, *J. Alloy. Compd.* 581 (2013) 71–78.
- [12] M. D. Coey, M. Venkatesan and C. B. Fitzgerald, Donor impurity band exchange in dilute ferromagnetic oxides, *Nat. Mater.* 4 (2005) 173–179. ^[1]_{SEP}
- [13] K. Kikoin and V. Fleurov, Superexchange in dilute magnetic dielectrics: Application to $(\text{Ti},\text{Co})\text{O}_2$, *Phys. Rev. B* 74 (2006) 174407(1)–174407(9).
- [14] R. Lardé, E. Talbot, P. Pareige, H. Bieber, G. Schmerber, S. Colis, V. Pierron-Bohnes and A. Dinia, Evidence of superparamagnetic Co clusters in pulsed laser deposition-grown $\text{Zn}_{0.9}\text{Co}_{0.1}\text{O}_3$ thin films using atom probe tomography, *J. Am. Chem. Soc.* 133 (2011) 1451–1458.
- [15] S. J. Stewart, S. J. A. Figueroa, J. M. Ramallo López, S. G. Marchetti, J. F. Bengoa, R. J. Prado, and F. G. Requejo, Cationic exchange in nanosized ZnFe_2O_4 spinel revealed by experimental and simulated near-edge absorption structure, *Phys. Rev. B* 75, 073408.
- [16] D. Makovec, A. Kodrelztok and A. Drogenik, The structure of compositionally constrained zinc-ferrite spinel nanoparticles, *J. Nanopart. Res.* 13 (2011) 1781–1790.
- [17] T. L. Hsiuna, H. P. Wang and H. P. Lin, Chemical structure of photocatalytic active sites in nanosize TiO_2 , *J. Phys. Chem. Solids*. 69 (2008) 383–385.
- [18] M. Ghaffari, T. Liu, H. Huang, O. K. Tan and M. Shannon, Investigation of local structure effect and X-ray absorption characteristics (EXAFS) of Fe (Ti) K-edge on photocatalyst properties of $\text{SrTi}_{(1-x)}\text{Fe}_x\text{O}$, *Mater. Chem. Phys.* 136 (2012) 347e357.
- [19] T. Yamamoto, T. Mizoguchi and I. Tanaka, Core-hole effect on dipolar and quad-rupolar transitions of SrTiO_3 and BaTiO_3 at Ti K edge, *Phys. Rev. B* 71 (2005) 245113.
- [20] V. Luca, S. Djajanti and R.F. Howe, Structural and electronic properties of sol–gel titanium oxides studied by X-ray absorption spectroscopy, *J. Phys. Chem. B* 102 (1998) 10650–10657.
- [21] Z.Y. Wu, G. Ouvrard, P. Gressier and C.R. Natoli, Ti and O K-edges for titanium oxides by multiple scattering calculations: comparison to XAS and EELS spectra, *Phys. Rev. B* 55 (1997) 10382–10391.
- [22] F. Farges, G. E. Brown and J. J. Rehr, Ti K-edge XANES studies of Ti coordination and disorder in oxide compounds: comparison theory and experiment, *Phys. Rev. B* 56 (1997) 1809–1819.

- [23] V.I. Anisimov, M. A. Korotin, I. A. Nekrasov, A. S. Mylnikova, A. V. Lukoyanov, J. L. Wang and Z. Zeng, The role of transition metal impurities and oxygen vacancies in the formation of ferromagnetism in Co-doped TiO_2 , J. Phys. Condens. Matter. 18 (2006) 1965-1704.

Research Topic 2.2: Synthesis of Samarium doped ZnAl₂O₄ powder by vibrational ball milling method assisted with calcination process

Zinc Aluminate (ZnAl₂O₄) or natural name in granite has been recently considered as a functional material in host luminescent applications due to its wide bandgap energy, high chemical and thermal stability. Moreover, ZnAl₂O₄ has been widely employed as a good host phosphor material as a result of uniform particle and narrow size distribution. ZnAl₂O₄ product as spinel crystalline structure was synthesized by vibrational ball milling method assisted with sintering treatment. Oxide precursor materials as Al₂O₃ and ZnO powder were used in the process. Several milling round and sintering treatment were the important parameters for studying phase transformation between Al₂O₃/ZnO to ZnAl₂O₄ phase.

Luminescent materials are considered as a kind of prominent technologies in various applications, for example, displays, luminescent pigments, luminescent lamp and X-ray detection. An increased number of the investigations of inorganic phosphor materials has received great attention for potential applications especially in solid state lighting technologies [1]. For effective doping candidate, rare earth or lanthanide-doped oxides are widely used as activators in luminescent materials due to high emission properties. Strong activator in red phosphor under ultraviolet excitation was successfully fabricated by the cooperation of Eu³⁺ ion in Lu₂O₃ nanofibers prepared by a simple sol-gel and electrospinning process researched by Z. Hao and co-worker [2]. Meanwhile, Z. Lou and J. Hao reported that luminescent material containing Tb³⁺ and Tm³⁺ ions in zinc aluminate films exhibited green and blue cathodoluminescence, respectively [3]. Host support material is a key parameter to concerning the enhancement of luminescence properties. Among various available host matrixes, oxide material is fascinatedly interested as an important host of phosphorescent materials. Due to trivalent ions and intra 4f shell luminescence of rare earth dopant, many oxide materials are properly studied for the possibility of host matrix.

There are various techniques for the synthesis of phosphor material in host oxide materials. Normally, wet chemical processes including hydrothermal process, sol-gel method, molten salt synthesis and co-precipitation method have been developed for ultrafine, homogenous powders and well-defined doping distribution [4,5]. Meanwhile, solid state reaction is convenient potential process for the synthesis in form of metal oxide precursors. The requirement by the process is high temperature system for its material formation. Therefore, several mechanical milling and heating process is proposed to good formation of homogenous phase [6]. However, high emission by the product in nanoscale should be significantly shown due to larger surface area per unit volume. Meanwhile, the homogeneity of dopant in a phosphor matrix is also a significant effect on luminescence properties. In this work, the authors believe that the product of homogenous powder and distributed doping material can be facilely synthesized via mechanical milling and calcination. Structural properties of as-synthesized samples and sintered powders in each condition were characterized by X-ray diffraction (XRD) and scanning electron microscope (SEM). Meanwhile, chemical structure of the product was investigated by FTIR spectroscopy. For optical properties, the products were analyzed via diffuse reflectance and photoluminescence spectroscopy.

- ***Materials and Method***

Sm:ZnAl₂O₄ materials were prepared by vibrational ball milling process assisted with calcined treatment. Al₂O₃ and ZnO powder supplied from Wako Company were used as oxide precursor materials. Sm metal phase was an alkaline element represented as doping material. Firstly, Al₂O₃ and ZnO powder was loaded in stainless steel holder with the ratio of material weight and ball at 1:10. For Sm loading, the amount of Sm doping was loaded in host matrix at 0, 0.5, 1 and 2 wt.%, respectively by vibrational ball milling process at 710 rpm for 4 h. Then, green powder was sintered at 1200 °C for 6 h. After that, obtained powder was re-milled in vibrational ball milling process and sintered at 1200 °C for 6 h to provide strong crystalline and uniform product. After third milling, the samples were annealed at 450 °C for 2 h to eliminate contaminated phase. Finally, Sm:ZnAl₂O₄ nanopowders were obtained as illustrated in Fig. 7. The structural and morphological samples were characterized by powder X-ray diffraction (XRD) and Fourier transform infrared spectroscopy (FTIR). The optical properties of phosphor materials were analyzed by UV-vis spectrometer and photoluminescence spectroscopy.

• *Results and discussion*

Structural properties - XRD patterns of Sm:ZnAl₂O₄ nanopowder prepared by vibrational ball milling process with different Sm doping are depicted in Fig. 8. Prominent XRD peaks of the sample without Sm loading were identified to ZnAl₂O₄ structure located at $2\theta = 30.8^\circ, 36.5^\circ, 44.4^\circ, 48.7^\circ, 55.3^\circ, 59.0^\circ, 65.0^\circ, 74.0^\circ$ and 77.0° corresponding to (220) (311) (400) (331) (422) (511) (440) (620) and (533) planes of spinel phase, respectively (JCPDF, No. 05-0669). The XRD pattern was certainly similar to well-defined ZnAl₂O₄ spinel phase. Owing to oxide precursor materials as Al₂O₃ and ZnO, several milling and sintering process are necessary to produce new phase in ZnAl₂O₄ formation. The decrease of precursor material size is obtained by milling process that easily to the diffusion of metal atoms under sintering method. In case of Sm doping, XRD patterns were identically with ZnAl₂O₄ pattern resulting in the interstitial position of Sm metal in ZnAl₂O₄ structure. The improvement of ZnAl₂O₄ could be occurred after Sm doping at 0.5 wt.% due to the partly replacement of Sm atoms in Zn atomic position [7]. However, ZnAl₂O₄ crystallite size was decreased by the addition of Sm concentration especially ratio at 1 wt.%. It can be seen that contaminated peak was also occurred at $2\theta = 33.6^\circ$ and 34.3° relating to SmAlO₃ (112 plane) and ZnO (002 plane) phase. This result indicated that Sm atoms were substituted in Zn atoms position due to milling and heating process leading to the decrease of ZnAl₂O₄ crystallite size.

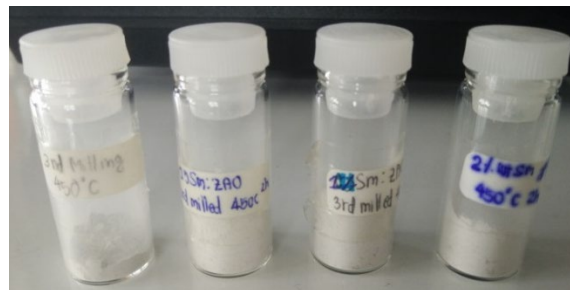


Fig. 7. Photograph of Sm:ZnAl₂O₄ nanopowder at different Sm doping.

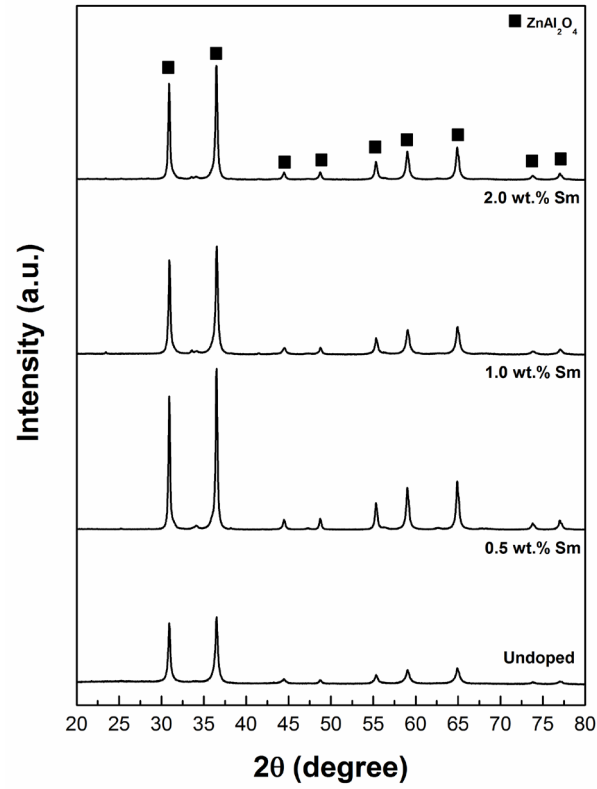


Fig. 8. XRD patterns of Sm:ZnAl₂O₄ nanopowder at different Sm doping.

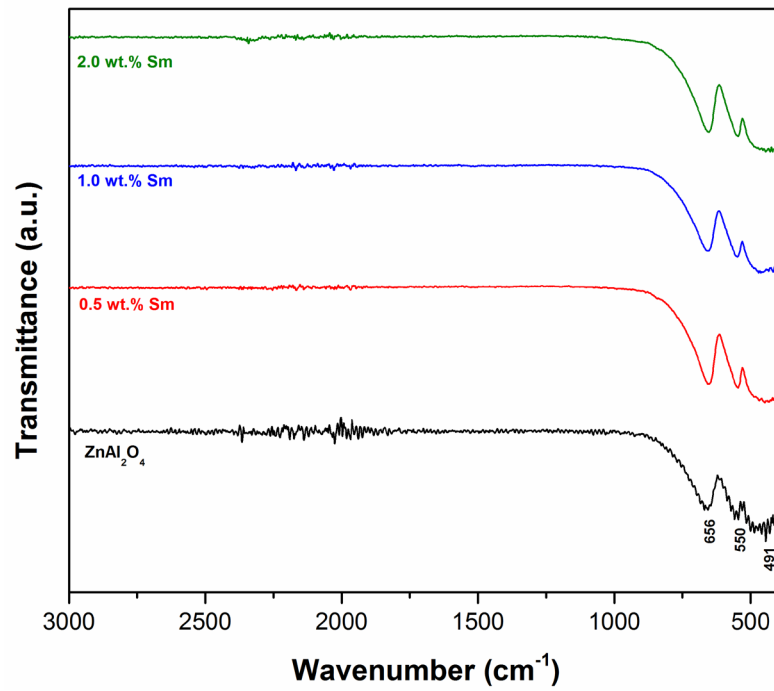


Fig. 9. FTIR spectra of Sm:ZnAl₂O₄ nanopowder at different Sm doping.

The infrared spectra of Sm doped ZnAl_2O_4 nanopowder prepared by vibrational milling process assisted with sintering method are shown in Fig. 9. The FT-IR spectra show a series of transmission peaks in the range of $3000\text{--}380\text{ cm}^{-1}$ which are related to spinel type pattern. Dominant peaks at 656 , 550 , and 491 cm^{-1} are same pattern in all samples corresponding to Al-O symmetric stretching vibration (ν_1), Al-O symmetric bending vibration (ν_2), and Al-O asymmetric stretching vibration (ν_3), respectively [10]. All peaks in FTIR spectra located in range of $750\text{--}450\text{ cm}^{-1}$. This result can be suggested that Al^{3+} ions are in octahedral sites of AlO_6 group related to normal spinel in the structure [11].

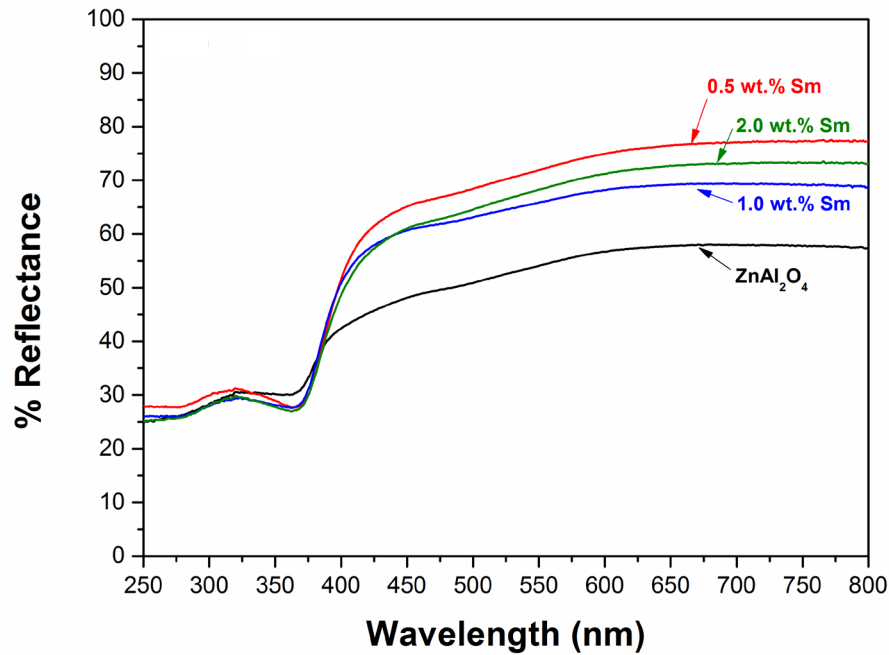


Fig. 10. Diffuse reflectance spectra of Sm: ZnAl_2O_4 nanopowder at different Sm doping.

Optical and luminescence properties - The optical properties in diffuse reflectance spectra of Sm: ZnAl_2O_4 nanopowder in range of $250\text{--}800\text{ nm}$ are depicted in Fig. 10. High absorption in UV region was obtained in all conditions. Optical reflectance spectra of Sm: ZnAl_2O_4 samples in visible range were enhanced by the influence of Sm metal compared to pure ZnAl_2O_4 material. Moreover, the absorption edge of Sm: ZnAl_2O_4 slightly shifted to higher wavelength by the increase of Sm dopant. These results showed that absorption edge of Sm: ZnAl_2O_4 had shifted to lower energy value by the addition of Sm content associated with the impurity energy level in ZnAl_2O_4 host matrix [10].

Luminescence spectra of ZnAl_2O_4 nanopowders with the amount of Sm dopant are shown in Fig. 11. The phosphor materials were measured at room temperature under excited at 404 nm in harmony with Sm excitation. Normally, the emission spectra of Sm characteristic produced in red-orange region at three strong peaks at 565 , 601 and 645 nm attributing to the direct emission of Sm^{3+} at $^4\text{G}_{5/2} \rightarrow ^6\text{H}_{5/2}$, $(^4\text{G}_{5/2} \rightarrow ^6\text{H}_{7/2})$ and $(^4\text{G}_{5/2} \rightarrow ^6\text{H}_{9/2})$, respectively [11]. However, the prominent structured band in the range of $630\text{--}730\text{ nm}$ as shown in the spectra was corresponding to the emission of residual chromium impurity [12]. Due to the operation at high speed vibrational process, the contamination of chromium phase can be blended by the stainless-

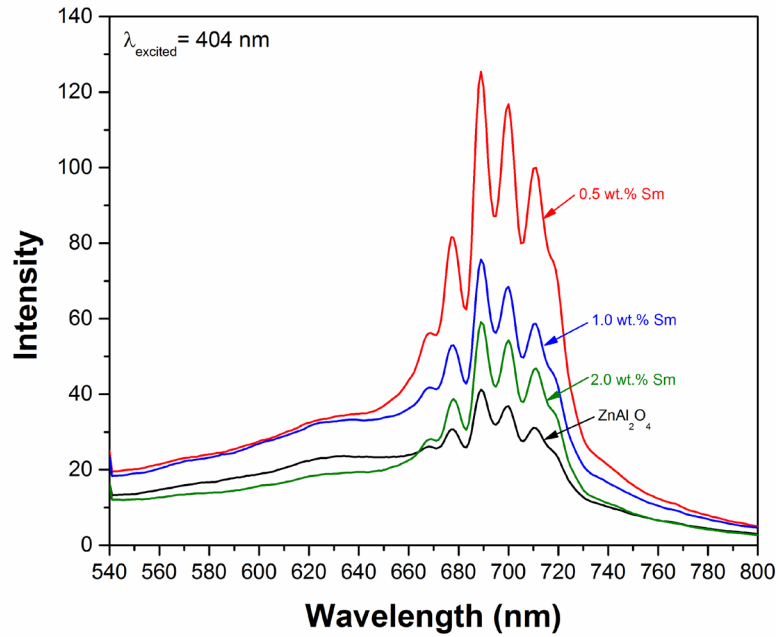


Fig. 11. Photoluminescence spectra of Sm:ZnAl₂O₄ nanopowder at different Sm loading.

steel container during the synthesis. The strongest emission was performed at 0.5 wt.% Sm in ZnAl₂O₄ matrix. Therefore, the enhancement of ZnAl₂O₄ spectra at 0.5 wt.% Sm was interpreted that Sm phase could be activated under this light irradiation relating to the energy transfer from Sm to luminescence material in the system. For 1 and 2 wt.% Sm doping in ZnAl₂O₄ samples, PL intensity was decreased owing to concentration quenching resulting in the increase of non-radiant energy transfer between adjacent activators [13].

• Conclusion

Sm:ZnAl₂O₄ nanopowders with different Sm loading were synthesized by vibrational ball milling process assisted with calcination treatment. XRD patterns of Sm:ZnAl₂O₄ were identically patterns compared with pure ZnAl₂O₄ material. Well-defined ZnAl₂O₄ spinel phase was enhanced by several milling and calcination process. FTIR result confirmed that the formation of ZnAl₂O₄ spinel was obtained after this synthesis accompanying with the presence of Al-O symmetric vibrational mode in octahedral sites of AlO₆ group. This bonding was related to normal spinel in the crystalline structure. Meanwhile, reflectance spectra revealed that absorption edge of ZnAl₂O₄ powder had shifted to lower energy by the addition of Sm content at less concentration due to the impurity level of Sm doping in the matrix. The emission spectra produced red-orange region at three strong peaks at 562, 600 and 645 nm corresponding to the influence of Sm dopant. However, the prominent structured band in the spectra was related to the emission of residual chromium impurity by stainless steel balls in high speed vibrational process. The strongest emission was performed at 0.5 wt.% Sm in ZnAl₂O₄ owing to the energy transfer from Sm to ZnAl₂O₄ matrix.

• References

- [1] D. Qingqing, Z. Guangjun, Z. Juan, Z. Haifeng, Z. Jie, Y. Zhongsen, Facile sol-gel combustion synthesis and photoluminescence enhancement of $\text{CaZrO}_3\text{:Sm}^{3+}$ nanophosphors via Gd^{3+} doping, *J. Rare Earth.* 30 (2012) 1000-1004.
- [2] Z. Hao, C. Jindeng, G. Hai, Electrospinning synthesis and luminescent properties of $\text{Lu}_2\text{O}_3\text{:Eu}^{3+}$ nanofibers, *J. Rare Earth.* 28 (2010) 232-235.
- [3] Z. Lou, J. Hao, Cathodoluminescence of rare-earth-doped zinc aluminate films, *Thin Solid Films* 450 (2004) 334-340.
- [4] Z. Chen, E. Shi., W. Li, Y. Zheng, N. Wu, W. Zhong, Particle size comparison of hydrothermally synthesized cobalt and zinc aluminate spinels, *J. Am. Ceram. Soc.* 85 (2002) 2949-2955.
- [5] M.T. Tsai, Y.S. Chang, I.B. Huang, B.Y. Pan, Luminescent and structural properties of manganese-doped zinc aluminate spinel nanocrystals, *Ceram. Int.* 39 (2013) 3691-3697.
- [6] C.C. Koch, Top-down synthesis of nanostructured materials: mechanical and thermal processing methods, *Rev. Adv. Mater. Sci.* 5 (2003) 91-99.
- [7] D. Arora, K. Asokan, A. Mahajan, H. Karu, D.P. Singh, Structural, optical and magnetic properties of Sm doped ZnO at dilute concentration, *Rsc. Adv.* 6 (2016) 78122-78131.
- [8] S.F. Wang, G.Z. Sun, L.M. Fang, L. Lei, X. Xiang, X.T. Zu, A comparative study of ZnAl_2O_4 nanoparticles synthesized from different aluminum salts for use as fluorescence materials, *Sci. Rep.* 5 (2015) 12849 DOI: 10.1038/srep12849.
- [9] D.L. Ge, Y.J. Fan, C.L. Qi, Z.X. Sun, X. Xiang, Facile synthesis of highly thermostable mesoporous ZnAl_2O_4 with adjustable pore size, *J. Mater. Chem. A* 1 (2013) 1651-1658.
- [10] C. Peng, J. Guo, M. Liu, Y. Zheng, T. Huang, D. Wu, Enhance ethanol sensing properties based on Sm_2O_3 -doped ZnO nanocomposites, *Rsc. Adv.* 4 (2014) 64093-64098.
- [11] G. An, S. Jin, C. Yang, Y. Zhou, X. Zhao, Photoluminescence enhancement and quenching of Sm, Au Co-doped TiO_2 , *Opt. Mater.* 35 (2012) 45-49.
- [12] E. Rusu, V. Ursaki, G. Novitschi, M. Vasile, P. Petrenco, L. Kulyuk, Luminescence properties ZnGa_2O_4 and ZnAl_2O_4 spinels doped with Eu^{3+} and Tb^{3+} ions, *Phys. Status Solidi C* 6 (2009) 1199-1202.
- [13] T. Wang, Y. Hu, L. Chen, X. Wang, G. Ju, Luminescent properties of a reddish orange long afterglow phosphor $\text{SrSnO}_3\text{:Sm}^{3+}$, *Radiat. Meas.* 73 (2015) 7-13.

Research Topic 2.3: Synthesis of bismuth oxide photocatalyst by thermal treatment assisted quenching process

Among functional metal oxide semiconductors, TiO_2 is currently one of the most widely used materials due to its distinguished properties including wide optical band gap (~ 3.2 eV), strong ultraviolet absorptivity, and non-toxicity [1]. Owing to its excellent properties, TiO_2 is utilized in various applications ranging from photocatalyst for organic pollutants degradation, the filler in polymer matrix in optical function as photo-carrier collector, and electron transport layer in optoelectronic device applications [2-3]. However, the rather high recombination of photogenerated electron-hole pairs and the weak absorption in visible region are its main drawbacks. Therefore, various techniques have been proposed in order to modify TiO_2 powder to overcome these inferiorities. A number of research works have employed the advantage of comparably large surface area of TiO_2 nanostructures such as thin film structure, nanoparticle, nanorod, nanosheet and nanotube to improve its performance. Recently, it was also reported that bismuth oxide (Bi_2O_3) is one of alternating method for efficient photocatalyst material [4]. The enhancement of the absorption in visible region is studied by Bi_2O_3 photocatalyst comparing with TiO_2 conventional material. The polymorphic forms of Bi_2O_3 are mainly in five phases as; α -, β -, γ -, δ - and ω - Bi_2O_3 [5]. The α -phase bismuth oxide is widely studied in photocatalytic properties due to stable phase at room temperature and direct band gap of 2.85 eV. Moreover, some researchers have been discovered high photocatalytic activity by β -phase bismuth oxide especially under visible light irradiation due to its small band gap (about 2.4 eV).

• ***Materials and Method***

Bi_2O_3 powder was prepared by thermal treatment assisted quenching process. Bismuth oxide carbonate ($(\text{BiO})_2\text{CO}_3$) supplied from Wako Company was used as precursor materials. Firstly, 3 g of $(\text{BiO})_2\text{CO}_3$ in white powder was loaded in alumina crucible following by annealed at 370 °C for 1.5 h. After that, obtained powder in orange color was contained in quenching process at 5 °C and 20 °C for 2 h. Finally, Bi_2O_3 powder was obtained in different color due to the effect of different phase as illustrated in Fig. 12. Bi_2O_3 powder at quenching temperature 5 °C appeared in strong orange powder, while, light yellow powder was obtained from Bi_2O_3 powder at quenching temperature 20 °C. The structural property was characterized by powder X-ray diffraction (XRD). The optical and photocatalytic properties of Bi_2O_3 powder were analyzed by UV-vis spectrometer. The photocatalytic efficiency of Bi_2O_3 powder with different phases was scrutinized by the photodegradation of aqueous methyl orange (MO) under Xenon lamp illumination and selected wavelength by solar simulator.

• ***Results and discussion***

Structural properties - XRD patterns of $(\text{BiO})_2\text{CO}_3$ precursor and Bi_2O_3 powder prepared by thermal treatment with different quenching temperatures were shown in Fig. 13. Prominent XRD peaks of $(\text{BiO})_2\text{CO}_3$ precursor as labeled at Fig. 10(a) were identified to $(\text{BiO})_2\text{CO}_3$ structure located at $2\theta = 23.7^\circ, 26.7^\circ, 30.0^\circ, 32.5^\circ, 35.1^\circ, 39.2^\circ, 42.0^\circ, 46.7^\circ, 48.7^\circ, 52.0^\circ, 53.2^\circ$, and 56.7° corresponding to (011) (004) (013) (110) (112) (006) (114) (020) (022) (116) and (113) planes of tetragonal phase, respectively (JCPDS No. 36-2450). Meanwhile, XRD peak at 50.1°

corresponded to graphite phase was clearly observed in precursor material. After thermal treatment and quenching process, XRD characteristics of the products were slightly different from $(\text{BiO})_2\text{CO}_3$ XRD pattern resulting in different crystalline structure by the effect of different rapid cooling system. XRD pattern of Bi_2O_3 powder at quenching temperature 20°C was certainly similar to well-defined $\alpha\text{-Bi}_2\text{O}_3$ structure (JCPDS No. 71-0465). For Bi_2O_3 powder at quenching temperature 5°C , XRD characteristic was identified to $\beta\text{-Bi}_2\text{O}_3$ structure (JCPDS No. 77-5341). This result indicated that the different phases of Bi_2O_3 powder were obtained due to the influence of quenching process leading to the color appearance of the products.

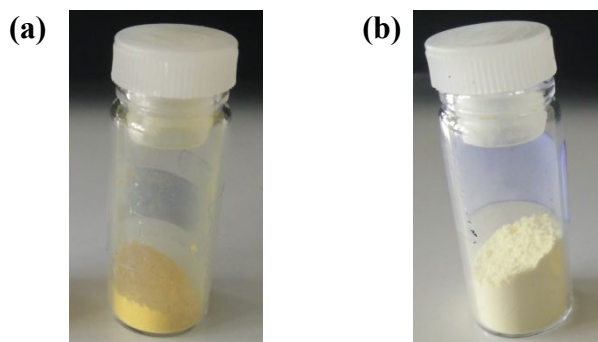


Fig. 12. Photographs of Bi_2O_3 powders by thermal treatment at different temperatures (a) 5°C and (b) 20°C .

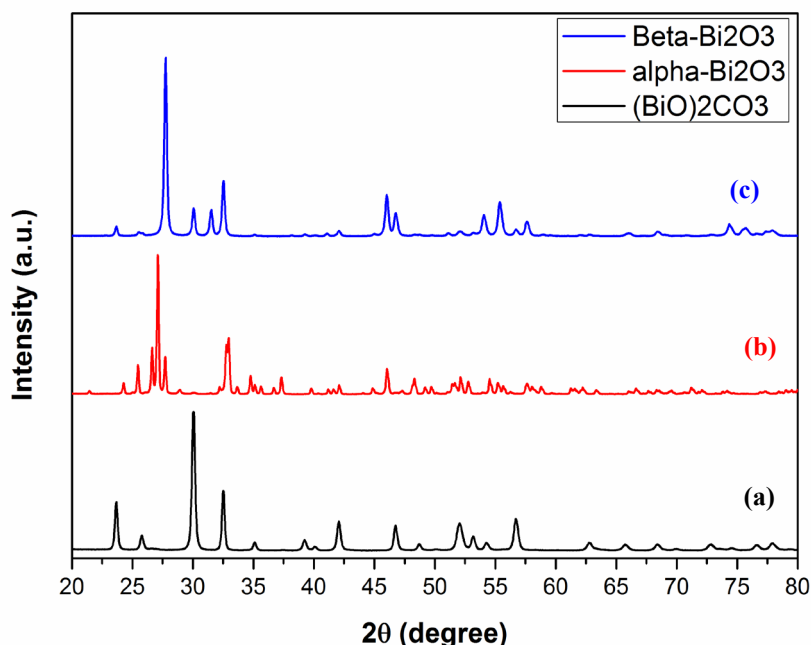


Fig. 13. XRD patterns of (a) $(\text{BiO})_2\text{CO}_3$ precursor and the products of (b) $\alpha\text{-Bi}_2\text{O}_3$ and (c) $\beta\text{-Bi}_2\text{O}_3$ powder at different quenching temperatures.

Optical properties - Reflectance spectra in the range 250-800 nm of $(\text{BiO})_2\text{CO}_3$ precursor and the products of Bi_2O_3 powder with different quenching temperatures are illustrated in Fig. 14. The strong absorption of $(\text{BiO})_2\text{CO}_3$ precursor in UV range as seen in Fig. 14(a) is originated from

a typical band gap energy at 2.94 eV [6]. The enhancement of optical absorption in visible light was clearly observed in the product of Bi_2O_3 powder after synthesized process. Moreover, the absorption edge of beta- Bi_2O_3 phase (Fig. 14(c)) slightly shifted to higher wavelength compared with alpha structure (Fig. 14(b)). These results showed that beta phase of Bi_2O_3 powder may associate with the absorption in visible region relating to the decrease of band gap energy in the material [7]. Therefore, the absorption spectra of β - Bi_2O_3 powder exhibits an obvious red-shift to higher wavelength in visible region relating to the study of its photocatalytic property in dye degradation under Xenon irradiation and solar simulator at specific wavelength.

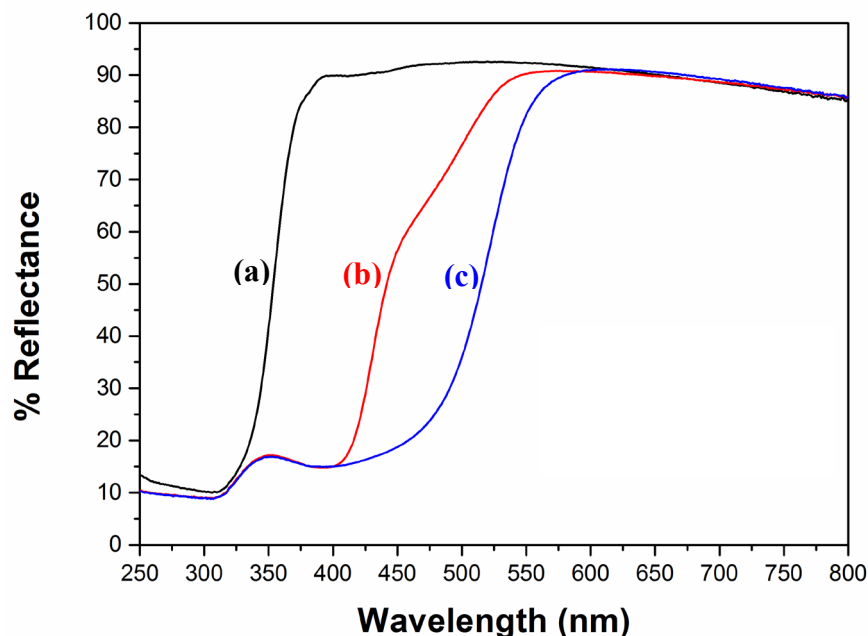


Fig. 14. UV-Vis spectra of (a) $(\text{BiO})_2\text{CO}_3$ precursor and the products of (b) alpha- Bi_2O_3 and (c) beta- Bi_2O_3 powder at different quenching temperatures.

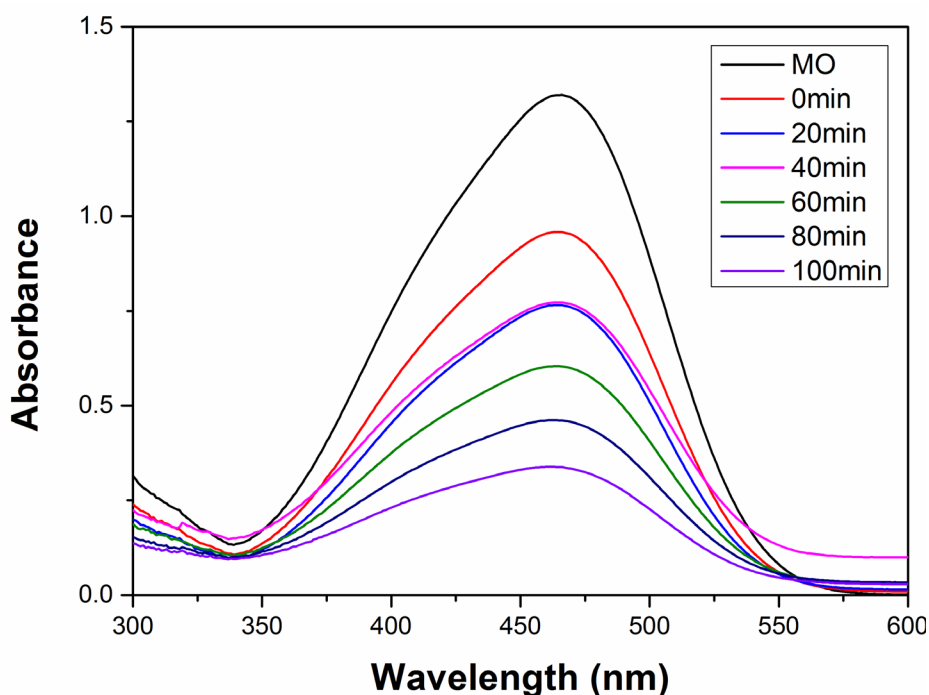


Fig. 15. Absorption spectra of MO under Xenon lamp irradiation using β - Bi_2O_3 photocatalyst.

Photocatalytic properties The photocatalytic efficiency of β - Bi_2O_3 photocatalyst was scrutinized by the photodegradation of aqueous MO under Xenon lamp illumination and corresponding results in term of reflectance spectrum are illustrated in Fig. 15. The photocatalytic activity by β - Bi_2O_3 photocatalyst is more effective, accompanying the continuous decrease of the absorption spectrum of the degradation of MO within 100 min. The hydroxyl and active oxygen groups from Bi_2O_3 photocatalyst play an important role in photocatalytic reaction to decompose a structure of organic molecules. If the photogenerated electron - hole pairs are unoccupied by water molecule or oxygen in the air to produce the radical groups.

• Conclusion

Bi_2O_3 powder was successfully prepared by facile process of heat treatment assisted with quenching process. For Bi_2O_3 photocatalyst utilization in MO degradation, excellent efficiency of the photocatalyst can be activated under visible light condition. In absence of light, MO concentration was decreased resulting in the adsorption on catalyst surface. Owing to high absorption in visible region, β -phase Bi_2O_3 can efficiently active in the catalytic performance in the photodegradation of aqueous MO. This feature could be explained by the decrease of band gap energy in this structure that synchronize with good absorption in visible light.

• References

- [1] B. Cheng, Y. Le, J. Yu, Preparation and enhanced photocatalytic activity of $\text{Ag}@\text{TiO}_2$ core-shell nanocomposite nanowires, *J. Hazard. Mater.* 177 (2010) 971-977.
- [2] Q. Chena, H. Liua, Y. Xin, W.X. Cheng, TiO_2 nanobelts - Effect of calcination temperature on optical, photoelectrochemical and photocatalytic properties, *Electroch. Acta.* 111 (2013) 284-291.
- [3] Y. Lee, J. Chae, M. Kang, Comparison of the photovoltaic efficiency on DSSC for nanometer sized TiO_2 using a conventional sol-gel and solvothermal methods, *J. Ind. Eng. Chem.* 16 (2010) 609-614.
- [4] G. Zhu, W. Que, J. Zhang, Synthesis and photocatalytic performance of Ag-loaded β - Bi_2O_3 microspheres under visible light irradiation, *J. Alloys Comp.* 509 (2011) 9479-9486.
- [5] P.Y. Ayekoe, D. Robert, D.L. Goné, $\text{TiO}_2/\text{Bi}_2\text{O}_3$ photocatalysts for elimination of water contaminants. Part 1: synthesis of α - and β - Bi_2O_3 nanoparticles, *Environ. Chem. Lett.* 13 (2015) 327-332.
- [6] J. Cao, X. Li, H. Lin, S. Chen, X. Fu, In situ preparation of novel p-n junction photocatalyst $\text{BiOI}/(\text{BiO})_2\text{CO}_3$ with enhanced visible light photocatalytic activity, *J. Hazard. Mater.* 239-240 (2012) 316-324.
- [7] M. Schlesinger, M. Weber, S. Schulze, M. Hietschold, M. Mehring, Metastable β - Bi_2O_3 nanoparticles with potential for photocatalytic water purification using visible light irradiation, *Chemistry Open* 2 (2013) 146-155.

Research Topic 2.4: Efficiency Enhancement of Natural-mineral-derived Titanium Dioxide Nanoparticle for earthenware-roof tile coating material.

Nowadays, titanium dioxide (TiO_2) materials are populating in many industrials because of their various properties such as self-cleaning application, antibacterial, white pigment and sunscreen component in cosmetic industrial [1] resulting to the increase of TiO_2 demand. Therefore, several research try to studying the product of synthesize TiO_2 from natural because TiO_2 is found in the natural in form of mineral ores such as ilmenite, leucoxene and rutile ores. There are various processes to synthesize TiO_2 from mineral, for example, hydrothermal and leaching process [2-3]. The leaching process was interested method due to non-complex system and facile equipment during synthesis. Meanwhile, high energy ball milling process is one of potential process for the reduction in precursor size relating to the enhancement of leaching reaction between precursor and acid solution [4]. TiO_2 material is proposed to good photocatalyst material in photocatalytic application. The applications of TiO_2 surface coating base on photocatalytic application were used in public furniture, manufacturing and building [6,7]. TiO_2 coating process on substrate has been reported by various methods such as thermal evaporation method, sputtering and wet chemical process [8]. Among of these methods, wet chemical

processes via spin coating and dip coating process is proposed due to facile operation and low cost. Mostly, TiO_2 films prepared from sol-gel solution process were chosen by optimized method depending on the application and specimen size.

- ***Materials and Method***

On this research, tetraethyl orthosilicate (TEOS) was purchased from Sigma Aldrich, hydrochloric acid from Ajax Finechem, absolute ethanol from Merck. Leucoxene ores were supported by Sakorn Minerals Co., Ltd. Leached leucoxene or synthetic rutile was derived from leucoxene mineral with high energy balling assist using speed at 600 rpm for 30 minutes. After milling process, fine leucoxene powder was treated with heated 7 M hydrochloric acid at 80 °C as reagent in acidic leaching process. This solution was continuously stirred for 5 h. After completely retention time, the residual was separated from the suspension. The leached residue was several washed with deionized water to obtain pH 7 and dried at 100 °C for 24 h to remove the moisture in the residue. For leucoxene ore, synthesized process was used as same condition for leached leucoxene residue. Completely, leached leucoxene or synthetic rutile was appeared as brown powder. Optical properties of synthetic rutile-based were investigated by UV-Visible spectroscopy technique; meanwhile, the relevant crystalline structure was characterized by X-ray diffraction. For coating material on earthenware-roof tile, leached leucoxene was coated on ceramic tile from Thailand by dip-coating method with TEOS or PEG as binder solution. After coating process, leached leucoxene coated on ceramic tiles were calcined by furnace at 500 °C for 2 h to obtain testing specimens. Degradation of organic dye (Rhodamine B) was used to study of photocatalytic activity of leached leucoxene under visible light exposed from solar simulator machine.

- ***Results and discussion***

- *TiO₂-based Material results*

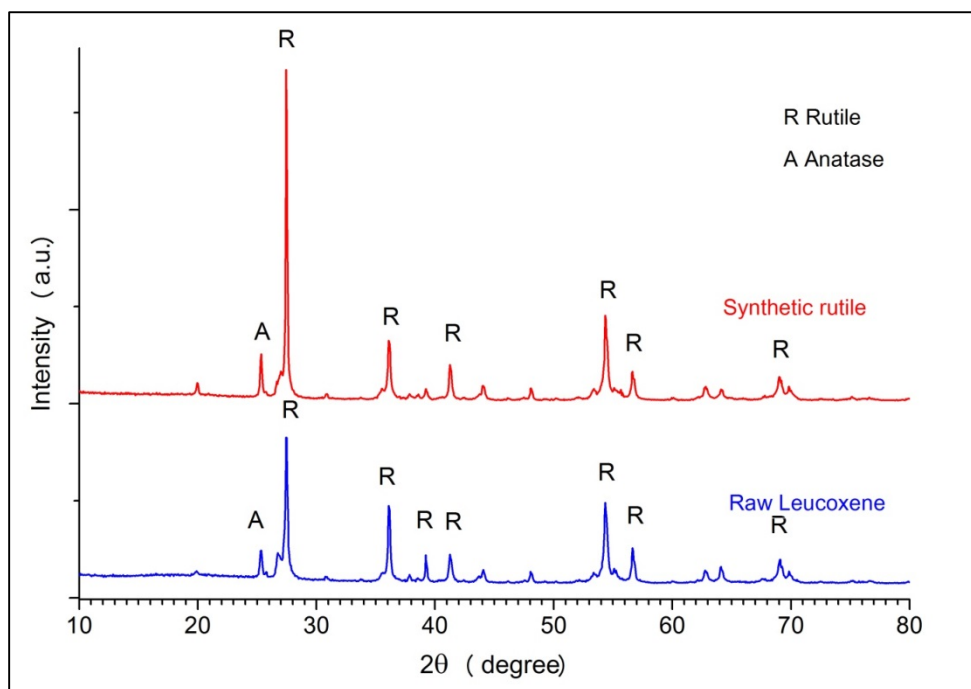


Fig. 16. XRD pattern of (a) raw leucoxene and (b) synthetic rutile residue.

Crystalline structure - Crystallinity of raw leucoxene and synthetic rutile were characterized by X-rays Diffraction technique. Crystalline structure of raw leucoxene was shown in Fig. 16. The majority crystalline fingerprint of raw leucoxene and synthetic rutile were indexed as rutile (R) structure at $2\theta = 27.4^\circ, 36.1^\circ, 39.2^\circ, 41.4^\circ, 44.2^\circ, 54.3^\circ$ and 56.6° [JCPDS 01-075-1755] corresponding to (110) (101) (200) (111) (210) (211) and (220). Meanwhile, the other diffracted peaks located at $2\theta = 25.4^\circ$ [JCPDS 21-1272] were related to anatase (A) phase at 101 plane. Comparison of crystalline structure between raw leucoxene and synthetic rutile, strong intensity of rutile phase was obviously appeared in synthetic rutile sample because of the influence of acidic leaching process relating to high crystallinity.

Optical property - The optical band gap of raw leucoxene and synthetic rutile were shown in Fig 17. Tauc – Plot equation was used to calculate optical band gap of both specimens. Calculation of optical band gap of raw leucoxene was appeared at $E_g = 3.07$ eV related to active wavelength about 400 nm while $E_g = 2.82$ eV was appeared for synthetic rutile refer to 440 nm was visible light active region. Optical band gap of synthetic rutile was decreased because of extraction of leucoxene mineral. Compared with TiO_2 (P25) commercial was 3.02 eV for optical band gap relate to ultraviolet active region. Synthetic rutile was had optical band gap lower than TiO_2 commercial because of behaviorism of impurity in mineral liked metal doped titanium dioxide.

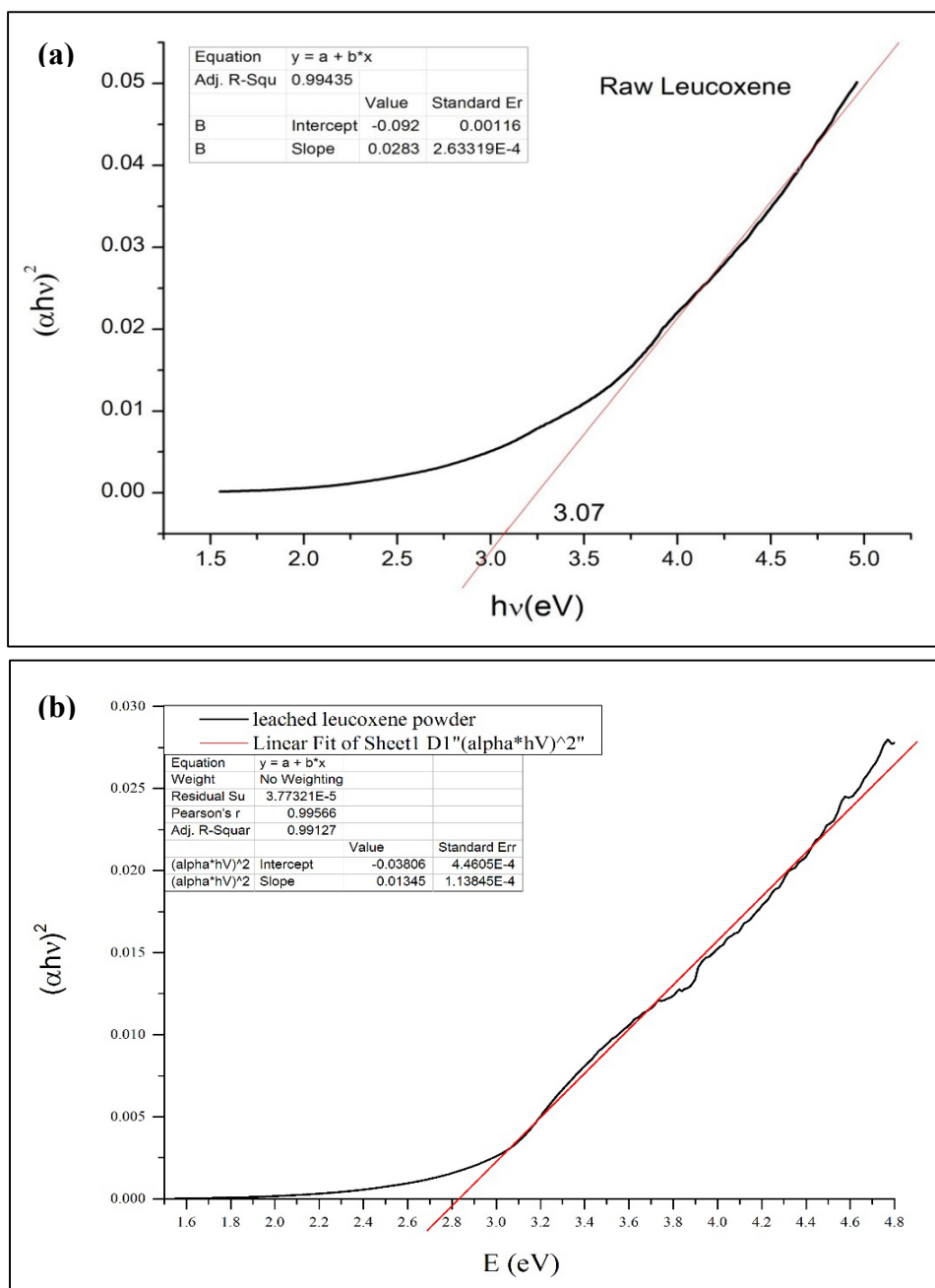


Fig 17. Tauc – Plot calculation of (a) raw leucoxene powder and (b) synthetic rutile powder.

Photocatalytic activity - Photocatalytic activity of raw leucoxene and synthetic rutile was studied by the degradation of Rhodamine B (RhB) organic dye under specific wavelength irradiation. In Fig.18, slightly changing of RhB concentration by raw leucoxene and synthetic rutile photocatalyst was occurred because of low intensity of solar light from simulator machine in photocatalytic reaction. Therefore, photocatalytic test under Xenon lamp illumination was instead of solar simulator as shown in Fig. 19. The decrease of RhB concentration was obviously occurred following by the increase of illumination time. RhB concentration was degraded to 40% by synthetic rutile photocatalyst. Meanwhile, raw leucoxene photocatalyst reduced RhB concentration to 30% due to the presence of rutile phase in the structure.

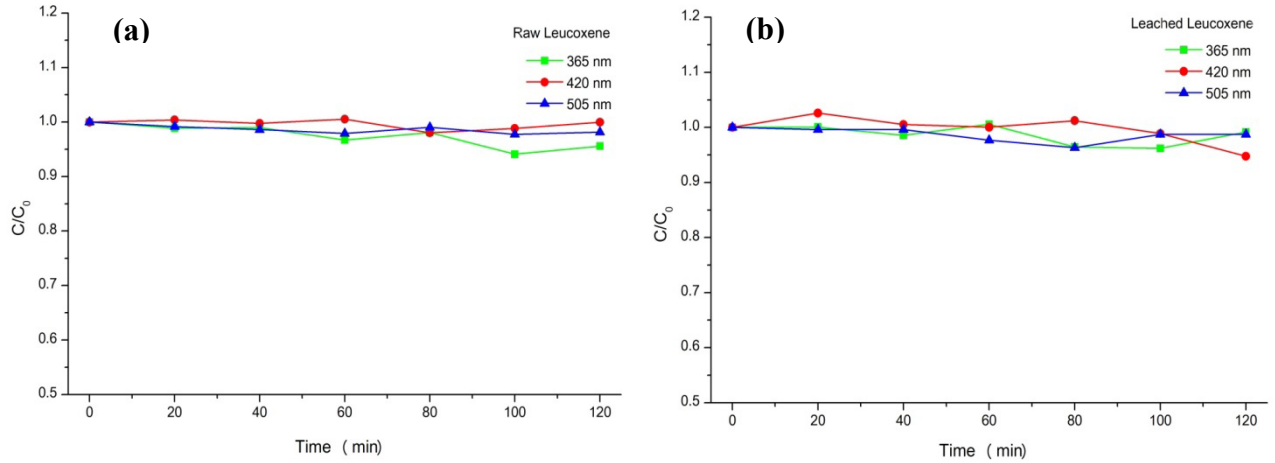


Fig. 18. Degradation of Rhodamine B organic dye under solar simulator light source using (a) raw leucoxene and (b) synthetic- rutile as photocatalyst materials.

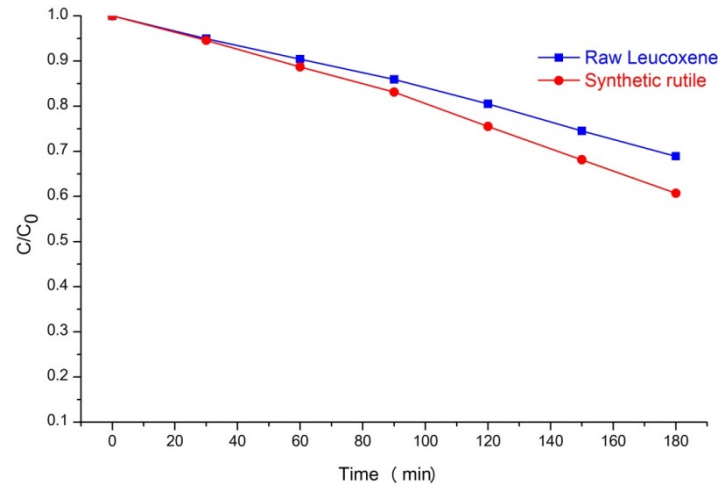


Fig. 19. Degradation rate of Rhodamine B organic dye under Xenon lamp irradiation using raw leucoxene and synthetic rutile as photocatalyst materials.

○ *The results of TiO_2 -based Material coating on tile*

Morphology- The morphologies of leucoxene/TEOS films were investigated by SEM images in Fig. 20. The morphology was obtained flack liked structure from TEOS used as binder solution and dispersion of leached leucoxene residue particle in film were obtained in SEM image. To confirm the presence of leached leucoxene residue in film, the element compositions of film, raw mineral and leached leucoxene powder were investigated by EDX technique as shown in Table 2. Ti element on the film from EDX data was identified by the leached leucoxene in film. However, high concentration of silicon element detected because of TEOS binder and glass substrate. The low concentration of Ti element on films because the TiO_2 was dispersed as particle

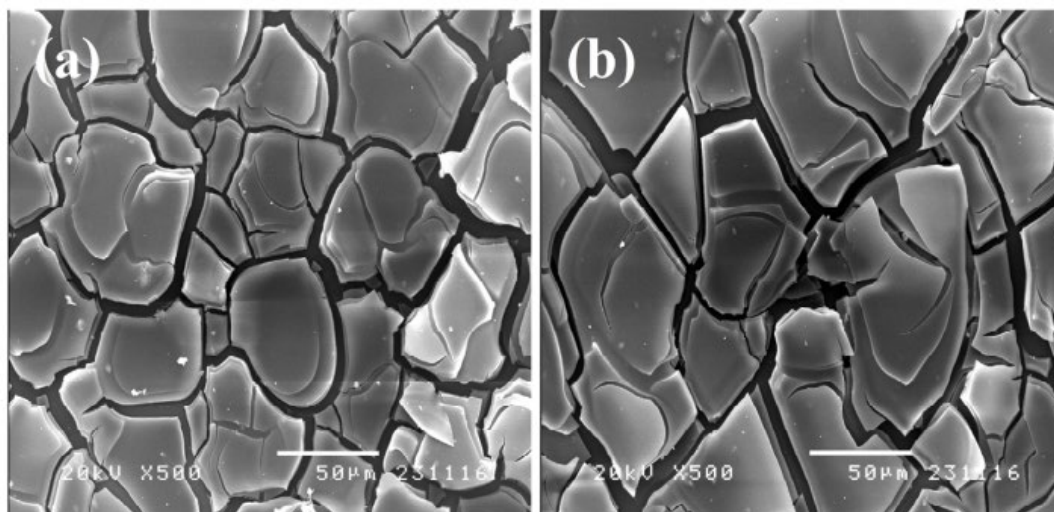


Fig. 20. SEM images of leucoxene film varied dip coating speed (a) 70 mm/min and (b) 100 mm/min

Table 2. Chemical elements on leucoxene/TEOS film by EDX analysis.

Element	70 mm/min		100 mm/min		Raw leucoxewne		leached leucoxene	
	wt%	Atomic%	wt%	Atomic%	wt%	Atomic%	wt%	Atomic%
C	26.28	38.03	26.82	38.27	-	-	-	-
O	35.22	38.27	37.27	39.93	48.69	73.99	46.18	71.98
Si	57.99	23.51	35.46	21.64	-	-	-	-
Ti	0.51	0.19	0.45	0.16	49.79	25.35	53.18	27.73
Total	100.00	100.00	100.00	100.00	100.00	100.00	100.00	100.00

Hydrophilic property-The hydrophilic property on leucoxene/TEOS films with different dip coating speed was investigated by contact angle measurement under various light source irradiation. The contact angle measurement data of leucoxene/TEOS films was shown in Table 3. High values of contact angle on leucoxene/TEOS films in non-irradiation condition were approximately 68° and 49° by dip coating speed at 70 and 100 mm/min, respectively. For UV irradiation on the films, the contact angle value of dip coating speed 70 and 100 mm/min were 22.28° and 15.12°. Meanwhile, the reduction of contact angle value on the film under visible light irradiation was approximately 40.18° and 22.00°, respectively. The improvement of hydrophilic property by leucoxene/TEOS films was obtained at dip coating speed at 70 mm/min due to high Ti content on the film according to EDX result in Table 2. The decrease of contact angle of leached leucoxene films under light irradiation was obtained due to hydrophilic property from the amount of TiO₂ on the films. The lowest value of contact angle by leucoxene/TEOS film was occurred under visible irradiation corresponding to the proper activated region of this material due to Fe impurity in leached leucoxene. Therefore, the active wavelength of leached leucoxene photocatalyst showed high absorption spectra in visible region compared with non-irradiation and UV treatment

Table 3. Contact angle measurement of leucoxene/TEOS films using different light source irradiation.

Sample	non irradiation	UV	Visible
TEOS+Leu 70mm/min	68.497	22.285	15.120
TEOS+Leu 100mm/min	49.472	40.184	22.002

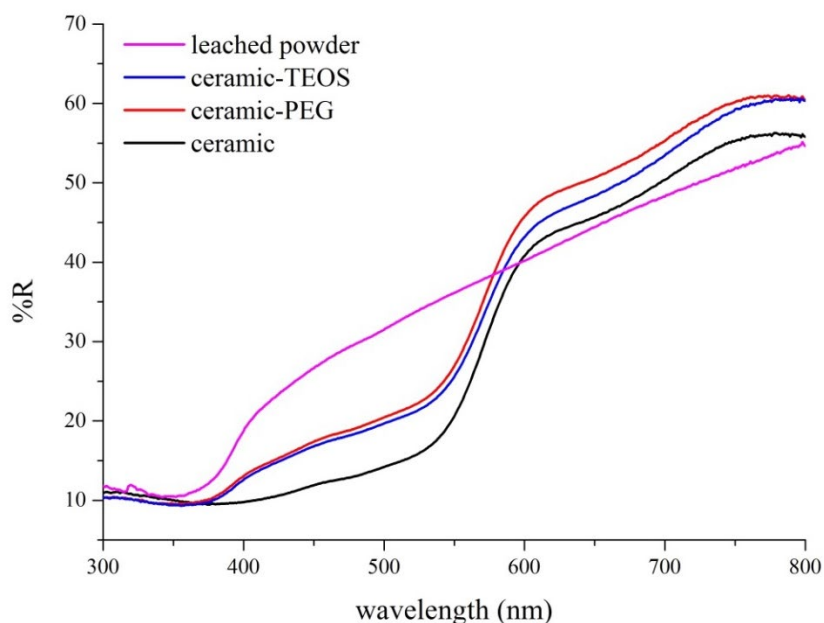


Fig. 21. Reflection results of synthetic rutile (leached powder), uncoated ceramic (ceramic), ceramic coated with PEG (ceramic-PEG) and TEOS (ceramic-TEOS) binder solution.

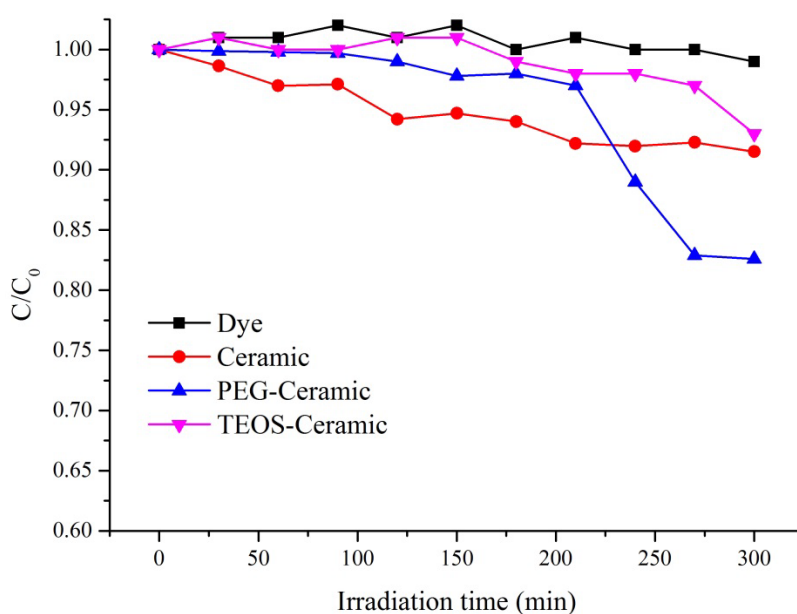


Fig. 22. Photocatalytic activity of synthetic rutile coated ceramic tile using different binder solution.

Optical and photocatalytic properties- For coating on earthenware-roof tile, synthetic rutile or leached leucoxene was used as coating materials on ceramic tile combined with binder solution such as polyethylene glycol (PEG) and Tetraethyl Orthosilicate (TEOS). Coating solution was coated on ceramic tile by dip coating method varies binder solution. After coating process, coated ceramic tiles were calcined in furnace at 500°C for 2 hours to obtain brown layer on ceramic tile. The optical property of synthetic rutile coated ceramic tile was studied by Diffuse Reflectance Spectroscopy (DRS) as shown in Fig. 21. Reflection spectra wavelength 400 – 550 nm was increased comparing with uncoated because of coating of synthetic rutile on ceramic. This result was confirmed the composition on ceramic surface composed with synthetic rutile. Photocatalytic activity of coated ceramic tile using different binder solution was studied by decomposition of RhB organic dye under visible irradiation as shown in Fig. 22. The good property of photocatalytic activity of coated ceramic tile was appeared 20% decomposition of RhB for synthetic rutilecoated ceramic tile using PEG as binder solution while TEOS as binder solution was slightly decomposed. This result presented PEG binder solution was good binder for coating of synthetic rutile on ceramic tile substrate.

• Conclusion

In this research, synthetic rutile photocatalyst dervied from natural mineral was successfully obtained by milling and acid leaching process. Band gap energy of synthetic rutile decreased to 2.8 eV after the acid purification relating to high photocatalytic activity under visible light irradiaiton. XRD results showed that the increase of anatase phase and synthetic rutile phase of leached leucoxene residue was evidently occurred. For the application of coated synthetic rutile on ceramic tile, well-defined formation of TiO₂ structure was occurred after leaching process as corresponding to absorbance spectrum. The photocatalyst and hydrophilic properties were depended on TiO₂ from leached leucoxene. The improvement of hydrophilic property of leached-leucoxene/TEOS film was shown by the decrease of contact angle under light irradiation. Due to the highest Ti element concentration on dip coating speed at 70 mm/s on the films as shown in EDX results, the lowest value of contact angle was obtained under visible light approached by mean of contact angle at 15.120° from 68.497° compared with non-irradiation condition. Meanwhile, the photocatalytic activity of leucoxene/TEOS film was higher than pure TEOS film due to the influence of high Ti composition and Fe dopant by leached leucoxene residue in the film. These propose can be increased valuable of leucoxene mineral and ceramic tile industry.

• Reference

- [1] N. E. Hazek, T.A.Lasheen, R. El-Sheikh, S.A. Zaki, Hydromatallurgy, 87 (2007) 45-50.
- [2] G.K. Das, Y. Pranolo, Z. Zhu, C.Y. Cheng, Hydromatallurgy, 133 (2013) 94-99.
- [3] P.G. Muñoz, G. Pliego, J.A. Zazo, A. Bahamocde, J.A. Casas, J. Environ. Chem. Eng. 4 (2016), 542-548.
- [4] J. Zhang, Q. Zhu, Z. Xie, H. Li, Hydrometallurgy, 157 (2015) 226-233.
- [5] T.S. Mackey, Ind. Eng. Chem. Res. 13 (1974).
- [6] H. Yaghoubi, N. Taghavinia, E.K. Alamdari, Surf. Coat. Tech. 203 (2010) 1562-1568.
- [7] R.J. Pan, S.L. Yang, Adv. Matter. Res. 704 (2013) 77-86.
- [8] J. Yu, Y. Chen, J. Alloys. Compd. 504S (2010) S364 - S367.

Research Topic 2.5: Size Reduction of Ultrafine ZnO Powder by High Energy Mechanical Milling Process

In presence, Zinc oxide (ZnO) is widely used as a functional material regarding its prominent properties including wide band gap semiconducting behavior (3.37 eV), high electron mobility, thermal and chemical stability, large exciton binding energy and non-toxicity [1]. Therefore, ZnO materials have been implemented in many demanding technological applications such as photocatalytic oxidation technology, transparent electronic device, ultrasonic transducers and gas sensors [2-5]. To enhance ZnO properties for specific applications, synthesis of ZnO particles in nano-scaled is required. Bottom-up process is a proper process to synthesize ZnO nanoparticles, for instance, chemical vapor deposition, hydrothermal process, spray pyrolysis, precipitation method [6-9]. However, commercial ZnO powder has been found in micron scale. Bottom-up techniques are unsuitable in ZnO powder precursor. On the other hand, top-down process could be alternative route to reduce material particles down to nano-scale and could be properly applied in industrial process. High energy ball milling process is a kind of appropriate technique for size reduction of materials by mechanical mechanism relating to high surface area of the product [10]. In milling process, the containers are rotated with high speed resulting to high centrifugal force for particle reduction. Hence, precursor material is milled by large energy in the process with the collision and friction of balls with the container wall under high speed milling process.

• *Materials and Method*

Commercial zinc oxide (ZnO) powder with average particle size of 800 nm was used as precursor material for high energy planetary ball milling method. 5 g of ZnO powder and 150 g of zirconia balls with diameter 1 mm were loaded in zirconia containers. The ball milling process was operated at room temperature and ambient air atmosphere. The milling speed was varied from 200 to 600 rpm for 10 min while milling time was varied in range of 0 to 30 min at speed 500 rpm. ZnO ultrafine powders after milling process were investigated by various techniques. Crystalline structure and phase identification was characterized by X-ray diffractometer (XRD). Surface morphologies of before/after-milled products were monitored by scanning electron microscopy (SEM). Meanwhile, averaged ZnO particle sizes were monitored by particle analyzer.

• *Results and discussion*

Particle size analysis- The average particle size of ZnO powders milled at different milling speeds and times is depicted in Fig. 23. Precursor ZnO powder is found to be in 0.5-0.8 microcrystal particles. Regarding the effect of milling speed, ZnO particle size is drastically decreased with increasing milling speed as shown in Fig. 23(a). Based on experimental result, the optimized speed for ZnO powder in high energy milling process is found to be at 500 rpm that results to the smallest average particle size of about 225 nm. Due to strong high impact in milling process, the fractures and collisions between balls and material are enhanced by higher speed resulting to particle size reduction in the product [11]. Meanwhile, size reduction of ZnO powder can be affected by milling time (Fig. 23(b)). In our case, the smallest particle size is

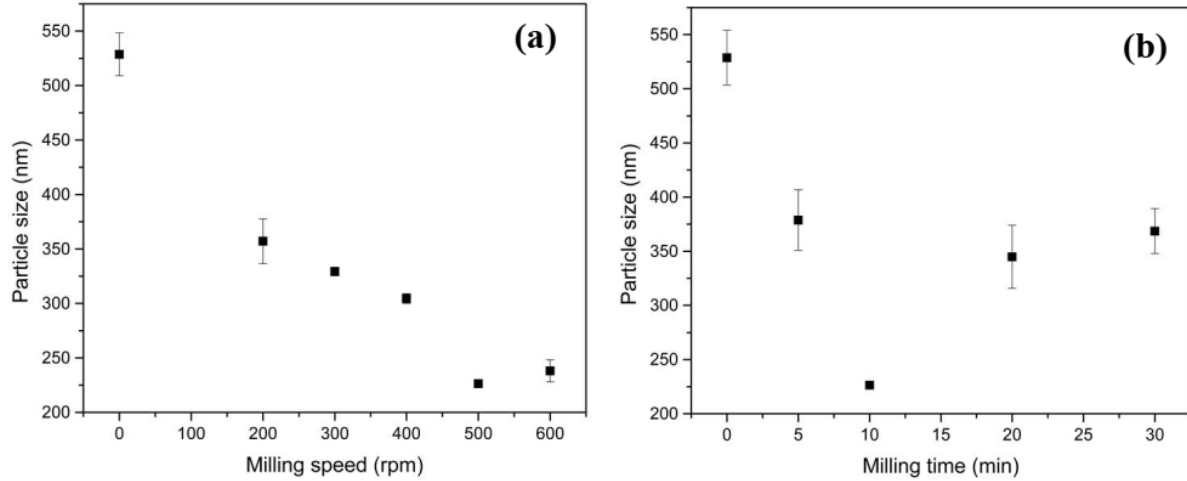


Fig. 23. Average particle size of ZnO powder with (a) different milling speeds during 10 min and (b) different milling times operated at 500 rpm.

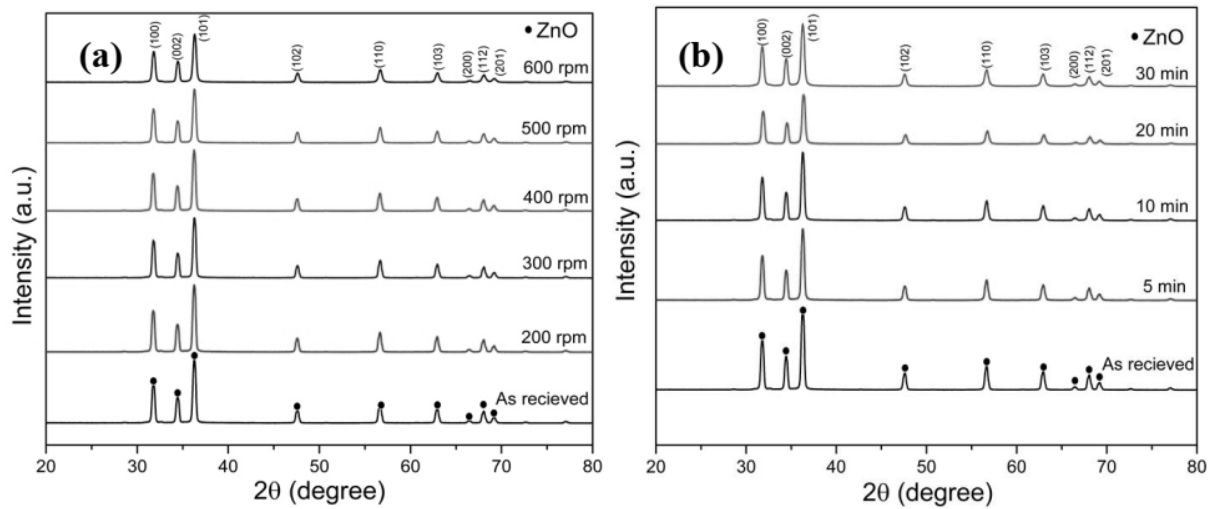


Fig. 24. XRD patterns of ZnO powder milled at (a) different milling speeds during 10 min and (b) different milling times operated at 500 rpm.

obviously occurred at 10 min operation time with milling speed of 500 rpm. After milling time increase beyond 10 min, ZnO particle size tends to increase owing to the agglomeration of ZnO particle by the accumulation of high energy in milling process.

Crystal structure- XRD patterns of ZnO powders milled at different speeds and times are shown in Fig. 25. The prominent peaks located at 2θ of 31.3° , 34.4° , 36.9° , 47.7° , 56.5° , 63.0° , 68.0° , 69.0° and 72.5° correspond to (100) (002) (101) (102) (110) (103) (200) (112) (201) and (004) planes, respectively (JCPDS No. 36-1451). All diffraction peaks of milled ZnO nanopowders with various operated speeds and times exhibit same pattern without impurity or contaminated phase comparing to precursor ZnO. For the samples operated at different milling speeds as illustrated in Fig. 24(a), the XRD patterns of milled ZnO powder show identical peak pattern and sharp intense peak of pure crystallite ZnO powder at low speed around 200 to 300 rpm. Moreover, peak intensity insignificantly drops by the effect of high attraction in high speed rotation around 500 rpm. Meanwhile, XRD patterns of ZnO nanopowders with various milling

times are also depicted in Fig. 24(b). As milling time increases, the (002) main peak is noticeably widened indicating the size reduction of the sample. The crystallite size of all samples by prominent three peaks at $2\theta = 31.7^\circ$, 34.5° and 36.6° were calculated by Scherrer's equation [12] as shown in Table 4. These results suggest that size of ZnO nanopowders could be significantly reduced by high energy milling method without post-annealing process corresponding to XRD patterns.

Table 4. Crystallite size of ZnO nanopowders with different milling speed and time by high energy ball milling process.

Crucial parameter	Crystalline size (nm)									
	ZnO precursor	200 rpm	300 rpm	400 rpm	500 rpm	600 rpm	5 min	10 min	20 min	30 min
Milling time	25	40	29	27	24	22	-	-	-	-
Milling speed	25	-	-	-	-	-	40	25	28	22

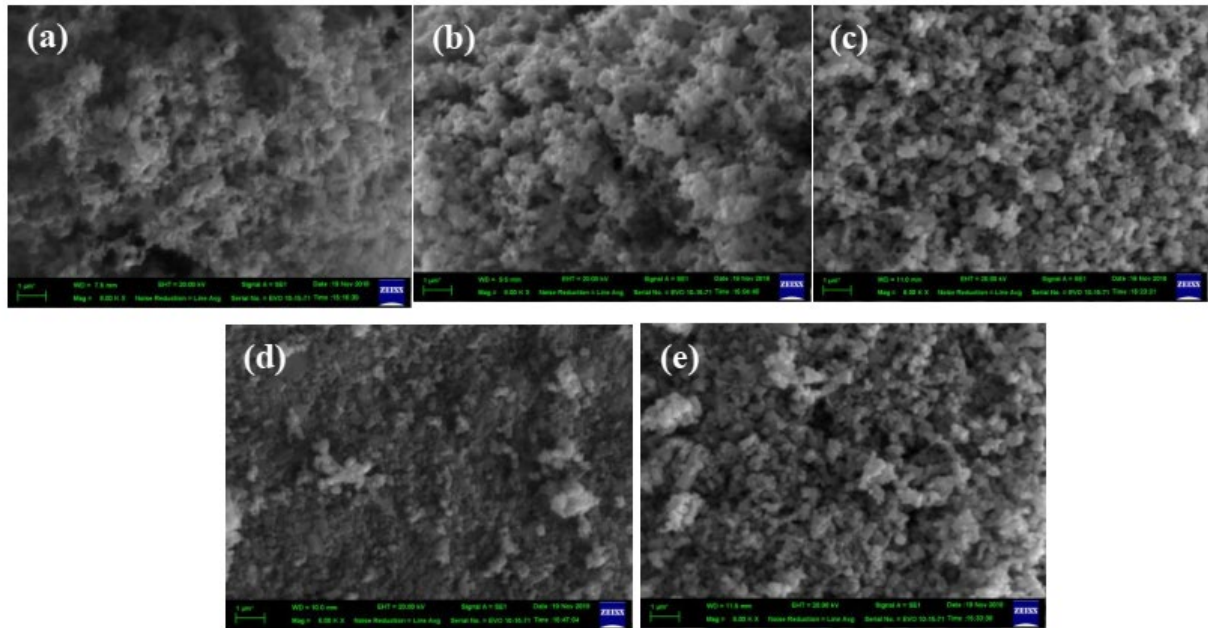


Fig. 25. SEM images of ZnO powder milled for 10 min with different speeds; (a) as-received, (b) 200 rpm, (c) 300 rpm, (d) 500 rpm and (e) 600 rpm.

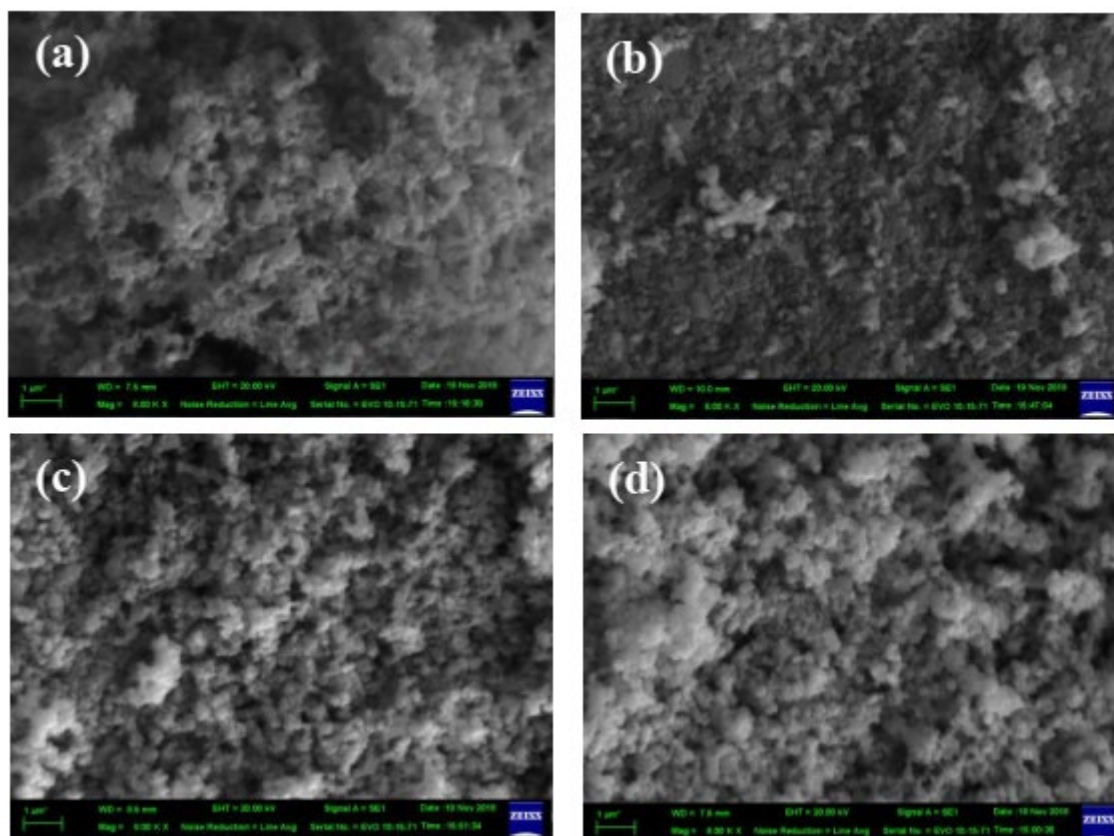


Fig. 26. SEM images of ZnO powders milled at 500 rpm with different times; (a) as-received, (b) 10 min, (c) 20 min, (d) 30 min.

Morphology- SEM morphologies of ZnO powders milled at different speeds at 0 to 600 rpm are depicted in Fig. 25. As-received ZnO powder exhibits the difference in its size and its morphology is found to be quasi spherical and rod shape. After milling process, ZnO particle size and shape significantly change to fine powder depending on the milling speed. In Fig. 26, the milling time was varied, ZnO particle size was slightly changed to small particles with good dispersion, specifically at operating time of 10 min corresponding to particle size analysis. However, ZnO particles could be aggregated with prolong milling time due to high accumulation of thermal energy relating to the induction of large particles. Therefore, particles size, size distribution, homogenous powder is highly influenced by milling speed and time. In addition, it is suggested that particle size reduction and shape morphology could be controlled by high speed and optimized milling time in milling process

• **Conclusions**

In summary, ZnO nanopowders were prepared by high energy ball milling process. ZnO particle size was reduced from 500 nm to 250 nm after milling process at 500 rpm in 10 min due to mechanical force with ball and material mechanism. XRD patterns of ZnO nanoparticles exhibit single phase of ZnO hexagonal structure without any impurities. Meanwhile, the reduction of ZnO crystallite size after milling process was obviously occurred depending on the variation of milling speed and time. Meanwhile, SEM images indicated that surface morphology of ZnO structures

were in small and fine particles corresponding to the deterioration of crystallite size at (101) plane in XRD.

• **Reference**

- [1] Karimi M, Ezzati M, Akbari S and Lejbini M B 2013 Curr. Appl. Phys. 13 1758.
- [2] Xie J, Li Y, Zhao W, Bian L and Wei Y 2011 Powder Technol. 207 140.
- [3] Muhammad N M, Duraisamy N, Dang H W, Jo J and Choi K H 2012 Thin Solid Films 520 6398.
- [4] Zhou X S, Zhang J, Hou R, Zhao C, Kirk K J, Hutson D, Hu P A, Peng S M, Zu X T and Fu Y Q 2014 Appl. Surf. Sci. 315 307.
- [5] Wen Z, Zhu L, Zhang Z and Ye Z 2015 Sens. Actuators B 208 112.
- [6] Burova L I, Perov N S, Semisalova A S, Kulbachinskii V A, Kytin V G, Roddatis V V, Vasiliev A L and Kaul A R 2012 Thin Solid Films 520 4580.
- [7] Sun Y, Guo H, Zhang W, Zhou T, Qiu Y, Xu K, Zhang B and Yang H 2016 Ceram. Int. 42 9648.
- [8] Lee S D, Nam S H, Kim M H and Boo J H 2012 Phys. Procedia. 32 320.
- [9] Junlabhut P, Mekprasart W, Noonuruk R, Chongsri K and Pecharapa W 2014 Energy Procedia 56 560.
- [10] Leonel E C, Nassar E J, Ciuffi K J, Reis M J and Calef P S 2014 Cerâmica 60 267.
- [11] Amirkhanlou S, Ketabchi M and Parvin N 2012 Mater. Lett. 86 122.
- [12] Chen Z, Shi E, Zheng Y, Li W, Wu N and Zhong W 2002 Mater. Lett. 56 601.

Research Topic 2.6: Characterization of BiVO₄ Nanoparticles Prepared by Sonochemical Process

Nowadays, environmental pollution has considerably increased and has been concerned with human health. Wastewater from many industries such as textile and paper industries highly contain various hazardous organic compounds [1]. Decomposition of highly toxic organic compound to the lowest toxic or nontoxic composition using photocatalytic reaction has been considered as an effective treatment route. Metal oxide photocatalyst materials such as BiWO₄ and BiVO₄ have obtained considerable interest regarding beneficial and green technology for addressing environmental pollutant problems. BiVO₄ is the one of effective photocatalyst materials because of its stability in environment, low toxicity, low energy band gap for octahedral structure (c-BiVO₄) that can be activated by visible light [2] and ease of synthesis by various facile synthesis processes. Referring to previous reports, BiVO₄ could be prepared by different processes including high temperature hydrothermal process (~200 °C), solid state reaction, coprecipitation with and without calcination treatment process (~700 °C for 8 h) [3]. However, those mentioned synthesis methods typically require many processing steps or using high temperature and long reaction time for synthesis. Hence, it is mandatory to find the simple and eco-friendly process or synthesis route for preparing BiVO₄ particles. Sonochemical technique has become a great challenge way for nanoparticle preparation that can shorten time of fabrication and provide uniformity of the product [4, 5]. During sonochemical process, collapse bubbles induced by ultrasonic wave can potentially generate extremely localized hot spot with high transient temperature ~5000 K and pressure ~20 MPa. This uttermost condition can effectively quicken the hydrolysis, condensation or correlated chemical reactions [6]. From the literature survey, BiVO₄ prepared by single step has been so far reported. In this report, the single step of sonochemical method was employed for synthesizing functional BiVO₄ nanoparticles proposed as a visible-driven photocatalyst. The crystallinity, morphology, chemical bonding of as-synthesized particles was scrutinized. The photocatalytic activity was tested by degradation of Rhodamine B dye in aqueous model solution under visible light irradiation.

• *Materials and Method*

Bismuth nitrate pentahydrate (Bi(NO₃)₃•5H₂O), Ammonium metavanadate (NH₄VO₃) purchased from Ajax Finechem were used as starting precursors of Bi and V sources. For preparation of BiVO₄ powder, the sonochemical process was used according to the following steps. Firstly, Bi(NO₃)₃•5H₂O and NH₄VO₃ powder was separately dissolved in deionized water (DI water) under continuous magnetical stirring at room temperature to obtain homogeneous aqueous solution. After that, both precursors were mixed then ammonium hydroxide (NH₄OH) solution was added dropwise into the mixed solution until designated pH value (3, 5, 7, 10 and 11) was reached. Finally, the mixed precursor was poured in sonochemical chamber and irradiated under ultrahigh sonicator (750W, 20kHz) operated at room temperature for 30 minutes. The after-sonicated colloidal solution was washed with DI water until the pH became neutral and then dried at 100 °C for 24 hours.

X-Ray diffraction technique was used to investigate the crystalline structure of the prepared samples. The synthesized particle size was measured by particle analyzer spectrometer by suspension in DI water. Relevant chemical bondings of the samples were characterized by Fourier transform infrared spectrometer (PerkinElmer Spectrum Two) and Raman spectroscopy (Thermo Scientific DRX SmartRaman).

The photocatalytic performance of prepared samples was evaluated using RhB degradation as a testing reaction. The photocatalytic activity was carried out by the degradation of aqueous Rhodamine B (0.01mmol) dye under visible light irradiation using the samples synthesized at various pH as photocatalysts. The 0.1 g of as-prepared catalyst was added into 100 ml of dye solution then the suspension was stirred for 30 min without irradiation to ensure the establishment of adsorption/desorption between dye and catalyst followed by the irradiation with visible light. During the photocatalytic reaction, 5mL of dye solution was taken at selected time interval. The concentration of RhB was measured by mean of its absorbance using UV-Vis spectroscopy. The degradation rate of RhB solution was defined by following equation: $D = A_t/A_0 \times 100\%$. Where A_0 is the absorbance value of initial RhB solution, A_t is a absorbance value of degraded RhB solution at the irradiation time t .

• Results and discussion

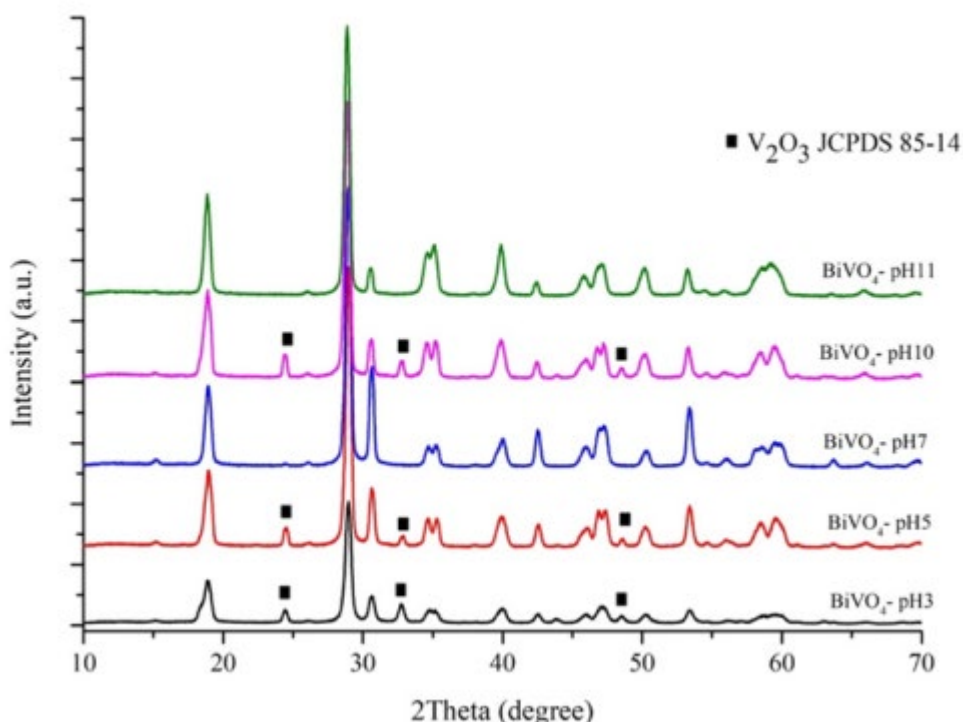


Fig. 27. X-rays diffractogram of as prepared BiVO_4 with different pH value of solution (pH = 3, 5, 7, 10 and 11).

The crystallinity of as-prepared samples was investigated by X-ray diffraction technique and the corresponding XRD results are illustrated in Fig. 27. The majority of XRD diffractograms of all samples are clearly corresponded to BiVO₄ monoclinic structure [JCPDS No. 00-058-0430]. The strong diffraction peak at $2\theta = 28.9^\circ$ assigns to (-1,1,2) plane of BiVO₄ monoclinic. It is observable that the impurity phases at $2\theta = 24.5^\circ$, 32.8° and 48.5° ascribed to V₂O₃ crystalline structure [JCPDS No. 85-1411] were obtained in the samples synthesized at pH = 3, 5 and 10 while the samples prepared at pH = 7 and 11 possess only BiVO₄ monoclinic structure without any existence of impurity phases. This feature suggests that BiVO₄ particles can be successfully prepared by facile and single-step sonochemical process at certain preparing precursor and pH of the precursor could be considered as a crucial synthesis factor. The possible reactions and mechanism taking the key role on the formation of BiVO₄ particles via sonochemical process can be proposed. During extreme ultrasonic radiation in sonochemical process, cavitation effect is initiated via rapid collision by great amount of ultrasound energy. This collision could quickly heighten specific temperature area

The possible reactions and mechanism taking the key role on the formation of BiVO₄ particles via sonochemical process can be proposed. During extreme ultrasonic radiation in sonochemical process, cavitation effect is initiated via rapid collision by great amount of ultrasound energy. This collision could quickly heighten specific temperature area that can effectively expedite the condensation reactions of hydroxyl groups and generate the nucleation of fine nanoparticles of BiVO₄ via following chemical reactions [7]:

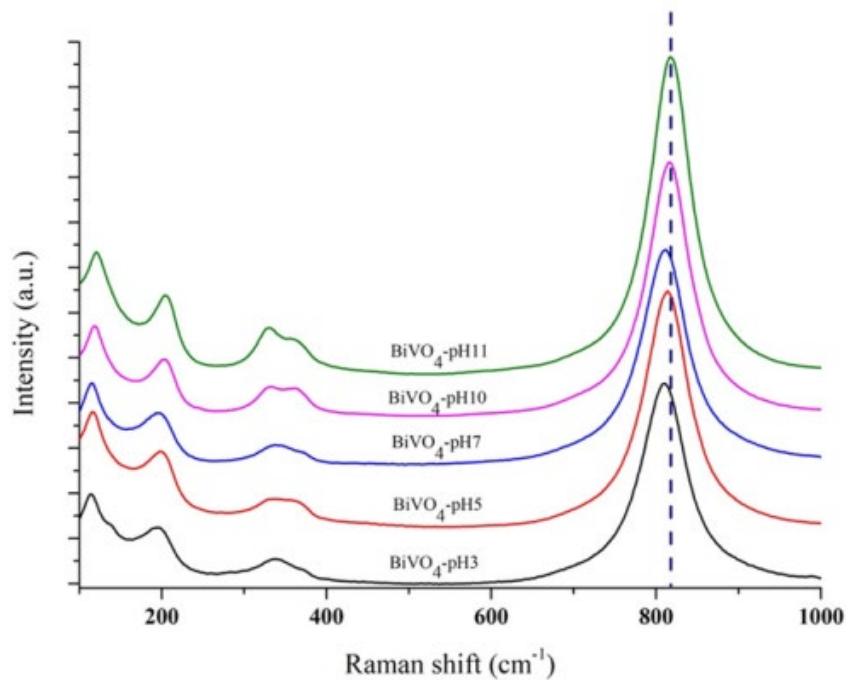
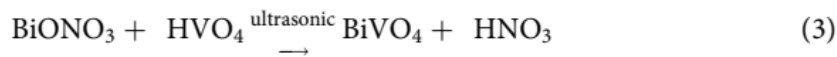


Fig. 28. Raman spectra of BiVO_4 specimens synthesized by sonochemical method with different pH= 3, 5, 7, 10 and 11.

Raman spectra of as-prepared BiVO_4 were measured using green laser (532 nm) as an excitation source and corresponding spectra are shown in Fig. 28. Raman shift around 210, 324, 366 and 826 cm^{-1} are observed for all prepared samples. Raman spectrum at around 210 cm^{-1} is correlated to the BiVO_4 structural formation while the higher band around $810\text{--}826\text{ cm}^{-1}$ is referred to the V-O vibration. Vibration peaks at 324 and 366 cm^{-1} are typically associated to the symmetric and asymmetric deformation mode of VO_4^{3-} [8]. The trifling redshift in Raman bands at 809, 814, 812, 816 and 824 cm^{-1} can be noticed for the samples prepared with different pH of 3, 5, 7, 10 and 11, respectively. This shift is correlated to the variation in bond length of V-O that is very sensitive for degree of crystallinity, defects, disorder aggregation and particle size [8]. The relation between metal-oxygen bond length and Raman stretching frequency shares an inverse relationship that is able to lower metal-oxygen bond length corresponding to the high stretch frequency [9, 10]. This feature implies that the pH value of starting precursor has significant influence on chemical bonding and related structural properties of the prepared BiVO_4 .

FTIR spectroscopy was used to verify chemical bondings of as-synthesized BiVO_4 prepared with different pH. Fig. 29 shows the corresponding results of all samples. The absorption spectra at wavenumber of 474 cm^{-1} could be assigned to the symmetric bending mode of VO_4^{3-} [11] while the broad band at $500\text{--}900\text{ cm}^{-1}$ of all specimens are generally characteristic band of asymmetric stretching and symmetric stretching vibration of the metal and oxygen bond. The strong peaks around 608, 615, 610, 624 and 626 cm^{-1} of BiVO_4 prepared with different pH value 3, 5, 7, 10 and 11, respectively are correlated to Bi-O vibration bonding [12]. Furthermore, the broad peak around $1200\text{--}1500\text{ cm}^{-1}$ is ascribed to O-H stretching due to incomplete reaction from the precursors and moisture.

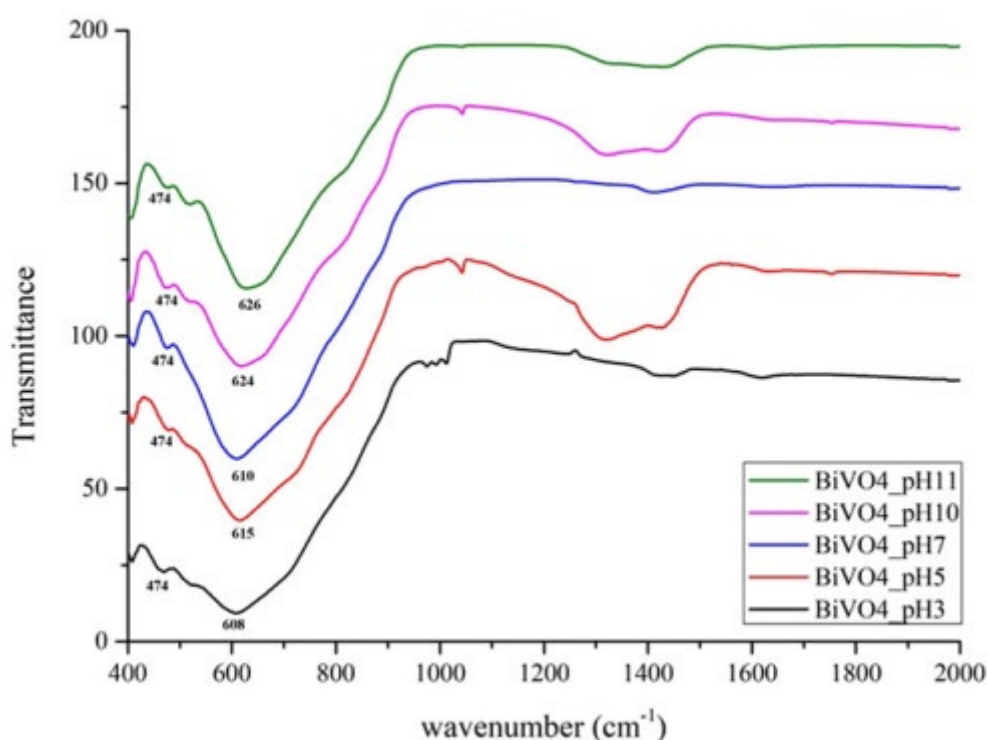


Fig. 29. FTIR spectra of BiVO₄ specimens synthesized by sonochemical method with different pH = 3, 5, 7, 10 and 11

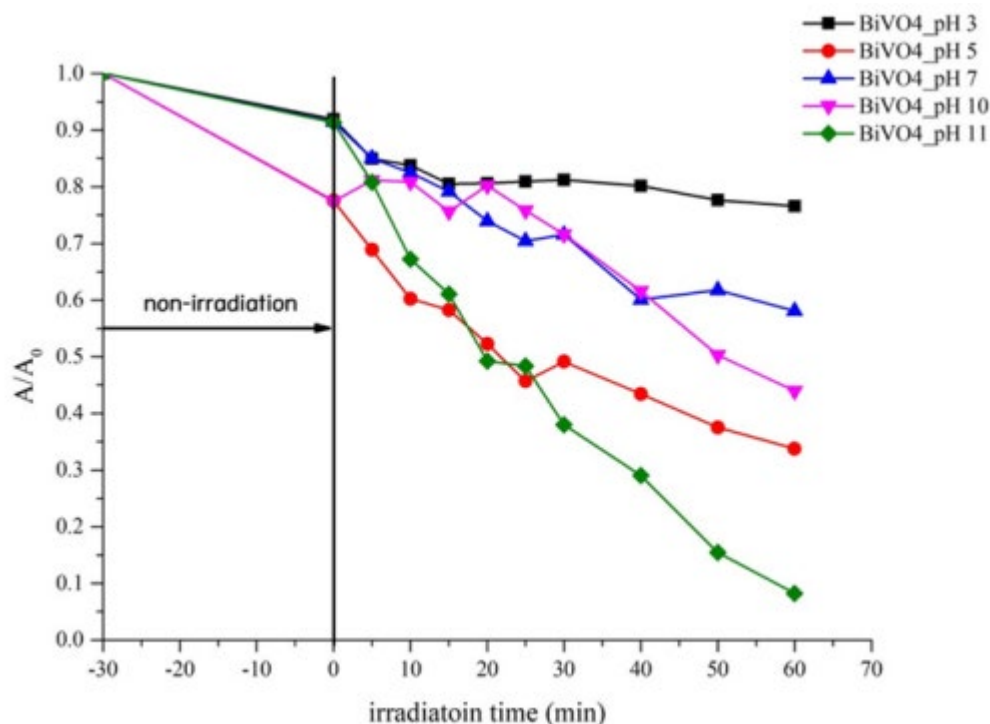


Fig. 30. Photocatalytic testing for decomposition of RhB dye solution with different photocatalyst materials under visible light irradiation.

The visible-light driven photocatalytic activities of the as-synthesized samples were evaluated through the photo-degradation of RhB dye solution. Fig. 30 shows the degradation curve of RhB using different catalysts under visible irradiation. It is clearly observed that the dye solution was degraded with increasing reaction time. The slight decrease of dye concentration before light illumination could be due to self-adsorption of the catalysts. At 60 min of irradiation time, 30% decomposition of dye solution was obtained in BiVO₄ catalyst prepared at pH 3. The superior degradation of dye solution was found in BiVO₄ prepared at pH 11 with almost 90% degradation while BiVO₄ prepared at pH = 5, 7, and 10 exhibited 70%, 40% and 60% of RhB degradation, respectively. According to the results, the high performance of photocatalytic behavior was found in BiVO₄ synthesized at pH 11 due to the complete formation of monoclinic BiVO₄ without impurity as shown in XRD and Raman spectra results and great active surface area of exceptional needlelike low-dimensional nanostructure of the obtained product.

• Conclusions

BiVO₄ nanoparticles can be synthesized by single-step sonochemical method operated at room temperature at different pH value of starting precursor without further thermal treatment process. The crystalline structures of as-prepared samples belong to monoclinic phase with V₂O₃ impurity phase when the samples were prepared at pH = 3, 5 and 10. The morphologies of as-prepared samples appear in various shapes depending on pH value of starting precursor. The superiority in photocatalytic performance of the sample acting as visible light activated catalyst is found in

BiVO₄ synthesized at higher pH value. The excellent photocatalytic activity could be attributed to the good crystallinity and great active surface area of low dimensional structure of BiVO₄ monoclinic sample.

• Reference

- [1] S. Chala et al., Enhanced visible-light-response photocatalytic degradation of methylene blue on Fe-loaded BiVO₄ photocatalyst, *J. Alloy Compd.* 597, 129 (2014). DOI: [10.1016/j.jallcom.2014.01.130](https://doi.org/10.1016/j.jallcom.2014.01.130).
- [2] A. Tayyebi, T. Soltani, and B. Lee, Effect of pH on photocatalytic and photoelectrochemical (PEC) properties of monoclinic bismuth vanadate, *J. Colloid Interf. Sci.* 534, 37 (2019).
- [3] M. Gotic et al., Synthesis and characterisation of bismuth(III) vanadate, *J. Mol. Struct.* 744–747, 535 (2005). DOI: [10.1016/j.molstruc.2004.10.075](https://doi.org/10.1016/j.molstruc.2004.10.075).
- [4] C. Wattanawikkam, and W. Pecharapa, Sonochemical synthesis, characterization, and photocatalytic activity of perovskite ZnTiO₃ nanopowders. *IEEE. Trans. Ultrason. Ferroelect. Freq. Control.* 63 (10), 1663 (2016). DOI: [10.1109/TUFFC.2016.2593002](https://doi.org/10.1109/TUFFC.2016.2593002).
- [5] U. O. Bhagwat et al., Sonochemical synthesis of Mg-TiO₂ nanoparticles for persistent Congo red dye degradation, *J. Photochem. Photobiol. A. Chem.* 346, 559 (2017). DOI: [10.1016/j.jphotochem.2017.06.043](https://doi.org/10.1016/j.jphotochem.2017.06.043).
- [6] T. J. Mason, and J. P. Lorimer, *The Uses of Power Ultrasound in Chemistry and Processing. Applied Sonochemistry* (Wiley-VCH Verlag, Weinheim, Germany, 2002), pp. 303.
- [7] L. Zhou et al., Single-crystalline BiVO₄ microtubes with square cross-sections: microstructure, growth mechanism, and photocatalytic property, *J. Phys. Chem. C.* 111 (37), 13659 (2007). DOI: [10.1021/jp065155t](https://doi.org/10.1021/jp065155t).
- [8] A. Zhang et al., Effects of pH on hydrothermal synthesis and characterization of visiblelight-driven BiVO₄ photocatalyst, *J. Mol. Catal. A. Chem.* 304 (1–2), 28 (2009). DOI: [10.1016/j.molcata.2009.01.019](https://doi.org/10.1016/j.molcata.2009.01.019).
- [9] S. R. M. Thalluri et al., Insights from crystal size and band gap on the catalytic activity of monoclinic BiVO₄, *Int. J. Chem. Eng. Appl.* 4 (5), 305 (2013). DOI: [10.7763/IJCEA.2013.V4.315](https://doi.org/10.7763/IJCEA.2013.V4.315).
- [10] F. D. Hardcastle, and I. E. Wachs, Determination of vanadium-oxygen bond distances and bond orders by Raman spectroscopy, *J. Phys. Chem.* 95 (13), 5031 (1991). DOI: [10.1021/j100166a025](https://doi.org/10.1021/j100166a025).
- [11] P. Pookmanee et al., Preparation and characterization of BiVO₄ powder by the sol-gel method, *Ferroelectrics.* 456 (1), 45 (2013). DOI: [10.1080/00150193.2013.846197](https://doi.org/10.1080/00150193.2013.846197).
- [12] Y. Astuti et al., Synthesis of a-bismuth oxide using solution combustion method and its photocatalytic properties, *IOP Conf. Ser.: Mater. Sci. Eng.* 107, 012006 (2016). DOI: [10.1088/1757-899X/107/1/012006](https://doi.org/10.1088/1757-899X/107/1/012006).
- [13] Y. Shen et al., The synthesis of bismuth vanadate powders and their photocatalytic properties under visible light irradiation, *J. Alloy Compd.* 496 (1–2), 287 (2010). DOI: [10.1016/j.jallcom.2010.01.144](https://doi.org/10.1016/j.jallcom.2010.01.144).
- [14] P. Dong et al., Template-free synthesis of monoclinic BiVO₄ with porous structure and its high photocatalytic activity, *Materials.* 9 (8), 685 (2016). DOI: [10.3390/ma9080685](https://doi.org/10.3390/ma9080685).

3. Project output

3.1 Publications

1. C. Wattanawikkam and W. Pecharapa, "Synthesis and characterization of Zn-doped TiO₂ nanoparticles via sonochemical method", *Integrated Ferroelectrics* Vol. 165, issue 1, pp. 165-173.
2. W. Mekprasart, T. Tangcharoen, P. Nakhanivej and W. Pecharapa, "Synthesis and characterization of cubic-like zinc stannate powders prepared by co-precipitation method", *Chiang Mai Journal of Science*, 43(2), (2016), pp 345-350.
3. Chakkaphan Wattanawikkam and Wisanu Pecharapa, "Sonochemical synthesis, characterization and photocatalytic activity of perovskite ZnTiO₃ nanopowders", *IEEE Transactions on Ultrasonics Ferroelectrics and Frequency Control*, Vol. 63, Issue 10, (2016) pp. 1663-1667.
4. Chakkaphan Wattanawikkam, Weerachon Phoothong and Wisanu Pecharapa, "Structural, Optical and Magnetic properties of Diluted Magnetic Perovskite ZnTiO₃ doped with Co and Mn Prepared by Sonochemical Method", *Journal of Nanoscience and Nanotechnology*, 17, (2017), pp. 3620-3628.
5. Chakkaphan Wattanawikkam, Wisanu Pecharapa and Keiichi Ishihara, "X-ray absorption spectroscopy analysis and magnetic properties of M-doped TiO₂ nanoparticles (M=Co, Mn, Ni and Zn) Prepared by co-precipitation method", *Ceramics International*, Vol. 43 S1, (2017) pp. s397-s402
6. Weerachon Phoothong, Sorapong Pavasupree, Anucha Wannagon, Kanokthip Boonyarattanakalin, Wanichaya Mekprasart, Wisanu Pecharapa, "Characterization and X-ray Absorption Near Edge Spectroscopy of Nanoparticles Derived from Natural Ilmenite Ore via Acid-assisted Mechanical Ball-milling Process", *Advances in Natural Sciences: Nanoscience and Nanotechnology*, 8, (2017) 035012 (8 pages)
7. W. Charerntanom, W. Pecharapa, S. Pavasupree, S. Pavasupree, "Effect of Calcination Temperature on Structure and Photocatalytic Activity Under UV and Visible Light of Nanosheets from Low-cost Magnetic Leucoxene Mineral", *Photonics and Nanostructures-Fundamentals and Applications*, 25 (2017), pp. 38-45
8. Thanaphon Kansaard, Weerachon Phoothong, Wanichaya Mekprasart, Samanya Sanguanpak, Anucha Wannakon, Wisanu Pecharapa, "Comparison Study of Photocatalytic Activity of Titanium-Rich Materials Derived from Natural Minerals Ores Using Acidic Leaching", *Key Engineering Materials*, 751 (2017), 813-818.
9. Wanichaya Mekprasart, Kanokthip Boonyarattanakalin, Wisanu Pecharapa, Keiichi N. Ishihara, "Optical Characteristics of Samarium doped ZnAl₂O₄ Nanomaterials Synthesized by Vibrational Milling Process", *Materials Today: Proceedings*, 5 (2018) 14126-14130.
10. Thanaphon Kansaard, Wadweaw Yimwan, Weerachon Phoothong, Wanichaya Mekprasart, Samanya Sanguanpak, Anucha Wannakon and Wisanu Pecharapa, "Hydrophilic and Photocatalytic Properties of Dip-coated Synthetic Rutile-based Thin Films Derived from Minerals Ores", *Materials Today: Proceedings*, 5 (2018) 11068-

11073.

11. C. Prommalikit, W. Mekprasart, W. Pecharapa, “Effect of Milling Speed and Time on Ultrafine ZnO Powder by High Energy Ball Milling Technique”, *IOP Conference Series: Journal of Physics*, 1259 (2019) 012023.

3.2 Conference

1. C. Wattanawikkam, W. Pecharapa, K. N. Ishihara, “Preparation and characterization of M-TiO₂ (M=Co, Mn, Zn, Ni) nanoparticles via co-precipitation method”, 23rd International Symposium on Metastable, Amorphous and Nanostructured Materials (ISMANAM 2016), 3-8 July 2016, Nara, Japan.
2. C. Wattanawikkam, W. Pecharapa, K. N. Ishihara, “Synthesis and Photocatalytic Activity of Perovskite Co-doped ZnTiO₃ Synthesized by Sonochemical Method”, Japan Society of Powder and Powder Metallurgy (JSPM) spring meeting, 2016, Kyoto Institute of Technology, Kyoto, Japan.
3. Thanaphon Kansa-ard, Wadweaw Yimwan, Weerachon Poohinkong, Samunya Sanguanpak, Anucha Wannakon and Wisanu Pecharapa, “Preparation of Synthetic Rutile by Acidic Leaching of Ilmenite Ores using HCl Acid as Leaching Agent”, International Conference on Science and Technology of Emerging Materials (STEMa2016), 27-29 Jul 2016, Pattaya, Thailand.
4. Thanaphon Kansa-ard, Wadweaw Yimwan, Weerachon Poohinkong, Wanichaya Mekprasart, Samunya Sanguanpak, Anucha Wannakon and Wisanu Pecharapa, “Hydrophilic and Photocatalytic Properties of Dip-coated Synthetic Rutile-based Thin Films Derived from Minerals Ores, The 5th Thailand International Nanotechnology Conference (Nano Thailand 2016), 27-29 Nov 2016, Nakorn Ratchasima, Thailand.
5. T. Kansaard, W. Poohinkong, W. Mekprasart, S. Sanguanpak, A. Wannakon and W. Pecharapa, “Comparison Study of Photocatalytic Activity of Titanium-rich Materials Derived from Natural minerals Ores using Acidic Leaching”, Southeast Asia Conference on Thermoelectrics (SACT2016), 15-18 Dec 2016, Danang, Vietnam.
6. Wanichaya Mekprasart, Titarat Thongpradith, Wisanu Pecharapa and Keiichi N. Ishihara, “Photocatalytic Properties and Plastic Degradation of Synthetic Rutile TiO₂ from Natural Ore”, JSPM International Conference on Powder and Powder Metallurgy ~ 60th Anniversary~ (JSPMIC2017), 7-9 Nov 2017, Kyoto, Japan.
7. Thanaphon Kansa-ard and Wisanu Pecharapa, “Characterization of BiVO₄ Nanoparticles Prepared by Sonochemical Process”, Southeast Asia Conference on Thermoelectrics (SACT2018), 14-17 Dec 2018, Siem Reap, Cambodia.
8. Thanaphon Kansaard, Wisanu Pecharapa and Chatpong Bangbai, “Effect of ultrasonic irradiation time on physical properties and photocatalytic performance of BiVO₄ nanoparticles prepared via sonochemical process”, The 2nd Materials Research Society of Thailand International Conference (MRS-Thailand 2019), 10-12 Jul 2019, Pattaya, Thailand.

9. Thanaphon Kansaard, Wanichaya Mekprasart, Keiichi Ishihara and Wisanu Pecharapa, “Optical and Structural Properties of BiVO₄ Nanoparticles Derived Via Rapid Synthesis Sonochemical Process”, The International Conference on Radiation and Emission in Materials (ICREM2019), 15-18 Dec 2019, Bangkok, Thailand.

3.3 Award

1. The Best Poster Award in The International Conference on Radiation and Emission in Materials (ICREM2019) (Mr. Thanaphon Kansaard)

3.4 Staff and student exchange

Name	Exchange period	Research Topic
Asst. Prof. Dr. Wanichaya Mekprasart	5 Oct – 25 Nov 2016	Synthesis of Samarium doped ZnAl ₂ O ₄ Nanomaterials by Vibrational Milling Process
Ammar		
Tittee		
Mr. Thanaphon Kansaard	28 May - 28 Jun 2017	Preparation of Synthetic Rutile by Acidic Leaching of Ilmenite Ores
Miss Titarat Thongpradith	28 May - 28 Jun 2017	Study of Synthetic Rutile TiO ₂ Photocatalyst Efficiency
Miss Kittiya Pluamjai	28 May - 28 Jun 2017	Synthesis of TiO ₂ /cellulose nanocomposite material
Asst. Prof. Dr. Wanichaya Mekprasart	2 Oct – 12 Nov 2017	Solid State Degradation of Plastic by Titania Nanocomposite Photocatalyst Synthesized from Natural Mineral
Mr. Thanaphon Kansaard	2 Oct – 2 Nov 2017	Photocatalytic Properties of Dip-coated Synthetic Rutile-based Thin Films Derived from Minerals Ores
Mr. Hambalee Mahamu	8-27 Oct 2019	Fabrication of ZnO rod pattern for optoelectronic device
Ms. Arisa Pornpugdewatana	8-27 Oct 2019	Preparation of Synthetic Rutile by Acidic Leaching of Hydroilmenite Ores
Mr. Thanaphon Kansaard	5 - 11 Jan 2020	Characterization of BiVO ₄ Nanoparticles Prepared by Sonochemical Process

3.5 Activities under collaborative research in the title of “Synthesis and characterization of new photocatalytic nano-materials”

Activity 1: Training and workshop on High energy ball milling machine by Mr.Daisuke Nagao, Managing Director, Nagao System INC. in College of Nanotechnology, KMITL.



Activity 2: Presentation in TiO₂ workshop for the production of TiO₂ nanomaterial by high energy ball milling machine at Rajabhat Rajanagarindra University, Chachoengsao, Thailand.



Activity 3: Mechanical Presentation of High energy milling machine with Tanaka Chemical (Thailand) Co., Ltd. to join the research in the topic of “How to decrease volcano clay size in nanoscale”



Activity 4: Presentation and Operation on High energy ball milling machine by Mr.Daisuke Nagao, Managing Director, Nagao System INC. in STEMa International conference at Pattaya, Thailand.



Activity 5: Usability table of High energy ball milling machine obtained from JASTIP Fund during March 2016 to August 2017 at College of Nanotechnology, KMITL

Date	Name	Affiliation	Propose	Usability
2016/03/02	3 rd year bachelor student	College of Nanotechnology, KMITL	To study milling mechanism of high energy ball milling system to produce nanoscaled product as the part of composite class in College of Nanotechnology, KMITL	1
2016/03/23	Assist. Prof. Dr. Wanichaya Mekprasart	College of Nanotechnology, KMITL	Presentation in TiO ₂ workshop for the production of TiO ₂ nanomaterial by high energy ball milling machine at Rajabhat Rajanagarindra University, Chachoengsao, Thailand.	1
2016/03/28	Ms. Talatda Saradat	Tanaka Chemical (Thailand) Co., Ltd	Mechanical Presentation of this machine to join the research in the topic of “How to decrease volcano clay size in nanoscale”	2
2016/05/12	Assist. Prof. Dr. Sorapong Pavasupree	Faculty of Engineering, RMUTT	To reduce mineral size and use the product in photocatalytic application as part of the project “Synthesis of Titanium Dioxide from Natural Minerals Used as Solar-light-activated Catalyst for dye degradation from laundry Industrial Applications”	3
2016/06/17	Dr. Samunya Sanguanpak	MTEC, NSTDA	To reduce mineral size and use the product in tile coating process as part of the project “The Application of Titanium Dioxide from Natural Minerals Used as coating material for Tile Industrial”	3
2016/07/27 to 29	Mr.Daisuke Nagao	Nagao System INC.	Product presentation in STEMa International conference at Pattaya, Thailand	-
2016/08/08 to 2016/11/14	Miss Nisarath Huilek	Suratthani Rajabhat University	Use the machine in cooperative project at College of Nanotechnology, KMITL in the topic of “ Effect of the crucial parameters in High-Energy Ball Milling and calcination process on the product of ZnO–Al ₂ O ₃ mixture”	60

2016/10/06, 13 and 20	Miss Tasama Pothang	College of Nanotechnology, KMITL	Mixed precursor materials of Sr_2CO_3 , Fe_2O_3 , $\text{Fe}_2\text{Mo}_3\text{O}_{12}$ and ZnO	3
Date	Name	Affiliation	Propose	Usability
2017/03/23	Assist. Prof. Dr. Wanichaya Mekprasart	College of Nanotechnology, KMITL	Milling of PE and PP sample	1
2017/04/21 to 2017/05/22	Ms. Ratchadaporn Chailor	Ubonrachatani Rajabhat University	Use the machine in cooperative project at College of Nanotechnology, KMITL in the topic of “ Mechanical Synthesis and Investigation of BiVO_4 Nanomaterial as the Possibility of Visible-light Photocatalyst ”	5
2017/06/12 to 2017/08/01	Assist. Prof. Dr. Winnadda Wongwiriyan	College of Nanotechnology, KMITL	To reduce carbon black powder	5
2017/08/04 to 2017/08/08	Mr. Kittipob Sermsukpradit	College of Nanotechnology, KMITL	To synthesize Sm_2O_3 doped in Zn_2SnO_4 material	4

Rural Electrification Study

1. Impacts Evaluation through Objective and Subjective Measurements in Rural Electrification Schemes in Southeast Asia

Hideaki Ohgaki^a, Hang Seng Che^b, Jordi Cravioto^a, Satoru Kobayashi^a, Hla Toe^c, Khin Khin Kyaw^c, Bun Long^d, Etu Ou Daya^d, Chia Kwang Tan^b, Nasrudin Abd Rahim^b

^aKyoto University, Kyoto, 611-0011 Japan

^bUMPEDAC, University of Malaya, Kuala Lumpur, 59990 Malaysia

^cPyaw University, Bago 08156, Myanmar

^dInstitute of Technology of Cambodia, Phnom Penh, Cambodia

Abstract

We analyze the impacts of rural electrification on the quality of life of four Southeast Asian rural villages in Malaysia, Cambodia, and Myanmar using the effect of different electrification schemes, namely grid extension, centralized solar system and solar home system. In a multidimensional approach we look into the effects on subjective well-being of the community through a quality of life index (QoLI), as well as objective indicators such as the multidimensional energy poverty index (MEPI) and active time usage by using two sets of interview data, a first one is prior to or right after the electrification, and the second one is after the electrification. Despite the common perception that the grid extension is a preferable scheme than the solar systems, we find no meaningful difference in terms of the impacts on the communities' quality of life, both from the subjective QoLI perspective as well as the objective MEPI and active time usage measures. As a matter of fact, one out of the two villages electrified through grid extension shows a reduction in satisfaction. Our findings highlight the level of deprivation of the villagers, their specific human needs, and their context (geography, demographics, and culture), which all play essential roles on the effect of any electrification scheme.

Keywords: rural electrification, QOL, energy poverty, Southeast Asia, before-and-after

1. Introduction

In 2017, the UN reported that about one billion people still live without electricity, especially in rural areas of developing countries [1]. While grid extension is

considered the conventional way of improving access to electricity, such a scheme is sometimes too expensive. The recent advancements in renewable energy technology, particularly solar energy, have opened new possibilities for supplying power via off-grid/microgrid systems. Over the past decades, various rural electrification projects have been implemented under each countries' national energy plan in line with the 7th objective in the Sustainable Development Goals (SDGs): "Energy for all"[2]. The topic of rural electrification has gained popularity among the researchers, with many papers dedicated to the feasibility or techno-economic studies on different rural electrification schemes [3]–[7] as well as rural electrification policies and framework [8]–[11].

With the enormous efforts and investment dedicated to rural electrifications, it is important to quantify their impacts. Some specific studies on the social-economic implication of rural electrification have been reported in the past, particularly for South Asia and African countries such as India [12], Bangladesh [13], Ghana [8], Nepal [14] Rwanda [15], etc. Generally, these studies concluded that electrifications brought positive changes to the rural communities with improved health, income, opportunity for education and jobs, environmental sustainability, creation of facility for social activities, etc., which are considered to improve the overall quality of life (QoL). However, in most of these studies, either macro-level data (such as those from World Bank or national statistics) were used or qualitative discussions were elaborated mostly based on authors' observations.

In some cases, the macro-level data might not be effective in reflecting the actual conditions of the rural communities. To understand the actual impacts of electrification on specific communities, detailed data collected via surveys or interviews were used for some studies. In [15], actual household data was collected, specifically on hours of lighting usage and children's study time at home, energy expenses as well as household income. In [14], national living standard survey data were used to relate access to electricity with the level of income, education, etc. Another study using surveys done in Nigeria [16] focused on the relation between electricity and household poverty. Analysis using village panel data in Cambodia [17] also suggested electrification increases the household energy expenditure but gives a positive change in terms of school enrollment. In [18], the authors developed a "user perceived value" framework to identify the priorities of the rural villagers in Uganda in terms of 64 categories. Another survey-based study was reported in [19] for villages in Bangladesh, using data collected from solar home system users. Despite the different contexts, these studies generally confirm a positive relation between electrification and household gain, in terms of the extent of energy utilization (in heating, cooling, cooking, etc), life

expectancy, or physical and material gains like the lighting hours and income. Yet, the effect on QoL measures is not as straightforward, particularly on subjective measures and dimensions indirectly related to electrification.

The concept of quality of life is a subject of open debate and can take different forms, where measurements can be done based on objective social indicators or on subjective indicators of well-being [20][21]. Between the two, the objective approach is more common and existing literature on the impact of rural electrification focuses mainly on objective indicators such infant mortality rate, life expectancy, mean years of schooling, gross domestic product, gross national income and water access [22]. There are less discussions on the subjective well-being of rural community related to access to electricity. Researchers in subjective well-being argue that people's own evaluation of their lives is important and needs to be considered as an aspect a "good quality life" [23]. As pointed out in [21], it is important to understand not just objective indicators, but also the subjective well-being of a community in order to fully comprehend the effects on quality of life. While there can be various approaches to measure subjective well-being of an individual or community, [24] provided the fundamental guidelines for such measurements, where three domains, i.e. Life Satisfaction, Affect and Eudaimonic well-being should be included. Alternatively, the five-domains approach was also suggested, covering material and physical well-being, relationships with other people, social, community and civic activities, personal development and fulfillment, as well as Recreation [25]. A notable method for representing subjective QoL is the use of Quality of Life Index [25] [26], where scores are given based on the perceived importance and satisfaction on various domains, and an index is obtained by aggregating the scores into a single figure. From the literature, it is clear that electrification brings improvements in terms of the objective indicators [14], [16], [27]. However, it is interesting to understand the perceived quality of life for a rural community by looking into the satisfactions they have on various aspect of their life with and without electrification.

Impact of rural electrification would also be dependent on the scheme adopted. Grid extension is considered the best option as it usually guarantees continuous supply with high power capability. However, numerous studies have demonstrated the feasibility of rural electrification using solar photovoltaic systems, in the forms of extra-low power solar lantern/solar light (usually not more than 100W) and low power solar home system (typically few tenths or hundreds Watt) [28] or even higher power centralized solar system (few to tenths of kilo Watts) [29]. While the systems' power capability (in terms of the loads that can be driven) is clear, there is a lack of unified discussion on the impacts of rural electrification using different schemes.

This paper intends to study the impacts of different rural electrification schemes in a multi-dimensional manner, considering both objective indicators as well as subjective QoL. Interviews were conducted in four different villages in the three Southeast Asian countries where different rural electrification schemes (grid extension, solar home system, centralized solar system) were implemented. In order to perform a unified discussion on the impacts of rural electrification using different schemes, two sets of interview data were taken, a first one to capture the condition prior to or right after electrification, and the second taken several months after electrification.

2. Rural Electrification Sites

To allow a comparative evaluation of different electrification schemes and communities, four separate villages have been included for this study, namely Kampung Sungai Merah and Menangkin in Malaysia, Oak Pho in Myanmar and Thmor Keo in Cambodia.

Table I: Rural Electrification Sites and Survey Details

Village	Country	Cultural profile	Demographics	Electrification Scheme	Surveys
Kampung Sungai Merah	Malaysia	Iban	5 households (20 inhab.) Mostly fishermen	Solar Home System	First: Prior to electrification (6 interviews) Second: Approximately 17 months after electrification (5 interviews)
Menangkin			22 households (100 inhab.) Mostly farmers	Grid Extension	First: Prior to electrification (19 interviews) Second: Approximately 18 months after electrification (12 interviews)
Oak Pho	Myanmar	Bamar	400 households (2000 inhab.) Mostly farmers	Centralized Solar System	First: 4 months after electrification (19 interviews) Second: Approximately 15 months after electrification (35 interviews)
Thmor Keo	Cambodia	Khmer	215 households (1200 inhab.) Mostly farmers	Grid Extension	First: Prior to electrification (17 interviews) Second: Approximately 13 months after electrification (21 interviews)

The selected villages represent the typical un-electrified households in the respective countries, with income level below their respective national average, and most of them are at the primary education level. Even though the culture for the four villages are slightly different, they have similar economic activities, where the community are mainly farmers and fishermen. The climate conditions for the selected villages are also similar, which is tropical climate typical to the Southeast Asian region. Other than Oak Pho (Myanmar), the first visits to the villages were done prior to electrification, while the second visit was done at least 1 year after electrification. A summary of the key data for the four rural electrification sites is given in Table I.

2.1. Malaysia - Kampung Sungai Merah and Menangkin

The electricity coverage in Malaysia was reported to be 100% in World Data Bank data since 2015. However, in reality, the coverage of electrification is not uniform, with the eastern states of Sabah and Sarawak still having some of their population living off-grid. As a matter of fact, it was reported that the electrification rate for Sarawak was around 89.8% in 2017 [30]. Over the past two decades, there has been a substantial effort by the government to improve electricity coverage in Sarawak, including the implementation of small-scale rural electrification projects using grid extension as well as standalone system utilizing hydro-diesel, solar-diesel hybrid system as well as solar home systems. For this study, two villages with different electrification schemes, i.e. grid extension and solar home system were considered. The communities in both villages are from the Iban tribe, which is the biggest aboriginal tribe in Sarawak. Traditionally, the Iban community lives in “Rumah Panjang”, or longhouse, where different families living in rooms of a single long and narrow building sharing a common veranda. While modern Iban communities such as in Menangkin and Kampung Sungai Merah no longer stay in longhouse, they still maintain the tradition of having strong knitted relation, where villagers usually socialize in the house of the prominent person, usually the head of village, during the evening time.

The first site, Kampung Sungai Merah, is small village located at the west side of Borneo Island and one-hour boat from the nearest town of Sebuyau. The village has a population of 20 inhabitants and 5 households (as of Dec 2018) who are mainly farmers and fishermen. The village was electrified using a 300W Solar Home systems (SHS) in February 2017 [31]. Prior to this, the villagers relied on their own diesel generators for powering lights, TV, and even freezer (for one household) during night time. The first survey was conducted in December 2016, prior to the installation of SHS. The follow-up survey was done in August 2018, approximately 17 months after electrification.

The second village, Menangkin, is located in the Pantu district of Sarawak, which is accessible by car around 4 hours' drive from the city of Kuching. The village has 22 households with approximately 100 residents. The villagers are mainly farmers, working on commercial crops, particularly pepper and oil palm. At the same time, paddy is planted in low volume for self-consumption. Due to its relative proximity to the main city, the village was electrified through grid extension in mid of 2017. The first survey was taken in April 2016, prior to the electrification, while the second survey was in July 2018, approximately one year after electrification. Prior to the grid extension, the villagers relied on individual gasoline generators for lighting at night.

2.2. Cambodia – Thmor Keo

Thmor Keo is an inland village located in Batheay district of Kompung Cham province, which is accessible by car around 2 hours' drive from the city of Phnom Penh. The village has around 215 households, where the villagers are mainly farmers. Prior to electrification, some houses were running their own diesel generator typically for 3-4 hours a day during evening and night time, and some houses used batteries for lighting, radio, and TV.

Electrification was done in August 2018, through grid extension from the private sector under the electricity authority and supplied by EDC (Electricite du Cambodge). The households are charged based on power meter installed. The first interview was done in March 2017 (prior to electrification), while the second interview was conducted in September 2018, approximately 13 months after electrification.

2.3. Myanmar – Oak Pho

The village of Oak Pho is in the Bago province of Myanmar, which is accessible by car around 6 hours' drive from the city of Yangon. There are about 400 households and approximately 2,000 residents in the village, where the villagers are mainly farmers. The village was partially electrified (180 households) in July 2017, where a hybrid mini-grid system (a 20 kW centralized PV system with 2 kAh lead acid battery and 30 kW diesel back-up generator system) has been installed. The villagers were charged based on prepaid meters installed in each household.

Since its installation, the diesel generator has not been turned on, due to the low energy usage in the village. Hence, the system can be considered as a centralized PV system. Unlike the previous 3 villages, the project team was unable to arrange the first visit to the village before electrification. However, the first interview was done in November 2017, just 4 months after the electrification. The second interview was then

conducted in October 2018, approximately 15 months after the installation.

3. Methodology

In order to have a multi-dimensional view on the impact of rural electrification, the interview has been structured to cover both objective indicators as well as subjective well-being indicators of the villagers. Each category contains several scale items from which questions will be asked to obtain responses terms of “satisfaction” and “importance” [26]. On the other hand, objective indicators will rely on items that can be easily quantified, such as physical properties and daily life patterns.

For this interview, the questions are structured to cover ten domains, as shown in Table II. Domains 2 till 7 covers the subjective well-being, while domains 8 and 9 addresses the objective indicators. On top of that, the “perceived” QoL is also asked, where the interviewee was instructed to rate his/her QoL based on a scale of 1 to 10. This overall perceived QoL is used to compare with the QoL Index.

Table II: Ten Domains Used in the Interview.

No	Domains	Scope
1	Background Information	<ul style="list-style-type: none"> Demographic information, such as age, gender, education, family member, living place, and occupation
2	General Satisfaction	<ul style="list-style-type: none"> General level of satisfaction as well as level of importance on time spent, housing, food, clothing, neighborhood, family and personal safety Answers are in 5 level Likert scales
3	Occupational activities	<ul style="list-style-type: none"> Current occupation and feeling toward these activities. Answers in 5 level Likert scales
4	Psychological Well-Being	<ul style="list-style-type: none"> Perceptions/ feeling on life Answer in the form of yes/no response.
5	Symptoms /Outlook	<ul style="list-style-type: none"> Outlook on life as well as symptoms of stress/anxiety Answers in yes/no as well as 5 level Likert scale
6	Social Relations	<ul style="list-style-type: none"> Social relation between neighborhood, family member, and outsiders Answers in 5 level Likert scale
7	Money	<ul style="list-style-type: none"> Satisfaction level and importance in 5 level Likert scale
8	Personal (family) Properties & Daily Life pattern	<ul style="list-style-type: none"> Personal (family) belonging, including TV/radio, refrigerator, cell phone, bicycle/motorbike/car, livestock etc. The fuel and method for cooking is also asked.
9	Electricity Demand & Affordability	<ul style="list-style-type: none"> Electricity demand, current and affordable expenditure for the future expansion
10	Perceived Quality of Life	<ul style="list-style-type: none"> The interviewee is asked to rate his/her quality of life on the scale of 1-10, with 1 being terrible and 10 being excellent.

3.1 Quality of Life Index (QoLI)

To allow numerical comparison of subjective well-being, QoL Index (QoLI) can be utilized by assigning values to the answers in the questionnaire and aggregating them into a single value. The calculation of QoLI here follows the similar procedures of the

Wisconsin Quality of Life Index coding method [26], which will be explained briefly.

For the calculation of the QoLI, only six domains, i.e. Domain 2 to 7 (according to Table II) are considered. Each domain contains questions from one or more of the following three categories:

- a. First is the satisfaction & importance question. For example, in terms of the relationship with family, the set of questions asked was “How satisfied or dissatisfied are you with the relation between you and your family?” and “How important is the relation with your family to you?”. The response for the satisfaction question is assigned a satisfaction level (SL) of -1 to 1 on a 5 level Likert scale, with -1 being very dissatisfied and 1 being very satisfied. Similarly, the importance question will be assigned an importance level (IL) value of 0 to 1, with 0 being not important at all and 1 being extremely important. The second type of questions.
- b. The second type is the multiple-choice question. For example, the interviewee is asked if he/she has “experienced symptoms of emotional distress in the past four weeks” and given five choices of “Not at all”, “A little”, “Some”, “A moderate amount” and “A lot”. Multiple-choice score (MS) are allocated such that 1 is given for “Not at all” and -1 for “A lot”.
- c. The third type is the “Yes-or-No” question, which is used mainly on the Symptom/Outlook part of the survey and marks of 1 or -1 will be given to depending if the question refers to a positive or negative outlook. For example, the interviewee will be asked if he/she “felt proud for having accomplished something in the past four weeks”. Accomplishment Score (AS) given will be 1 for Yes and 0 for No. On the other hand, scores of -1 and 0 will be given for negative outlook question, such as if he/she “felt upset for being criticized in the past four weeks”.

From these, the Domain Score (DS) of each domain can be calculated. For Domain 2, which contains satisfaction & importance question, the DS can be calculated as:

$$DS = \frac{(\sum_{i=1}^m IL_i \times SL_i) + \left(\frac{\sum_{j=1}^n MS_j + \sum_{k=1}^p AS_k}{n + p} \right)}{\sum_{i=1}^m IL_i}$$

where m , n and p are the number satisfaction & importance, multiple-choice and Yes-or-No questions, respectively. For Domains 3, 4, 6, and 7, which do not contain satisfaction & importance question, the domain score is given as:

$$DS = \frac{\sum_{j=1}^n MS_j + \sum_{k=1}^p AS_k}{n + p}$$

In addition, the interviewees are asked on the importance level of Domains 3 to 7. These are considered as the weighting factor (w), with values in the range of 0 to 1 given on a 5 level scale, similar to the importance level question explained earlier. Since there is no weightage assigned to Domain 2, two different variables were considered:

Average Domain Score (ADS) for Domain 2, defined as

$$ADS_2 = \frac{\sum_{i=1}^m SL_i}{m}$$

and Average Weight Score (AWS), defined as

$$AWS_2 = \frac{\sum_{i=1}^m IL_i}{m}$$

The overall quality of life index is then calculated based on the following equation:

$$QoLI = \frac{ADS_2 + (\sum_{i=3}^7 w_i DS_i)}{AWS_2 + \sum_{i=3}^7 w_i}$$

with the subscript representing the Domain index. Since the QoLI is a weighted average of the total domain satisfactions from the interviewees, any missing data will severely skew the calculation. To ensure that the QoLI can accurately reflect the average satisfaction of the interviewees, the survey with incomplete data in one or more of the six domains were completely excluded from the calculation whose number are indicated as the interview number of Table I. In addition, we interviewed the same households for the before-and-after surveys as far as possible to ensure the changes of QoLI reflects the actual changes experienced by the same households.

3.2. Multidimensional Energy Poverty Index and Active Time

Apart from the subjective well-being determined using QoLI explained in the previous section, the impact of electrification should also be quantified using some objective indicators. One of the common measurement of energy poverty is based on the subsistence approach by measuring the percentage of income used for purchasing fuel [32]. This, however, is not too applicable for the communities concerned for two reasons: Firstly, because of difficulty in getting accurate information on the actual household income since the villagers are mainly farmers and fishermen with highly seasonal income; secondly, the villagers have a very low need to spend money on food and house, as they usually grow their own food and build their own house. This means that they can afford to spend more than 10% on fuel, without seriously affecting their financial condition. For this study, Multidimensional Energy Poverty Index (MEPI) [33], [34], as shown in Table III, is used. The MEPI allows the micro-level analysis on five

Table III: Multidimensional Energy Poverty Index

Energy Service	Indicator	Condition to be considered deprived	Weight
Cooking	Modern cooking fuel	Using any fuel besides electricity, LPG, kerosene, natural gas or biogas	0.2
	Indoor Pollution	Food cooked on stove or open fire (no hood/chimney) if using fuel beside electricity, LPG, natural gas or biogas	0.2
Lighting	Electricity access	Does not have access to electricity	0.2
Service provided by means of household appliances	Household appliances ownership	Does not have a fridge	0.13
	Entertainment/ education appliance ownership	Does not have a radio OR television	0.13
Communication	Telecommunication means	Does not have a phone land line OR a mobile phone	0.13

important fundamental energy use, which allow better insights on a community's development from the energy perspective.

Apart from that, the interviewees were also asked on their daily routine (Domain 8), such that their Active Time, defined as the duration from the time they wake up till the time they go to sleep, can be obtained. This can be seen as an indirect measurement of the lighting hours, which is considered as one of the common indicators of rural electrification [3]. Together with MEPI, this forms the objective indicators used to correlate the impact of different rural electrification schemes on the quality of life.

4. Results and discussion

4.1. QoLI and Perceived QoL

Figure 1 shows the average QoLI (calculated based on Section III-A) and the perceived QoL (Domain 10) for the four villages during the first and second visits. It can be observed that both QoLI and perceived QoL showed a similar trend of changes: Out of the four villages, only the villagers in Mengankin showed a reduction in QoLI and perceived QoL, while the remaining three villagers reported a positive increase in both indicators.

However, it is insufficient to just observe the increase or decrease in these indicators, but instead, it is important to understand what constituted to such changes. For the case of the perceived QoL, it is simply impossible to know the reason for this change. However, we could observe a correlation between QoL and QoLI, and for the average QoLI, more insights can be obtained by looking at the six domain scores within the index (Fig. 2).

Generally, it can be observed that SHS associates with a positive increase in most QoL domains. For the case of Kampung Sungai Merah, the villagers reported

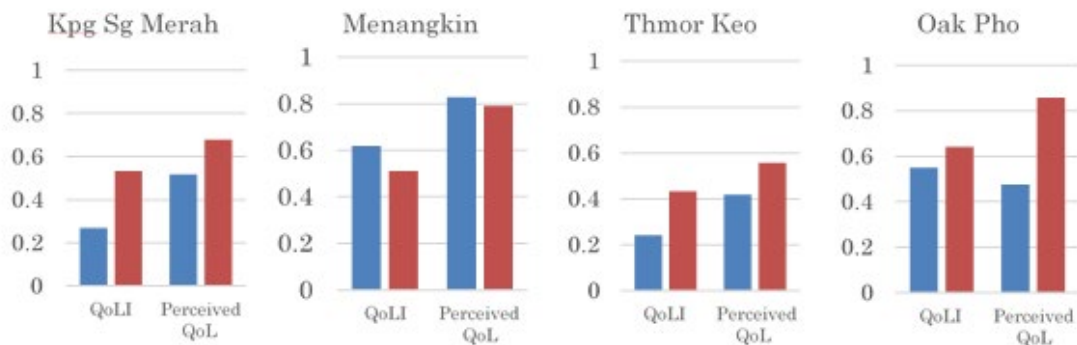
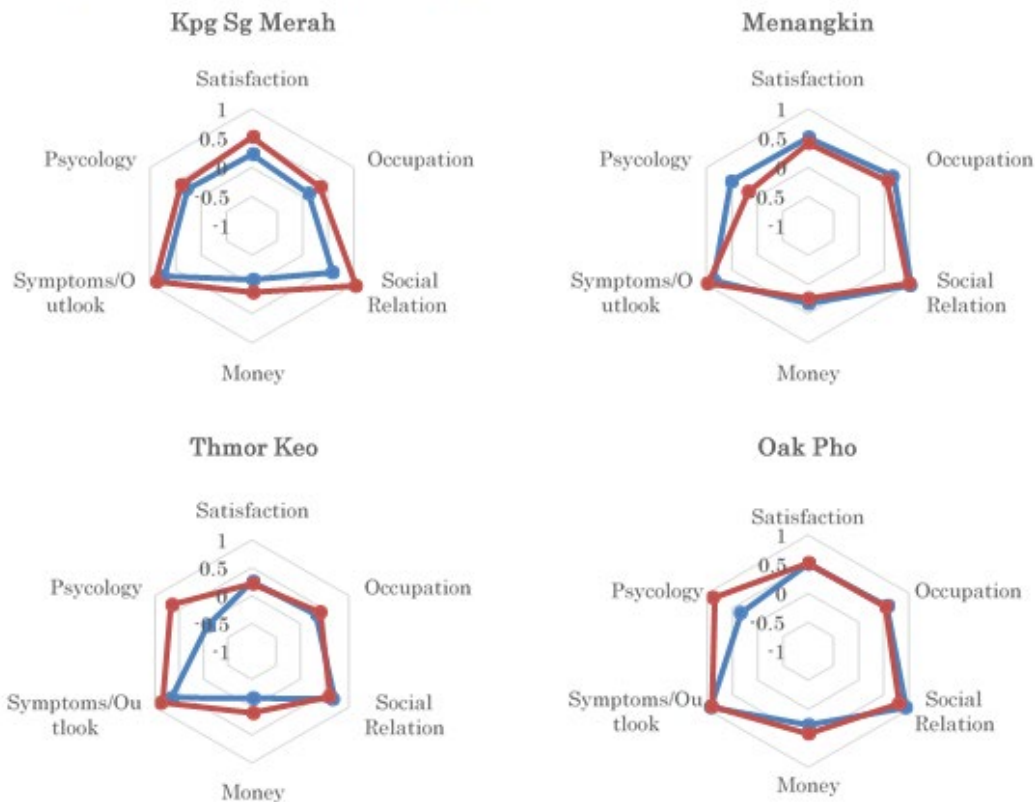


Fig1. Quality of Life Index (QoLI) and perceived QoL for first (blue) and second (red) visits.



increase in all six domains in the second visit, which took place after electrification. For Thmor Keo and Oak Pho, however, there is almost no change in General Satisfaction, Occupation, and Symptom/Outlook. As a matter of fact, a slight decrease in Social Relation satisfaction was observed in the two villages. However, this reduction was compensated by greater improvements in Money and Psychology. For Menangkin, slight reductions were observed in most of the domains, particularly in Psychology. The marginal increase in Symptom/outlook was not able to offset the negative changes in other domain, resulting in an overall reduction in QoLI.

The results showed that there is no considerable difference in terms of the subjective well-being of different rural electrification schemes. Grid extension, which are

traditionally considered to be the best form of rural electrification, does not necessarily result in more satisfaction among the rural community. As a matter of fact, between the two villages that were electrified by grid extension, Menangkin showed a reduction in QoL while Thmor Keo showed an increase in QoL. The difference can be attributed to the different community style and distance from nearby villages. Compared to Thmor Keo, Menangkin is a more modernized society with more access to technologies. Furthermore, the villagers often gather and socialize in a one house, a practice that was not seen in Thmor Keo. Prior to electrification, the difference in electricity usage between households in Menangkin is not obvious, as most of the households rely on their generator sets for electricity. However, after grid extension, the project team observed that there was a greater difference between the households, where richer families can afford more electrical appliances (such as washing machines and rice cookers), while poorer families can only afford to use electricity for basic needs like lightings and fans. This can be a factor affecting the psychological satisfaction of the less well-off villagers, resulting in a drop of the QoL. In case of Thmor Keo, the distance from neighbor villages, which have already been electrified, is very close, within few km. Therefore, villagers have been desiring to have electricity for a long time. On the other hand, Menangkin locates very far from the electrified villages.

Among the three rural electrification schemes, solar home system is considered to be inferior compared to centralized solar system (micro-grid) and grid extension due to its limited power capability. However, this study showed that the highest QoL improvement is for Kampung Sungai Merah, which is electrified via solar home system when compared to the other three villages which received “more superior” electrification scheme.

4.2. MEPI and Active Time

Figure 3 shows the MEPI and Active Time results obtained from the four villages. In terms of MEPI, it is observed that all villages experience positive changes, where the energy poverty level has reduced. The reduction level is much lower in the two Malaysian villages when compared to the Cambodian and Myanmar villages. This is understandable, as the Malaysian villages already have relatively low energy poverty level prior to the electrification scheme. In particular, the two villages were using liquefied petroleum gas for cooking and have some access to electricity using generator sets. The changes in MEPI is mainly driven by the changes in the ownership of household appliance and communication. On the other hand, Thmor Keo and Oak Pho experienced more improvement due to the increased access to lightings as well as entertainment and

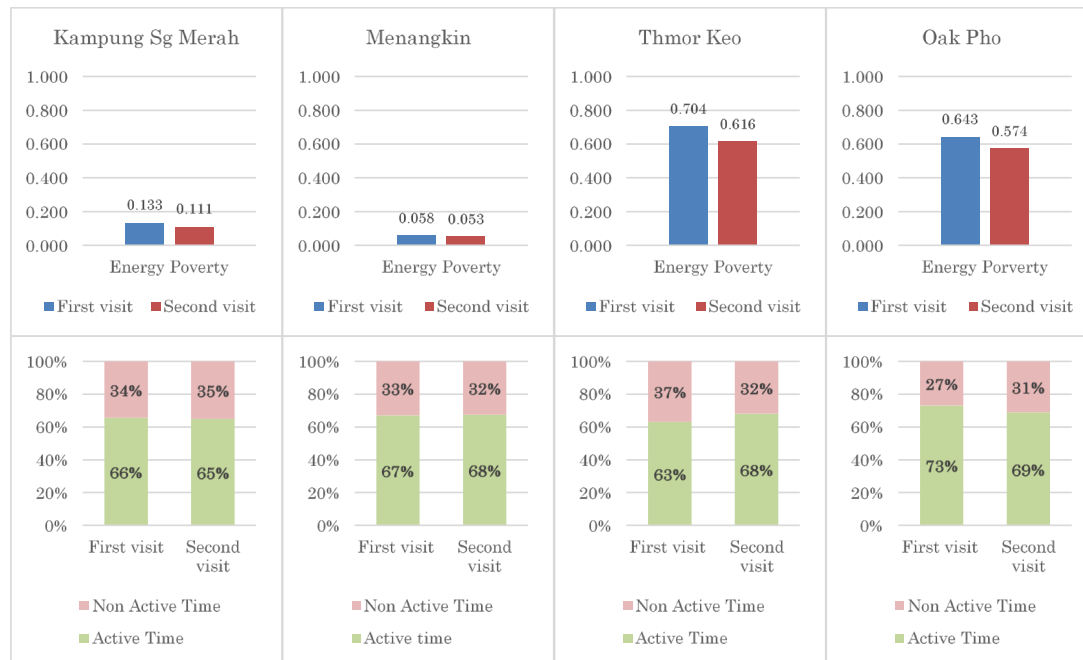


Fig. 3. MEPI (top) and Active/Non-Active Time usage (bottom) for the Four Villages.

communication.

In terms of active time, the changes are almost negligible for Kampung Sungai Merah and Menangkln. For Thmor Keo, the active time showed some increase, but relatively lower than expected with only 5% (approximately 1 hour) from 63% to 68%. Interestingly, the active time for Oak Pho reduced from 73% to 69% between the two visits. It should be recalled here that for Oak Pho, the first visit was shortly after the electrification was done while the second visit is around 1 year after electrification. The changes in active time here may be considered as the diminished hype from electrification: at the early stage, the villagers were excited with the newly installed lights and were staying up later than usual, increasing their active time to around 73%. However, after some time, the excitement has reduced and the active time settled at a more reasonable percentage of 69%, which is consistent with the other 3 villages.

From the MEPI and Active Time results, it can be concluded that the different electrification schemes did not have considerably different impacts. Again, grid extension did not provide higher improvements when compared to electrification through solar systems. Overall, rural electrification brings positive changes to energy poverty reduction and time usage of the rural community, regardless of the scheme used.

4.3. Other Qualitative Observations

Apart from the QoLI, MEPI and Active Time reported in the preceding sections of this paper, and some notable qualitative observations from the villages should be highlighted here.

It is noted that electrification in the four villages did not translate directly into a substantial increase in income or working time as suggested in some literature. This is mainly due to two reasons: Firstly, the villagers, who were mostly farmers and fishermen who could not directly increase their working time or productivity through the use of electricity. Instead, they improved their comfort level through more extensive use of electric power for light bulbs and fans. In other words, electrification translated into the possibility to spend income on housing as observed in the official household survey in Cambodia [35]. This also evoked the energy services ladder hypothesis, where subsistence needs among low-incomes shift to “comfort and cleanliness” as income increase [36]–[38]. Our analysis might be testifying how electrification associates with such a shift in needs, directing preferences for household equipment associated with energy services connected with such “new” needs. As a matter of fact, the income of the villagers was heavily influenced by the commodity prices, which fluctuate with market demand and thus supports our argument.

Secondly, the actual utilization of electricity greatly depends on the level of deprivation of the villagers prior to electrification. Some of the villagers were already accustomed to electricity, using generators or individual small power solar systems. For instance, the villagers in Malaysia (Kampung Sungai Merah and Menangkin) were generally running generators for 3-4 hours prior to the electrification, so the electrification scheme did not influence their active time meaningfully. In contrast, the villagers from Cambodia were generally on a more deprived condition with limited or no access to electricity before electrification. Consequently, there was a more notable increase in their active time after electrification. This also showed that there is an upper limit to which access to electricity can do in terms of extending the active hours.

Another aspect is that the existing objective indicators, including the MEPI presented here, is not able to clearly quantify the impact of electrification on the rural communities. For instance, the replacement of kerosene light with electric light is commonly regarded as a substantial change in measuring energy poverty. However, based on our observations, kerosene lamps are almost non-existing in the Southeast Asian villages due to the low cost and wide availability of solar lamps. The increasing use of smartphones in rural villages blur the line between communication and entertainment, where TV and radio are no longer considered the main sources of entertaining or channels for information.

Additionally, some aspects related to geography, demographics or culture might be in connection with the outcomes. As pointed out in our first analysis of electrification in Malaysia [31] and briefly mentioned in section II, Iban communities are close-knitted societies with traditions of socializing in one specific communal area of the households, i.e. the “rumah panjang”, reducing the use of electricity in private space for diverse energy services, e.g. room temperature regulation, entertainment, etc. While both communities in Menangkin and Kampug Sungai Merah still maintain such culture, the increase electrification can reduce the communal activities as each individual household starts to have their own entertainment and other electrical appliances. On the other hand, climate needs can also affect certain appliance use, and cultural preferences such as ingredients in the regular diet do not reflect on higher electricity needs for food preservation.

Finally, although the rural electrification scheme did not show significant differences between grid extension and solar panels, there might be long-term effects of SHS and central solar systems which are not considered in our analysis, e.g. problems arising from system management and maintenance, as well as post-operation waste management. All of these aspects are interesting and important to consider in more inclusive studies on implications of the selection of the electrification scheme. This is one fertile ground for future studies. In addition, in terms of the long-term effect, we should note that the impact of the electrification on the education and physical health did not measure in this study. Different electrification schemes could also make some significant differences in these long-term effects.

5. Conclusion and Policy Implications

This paper presented a comparative impact study of different rural electrification schemes in four Southeast Asian rural villages using both objective indicators and subjective well-being measurements. Despite a common belief that rural electrification through grid extension is superior to using solar systems, there was no major change in terms of the quality of life felt by the community as well as the objective indicators using MEPI and active hours. Regardless of the scheme, improving access to electricity generally bring positive changes to the rural community. Furthermore, it is observed that existing objective indicators, such as MEPI is not able to accurately highlight the impacts of rural electrification. Yet, several aspects elucidated through the examination of the outcomes point to suggest that the level of deprivation of the villagers, their specific human needs, and their context (geography, demographics and culture) also play important roles on the effect of any electrification scheme. The present study is a first

approximation to the analysis of electrification schemes in South East Asia. A long term observation and more comprehensive assessment approach, taking into account the utilization of electricity as well as the pre-electrification conditions of the rural community is necessary to allow holistic evaluation on the impact of rural electrification.

References

- [1] International Energy Agency, International Renewable Energy Agency, United Nations Statistics Division, World Bank, and World Health Organization, "Tracking SDG7: The energy progress report 2018," 2018.
- [2] International Energy Agency, "WEO-2017 Special Report: Energy Access Outlook," 2030.
- [3] M. Barman, S. Mahapatra, D. Palit, and M. K. Chaudhury, "Performance and impact evaluation of solar home lighting systems on the rural livelihood in Assam, India," *Energy Sustain. Dev.*, vol. 38, pp. 10–20, Jun. 2017.
- [4] S. Mandal, B. K. Das, and N. Hoque, "Optimum sizing of a stand-alone hybrid energy system for rural electrification in Bangladesh," *J. Clean. Prod.*, vol. 200, pp. 12–27, Nov. 2018.
- [5] S. Mazzola, M. Astolfi, and E. Macchi, "The potential role of solid biomass for rural electrification: A techno economic analysis for a hybrid microgrid in India," *Appl. Energy*, vol. 169, pp. 370–383, May 2016.
- [6] M. S. Ismail, M. Moghavvemi, and T. M. I. Mahlia, "Techno-economic analysis of an optimized photovoltaic and diesel generator hybrid power system for remote houses in a tropical climate," *Energy Convers. Manag.*, vol. 69, pp. 163–173, May 2013.
- [7] C. Smith et al., "Comparative Life Cycle Assessment of a Thai Island's diesel/PV/wind hybrid microgrid," *Renew. Energy*, vol. 80, pp. 85–100, Aug. 2015.
- [8] M. K. Aglina, A. Agbejule, and G. Y. Nyamuame, "Policy framework on energy access and key development indicators: ECOWAS interventions and the case of Ghana," *Energy Policy*, vol. 97, pp. 332–342, Oct. 2016.
- [9] D. Palit and K. R. Bandyopadhyay, "Rural electricity access in South Asia: Is grid extension the remedy? A critical review," *Renew. Sustain. Energy Rev.*, vol. 60, pp. 1505–1515, Jul. 2016.
- [10] T. Urmee and A. Md, "Social, cultural and political dimensions of off-grid renewable energy programs in developing countries," *Renew. Energy*, vol. 93, pp. 159–167, Aug. 2016.
- [11] Y. Malakar, "Evaluating the role of rural electrification in expanding people's capabilities in India," *Energy Policy*, vol. 114, pp. 492–498, Mar. 2018.

- [12] P. Mishra and B. Behera, "Socio-economic and environmental implications of solar electrification: Experience of rural Odisha," *Renew. Sustain. Energy Rev.*, vol. 56, pp. 953–964, Apr. 2016.
- [13] P. K. Halder, "Potential and economic feasibility of solar home systems implementation in Bangladesh," *Renew. Sustain. Energy Rev.*, vol. 65, pp. 568–576, Nov. 2016.
- [14] B. A. Bridge, D. Adhikari, and M. Fontenla, "Electricity, income, and quality of life," *Soc. Sci. J.*, vol. 53, no. 1, pp. 33–39, Mar. 2016.
- [15] G. Bensch, J. Kluve, and J. Peters, "Impacts of rural electrification in Rwanda," *J. Dev. Eff.*, vol. 3, no. 4, pp. 567–588, Dec. 2011.
- [16] O. I. Osanyinlusi, B. A. Awotide, T. T. Awoyemi, A. I. Ogunniyi, and A. A. Ogundipe, "An Evaluation of Rural Electrification and Households' Poverty in Ikole Local Government Area, Ekiti State, Nigeria: An Foster, Greer and Thorbecke Approach," *Int. J. Energy Econ. Policy*, vol. 7, no. 3, pp. 24–30, Jul. 2017.
- [17] C. H. Saing, "Rural electrification in Cambodia: does it improve the welfare of households?," *Oxford Dev. Stud.*, vol. 46, no. 2, pp. 147–163, 2018.
- [18] S. Hirmer and P. Guthrie, "Identifying the needs of communities in rural Uganda: A method for determining the 'User-Perceived Value' of rural electrification initiatives," *Renew. Sustain. Energy Rev.*, vol. 66, pp. 476–486, Dec. 2016.
- [19] E. Kabir, K.-H. Kim, J. Szulejko, E. Kabir, K.-H. Kim, and J. E. Szulejko, "Social Impacts of Solar Home Systems in Rural Areas: A Case Study in Bangladesh," *Energies*, vol. 10, no. 10, p. 1615, Oct. 2017.
- [20] K. C. Land, C. Michalos, Alex, and M. J. Sirgy, Eds., *Handbook of Social Indicators and Quality of Life Research*. New York: Springer Dordrecht Heidelberg, 2012.
- [21] E. Diener and E. Suh, "Measuring Quality of Life: Economic, Social and Subjective Indicators," *Soc. Indic. Res.*, vol. 40, no. 1/2, pp. 189–216, 1997.
- [22] R. Nadimi and K. Tokimatsu, "Modeling of quality of life in terms of energy and electricity consumption," *Appl. Energy*, vol. 212, pp. 1282–1294, Feb. 2018.
- [23] E. Diener, S. Oishi, and L. Tay, "Advances in subjective well-being research," *Nat. Hum. Behav.*, vol. 2, no. 4, pp. 253–260, 2018.
- [24] OECD Guidelines on Measuring Subjective Well-being. OECD, 2013.
- [25] C. S. Burckhardt and K. L. Anderson, "The Quality of Life Scale (QOLS): reliability, validity, and utilization.," *Health Qual. Life Outcomes*, vol. 1, p. 60, Oct. 2003.
- [26] R. Diamond, M. Becker, and R. Becker, "Wisconsin Quality of Life Index (W-QLI): A Multidimensional Model for Measuring Quality of Life," *J Clin Psychiatry*, vol. 60, pp. 29–31, 1999.

- [27] S. Ntanos et al., "A Social Assessment of the Usage of Renewable Energy Sources and Its Contribution to Life Quality: The Case of an Attica Urban Area in Greece," *Sustainability*, vol. 10, no. 5, p. 1414, May 2018.
- [28] X. Lemaire, "Solar home systems and solar lanterns in rural areas of the Global South: What impact?," *Wiley Interdiscip. Rev. Energy Environ.*, vol. 7, no. 5, p. e301, Sep. 2018.
- [29] A. Bilich et al., "Life Cycle Assessment of Solar Photovoltaic Microgrid Systems in Off-Grid Communities," *Environ. Sci. Technol.*, vol. 51, no. 2, pp. 1043–1052, Jan. 2017.
- [30] C. W. Ajan, "Sarawak Alternative Rural Electrification Scheme Providing electricity to off-grid communities in Sarawak," 2018.
- [31] H. Ohgaki et al., "Study on Quality of Life Change for Rural Community through Rural Electrification by Renewable Energy: Preliminary Result," *AJMI - ASEAN J. Manag. Innov.*, vol. 4, no. 2, pp. 1–8, Dec. 2017.
- [32] B. Broadman, *Fuel Poverty: From Cold Homes to Affordable Warmth*. Belhaven Press, 1991.
- [33] P. Nussbaumer et al., "Global Insights Based on the Multidimensional Energy Poverty Index (MEPI)," *Sustainability*, vol. 5, no. 5, pp. 2060–2076, May 2013.
- [34] S. Pelz, S. Pachauri, and S. Groh, "A critical review of modern approaches for multidimensional energy poverty measurement," *Wiley Interdiscip. Rev. Energy Environ.*, vol. 7, no. 6, p. e304, Nov. 2018.
- [35] W. Bank, "Global Consumption Database – Cambodia," 2019. [Online]. Available: <http://datatopics.worldbank.org/consumption/country/Cambodia>. [Accessed: 07-Apr-2019].
- [36] J. Cravioto, E. Yamasue, H. Okumura, and K. N. Ishihara, "Energy service satisfaction in two Mexican communities: A study on demographic, household, equipment and energy related predictors," *Energy Policy*, vol. 73, pp. 110–126, Oct. 2014.
- [37] J. Cravioto and E. Yamasue, "Energy services and life satisfaction: a study on households in two Mexican communities," in *Energy for Society: 1st International Conference on Energy Research & Social Science*, 2017.
- [38] B. K. Sovacool and I. Mukherjee, "Conceptualizing and measuring energy security: A synthesized approach," *Energy*, vol. 36, no. 8, pp. 5343–5355, Aug. 2011.

Project Output

Journal paper

Hideaki Ohgaki, Hooman Farzaneh, Nasrudin Abd Rahim, Hang Seng Che, Mohd Amran

Mohd Radzi, Wallace ShungHui Wong, Lai Chean Hung, "Study on Quality of Life Change for Rural Community through Rural Electrification by Renewable Energy: Preliminary Result", ASEAN Journal of Management & Innovation, ISSN 2351-0307, in Volume 4 Number 2 (2017).

Chaichana, C., Wongsapai, W., Damrongsak, D., Ishihara, N. I., & Luangchosiri, N. "Promoting Community Renewable Energy as a tool for Sustainable Development in Rural Areas of Thailand", Energy Procedia, 141, 114–118. (2017).

竹内亮、「経済成長にともなうベトナム農村におけるエネルギー利用の変化と政策提言-木質バイオマス利用の効率化の必要性」-、「環境経済・政策研究」10 巻、1 号、2017

P. Bhumkittipich, H. Ohgaki, "Development Strategy for Sustainable Solar Home System in the Akha Upland Community of Thailand", Energies. Vol.11 1509 (2019).

Radzi, Mohd Amran Mohd, Rahim, Nasrudin Abd, Che, Hang Seng, Ohgaki, Hideaki, Farzaneh, Hooman, Wong, Wallace Shung Hui, Hung, Lai Chean, "OPTIMAL SOLAR POWERED SYSTEM FOR LONG HOUSES IN SARAWAK BY USING HOMER TOOL", ASEAN Engineering Journal, Vol 9 No 1 (2019), e-ISSN 2586-9159

Jordi Cravioto, Hideaki Ohgaki, Hang Seng Che, ChiaKwang Tan, Satoru Kobayashi, Hla Toe, Bun Long, Eth Oudaya, Nasrudin Abd Rahim, and Hooman Farzaneh, "The Effects of Rural Electrification on Quality of Life: A Southeast Asian Perspective", Energies, 13, 2410 (2020)

Presentation

Hideaki Ohgaki, Hooman Farzaneh, Nasrudin Abd Rahim, Hang Seng Che, Mohd Amran Mohd Radzi, Wallace ShungHui Wong, Lai Chean Hung, "Study on Energy Usage and Quality of Life Change for Rural Community through Rural Electrification by Renewable Energy : Preliminary Result", 6th INTERNATIONAL SYMPOSIUM ON THE FUSION OF SCIENCE AND TECHNOLOGIES, Jeju-si, Korea, (July 18, 2017)

Hideaki Ohgaki, Hooman Farzaneh, Nasrudin Abd Rahim, Hang Seng Che, Mohd Amran Mohd Radzi, Wallace ShungHui Wong, Lai Chean Hung, Long Bun, Oudaya Eth, Wint Wint Kyaw, Hla Toe, "Impact of Solar Home System on Change of Quality of Life in Rural

Community in Sarawak, Malaysia", 6th World Conference on Applied Sciences, Engineering and Technology (Universitas Muhammadiyah Ponorogo, INDONESIA, 2017/8/26)

Hideaki Ohgaki, Hooman Farzaneh, Nasrudin Abd Rahim, Hang Seng Che, Mohd Amran Mohd Radzi, Wallace ShungHui Wong, Lai Chean Hung, Long Bun, Oudaya Eth, Wint Wint Kyaw, Hla Toe, "Impact of Solar Home System on Change of Quality of Life in Rural Community in Sarawak, Malaysia", The 10th Regional Conference on Energy Engineering (RCEnE2017) "Energy Sufficiency and Efficiency through Regional Collaboration" (Yangon Technological University, Yangon, Myanmar, 2017/11/9)

Hideaki Ohgaki, Hooman Farzaneh, Nasrudin Abd Rahim, Hang Seng Che, Mohd Amran Mohd Radzi, Wallace ShungHui Wong, Lai Chean Hung, Long Bun, Oudaya Eth, Wint Wint Kyaw, Hla Toe, "Study on Energy Usage and Quality of Life for Rural Community Through Rural Electrification using Renewable Energy", The 3rd ASEAN Smart Grid Congress and the 5th International Conference on Sustainable Energy (Ho Chi Minh City University of Technology, Ho Chi Minh, Vietnam, 2017/12/4)

Hideaki Ohgaki, Hooman Farzaneh, Nasrudin Abd Rahim, Hang Seng Che, Mohd Amran Mohd Radzi, Wallace ShungHui Wong, Lai Chean Hung, "Study on QOL Change in Rural Community by Renewable Energy Electrification ", 1st International Conference on New Frontiers in Engineering, Science and Technology (Delhi Technological University, New Delhi, India, 2018/1/9)

H. Ohgaki, S. Kobayashi, H. Farzaneh, N.A. Rahim, H.S. Che, M.A.M. Radzi, W.S.H. Wong, L.C. Hung, L. Bun, O. Eth, W.W. Kyaw, H. Toe. A Study on Impact on QOL in Rural Communities in ASEAN by Renewable Energy. The 11th AUN/SEED-Net Regional Conference on Energy Engineering. Manila, Philippines, 27 Sep 2018

H. Ohgaki, S. Kobayashi, H. Farzaneh, N.A. Rahim, H.S. Che, M.A.M. Radzi, W.S.H. Wong, L.C. Hung. Before and After Study on Renewable Energy Installation in Rural Community in Sarawak. 5th JASTIP Symposium "Disaster Risk Reduction and Environmental Sustainability for Social Resilience". Kuala Lumpur, 18 Oct 2018

Yosuke Nakanishi, Kanokvate Tungpimolrut, "Optimal design platform for smart integration of renewable energy in rural area Micro-grid For Rural Areas (Ubon

Ratchathani and Chiang Mai)", mini-workshop on rural electrification research in JASTIP-net, Swissotel Bangkok Ratchada, Bangkok, 2019.2.2

Nasrudin Abd Rahim, Che Hang Seng, Hideaki OHGAKI, ""Rural Electrification using Renewable Energy: Towards Better Sustainability for Rural Community"", mini-workshop on rural electrification research in JASTIP-net, Swissotel Bangkok Ratchada, Bangkok, 2019.2.2

Bun Long, Hideaki OHGAKI, "Innovative DC grid for improving the quality of life of rural area in Cambodia", mini-workshop on rural electrification research in JASTIP-net, Swissotel Bangkok Ratchada, Bangkok, 2019.2.2

Wint Wint Kyaw, Hideaki OHGAKI, "Minigrid using Renewable Energy Sources for rural electrification in Myanmar", mini-workshop on rural electrification research in JASTIP-net, Swissotel Bangkok Ratchada, Bangkok, 2019.2.2

Anugerah Yuka Asmara, Toshio Mitsufuji, AR Rohman Taufik, Hideaki OHGAKI, "Realizing Feasible Solar Cell Project through Appropriate Funding Mechanism and Awareness of Local People in Indonesia", mini-workshop on rural electrification research in JASTIP-net, Swissotel Bangkok Ratchada, Bangkok, 2019.2.2

Hideaki OHGAKI, "RE Implementation: Report from mini-workshop of JASTIP-Net", The 4th JASTIP-WP2 Annual Workshop, Swissotel Bangkok Ratchada, Bangkok, 2019.2.2

Hideaki Ohgaki, Hang Seng Che, Jordi Cravioto, Satoru Kobayashi, Hla Toe, Bun Long, Etu Ou Daya, Chia Kwang Tan, Nasrudin Abd Rahim, Hooman Farzeneh, "Our Findings in Impact of Rural Electrification in ASEAN", Rural Electrification Workshop in KL, Hilton Double Tree Kuala Lumpur, Kuala Lumpur, 2019.6.24

Hideaki Ohgaki, Hang Seng Che, Jordi Cravioto, Satoru Kobayashi, Hla Toe, Bun Long, Etu Ou Daya, Chia Kwang Tan, Nasrudin Abd Rahim, Hooman Farzeneh, "Study on Social Impacts of Rural Electrification in ASEAN", Workshop on Current Status of Renewable Energy in Myanmar and Key Recommendations, Yangon Technological University, Yangon, 2019.7.11

Thein Min Htike, Hideaki Ohgaki, "Renewable Energy Installed Capacity and Recommendations for Renewable Energy Deployment in Myanmar", Workshop on

Current Status of Renewable Energy in Myanmar and Key Recommendations, Yangon Technological University, Yangon, 2019.7.11

Hideaki OHGAKI, "RE Implementation: Report from mini-workshop of JASTIP-net", The 5th JASTIP-WP2 Annual Workshop, Ibis Style Ratchada, Bangkok, 2020.1.20 Workshop

Chatchawan Chaichana, Takuo Nakayama, International Workshop on "Community Renewable Energy", Chiang Mai, Thailand, 2016. 10. 24-25

Nguyen Huu Chiem, Keiishi Ishihara, JASTIP-net Workshop on "Community Renewable Energy in Vietnam, Thailand and Japan 2017", Can Tho, Vietnam, 2017. 7. 28-29

Win Win Kyaw, Hideaki OHGAKI, Workshop on PV Minigird System for Rural Electrification in Myanmar, Technological University, Hmawbi, Myanmar, 2018.12.12

Hideaki Ohgaki, The mini-workshop on rural electrification research in JASTIP-net, Swisshotel Bangkok Ratchada, Thailand, 2019. 2. 2

Nasrudin Abd Rahim, Hideaki Ohgaki, Rural Electrification Workshop, Hilton Double Tree Kuala Lumpur, 2019. 6. 24

Thein Min Htike, Hideaki Ohgaki, Workshop on Current Status of Renewable Energy in Myanmar and Key Recommendations, Yangon Technological University, 2019. July 11